let./vol. **51** - št./no. **7-8/05** - str./pp. **363-540**
zvezek/issue **483-484**

STROJNIŠKI VESTNIK

JOURNAL OF MECHANICAL ENGINEERING

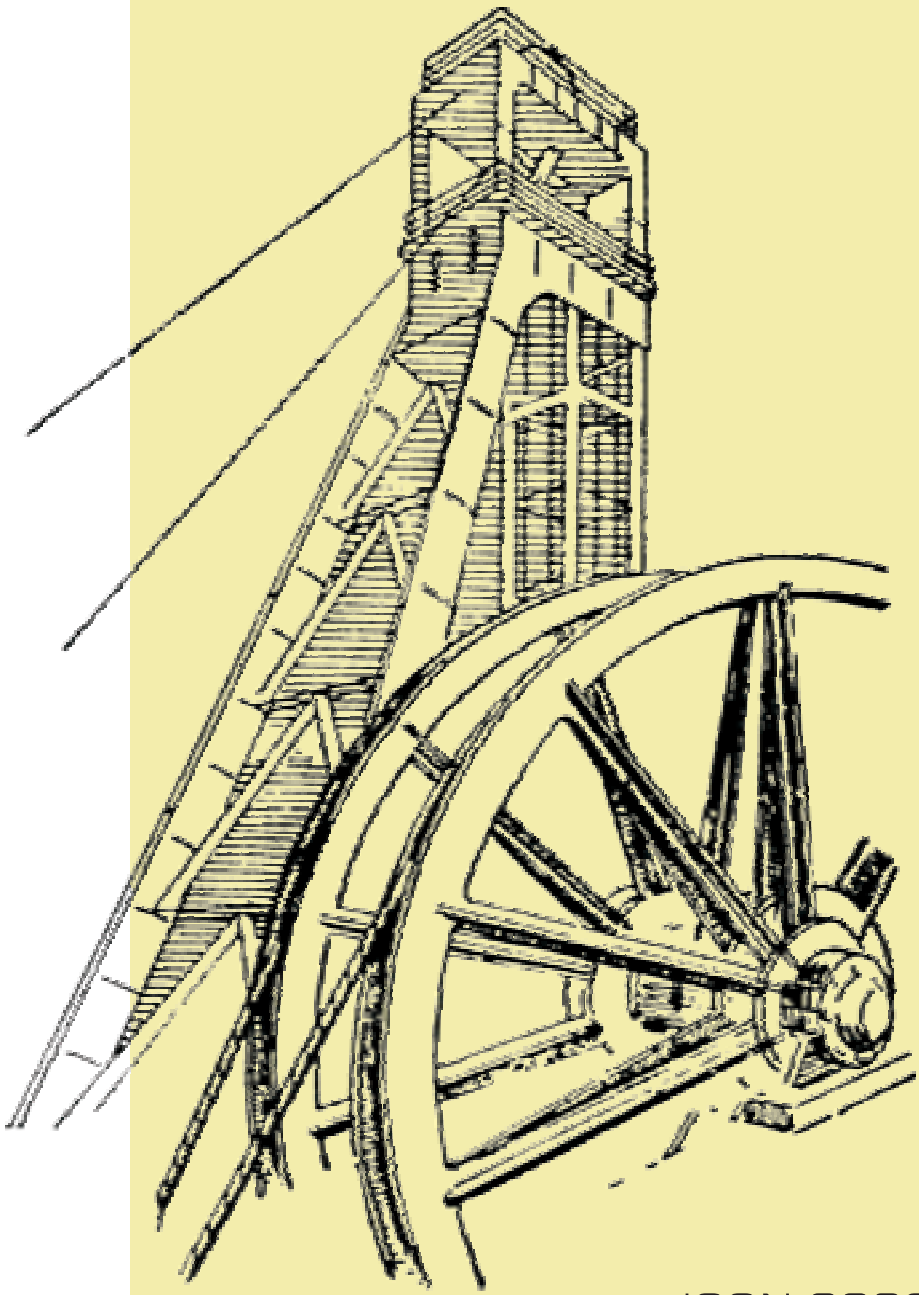

cena 800 SIT

9 770039 248001

ISSN 0039-2480

Vsebina - Contents

Strojniški vestnik - Journal of Mechanical Engineering
letnik - volume 51, (2005), številka - number 7-8
ISSN 0039-2480

Izhaja mesečno - Published monthly

Uvodnik – Editorial

This issue is dedicated to the ASME-ZSIS International Thermal Science Seminar (ITSS) II, co-sponsored by the American Society of Mechanical Engineers (ASME International), the Association of Mechanical Engineers of Slovenia (ZSIS), the International Institute for Refrigeration, Commission B1 (IIR/B1), and the International Centre for Heat and Mass Transfer (ICHMT), which was held in Bled, Slovenia, on June 13-16, 2004.

The ITSS II conference came at a historic moment for Slovenia, which had just become a member of the European Union (EU) on May 1, 2004. The expansion of the EU to 25 members has great implications not only for the politics and economy of Slovenia but also for the science and technology. This will have important and lasting effects such as strengthening the scientific and technology development in the EU as well as throughout the world.

ITSS II provided ample opportunities for discussing individual papers and general issues facing the thermal sciences. The technical program included 128 peer reviewed paper presentations from 36 countries on the following topics: Fundamentals, Energy Systems, Electronics Cooling and Thermal Management, Equipment, Environmental, Measurement Techniques, Micro- and Nano-scale Thermal Phenomenon, Numerical Heat Transfer, and Heat Transfer Enhancement.

In this issue of Strojniški Vestnik - Journal of Mechanical Engineering, 26 selected papers are published, which cover thermal science topics discussed at the ASME-ZSIS International Thermal Science Seminar II.

We would like to gratefully acknowledge the support provided by Professor Andro Alujevič, editor-in-chief of the Strojniški Vestnik - Journal of Mechanical Engineering, and the diligence of Mrs. Suzana Domjan and Dr. Henrik Gjerkeš.

Pričujoč zvezek je posvečen ASME-ZSIS Mednarodnemu seminarju toplotnih znanosti (ITSS) II, ki se je pod pokroviteljstvom ameriškega združenja strojnih inženirjev (ASME International), Zveze strojnih inženirjev Slovenije (ZSIS), Mednarodnega inštituta za hlajenje, komisije B1 (IIR/B1), in Mednarodnega centra za prenos toplote in snovi (ICHMT) odvijal od 13. do 16. junija 2004 na Bledu.

Konferenca je sovpadla z zgodovinskim dogodkom za Slovenijo, ki je s 1. majem 2004, postala članica Evropske zveze (EU). Razširitev EU na 25 članic bo imela velik vpliv ne samo na politiko in gospodarstvo v Sloveniji, ampak tudi na znanost in tehnologijo ter bo pomembno in trajno okrepilo razvoj znanosti in tehnologije v EU in v svetu.

ITSS II je omogočil obilo možnosti za razprave tako o posameznih prispevkih, kot tudi o splošnih zadevah, ki se dotikajo toplotne znanosti. Tehnični program je vključeval predstavitev 128 recenziranih prispevkov iz 36 držav. Razdeljen je bil na naslednja poglavja: Osnove, Energetski sistemi, Hlajenje elektronike in upravljanje s toploto, Oprema, Okolje, Merilna tehnika, Toplotni pojavi na mikro in nano skali, Numerika pri prenosu toplote in Izboljšanje prenosa toplote.

V pričujočem zvezku Strojniškega Vestnika - Journal of Mechanical Engineering, je objavljenih 26 prispevkov, ki zajemajo poglavja toplotne znanosti, o katerih je bilo govora na ASME-ZSIS Mednarodnemu seminarju toplotnih znanosti II.

Radi bi se zahvalili za podporo profesorja Andra Alujeviča, urednika Strojniškega Vestnika - Journal of Mechanical Engineering, in za prizadevnost ga. Suzane Domjan in dr. Henrika Gjerkeša.

Arthur E. Bergles
Rensselaer Polytechnic Institute
Troy, New York
University of Maryland
College Park, Maryland
Massachusetts Institute of Technology
Cambridge, Massachusetts

Iztok Golobič
University of Ljubljana
Faculty of Mechanical Engineering
Ljubljana, Slovenia

Cristina H. Amon
Carnegie Mellon University
Pittsburgh, Pennsylvania

Adrian Bejan
Duke University
Durham, North Carolina

Strojniški vestnik - Journal of Mechanical Engineering 51(2005)7-8, 366-373
UDK - UDC 536.2
Izvirni znanstveni članek - Original scientific paper (1.01)

A Novel Concept for Boiling Heat Transfer Enhancement

D. W. Zhou

Institute of Engineering Thermophysics, Chinese Academy of Sciences
B12, Zhongguancun, Haidian District, Beijing 100080, P.R. China, drdwzhou@hotmail.com

Abstract

The effect of bubble nucleation on boiling heat transfer enhancement has been investigated experimentally. Results show whether boiling heat transfer is enhanced or not depends directly on effective activation of vapor embryos on the heat transfer surface to initiate boiling. The mechanism of boiling heat transfer enhancement is analyzed and the influence factors of incipient boiling superheat are summarized. In light of bubble nucleation effect, the possible techniques for enhancing boiling heat transfer and eliminating boiling hysteresis are proposed and further developed as a principle to guide the research of boiling heat transfer enhancement.

1. Introduction

Boiling heat transfer has received an extensive attention because of its high heat transfer rate. However, most of the previous studies have been carried out to investigate the effects of such single or multi-ply factors as surface roughness [1], liquid temperature [2, 3], flow velocity [4, 5] and system pressure [6, 7] on boiling heat transfer, or to estimate the heat transfer performance through the established mathematical-physical model. Based on the presentation of the experimental data in the forms of $q'' \sim \Delta T_{sat}$ and/or $h \sim q''$, the former elucidates the macro-phenomenon of boiling heat transfer while the latter tries to explore the inherent mechanism of boiling heat transfer by comparing the numerical and experimental results. Consequently, it is assumed here that the primary objective of two above-mentioned methodologies is to study the boiling heat transfer only from the macroscopical point of view.

On the other hand, the heat transfer enhancement is an everlasting subject for both the researchers of heat transfer community of academia and technicians in industry, irrespectively of applied heat flux. Numerous investigations have been conducted experimentally and numerically and hence great achievements have been obtained. For single-phase convective heat transfer, Guo et al. [8] proposed a field synergy principle which can reveal the essence of heat transfer enhancement common to all enhancement methods. Subsequently, Tao and his co-workers [9, 10] extended this principle to elliptic fluid flow and other transport phenomena. This opens the way to active control of convective heat transfer enhancement. To the knowledge of the present author, a similar unified theory for boiling heat transfer enhancement is difficult to find in literatures.

A new means for the data presentation of the experimental results was adopted in this study to investigate the effects of acoustic cavitation, $CaCO_3$ nanoparticles and fluid subcooling on boiling heat transfer. The purpose of the present study are threefold: the effect of bubble nucleation on boiling curves presented in terms of local wall temperature will be depicted; the mechanism of boiling heat transfer enhancement will be analyzed; and the techniques of boiling heat transfer enhancement will be provided to show the importance of this new concept.

2. Experimental Apparatus and Methods

The experimental apparatus and instrumentation are shown schematically in Fig. 1. The test chamber consisted of a cubical vessel made of stainless steel with inside dimensions of 200 mm × 200 mm × 230 mm. A horizontal copper tube with an electrical heating element inside passed through one pair of opposing walls 50 mm above the vessel base. Two viewing windows were installed on opposite sides of the vessel in parallel with the test tube for easy observation and taking pictures of the boiling heat transfer phenomena outside the test section. The vapor was condensed on the surface of a tap-water cooled condenser installed at the top of the vessel and then returned to the pool by gravity. Two

Nomenclature

C	concentration of nanometer particles, grams/lit	d	interior diameter of jet nozzle, m
h	heat transfer coefficient ($q''/(T_w-T_l)$), W/(m^{2}K)	L	sound source distance between the vibrator head and the central horizontal plane, m
P	sound source intensity, expressed by the power actually consumed by the ultrasonic vibrator, W	q''	heat flux, W/m^2
r/d	dimensionless radial distance from stagnation point	T_l	liquid temperature, K
$T_{3\text{-}6}$	local wall temperature on the bottom, top, (forward) side and backward (side) of the tube, K	T_w	arithmetic average of eight local wall temperatures, K
ΔT_{sat}	wall superheat (T_w-T_{sat}), K	$(\Delta T_{sat})_{ONB}$	incipient boiling superheat, K
ΔT_{sub}	fluid subcooling ($T_{sat} - T_l$), K	u	jet velocity, m/s
z/d	dimensionless nozzle-to-plate spacing		

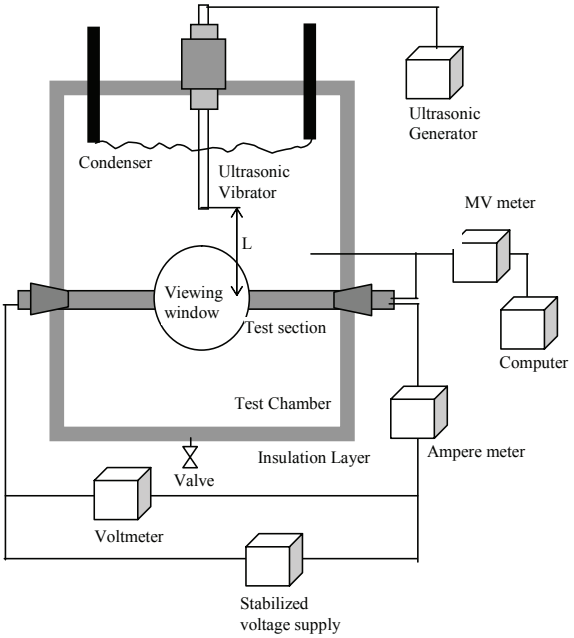

Fig. 1 Schematic layout of experimental setup

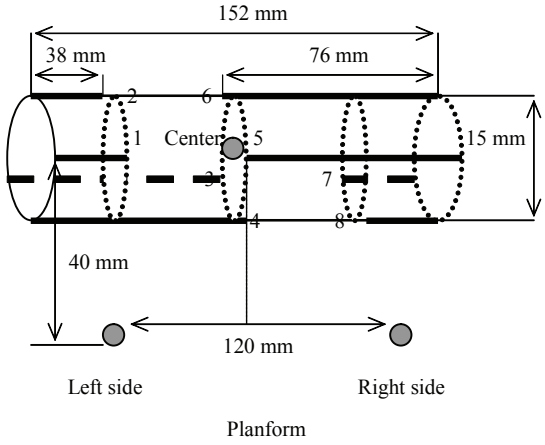

Fig. 2 Details of the electrically heated Test section assembly

thermocouples located near the test section were used to measure the liquid pool temperature.

The details of the copper tube-heating element assembly are shown in Fig. 2. All test tubes were made of two copper tubes, the gap between which was fully filled with solder tin. The outer copper tube had an outer diameter of Ø20 mm, an inner diameter of Ø16 mm and a length of 152 mm and its outer surface was the test surface. The heater was inserted in the inner tube with a length of 138 mm, the outer and inner diameters of which were 15 mm and 12 mm, respectively. Eight nichrome-nisiloy thermocouples were arranged in eight 1.5 mm × 1.0 mm grooves on the outer surface of the inner tube to measure the wall temperature shown in Fig. 2. The wall temperature was determined from the arithmetic average of the eight thermocouples after proper corrections of the conduction effect across the thickness of the copper tube.

The acoustical excitation was generated with an ultrasonic vibrator, which was operated by the electric current from an ultrasonic generator. The effect of the acoustical field intensity on boiling heat transfer can be expressed in terms of three parameters: the ultrasonic source intensity P, the vibrator's location (left or right side or center) and the distance from the vibrator head to the horizontal plane containing the tube axis L (see Fig. 1), which is referred to as the sound source distance in this paper. More detailed experimental apparatus and procedure are described in [11, 12]. The input power was determined with a precision of 3.2%. The uncertainties in heat fluxes and heat transfer coefficients were estimated to be less than ±5.5% and ±6.0%, respectively.

3. Results and Discussion

3.1 Boiling heat transfer enhancement from activated bubble nucleation

3.1.1 Acoustic cavitation

The effect of acoustic cavitation with sound source distance of L= 40 mm on local boiling curves obtained around the heated copper tube is presented in Fig. 3. You et al. [13] defined the superheat excursion at boiling inception as the maximum temperature difference (along a line of constant heat flux) between the surface

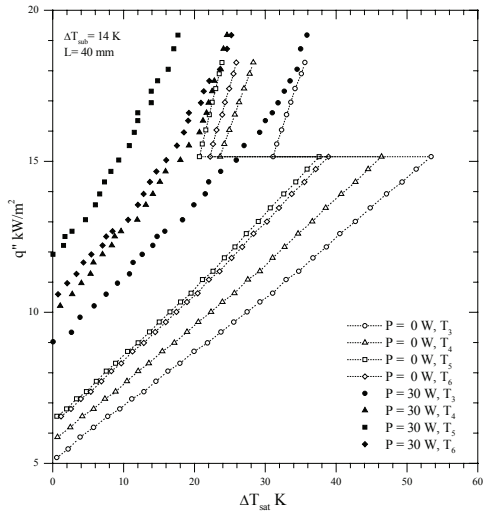

Fig. 3 Effect of sound source intensity on local wall temperature

temperature for increasing heat flux and that for decreasing heat flux. At given fluid subcooling of 14 K, boiling hysteresis with a maximum superheat excursion of 22.3 K occurred, irrespectively of the location of the thermocouple. However, as the sound source intensity is P= 30 W, boiling hysteresis disappears and the nucleate boiling curve shifts to the left of the corresponding pool curve without acoustic cavitation (P= 0 W) although the magnitude is different from each other. T_3, T_4, T_5 and T_6 represent the local wall temperature obtained from the bottom, side (forward), top and side (backward) of the tube shown in Fig. 2, respectively. Figure 3 shows that acoustic cavitation has much or less influence on four local wall temperatures around the tube and the wall temperature with higher heat transfer rate is in the following sequence: T_5, T_6, T_4, and T_3. It indicates that the copper tube obtained a minimum wall temperature on the top of the tube on which cavitation bubbles cluster impinges directly and a maximum wall temperature on the bottom of the tube where the impingement impact of cavitation bubbles cluster can be neglected. This causes the temperature difference around the tube at an identical applied heat flux increase because of the presence of acoustic cavitation, i.e., the nonuniformity of heat transfer rate at the same section of the tube increases.

We now discuss the reason for the above behavior. For pool boiling of the tube without acoustic cavitation, there is a higher heat transfer rate on the top of the tube than that on the bottom of the tube. The vapor embryos generated from the downside of the tube slide along the tube surface due to buoyancy and hence cause the boundary layer become thinner, contributing to higher high transfer rate there. When the vapor embryo arrive the upside of the tube, it is observed that: (i) the oncoming vapor embryos merge consecutively with the

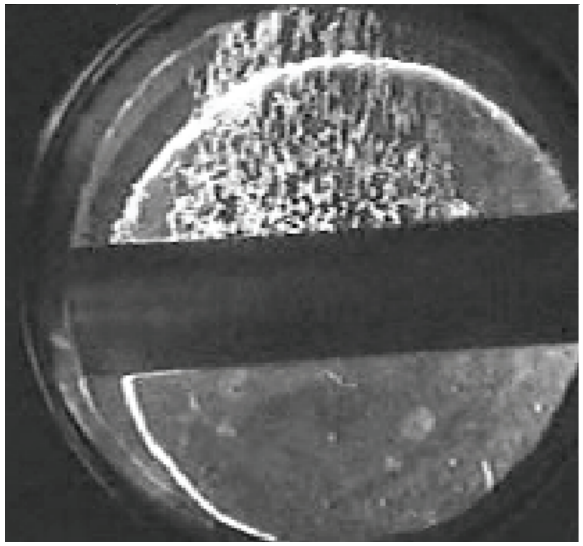

(a) without acoustic cavitation (P= 0 W)

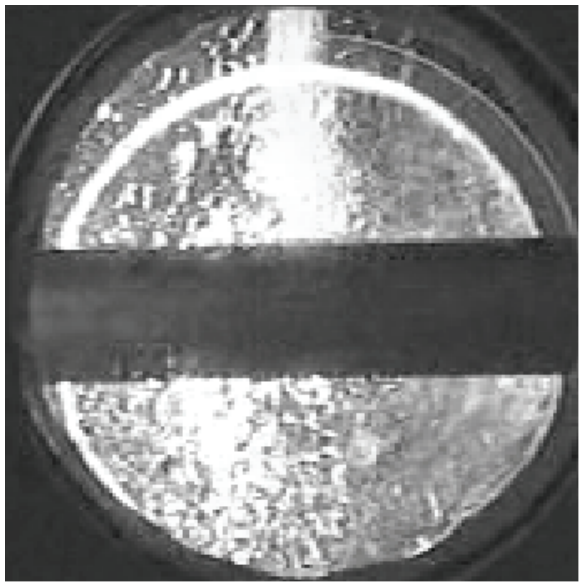

(b) with acoustic cavitation (P= 60 W)

Fig. 4 Bubble distributions around the tube surface (a) with and (b) without acoustic cavitation

local vapor embryos and hence much latent heat of vaporization is dissipated after departure from the surface of the heated tube; and (ii) the updraft bubbles disturb the boundary layer and hence heat is transferred through convection into the surrounding liquid. The combined influences of above-mentioned factors increase notably heat transfer rate on the top of the tube.

Figures 4a and 4b depict the bubble distributions around the tube surface during pool boiling with and without acoustic cavitation, respectively. Figure 4a presents the boiling behaviors of the copper tube without acoustic cavitation. It is concluded that no bubble is visible on the bottom of the tube. However, once acoustic

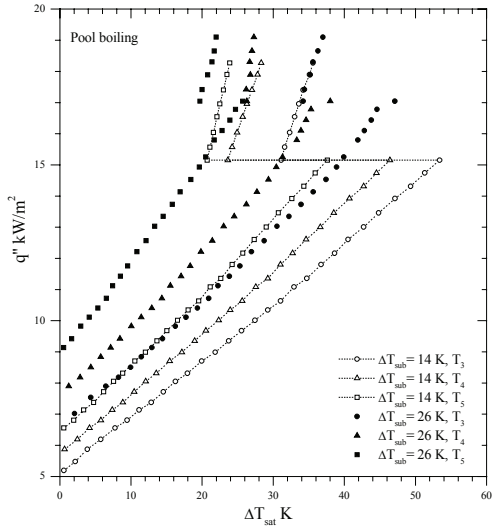

Fig. 5 Variation of local wall temperature with respective to fluid subcooling

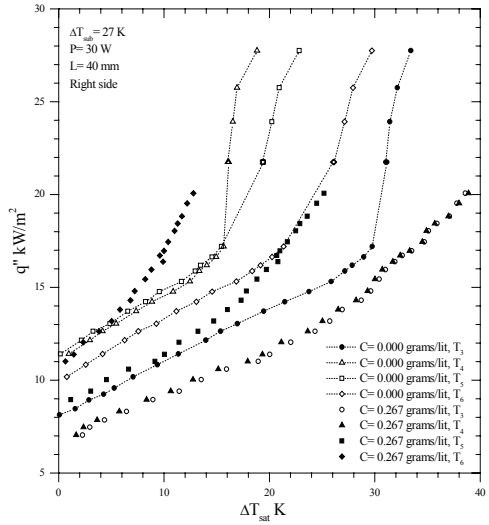

Fig. 6 Effect of nanoparticles on boiling heat transfer enhancement

cavitation shown in Fig. 4b with P= 60 W is generated, these cavitation bubbles excite consecutively vapor embryos harbored within the cavities on the tube surface by increasing or decreasing the pressure there. Therefore, bubbles that did not reach their critical radius are then fully activated by the cavitation bubbles [11]. Figure 4b shows that bubbles are visible not only on the top but also on the bottom of the tube. These bubbles activated by acoustic cavitation are clearly seen on the bottom of the tube from the videotape of the experiment. This in turn causes incipient boiling superheat decrease and eventually eliminate boiling hysteresis occurred on the smooth surface of the tube due to the use of highly-wetting liquid. On the other hand, the cavitation bubbles existed around the downside of the tube activated the liquid-gas interface within cavities, expediting the transportation of heat and mass there. It increases the actual areas for boiling heat transfer, which is believed to be another inherent mechanism of heat transfer enhancement by acoustic cavitation.

3.1.2 Fluid subcooling

Fluid subcooling influence on nucleate boiling heat transfer is another ambiguous academic problem remaining in this field. The experiments were carried out to investigate the fluid subcooling effect without acoustic cavitation on boiling heat transfer enhancement. Figure 5 presented the variation of local wall temperature obtained from the same section of the tube with respective to fluid subcooling. Independent of the location of the thermocouple, the pool boiling curves shift remarkably to the left with the increasing of fluid subcooling. That is to say, pool boiling heat transfer is enhanced. Although the applied heat flux at boiling inception increases, the incipient boiling superheat and superheat excursion decrease. This is in agreement with the results reported by Ma and Bergles [5] and Zhou and Ma [4] for jet impingement boiling heat transfer. Figure 5 also shows that boiling heat transfer enhancement by fluid subcooling at the same section of the tube is different from each other. At $q" = 1.52 \times 10^4$ W/m^2 for example, the decrease in the wall superheat at T_3 and T_5 between ΔT_{sub}= 26 K and 14 K were 14 K and 16.2 K, respectively.

The afore-mentioned enhancement is believed to be caused mainly by two factors. With the increase of fluid subcooling, the thickness of the thermal boundary layer around the tube decreases, leading to an increase of convection heat transfer rate. Tong et al. [14] found that the surface tension of highly-wetting liquids usually increased with fluid subcooling, which makes the noncondensable gas dissolved in the working fluid be easy to be trapped. Both factors are helpful for greater cavities on the smooth heater surface to entrap vapor residues to initiate boiling. In other words, the ability for cavities on the heater surface to trap residues vapor increases and the corresponding size of cavities in which vapor residues were entrapped increases. Consequently, the boiling occurs at lower wall superheat and applied heat flux. The bubble nucleation within greater cavity size at boiling inception dissipates much heat to the surrounding fluid. Therefore, the boiling heat transfer is enhanced.

3.2 Boiling heat transfer reduction from suppressed bubble nucleation

3.2.1 The addition of nanoparticles

At fixed fluid subcooling of 27 K, the effect of $CaCO_3$ nanoparticles on local boiling curves obtained at same

section of the copper tube was presented in Fig. 6. The data are for P= 30 W and L= 40 mm where the ultrasonic vibrator locates on the right side of the test section. As shown in Fig. 6, the maximum temperature difference around the tube at fixed applied heat flux increases. Furthermore, the effect of acoustic cavitation on local wall temperature varied due to the presence of nanoparticles. As the $CaCO_3$ nanoparticles were added into the working fluid, the heated tube had a highest local wall temperature at T_6 rather than T_5.

The $CaCO_3$ nanoparticles disperse uniformly in the working fluid under the impingement and disturbance of cavitation bubbles cluster. The uniformly-distributed nanoparticles counteract the generation and motion of cavitation bubbles, weakening acoustic cavitation influence there. It is assumed that little of nanoparticles deposit on the downside of the tube due to gravity, resulting in a weak influence on local wall temperature T_3. The combined effect of two above-mentioned factors decreases the numbers of nucleation embryos, contributing to a low heat transfer rate of nucleate boiling. The corresponding boiling curve shifts to the right. It should be noted here that the size of nanoparticles (about 80-100 nm) is much less than that of cavities in which vapor embryos will be activated to initiate boiling. As a result, more nanoparticles deposit on the upside of the heated tube under the impingement and disturbance of acoustic cavitation cluster. Due to the deposition of nanoparticles, the surface roughness of the tube decreases. It would then require elevated applied heat flux to activate vapor embryos at the remaining smaller cavities prior to boiling inception, i.e., the presence of nanoparticles suppresses bubble nucleation within the cavities on the surface of the heated tube. At the same test conditions, heat is dissipated only by convection rather than by latent heat of vaporization and the mode of heat transfer is single-phase convection. Consequently, the incipient boiling superheat increases and the corresponding local boiling curve shifts to the right. This has been verified by the data indicated by thermocouple of T_5 shown in Fig. 6.

3.2.2 High jet exit velocity impinged at the stagnation point

Zhou and Ma confirmed [4] that, as the exit velocity of circular jet did not exceed 10 m/s, both the pool and impingement nucleate boiling curves at the same subcooling condition were well correlated with an equation. However, as shown in Fig. 7, the impingement boiling curve obtained at the stagnation point with higher jet exit velocity of 11.36 m/s shifts to the right of the low velocity curve. Ma and Bergles [5] reported this phenomenon, yet did not give any explanation for it.

Zhou and Ma [4] concluded that the pressure distribution controlled the local saturation conditions along the impingement plate surface. At the stagnation point, impingement velocity sharply decreases to zero while the pressure increases correspondingly to a maximum value. This in turn causes the saturation temperature of the working fluid increase. Therefore, the

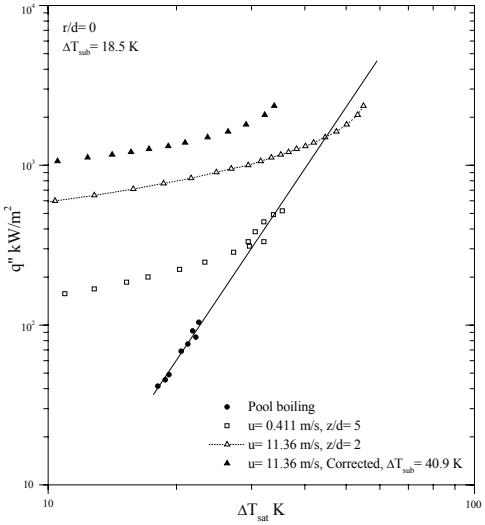

Fig. 7 Effect of jet exit velocity on the stagnation boiling curve

boiling curve with higher jet exit velocity and the corresponding fluid subcooling were corrected in terms of the elevated saturation temperature. As can be seen in Fig. 7, the corrected fluid subcooling is increased sharply from 18.5 K to 40.9 K and the corresponding boiling curve is located to the left of the original boiling curve.

We now analyze the displacement of impingement nucleate boiling curve in light of bubble generation behavior. As the jet impinges the heater surface, a local thinner thermal boundary layer at the impingement zone is available due to its normal flow, contributing to higher heat transfer rate there. Since the working fluid (R113) has low surface tension and small contact angle, they flood all but the smallest cavities on the heat transfer surface (smooth constantan foil), depleting vapor embryos needed for boiling inception [15]. The vapor embryos can not be activated due to unavailable residual gas within greater cavities. The heater surface dissipates the heat only by conduction and convection prior to bubble nucleation. Only when the applied heat flux increases to a certain value, vapor embryos within cavities on the heater surface can generate, grow up and separate. Thus, the boiling commences. Since the effects of jet exit velocity cannot reach the interior surface of these cavities, the incipient boiling superheat is irrelevant to jet exit velocity. But, as the jet with higher exit velocity of 10 m/s impinges at the stagnant point, it is inferred that the bubble nucleation occurred within the cavities on the heater surface are spoilt by the impingement liquid. The high-speed flowing fluid dissipates much heat by convection and more latent heat of vaporization by bubble nucleation, resulting in significant increase in heat transfer rate. It should be stressed that vapor embryos could be activated in this

case but could not grow up easily. This maintains a low wall superheat although the applied heat flux reaches a higher level. As the heat flux is increased further, the heat transfer mode on the impingement surface converts gradually from single-phase forced convection into fully-developed nucleate boiling. It seems that the suppression effect of jet velocity on bubble nucleation within the cavities is more sensible at higher jet exit velocity. As the jet exit velocity exceeds 10 m/s, the displacement of impingement boiling curve obtained at the stagnation point occurs in comparison with that of the low velocity with an identical fluid subcooling.

As the highly-wetting liquid is used as the working fluid, both acoustic cavitation and impinging jet can eliminate boiling hysteresis, but in different way. Acoustic cavitation activates more vapor embryos below the critical radius to boil while the jet with higher jet exit velocity of 10 m/s impinging at the stagnation point suppresses the bubble nucleation. It is believed whether or not vapor embryos are activated not only indicates the heat transfer mode on the heater surface, but also determines the slope and location of the boiling curve. Consequently, it is concluded here that boiling heat transfer enhancement results from the activated bubble nucleation and vice versa.

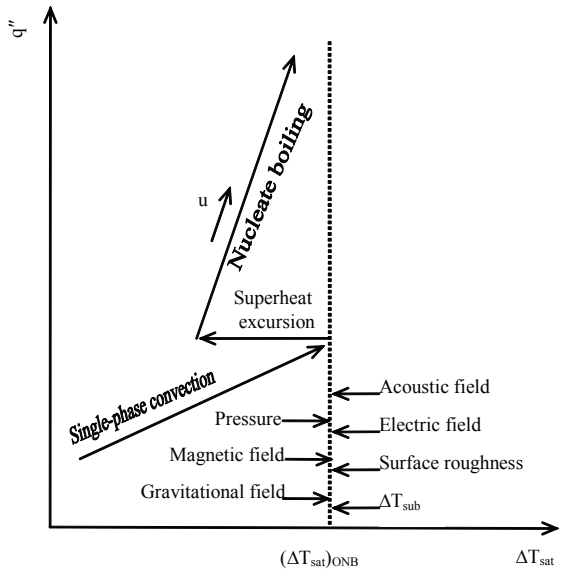

Fig. 8 Effects of various factors on incipient boiling superheat

4 Controlling techniques for enhancing boiling heat transfer

4.1 Influence factors of incipient boiling superheat

From previous literatures, we may summarize the main factors which influence incipient boiling superheat as follow: thermal properties of the liquid coolant and wall [16] and the corresponding contact angle [14], thermal history of the wall (i.e., surface aging) and the heating procedure [17], heater size and orientation [18], system pressure [6, 7, 19], fluid subcooling [2, 3, 17], surface roughness [1] and additional field (such as gravitational field [6, 20], electric field [21, 22], acoustic field [23, 11] and magnetic field [24]), etc. Once the working fluid and the material of the heat transfer surface are selected, the contact angle between them is determined. Generally speaking, the thermal behavior at boiling inception is influenced not only by the surface condition at the moment of boiling inception but also by the thermal processes associated with the surface before this moment. Thus, an experimental procedure of boiling heat transfer proposed recently by Zhou et al. [17] should be rigorously performed to eliminate the effects of such factors as surface aging, noncondensable gas and the heating procedure on boiling heat transfer, especially for the case of highly-wetting liquid.

For a clean heat transfer surface, the incipient boiling superheat is only related with the system pressure, fluid subcooling, surface roughness and the additional fields after the above-mentioned factors are determined. Figure 8 presented these factors influences on incipient boiling superheat. Since such factors as fluid subcooling, surface roughness, electric field and acoustic field can activate vapor embryos on the heater surface, the incipient boiling superheat decreases with the increased intensity of these factors. On the contrary, the bubble nucleation process is suppressed with the increased intensity of system pressure, magnetic field and gravitational field. Figure 8 also shows the fluid velocity effect on incipient boiling superheat. It is believed that low fluid velocity has a negligible influence on incipient boiling superheat and only pushes the high heat flux regime of boiling curve to higher heat fluxes. This has been verified by the experimental data of Yin and Abdelmessih [25] for an R11 flow boiling and Zhou et al. [17] for R113 impingement boiling.

The above analysis shows that the incipient boiling superheat is closely related with the thermal and mechanical properties of the liquid coolant and wall, the experimental procedure, system pressure, fluid subcooling, surface roughness and the additional field. It should be noted here that the first two factors have been determined prior to the experimental runs. According to the analysis in section 3, it is concluded that the remainder factors influence the incipient boiling superheat by changing the system pressure, saturation temperature of the working fluid, surface roughness, or fluid subcooling. This in turn indicates that the incipient boiling superheat can be increased or decreased by changing directly or indirectly these factors.

4.2 Possible technique to enhance boiling heat transfer

Extensive consideration has been given to boiling heat transfer enhancement. The possible techniques for enhance boiling heat transfer prior to 1998 have been reviewed by Rohsenow [26] in detail. However, as we

know from the afore-mentioned analysis, once vapor embryos are effectively activated to initiate boiling, the boiling heat transfer is enhanced, irrespectively of the techniques of bubble nucleation. On the contrary, the boiling heat transfer is reduced while bubble nucleation is suppressed to initiate boiling. Due to the suppression of bubble nucleation by the Lorentz force, Wagner and Lykoudis [24] and Takahashi et al. [27] found that the boiling heat transfer was reduced with increasing the magnetic flux density in comparison with the case of non-magnetic field. Consequently, in order to actively develop the techniques of boiling heat transfer enhancement, we should understand thoroughly the potential techniques which can activate vapor embryos to initiate boiling.

Probably the most challenging task of performing the principle is to develop boiling heat transfer enhancement techniques at the guidance of the principle. However, such work is now underway in the authors' group. Several examples are presented for illustration. Fukusako et al. [28] confirmed that porous medium could contain more dissolved noncondensable gases than a smooth surface. Thus, it would lead to an increase of nucleation nuclei density. For a heated horizontal copper tube embedded in a porous medium, Zhou et al. [12] verified that the boiling heat transfer was enhanced due to the presence of porous medium. Since acoustic cavitation can activate residual gas harbored within the cavities on the heat transfer surface, the experimental data of Zhou et al. [11] indicated that the boiling heat transfer was enhanced notably while the acoustic source intensity exceeded a certain value. Zhou [29] also investigated the effect of copper nanofluid on boiling heat transfer of the horizontal tube and concluded that the deposition of copper nanoparticles on the heater surface suppressed the bubble nucleation, leading to reduction in boiling heat transfer.

4.3 Possible techniques to eliminate boiling hysteresis

Due to unfavorable influence, the boiling hysteresis must be eliminated in its practical applications. Therefore, options for eliminating boiling hysteresis and enhancing boiling heat transfer have been considered. The mechanism of boiling hysteresis reported by Zhou et al. [17] and carried out in section 3 showed that the occurrence of boiling hysteresis was primarily attributed to the delayed nucleation of vapor embryos. It occurs due to the smooth heater surface, and is exacerbated by the small surface tension of highly-wetting liquid. The basic characteristic of boiling hysteresis is its higher incipient boiling superheat prior to boiling inception. As a result, the fundamental way to eliminate boiling hysteresis is to activate effectively vapor embryos so as to initiate boiling at normal wall superheat. Since boiling hysteresis is accompanied with lower heat transfer rates prior to boiling inception, it implies that the elimination of boiling hysteresis is an extreme case of boiling heat transfer enhancement.

It is believed that the possible techniques to enhance boiling heat transfer can also be utilized to eliminate boiling hysteresis. For example, Cooper [21] and Zaghdoudi and Lallemand [22] found that the uses of electric field enhanced boiling heat transfer and eliminated boiling hysteresis. Zhou et al. [11] reported a similar result for an acoustic field. Joudi and James [7] observed the incipient boiling characteristics at atmospheric and subatmospheric pressures, and found that many nucleation sites on the surface would be active at decreased pressures, leading to disappearance of boiling hysteresis. These examples indicate that the normal activation of vapor embryos occurs due to the presence of electric field, acoustic field and decreased pressures, leading to boiling heat transfer enhancement.

Considerable attention has been given to either altering the surface or attaching it to a heat sink. Information on reentrant cavity published prior to 1997 was summarized by Bergles [30]. Recently, with the use of compound surface and "doubly reentrant" cavity on the boiling surface respectively, Liang and Yang [31] and Reed and Mudawar [32] eliminated successfully boiling hysteresis because vapor embryos were easily activated on the two kinds of surfaces.

5. Conclusions

The most important findings of this study are:

(1) Boiling heat transfer enhancement results from effective bubble nucleation on the heat transfer surface at normal wall superheat and vice versa.

(2) In light of the bubble nucleation effect on boiling heat transfer enhancement, a new principle is proposed to guide the research of enhancing boiling heat transfer and eliminating boiling hysteresis. Some typical examples are presented in the paper for illustration.

Acknowledgements

The assistance and valuable suggestions of Professor Arthur E. Bergles of Massachusetts Institute of Technology (Cambridge) is highly appreciated.

References

[1] S.K. Roy Chowdhury, R. H. S. Winterton, Surface effects in pool boiling, International Journal of Heat Mass Transfer, 28 (3) (1985) 1881-1889.

[2] R.L. Judd, H.JR. Merte, Evaluation of nucleate boiling heat flux predictions at varying levels of subcooling and acceleration, International Journal of Heat Mass Transfer, (15) (1972) 1075-1096.

[3] V.H.Del Valle M, Kenning D B R, Subcooled flow boiling at high flux, International Journal of Heat Mass Transfer, 28 (6) (1985) 1907-1920.

[4] D. W. Zhou, C. F. Ma, Local jet impingement boiling heat transfer with R113, Heat and Mass Transfer, 40 (6) (2004) 91-100.

[5] C. F. Ma, A. E. Bergles, Jet impingement nucleate boiling, International Journal of Heat Mass Transfer, 29 (2) (1986) 1095-1100.
[6] J. S. Turton, The effects of pressure and acceleration on the pool boiling of water and acetone 11, International Journal of Heat Mass Transfer, (11) (1968) 1295-1303.
[7] K.A. Joudi, D.D. James, Incipient boiling characteristic at atmospheric and sub-atmospheric pressure, Journal of Heat Transfer, (99) (1977) 398-404.
[8] Z. Y. Guo, D. Y. Li, B. X. Wang, A novel concept for convective heat transfer enhancement, International Journal of Heat Mass Transfer, (41) (1998) 2221-2225.
[9] W. Q. Tao, Z. Y. Guo, B. X. Wang, Field synergy principle for enhancing convective heat transfer- its extension and numerical verifications, International Journal of Heat Mass Transfer, (45) (2002) 3849-3856.
[10] W. Q. Tao, Y. L. He, Q. W. Wang, Z. G. Qu, F. Q. Song, A unified analysis on enhancing single phase convective heat transfer with field synergy principle, International Journal of Heat Mass Transfer, (45) (2002) 4871-4879.
[11] D. W. Zhou, D. Y. Liu, X. G. Hu, C. F. Ma, Effect of acoustic cavitation on boiling heat transfer, Experimental Thermal Fluid Science, 26 (10) (2002) 931-938.
[12] D. W. Zhou, D. Y. Liu, P. Cheng, Boiling heat transfer characteristics from a horizontal tube embedded in a porous medium with acoustic excitation, Journal of Enhanced Heat Transfer, (11) (3) (2004) 91-100.
[13] S. M. You, T. W. Simon, A. Bar-Cohen, W. Tong, Experimental investigation of nucleate boiling incipience with a highly wetting dielectric fluid (R113), International Journal of Heat Mass Transfer, (33) (1990) 105-117.
[14] W. Tong, A. Bar-Cohen, S. M. You, Contact angle effects on boiling incipience of highly-wetting liquids, International Journal of Heat Mass Transfer, (33) (1) (1990) 91-100.
[15] A. Bar-Cohen, T. W. Simon, Wall superheat excursions in the boiling incipience of dielectric fluids, Heat Transfer Engineering, 9(3) (1988) 19-31.
[16] K. A. Joudi, D. D. James, Surface contamination, rejuvenation, and the reproducibility of results in nucleate pool boiling. Journal of Heat Transfer, 103 (8) (1981) 453-460.
[17] D. W. Zhou, C. F. Ma, J. Yu, Boiling hysteresis of impinging circular submerged jets with highly wetting liquids, International Journal of Heat and Fluid Flow, 25 (1) (2004) 81-90.
[18] K. N. Rainey, S. M. You, Effects of heater size and orientation on pool boiling heat transfer from microporous coated surfaces, International Journal of Heat Mass Transfer, (44) (2001) 2589-2599.
[19] A. E. Bergles, W. M. Rohsenow, The determination of forced convection surface boiling heat transfer, Journal of Heat Transfer, 86 (8) (1964) 365-370.
[20] H. S. Lee, H. Merte, F. Chiaramonte, Pool boiling curve in microgravity, Journal of Thermophysics and Heat Transfer, 11 (2) (1997) 216-222.
[21] P. Cooper, EHD enhancement of nucleate boiling, Journal of Heat Transfer, (112) (1990) 458-464.
[22] M. C. Zaghdoudi, M. Lallemand, Electric Field Effects on Pool Boiling, Journal of Enhanced Heat Transfer, 9(5-6) (2002) 187-208.
[23] K.A. Park, A. E. Bergles, Ultrasonic enhancement of saturated and subcooled pool boiling, International Journal of Heat Mass Transfer, (31) (1988) 664-667.
[24] L. Y. Wagner, P. S. Lykoudis, Mercury pool boiling under the influence of a horizontal magnetic field, International Journal of Heat Mass Transfer, 24 (4) (1981) 635-643.
[25] S. T. Yin, A. H. Abdelmessih, Prediction of incipient flow boiling from a uniformly heated surface. Nuclear, Solar, and Process Heat Transfer-St. Louis, (73) (1977) 236-242.
[26] W. M. Rohsenow, Boiling, in: W.M. Rohsenow, J. P. Hartnett, Y. I. Chi (Eds.), Handbook of Heat Transfer, third ed., McGraw-Hill, New York, 1998, pp. 13.1-13.76.
[27] O. Takahashi, M. Nishida, N. Takenaka, I. Michiyoshi, Pool boiling heat transfer from horizontal plane heater to mercury under magnetic field, International Journal of Heat Mass Transfer, (23) (1980) 27-36.
[28] S. Fukusako, T. Komoriya, N. Seki, An experimental study of transition and film boiling heat transfer in liquid-saturated porous bed, Journal of Heat Transfer, (108) (1986) 117-124.
[29] D. W. Zhou, Heat transfer enhancement of copper nanofluid with acoustic cavitation, International Journal of Heat Mass Transfer, (47) (14-16) (2004) 3109-3117.
[30] A. E. Bergles, Heat transfer enhancement- The encouragement and accommodation of high heat fluxes, Journal of Heat Transfer, (119) (2) (1997) 8-18.
[31] H. S. Liang, W. J. Yang, Nucleate pool boiling heat transfer in a highly wetting liquid on micro-graphite fiber composite surfaces, International Journal of Heat Mass Transfer, 41 (13) (1998) 1993-2000.
[32] R. J. Reed, I. Mudawar, Elimination of boiling incipience temperature drop in highly wetting fluids using spherical contact with a flat surface, International Journal of Heat Mass Transfer, (42) (1999) 2439-2454.

Strojniški vestnik - Journal of Mechanical Engineering 51(2005)7-8, 374-378
UDK - UDC 536.2
Izvirni znanstveni članek - Original scientific paper (1.01)

An Improved Form for Natural Convection Heat Transfer Correlations

Eugene F. Adiutori
Ventuno Press
12887 Valewood Drive
Naples, Florida 34119
United States of America
efadiutori@aol.com

Abstract

Natural convection heat transfer correlations are usually in the form Nusselt{Rayleigh}, and occasionally in the form Nusselt{Rayleigh*}. Both forms are inconvenient because they oftentimes require indirect solution:

- When Nusselt{Rayleigh} correlations are used to calculate heat flux, solution is simple and direct. But when they are used to calculate boundary layer temperature difference, solution must be indirect—i.e. must be based on an indirect method such as iteration or trial-and-error.

- When Nusselt{Rayleigh*} correlations are used to calculate boundary layer temperature difference, solution is direct. But when they are used to calculate heat flux, solution must be indirect.

This manuscript describes an improved form for natural convection heat transfer correlations. The improved form allows direct solution for heat flux *and* for boundary layer temperature difference.

Included in this manuscript are graphical and analytical correlations in the improved form obtained by transforming Nu{Ra} correlations from the literature.

Introduction

In forced convection, the heat flux (q) is essentially proportional to the boundary layer temperature difference (ΔT). Therefore the heat transfer coefficient (h) is a *constant* coefficient—ie its value is independent of ΔT and q. Because h is a constant coefficient, correlations in the usual form Nu{Re,Pr} can be solved directly for q *and* for ΔT.

In natural convection, q is a nonlinear function of ΔT, and therefore h is a *variable* coefficient—ie its value is dependent on ΔT (or equally on q). Because h is a variable coefficient, correlations in the form Nu{Ra} cannot be solved directly for ΔT. They must be solved using an indirect method such as iteration or trial-and-error. Similarly, correlations in the form Nu{Ra*} cannot be solved directly for q, but must be solved using an indirect method.

This manuscript describes an improved form for natural convection heat transfer correlations. The improved form allows direct solution for q *and* for ΔT.

Applications in which Nu{Ra} and Nu{Ra*} correlations are solved directly

Nu{Ra} correlations are solved directly if the value of q is to be calculated. The solution is obtained as follows:

- Note that Nu{Ra} is $(hD/k)\{c_p\rho^2g\beta\Delta TD^3/\mu k\}$.
- Calculate the value of $(c_p\rho^2g\beta\Delta TD^3/\mu k)$ from the given information.
- Calculate the value of (hD/k) from the given Nu{Ra} correlation and the calculated value of $(c_p\rho^2g\beta\Delta TD^3/\mu k)$.
- Calculate the value of h from the calculated value of (hD/k) and the given information.
- Calculate q from the calculated value of h, the given value of ΔT, and $q = h\Delta T$.

Nu{Ra*} correlations are solved directly if the value of ΔT is to be determined. The solution is obtained as follows:

- Note that Nu{Ra*} is $(hD/k)\{qc_p\rho^2g\beta D^4/\mu k^2\}$.
- Calculate the value of $(qc_p\rho^2g\beta D^4/\mu k^2)$ from the given information.

b unspecified function of fluid flow rate, fluid properties, and geometry
Bu symbol arbitrarily assigned to $qc_p\rho^2g\beta D^4/\mu k^2$; identical to NuRa and Ra* (dimensionless)
c_p specific heat, J/kgK
D diameter, m
G mass flow rate, kg/s
g gravity constant, m/s^2
h heat transfer coefficient, W/m^2K
k thermal conductivity, W/mK
L length, m
Nu Nusselt number hD/k (dimensionless)
Pr Prandtl number $c_p\mu/k$ (dimensionless)
q heat flux, W/m^2
Ra Rayleigh number $c_p\rho^2g\beta\Delta TD^3/\mu k$ (dimensionless)
Ra* modified Rayleigh number, RaNu (dimensionless)
Re Reynolds number DG/μ (dimensionless)
T temperature, K
β temperature coefficient of volume expansion, K^{-1}
μ dynamic viscosity, kg/m s
ρ density, kg/m^3

- Calculate the value of (hD/k) from the calculated value of $\{qc_p\rho^2g\beta D^4/\mu k^2\}$ and the given Nu{Ra*} correlation.
- Calculate the value of h from the calculated value of (hD/k) and the given information.
- Calculate ΔT from the calculated value of h, the given value of q, and ΔT = q/h.

Applications in which Nu{Ra} and Nu{Ra*} correlations cannot be solved directly

Nu{Ra} correlations cannot be solved directly for ΔT because neither $(c_p\rho^2g\beta\Delta TD^3/\mu k)$ nor (hD/k) can be calculated if ΔT is not included in the given information. An indirect solution such as the following is required:

- Note that Nu{Ra} is $(hD/k)\{c_p\rho^2g\beta\Delta TD^3/\mu k\}$.
- Select ΔT_1, an initial estimate of ΔT.
- Calculate $\{c_p\rho^2g\beta\Delta T_1D^3/\mu k\}$ from ΔT_1 and the given information.
- Calculate $(hD/k)_1$ from the given correlation and the calculated value of $\{c_p\rho^2g\beta\Delta T_1D^3/\mu k\}$.
- Calculate h_1 from $(hD/k)_1$ and the given information.
- Calculate ΔT_2 from the calculated value of h_1, the given value of q, and Equation (1).

$$\Delta T_2 = q/h_1 \tag{1}$$

- Iterate until convergence is obtained.
- If the solution diverges, select a different iteration scheme. Or select a different indirect method, such as trial-and-error.

Nu{Ra*} correlations cannot be solved directly for q because neither (hd/k) nor $(qc_p\rho^2g\beta D^4/\mu k^2)$ can be calculated if q is not included in the given information. An indirect solution analogous to the above is required.

The underlying problem with Nu{Ra} and Nu{Ra*}

The problem with Nu{Ra} may be seen by noting that

$$Nu \alpha h \tag{2}$$

$$Ra \alpha \Delta T \tag{3}$$

Relations (2) and (3) indicate that Nu{Ra} correlations are in the form

$$h = b\,f\{\Delta T\} \tag{4}$$

where b is a function of fluid properties, fluid flow rate, and geometry. The underlying problem with Nu{Ra} correlations is that they are in the form of Eq. (4), a form that allows direct solution for h if ΔT is given, but does not allow direct solution for h if q is given.

The problem with Nu{Ra*} may be seen by noting that

$$Ra^* \alpha q \tag{5}$$

Relations (2) and (5) indicate that Nu{Ra*} correlations are in the form

$$h = b\,f\{q\} \tag{6}$$

The underlying problem with Nu{Ra*} correlations is that they are in the form of Eq. (6), a form that allows direct solution for h if q is given, but does not allow direct solution for h if ΔT is given.

An improved correlation form that allows direct solution for *both* q and ΔT

Equation (7) is in a form that allows direct solution for *both* q and ΔT because the left side is dependent on q but independent of ΔT, and the right side is dependent on ΔT but independent of q.

$$q = b\,f\{\Delta T\} \tag{7}$$

A dimensionless correlation in the form of Eq. (7) requires the following:

- A dimensionless group that is dependent on ΔT and independent of q.
- A dimensionless group that is dependent on q and independent of ΔT.

Ra satisfies the first requirement. The second requirement is satisfied by the dimensionless group $qc_p\rho^2g\beta D^4/\mu k^2$. Let us arbitrarily assign the symbol Bu to this dimensionless group. (Note that Bu is identical to Ra*, the product of Ra

and Nu. Also note that $q\rho^2g\beta D^4/\mu^2k$ also satisfies the second requirement.)

Since Bu is dependent on q and independent of ΔT, and since Ra is dependent on ΔT and independent of q, Bu{Ra} correlations are in the form of Eq. (7).

Transforming graphical Nu{Ra} and Nu{Ra*} correlations to the form of Eq. (7)

Graphical Nu{Ra} correlations are transformed to the form of Eq. (7) in the following manner :

- List the Nu,Ra coordinates on a spreadsheet.
- Multiply each Nu coordinate by the corresponding Ra coordinate to obtain Bu,Ra coordinates.
- Prepare a Bu{Ra} graphical correlation by plotting the Bu,Ra coordinates.

Figure 1 is a Bu{Ra} chart obtained by transforming a Nu{Ra} chart that appears in McAdams[1] and also in Kreith and Bohn [2]. Table 1 contains the spreadsheet calculations for the transformation. The Nu,Ra coordinates in Table 1 are those listed on the Nu{Ra} chart in Kreith and Bohn [2].

Graphical Nu{Ra*} charts are transformed to the form of Eq. (7) as follows:

- List the Nu,Ra* coordinates on a spreadsheet.
- Divide each Ra* coordinate by the corresponding Nu coordinate to obtain Ra coordinates.
- Multiply each Nu coordinate by the corresponding Ra coordinate to obtain Bu coordinates.
- Prepare a Bu{Ra} graphical correlation by plotting the Bu,Ra coordinates.

Transforming analytical Nu{Ra} and Nu{Ra*}correlations to dimensionless correlations in the form of Eq. (7)

Analytical Nu{Ra} correlations are transformed to dimensionless correlations in the form of Eq. (7) by multiplying both sides of Nu{Ra} correlations by Ra or Gr. Multiplying by Ra results in dimensionless Bu{Ra} correlations. Table 2 lists several Bu{Ra} correlations obtained by transforming Nu{Ra} correlations from the literature.

Analytical Nu{Ra*} correlations are transformed to dimensionless correlations in the form of Eq. (7) in the following manner:

- Substitute RaNu for Ra* to obtain Nu{RaNu} correlation.
- Separate Ra and Nu to obtain Nu{Ra} correlation.
- Multiply both sides of the Nu{Ra} correlation by Ra to obtain a Bu{Ra} correlation in the form of Eq. (7).

Improving the reading precision of Bu{Ra} charts

Figure 1 illustrates that Bu{Ra} charts of reasonable size cannot be read with acceptable precision because of the very large range in Bu. However, the precision of charts of reasonable size can be made acceptable by plotting (log Bu – log Ra) vs (log Bu or log Ra) as in Figure 2. (Table 1 lists the calculations that underlie Figure 2.) Figure 2 is read in the following manner:

- From the given information, calculate log Ra or log Bu. This value establishes the horizontal coordinate.
- If log Ra was calculated in the first step, determine (log Bu – log Ra) from the curve marked Ra. Determine log Bu from log Bu = log Ra + (log Bu – log Ra).
- If log Bu was calculated in the first step, determine (log Bu – log Ra) from the curve marked Bu. Determine log Ra from log Ra = log Bu – (log Bu – log Ra).

The impact of film temperature

The fluid properties in natural convection heat transfer correlations are usually evaluated at the film temperature—i.e. at the average temperature in the boundary layer. Since the film temperature usually cannot be determined from the given information, an initial estimate of film temperature must be made, and verified by the subsequent analysis. Thus the use of Nu{Ra} and Bu{Ra} correlations generally involves iteration on the film temperature.

However, the effect is usually so small that the first estimate of film temperature yields a result of sufficient accuracy, and no iteration on film temperature is required.

Selecting a name for the group $(qc_p\rho^2g\beta D^4/\mu k^2)$

The group $(qc_p\rho^2g\beta D^4/\mu k^2)$ is often assigned the name "modified Rayleigh number" and the symbol Ra*. Since Bu and Ra* are identical, Bu{Ra} correlations are also Ra*{Ra} correlations. Since Ra*{Ra} seems poor terminology, it would be desirable to assign a different name and symbol to the group $(qc_p\rho^2g\beta D^4/\mu k^2)$.

Lienhard and Lienhard [3] discuss the name and symbol usually assigned to $(qc_p\rho^2g\beta D^4/\mu k^2)$:

> *To avoid iterating, we need to eliminate ΔT from the Rayleigh number. We can do this by introducing a modified Rayleigh number, Ra*, defined as Ra* = RaNu.*

In the application discussed herein, a modified Nu is created by multiplying Nu by Ra. Based on the reasoning that leads to Ra*, the group $(qc_p\rho^2g\beta D^4/\mu k^2)$ as used herein would be a "modified Nusselt number", symbol Nu*.

It would be misleading to use "modified Nusselt number" and Nu* for the group $(qc_p\rho^2g\beta D^4/\mu k^2)$. Nusselt number is closely identified with h, and the group $(qc_p\rho^2g\beta D^4/\mu k^2)$ does not contain h.

It therefore seems advisable to assign a new name and symbol to the group $(qc_p\rho^2g\beta D^4/\mu k^2)$.

Conclusions

- Bu{Ra} should replace both Nu{Ra} and Nu{Ra*} because Bu{Ra} allows direct solution for *both* q and ΔT, whereas Nu{Ra} and Nu{Ra*} do not.

- Graphical and analytical Nu{Ra} and Nu{Ra*} correlations are readily transformed to Bu{Ra} correlations.
- The group $(qc_p\rho^2g\beta D^4/\mu k^2)$ should be assigned a new name and a new symbol.

References

[1] McAdams, W.H., (1954), *Heat Transmission*, p. 176, McGraw-Hill, New York

[2] Kreith, F. and Bohn, M.S., (1986), *Principles of Heat Transfer*, p. 251, Harper and Row, New York

[3] Lienhard, J.H. IV, and Lienhard, J.H. V, (2003), *A Heat Transfer Textbook*, version 1.21, p. 424, Phlogiston Press, Cambridge

[4] Holman, J.P. (1981), *Heat Transfer*, p. 275, McGraw-Hill, New York

Table 1 Generation of coordinates used in Figures 1 and 2

Nu[1]	Ra[1]	Bu = NuRa	log Ra	log Bu	(log(Bu) – log(Ra))
0.49	**1.E-04**	4.90E-05	-4	-4.31	-0.31
0.55	**1.E-03**	5.50E-04	-3	-3.26	-0.26
0.66	**1.E-02**	6.61E-03	-2	-2.18	-0.18
0.84	**1.E-01**	8.41E-02	-1	-1.08	-0.08
1.08	**1.E+00**	1.08E+00	0	0.03	0.03
1.51	**1.E+01**	1.51E+01	1	1.18	0.18
2.11	**1.E+02**	2.11E+02	2	2.32	0.32
3.16	**1.E+03**	3.16E+03	3	3.50	0.50
5.37	**1.E+04**	5.37E+04	4	4.73	0.73
9.33	**1.E+05**	9.33E+05	5	5.97	0.97
16.2	**1.E+06**	1.62E+07	6	7.21	1.21
28.8	**1.E+07**	2.88E+08	7	8.46	1.46
51.3	**1.E+08**	5.13E+09	8	9.71	1.71
93.3	**1.E+09**	9.33E+10	9	10.97	1.97

[1] **From Kreith & Bohn [2], p. 251**

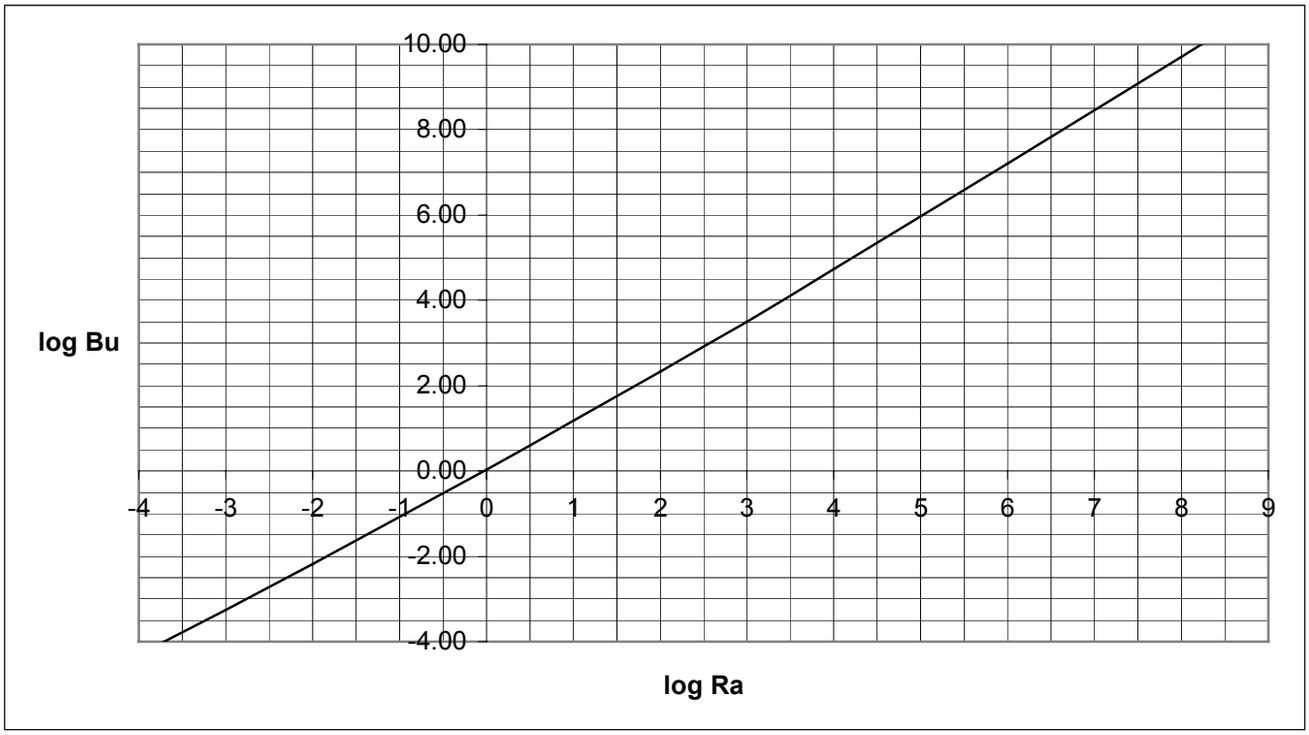

Figure 1 Natural convection heat transfer from horizontal cylinders

Table 2 Transformation of literature correlations

Literature Correlation	Dimensionless transformation	Dimensioned transformation
Nu = .10 Ra^1/3 Holman [4] p 275	Bu = .10 Ra^4/3	q = .10 (ΔTk/D)Ra^1/3
Nu = .0210Ra^2/5 Kreith&Bohn [2] p 253	Bu = .0210 Ra^7/5	q = .021(ΔTk/L)Ra^2/5
Nu = .58 Ra^1/5 Lienhard & Lienhard [3] p 423	Bu = .58 Ra^6/5	q = .58 (ΔTk/L)Ra^1/5

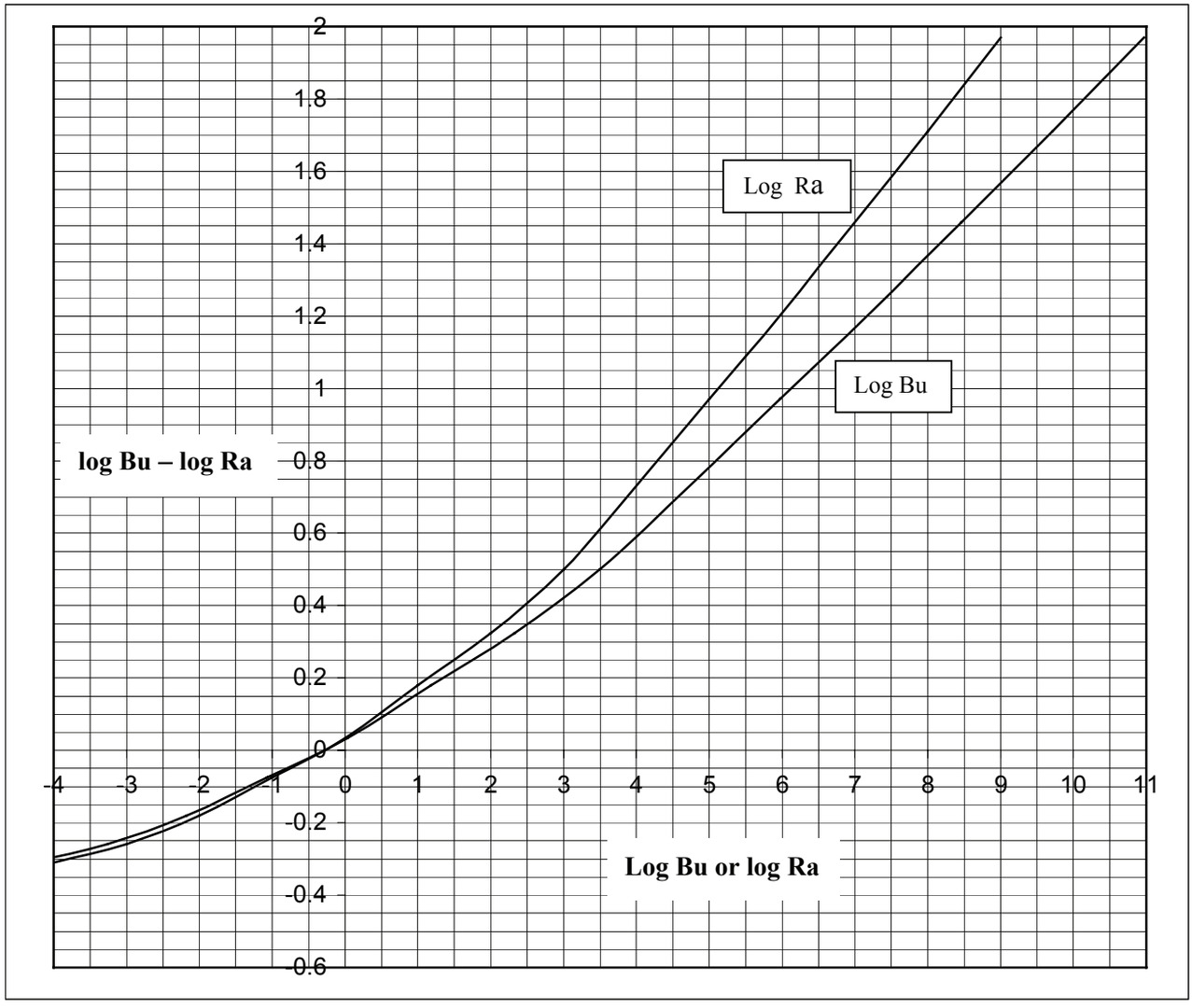

Figure 2 Natural convection heat transfer from horizontal cylinders

Strojniški vestnik - Journal of Mechanical Engineering 51(2005)7-8, 379-385
UDK - UDC 536.2
Izvirni znanstveni članek - Original scientific paper (1.01)

Heat transfer during transverse air flow around a cylinder

Wladysław Nowak, Aleksander A. Stachel*

Department of Heat Engineering, Technical University of Szczecin,
al. Piastów 19, PL 70-310, Szczecin, Poland
e-mail: andrzej.stachel@ps.pl

Abstract

The principal objective of the present work is to conduct investigations leading to a fuller explanation of heat transfer process on the external wall of a heated cylinder under conditions of laminar flow at transverse of a flow around the cylinder under high pressures conditions. Investigations are aiming at determination of the limits of existence of mixed convection and explanation, amongst the others, of the influence of free convection on the disturbances of heat transport during laminar flow of a medium and finally explanation of the intensification of heat transfer process occurring during a flow under conditions of high pressures.

1. Introduction

A majority of convective heat transfer processes occur under moderate pressures (below 1MPa) and significant flow velocities (turbulent flow). However, there are branches of technology, where the velocities of the working medium are small and the flow is of laminar or transitional nature. There are also such cases, where the processes of heat transfer occur at very high pressures.

In the description of heat transfer at high pressures conditions are used the relations developed for pressures around normal pressure. On the other hand, the results of some works suggest that the convective processes under conditions distanced from normobaric conditions do not obey the relations generally acknowledged for the description of heat transport [3,4,6,8]. The phenomenon is best observed in the laminar flow regime. The analysis of the problem enables to draw a conclusion that the reason for such discrepancies is the superposition of free convection and forced convection, hence the existence of mixed convection. Under high pressures conditions the process is much more intense.

The present work is an experimental attempt to understand the issue of mixed convection under hyperbaric conditions. The principal objective of the present work is to conduct investigations leading to a fuller explanation of heat transfer process on the external wall of a heated cylinder under conditions of laminar flow around the cylinder. Investigations are aiming at determination of the limits of existence of mixed convection and explanation, amongst the others, of the influence of free convection on the disturbances of heat transport during laminar flow of a medium and finally explanation of the intensification of heat transfer process occurring during a flow under high pressures.

2. Pressurised research rig

In investigations of heat transfer processes under conditions of mixed convection utilised has been a unique research rig. The rig has been designed and manufactured at the Department of Heat Engineering of TU of Szczecin in connection with realisation of numerous works regarding the heat transfer processes under high pressure conditions [3,4,6,7,8]. View of a rig is presented in Fig. 1.

The main element of a rig is a pressure chamber with internal diameter of 113 mm and working length of 1500 mm, adequate for operation in the range of absolute pressures ranging from 0.1 MPa to 16 MPa. According to the needs, the research chamber can be positioned horizontally or vertically. Investigated element (for example the heat exchanger), of a specified geometry resulting from the research agenda, is placed inside the chamber. Such solution enables attainment of high Grashof numbers without the necessity of change of a kind of medium flowing through the heat exchanger, as well as enabling sustaining of small values of temperature differences inducing the free flow of medium [1,2,5].

Nomenclature

Gr	- Grashof Number	*Q*	- *heat, J*
L	- dimension of the cylinder, m	*Re*	- *Reynolds Number*
Nu	- Nusselt Number	*T*	- temperature of medium, K
Pr	- Prandtl Number	λ	- the thermal conductivity, W/mK

A detailed schematic of hydraulic installation of the rig has been presented in Fig. 2. A research chamber (1) is connected with a set of pressure tanks (2). The first tank (2a) has to separate water droplets from the compressed air. The next tank (2b) contains a dehydration substance in the form of an exchangeable insert (8), which objective is to remove moisture from the air supplied to the research chamber. In the last tank, (2c), installed is a mesh filter (9) for elimination of solid contaminants from pumped air.

The system of pressure tanks (2) is connected with a spherical storage air tank (3), which also serves as a balancing tank, where gas pulsations from the compressor operation are initially damped. The major source of compressed air is a four-stage compressor set (4) with the efficiency rate of 50 m^3/h and maximum pumping pressure of 16 MPa. An additional source of air is a membrane compressor (5) with the efficiency rate of 20 m^3/h.

During measurements the research rig operated in the open mode, where the used air has been released to the atmosphere. Such solution is permissible due to the kind of a utilised working medium. The hydraulic installation (after small adaptations) enables operation in a closed-loop mode. Such solution can be interesting in the case of conducting experiments with other than air gases.

In conducted experiments the circulation of the medium (air) is as follows.

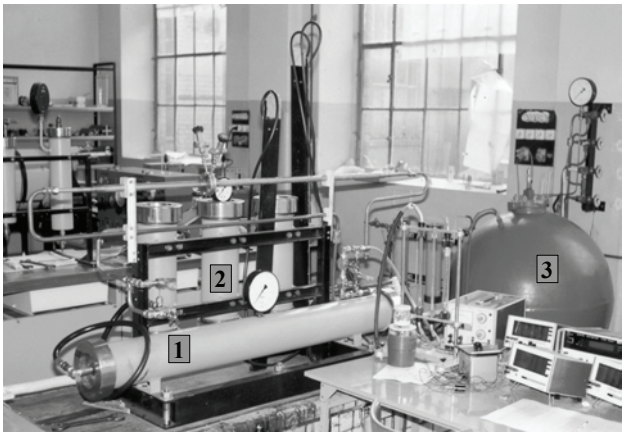

Fig. 1. A view of a rig for investigations of convective processes under high pressure conditions.
1-research chamber, 2-pressure tanks, 3-storage tank

Air pumped by the compressor (4) and/or (5), is directed to the spherical tank (3) and further through the set of cut-off valves (13) to the first tank (2a). Then, after eventual separation of contained water, the air flows through a controllable reductor (10), where initial regulation of pressure to the required level takes place, and then flows to the tank (2b) equipped with a dehydrator (8) and finally to the tank (2c), where filtration from solid particles takes place.

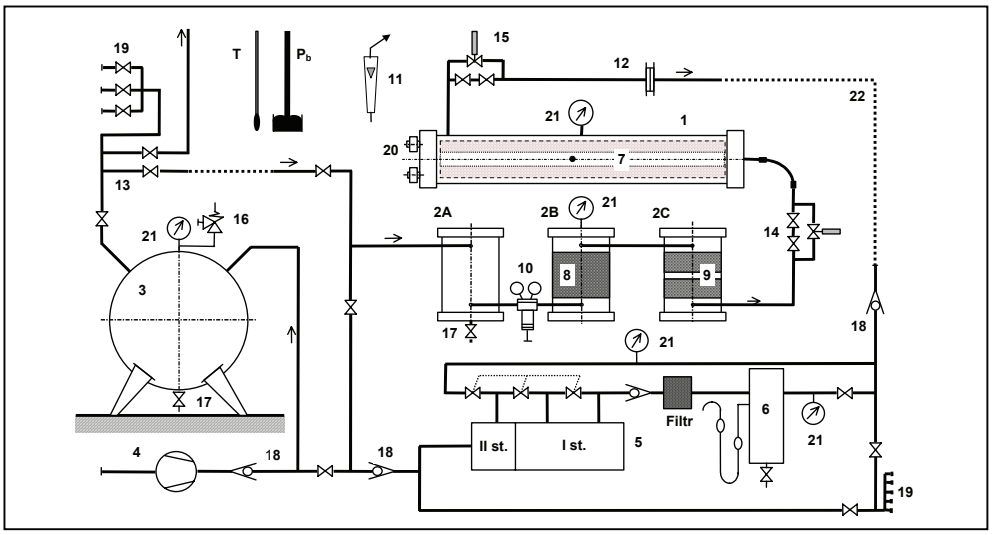

Fig. 2. A hydraulic schematic of a research rig for investigations of mixed convection (description in the text)

Air is supplied through the set of control valves (14) to the pressurised research chamber (1), where it flows through an investigated element (7) and heats up. Heated air leaves the chamber through the outlet pipeline equipped with a set of control valves (15) and flows out to surroundings. In the outlet pipeline installed are flowmeters, which enable measurement of the amount of flowing out air. There has been envisaged a possibility of measurement of the stream of air by means of a set of rotameters (11) or an orifice (12).

Pressure control in the research chamber and the control of a stream of flowing air takes place by means of the sets of valves (14, 15) installed at the inlet and outlet from the chamber. Manometers (21) serve for pressure control in the system.

A research chamber (1) is equipped with two electric multi-sockets (20) enabling connection of measurement sensors situated inside chamber with the necessary meant equipment.

3. The merit of investigations – heated cylinder

Experimental investigations regarded convection heat transfer during a flow of air around the cylinder. An experimental cylinder with circular cross-section, equipped with internal electric heater, is flown by a stream of air, during which the heat transfer to the flowing gas takes place. During investigations a specially designed cylinder has been used with external diameter of 10 mm and a total length of 60 mm. A construction of the cylinder is presented in Fig. 3.

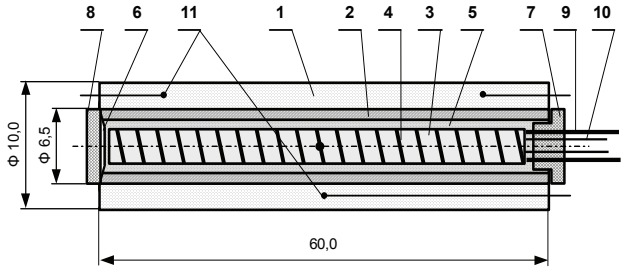

Fig. 3. Investigated cylinder – construction. (description in the text)

The body of a cylinder (1) consists of a copper sleeve, with external diameter of 10 mm, internal diameter of 6,5 mm and a total length of 60 mm. Inside the sleeve located is the heating insert, so called patron. The heating insert is manufactured from the chromium-nickel resistance wire (4), wounded up the ceramic core (3) and centrally placed inside the steel body (2). The space between the ceramic core and the wall are filled with the pulverised insulation material (5), in order to stabilise the heater position inside the body. The body of the heating insert is closed on one side with the steel bottom (6) with additional insulation sleeve (8), and on the other side with the ceramic insulator (7) with electric sockets (9). Additionally, inside the heater there is located a ferric-constantan thermocouple for measurements of the inner temperature. The connection sockets (10) are taken out through a ceramic culvert in the heater. In the selected external points of the cylinder body (the copper sleeve) fixed are sub-miniature measurement sensors for temperature determination on the cylinder surface. The copper-constantan thermocouples (11) have been used for that reason, where as a copper electrode is selected the sleeve of the body.

4. Cylinder positioning – investigation channel

In the work analysed have been three various cases of the flow of air around the cylinder, namely a transverse horizontal flow and transverse vertical flow (from the top and from the bottom). In all cases investigations have been conducted using the same model of the cylinder. The difference was only in the positioning of the cylinder and the direction of air flow. A schematic of the positioning of the cylinder in the measurement channel in the case of a horizontal flow of air around the cylinder is presented in Fig. 4.

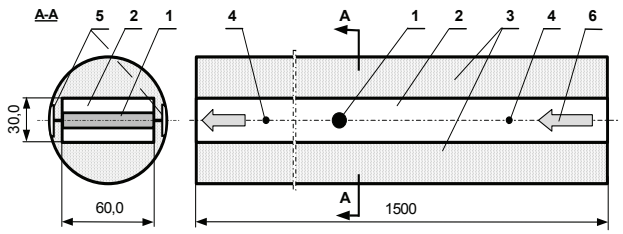

Fig. 4. Positioning of a cylinder in the measurement channel - transverse flow of air around the cylinder. (description in the text)

During conducted investigations the cylinder was placed inside the measurement channel with square cross-section in the half of it length and half of its height. The measurement channel has the following dimensions: width - 59,6 mm, height - 25 mm and length - 1500 mm. The channel has been manufactured from the axially divided wooden block, where the external form was of the form of the shaft with dimensions corresponding to the external dimensions of the pressurised research chamber. In both halves of the block milled are two parts of the channel, which after combination and fixing form a rectangular channel with given dimensions. The cylinder can be situated transversely with respect to the channel axis.

The channel is equipped with sensors for measurements of temperature at the inlet and outlet from the cylinder. For that reason sub-miniature measurement sensors Pt-100, are located at the initial and final part of the channel. Additionally, in order to determine the heat

flux through radiation from the surface of a cylinder to the channel walls as well as conduction in the sockets and heater fixing, the channel walls have been equipped with a set of adequately distributed copper-constantan thermocouples.

A complete channel together with installed investigated model of a cylinder and measurement sensors is placed inside the pressure chamber.

5. A measurement system in the research rig

A schematic of the measurement installation for investigations of convection during the flow around the cylinder has been presented in Fig. 5.

The heat flux released by the heating element of the cylinder (1) has been determined on the basis of measurements of the current (13) and voltage (12) drop through the heating spiral. The heater has been fed from a stabilised laboratory feeder of direct current (11).

A measurement of the amount of air flowing through a channel (10) and flowing past the investigated cylinder (1) was taking place by means of a set of calibrated (for air) rotameters (7), where their readings have been converted into the real conditions present inside the pressurised chamber (2) containing the investigated element (1). According to the needs, during the experiments the rotameters (7) could be used alternatively with the orifice (8). Both apparatus were placed in a low-pressure part of the outlet pipeline (4), removing the expanded air from the pressure chamber (2). At that location measured also has been a temperature of outlet air by means of copper-constantan thermocouple (20). Regulation of air stream flowing through the heat exchanger was taking place by means of valves (5,6) placed at inlet and outlet from the heat exchanger.

For measurement of pressure in the research chamber utilised have been precision piezoelectric pressure transducers (22) with adequate measurement ranges. Static pressure of air in the outlet pipeline (4) and the pressure drop in the case of using an orifice (8) have been measured by means of precision liquid manometers (9).

Determination of a mean surface temperature of the cylinder was made on the basis of measurement of electromotive force of a set of Cu-constantan thermocouples located just underneath the cylinder body (1). In the similar way, by means of Cu-constantan thermocouples, were conducted measurements of internal temperature of the channel and the heater contacts. A milivoltmeter (17) was used for measurements of voltage present at particular thermometric sensors. A selection between the measurement sensor and the measured temperature was made by means of a switch (18). Inlet and outlet air temperatures in the heat exchanger were determined by means of measurement of voltage drop (17') by the resistance measurement sensors of Pt-100 type (15) fed from a direct current source (16',19').

Values of temperatures, humidity and atmospheric pressure, necessary for reduction of data, were determined on the basis of indications of laboratory thermometers (23), capacity-based humidity meters and a precision mercury barometer (24).

6. The analytical method

The heat transfer effect observed during the forced flux of working medium (air) in the measurement channels at the steady heat flux state can be described by means of a general dimensionless equation form, taking the following [6,9]:

$$Nu = f(Re, Pr, Gr, ...) \tag{1}$$

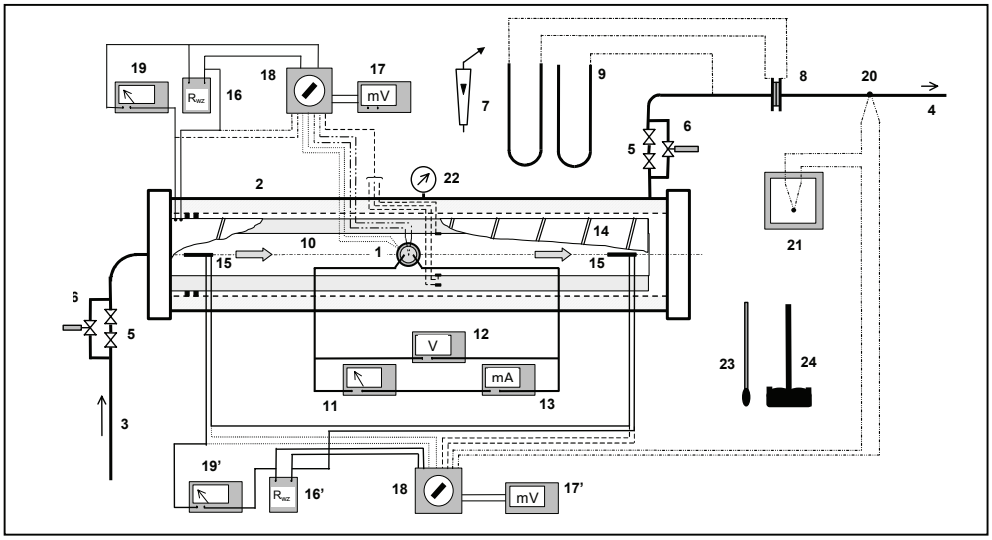

Fig. 5. A schematic of the measurement system in the research rig for investigations of mixed convection under conditions of high pressures (description in the text).

On the grounds of calculating such prime quantities, as heat flux transmitted in the experimental exchanger to the flowing medium, air temperature at the inflow and the outflow of the meassuring channel, temperature of the exchanger wall surface as well as the insulation layer etc., the quantities constituting the dimensionless equation were defined. For example, the Nusselt number was defined according to the following dependence [11]:

$$Nu = \frac{\dot{Q}}{\pi \cdot L \cdot \Delta T \cdot \lambda} \qquad (2)$$

where: $\dot{Q}$ - the heat flux transmitted in the experimental cylinder to the flowing medium (air).

On the basis of the data obtained from the measurements the values of Nusselt, Reynolds, Prandtl and Grashof numbers for the tested cases were calculated.

7. Results of investigations

Experimental studies have been conducted at pressures ranging from 0.1 to 10 MPa [11]. In effect obtained has been a set of results describing the convective heat transfer in different geometrical arrangements as well as different flow regimes. In the present paper presented are only the results regarding a transverse horizontal flow and transverse vertical flow (from the top and from the bottom) of air around the cylinder (Fig. 6).

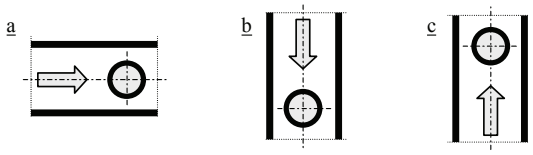

Fig. 6. Analysed configurations of the transverse air onflow on the cylinder:
a-horizontal, b-from the top, c-from the bottom

Sample results of investigations regarding the horizontal and vertical (from the top and from the bottom) air onflow have been presented graphically in Figures 7, 8 and 9. The results have been shown in the form of two-dimensional graphs with one variable depicting the dependence of the Nusselt number on the Reynolds number, developed for the subsequent values of pressures. Such a way of description in the form of relation *Nu = f(Re)* is typical for the forced convection, but implemented for the mixed convection depicts the influence of pressure on the heat transfer processes.

For comparison in the graphs presented also are the curves developed from the non-dimensional analysis according to Hilpert, Van der Hegge Zijnen and Mc Adams [2,11].

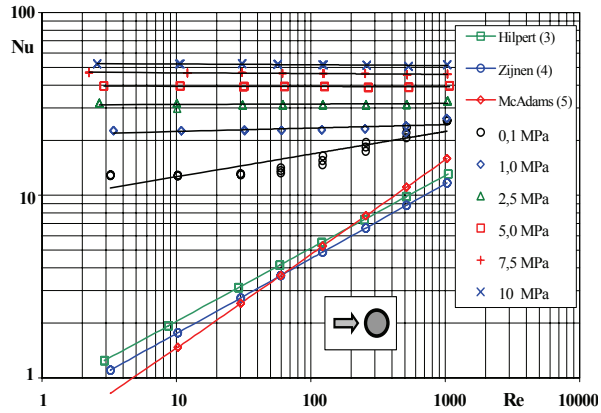

Fig. 7. Nu = f(Re) dependence for a horizontal transverse air onflow on the cylinder

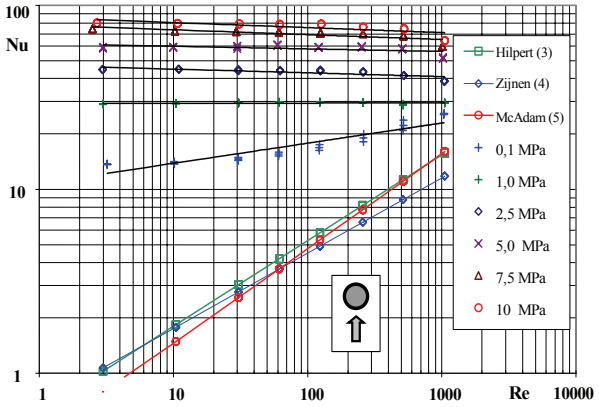

Fig. 8. Nu = f(Re) dependence for a vertical transverse air onflow on the cylinder (from the bottom)

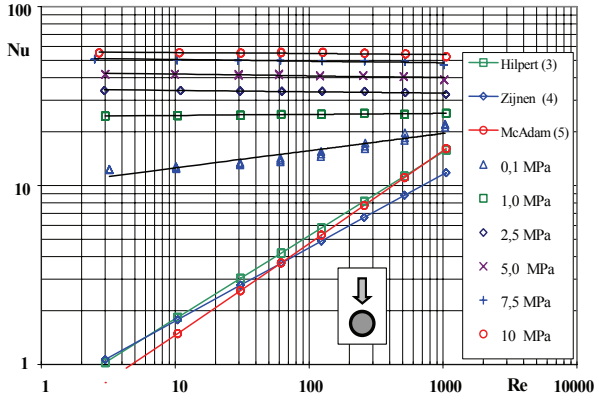

Fig. 9. Nu = f(Re) dependence for a vertical transverse air onflow on the cylinder (from the top)

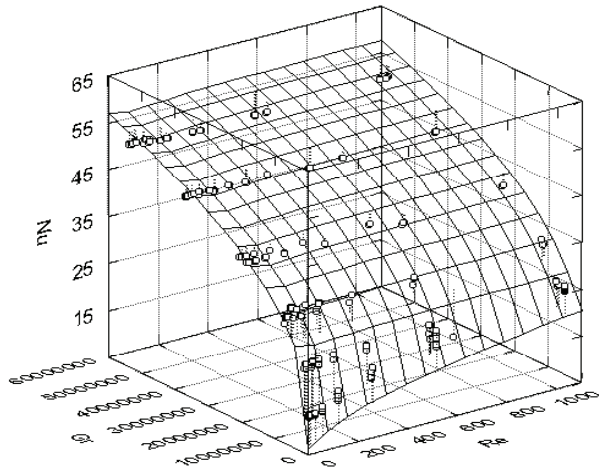

Fig. 10. Nu = f(Re,Gr) dependence for a horizontal transverse air onflow on the cylinder

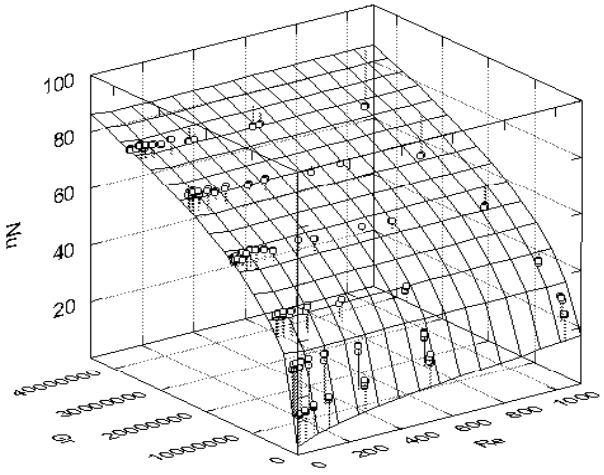

Fig. 11. Nu = f(Re,Gr) dependence for a vertical transverse air onflow on the cylinder (from the bottom)

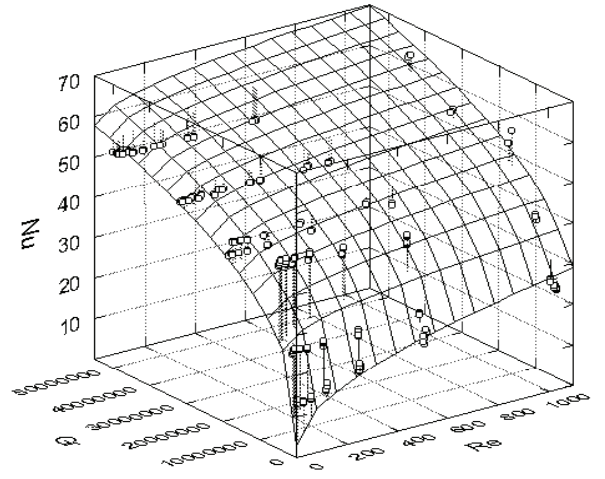

Fig. 11. Nu = f(Re,Gr) dependence for a vertical transverse air onflow on the cylinder (from the top)

Obtained results have also been presented in the form of three dimensional distributions depicting the *Nu = f(Re,Gr)* dependence. Such type of presentation is advantageous for the analysed cases of convection due to the fact that it reveals the influence of particular modes of convection (both of free and forced type) on values of the Nusselt number (Fig. 10, Fig. 11, Fig. 12).

A mathematical description of investigated phenomena of mixed convection has been conducted using the equation in the form of a sum of exponential terms, applied in such a way for the first time by Hausen [11]. Such way of description of convection has also been applied by Budzyński [1,11].

In such equation subsequent terms describe a certain part of considered phenomenon. The first term describes forced convection at small values of the Reynolds number whereas the second – forced convection in the full regime, and the third one – mixed convection. The specifics of the equation is that its particular terms cannot be applied in a sole description of „pure" types of convection. Obtained in such analysis equations describing particular modes of convection at axial flow around the investigated cylinder are presented in Table 1.

Table 1. Dimensionless equations describing heat transfer for cases of transverse flow of air around the cylinder

Cases of flow:	Equations
Horizontal	$Nu = 1{,}31\,\mathrm{Re}^{-0{,}44} + 3{,}01\,\mathrm{Re}^{0{,}11} + 0{,}5\left(5\cdot 10^{-1}\,\mathrm{Re}^{6{,}04} + 4\cdot 10^{-9}\,Gr^{4{,}31}\right)^{0{,}08}$
Vertical - from the bottom	$Nu = 0{,}63\,\mathrm{Re}^{-0{,}48} + 87\,\mathrm{Re}^{0{,}15} + 0{,}5\left(5\cdot 10^{-1}\,\mathrm{Re}^{6{,}11} + 11\cdot 10^{-9}\,Gr^{4{,}67}\right)^{0{,}08}$
Vertical – from the top	$Nu = 0{,}57\,\mathrm{Re}^{-0{,}57} + 1{,}67\,\mathrm{Re}^{0{,}31} + 0{,}5\left(5\cdot 10^{-1}\,\mathrm{Re}^{6{,}08} + 7\cdot 10^{-9}\,Gr^{4{,}35}\right)^{0{,}08}$

A reflection of dimensionless equations are presented in the figures surfaces expressing described in such way dependence between the Nusselt number and the Reynolds and Grashof numbers. On the basis of comparative analysis it can be concluded that those surfaces correlate well with presented in particular graphs point denoting values of the Nusselt number, determined as a result of performed measurements. Obtained consistency is satisfactory particularly in the range of high Grashof numbers, which corresponds to high experimental pressures.

6. Conclusions

Analysis of obtained results enables to conclude that in all considered cases the increase of pressure is accompanied by the increase of Nusselt number, which

results from superposition of free convection on the forced convection. Such process has been described on the basis of obtained results using the non-dimensional numbers developed for particular variants of the flow around the considered cylinder.

In the performed experiments it has been concluded that the heat transfer intensity depends on the way of the air flow around the cylinder. The highest values of Nusselt number have been obtained for a vertical flow directed on the cylinder from the bottom. On the other hand the lowest values of Nusselt number have been achieved for a vertical air onflow from the top. Such phenomenon is observed in the entire range of investigated pressures and the discrepancy of developed results increases with the increase of pressure, particularly for the vertical onflow from the bottom.

Presented in the paper results regard only a narrow range of conduced experiments. For example in the present work have not been presented the results of investigations of convection at different configurations of the transverse flow around the cylinder [12]. Obtained results did not also give the answer to the all questions raised in the paper. For example the borders between the mixed convection and free and forces convection have not been set. Bearing that in mind, both experimental and theoretical studies regarding mixed convection at different configurations of the air onflow will be continued and the results successively published.

References

[1] Budzyński R.: *Three-dimensional surface of heat for laminar forced and mixed convection from circular cylinder*. Int. Comm. Heat Mass Transfer, Vol. 19, No. 4, pp. 461-471, 1992.

[2] Budzyński R., Nowak W.: *Mixed convection heat transfer in a horizontal concentric cylindrical annulus at small Reynolds and large Grashof numbers*. 6th International Energy Conference, Mansoura University, Alexandria, 1993.

[3] Budzyński R., Nowak W., Stachel A. A.: *Effect of high pressure on convective heat transfer of forced laminar and transitional flow in horizontal concentric cylindrical annulus*. 2nd Baltic Heat Transfer Conference, Riga – Jurmala, Latvia, 1995.

[4] Budzyński R., Nowak W., Stachel A. A. and all: *Convective heat transfer in the flow of gas in the channel*. TU of Szczecin, DHE, Grant of PAS, 1999. (Non published research work).

[5] Maj A., Nowak W., Stachel A. A.: *Mixed convection in a horizontal circular channel in high pressure conditions*. II Int. Conference on Advances in Fluid Mechanics, Udine, 1998.

[6] Metais B., Eckert, E.R.G.: *Forced, mixed and free convection regimes*, ASME J. Heat Transfer, Vol.10, pp. 295-296, 1964.

[7] Nowak W., Stachel A. A.: *Effect of pressure on heat exchange at a forced flow in annular channel.* 2nd International Heat and Mass Transfer Forum. Minsk, 1992

[8] Nowak W., Stachel A.: *Experimentelle Ermittlung der Wärmeübergangs-koeffizienten bei Hochdruck-strömung im Ringkanal.* Wiss. Zeit. der TU Dresden, 42 (1993) Heft 4.

[9] Oostthuizen P.H., Naylor D.: *Introduction to Convective Heat Transfer Analysis*. McGraw-Hill International Editions, New York, 1999.

[10] Stachel A. A.: *Mixed convection during a flow around a cylinder. Part I.* Acta Mechanica Slovaca, 2/2002, Ročnik 6. pp. 151-158, Košice, 2002.

[11] Stachel A. A., Nowak W. and all: *Mixed convection during a flow around a cylinder in high pressure conditions*. TU of Szczecin, DHE, Grant of PAS, 2002. (Non published research work).

[12] Stachel A. A., Nowak W.: *Mixed convection during a transient flow around a cylinder.* Proceedings of the 4th Baltic Heat Transfer Conference, Kaunas, Lithuania, 2003.

[13] Stachel A. A.: *Mixed convection during of an axial flow around a cylinder.*Acta Mechanica Slovaca, 3/2003, Ročnik 7. pp. 473-478, Košice, 2003.

Strojniški vestnik - Journal of Mechanical Engineering 51(2005)7-8, 386-390
UDK - UDC 536.2
Izvirni znanstveni članek - Original scientific paper (1.01)

Numerical Simulation of Scalp Cooling to Prevent Chemotherapy–Induced Alopecia.

Francis-Paul E.M. Janssen*, Gerard M.J. van Leeuwen, Anton A. van Steenhoven.

[1]*Department of Biomedical Engineering, Eindhoven University of Technology, PO Box 513, Eindhoven, The Netherlands,* f.e.m.janssen@tue.nl.*

Abstract

One way of treating cancer is by chemotherapy. Side–effects of chemotherapy include hair loss. Cooling the scalp during treatment can reduce hair loss. For this cooling, a cap containing a cold fluid (cold cap) is used. However, the rate of success of this method varies strongly, because precise mechanisms of preservation are unknown.

Temperature and perfusion are thought to play an important role in the hair preservative effect of scalp cooling. To gain more insight into these parameters, a computer model has been developed. With this, the influence of perfusion models is studied.

The computer model comprises a head and cold cap, modeled with concentric shells representing brain, skull, fat, skin, hair and cold cap. Metabolism is temperature dependent and two relations from literature are used to model temperature dependent perfusion. Pennes' bio–heat equation is used to determine the heat transfer in the head. Steady state temperatures without cold cap are calculated and used as basal temperatures for metabolism and perfusion. Then, a cold cap (T = -30˚C) is added and the development of temperature in time is calculated. For constant perfusion, a minimum skin temperature of 16.0˚C is reached after 476 seconds. When skin blood flow is set to zero, the minimum temperature drops a further 1.5˚C to 14.5˚C. For the perfusion models, the drop in skin temperature results in a decreased perfusion, down to a value ranging from 19% to 33% of base level.

The thickness of the hair layer is of great importance for both perfusion and temperature. Reducing the thickness resulted in a decrease in temperature of 5.7˚C, and decreased relative perfusion by a further 0.10, indicating that chances of preserving hair are higher. For optimal protection against hair loss, the cold cap should fit the scalp as tightly as possible.

Introduction

Cancer is a common illness. Each year, 0.5% of the US population is newly diagnosed with cancer [8]. One way of treating cancer is by chemotherapy. It kills rapidly dividing cells, and usually it is relatively specific for cancer cells. However, other constantly dividing cells are also affected, such as the matrix cells in the hair follicle that produce the hair shaft.

Administration of chemotherapy induces toxicity in these matrix cells. The root sheaths may become necrotic, or, in less severe cases, form a weak, constricted hair shaft that then easily breaks [10]. The resulting hair loss is rapid and extensive, since more than 90% of scalp follicles are in a growing phase at any given time [5].

Although temporarily, hair loss is one of the most feared side effects of cancer therapy [4]. It causes psychological stress, which may even lead some patients to reject potentially curative treatment [9]. It has been shown that scalp cooling during the administration of the cytotoxic drugs can reduce hair loss (e.g., [12]). For this, a cap containing a cold fluid (cold cap) is placed.

The current hypothesis for the mechanism is that by cooling the scalp skin, blood perfusion is reduced. This reduces the total amount of cytotoxic drugs that are available for uptake in the matrix cells. In addition, reaction rates decrease with lower temperature, reducing chemotherapy uptake. The combined effect gives a drastic reduction in cell damage, such that hairs are preserved.

However, the effect of scalp cooling varies strongly [9]. One of the reasons for the varying success of scalp cooling is that current day treatment is based on trial and error [3]. A systematic evaluation of the current hypothesis is necessary for a better understanding of the various important parameters of scalp cooling. To gain

Nomenclature

c	Specific heat	J/kg K	**Greek**		
Cs	Vasoconstriction	-	α	Proportional model constant	-
h	Heat transfer coefficient	W/m^2 K	ε	Emissivity	-
k	Thermal conductivity	W/m K	ω	Blood perfusion rate	kg/m^3 s
M	Metabolic rate	W/m^3	ρ	Density	kg/m^3
T	Temperature	K			
t	Time	s	**Subscript**		
q''	Heat flux	W/m^2	0	Basal	
			sk	Skin	

more insight into the effect of cooling, a computer model has been developed to study the mutual influence of temperature on perfusion during cooling with a cold cap, using different perfusion models. With temperature–perfusion relations from the literature, estimates can be found for the decrease in local drug delivery.

Methods

The heat produced by metabolic processes in the human body is transported by means of conduction and convection. These heat transport mechanisms occurring in the living tissue were modeled by Pennes [11] in the well–known "bio–heat transfer" equation:

$$\rho c \frac{\partial T}{\partial t} = \nabla(k \nabla T) + (c\omega)_{\text{blood}}\left(T_{\text{artery}} - T\right) + \text{M} \tag{1}$$

in which ρ, c and k are the density, specific heat and conductivity, respectively. T is the local tissue temperature and T_{artery} the temperature of the blood, in this study assumed to be constant and set to 37°C. ω and M are the blood perfusion rate and the metabolic heat production in the tissue, respectively.

The Pennes' model uses a "heat–sink" approach to model perfusion. It assumes that all heat transfer takes place in the capillaries in the tissue. Although this assumption has been debated for its validity [1], it has been shown that this equation produces accurate results for the temperature distribution in the head during scalp cooling [14].

During scalp cooling, a large drop in skin temperature occurs. This influences both metabolism and perfusion.

Metabolic heat production is modeled according to the so–called Q10–effect [13]. It states that a temperature drop of ten degrees Celsius results in a 50% decrease in heat production:

$$\text{M} = \text{M}_0 \cdot 2^{(T - T_0)/10} \tag{2}$$

Local skin blood flow is also affected by this reduction in metabolic heat production [7].

In addition, the decrease in temperature may trigger changes in blood flow by thermoregulation. To see the influence of these two mechanisms, three different perfusion models are used.

Perfusion models

The first model (constant model) uses a constant α ($0 < \alpha < 1$), to obtain a constant perfusion, proportional to basal perfusion:

$$\omega_{\text{sk}} = \alpha \cdot \omega_{\text{sk},0} \tag{3}$$

The second model (Stolwijk model) uses the reduced perfusion corresponding to the decrease in metabolic heat production (Q10–effect):

$$\omega_{\text{sk}} = \omega_{\text{sk},0} \cdot 2^{\left(T_{sk} - T_{\text{sk},0}\right)/10} \tag{4}$$

In this equation, T_0 is the local neutral temperature, obtained from steady state calculations.

Finally, the third model (Fiala model) incorporates the Q10–effect and an extra term to represent vasoconstriction (Cs):

$$\omega_{\text{sk}} = \frac{\omega_{\text{sk},0}}{1 + \text{Cs}} \cdot 2^{\left(T_{sk} - T_{\text{sk},0}\right)/10} \tag{5}$$

Fiala [7] used the Cs term to describe the reaction of local skin blood flow to variations in mean skin temperature of the whole body. For this study, an adapted equation for Cs is used, since only scalp skin temperature is affected:

$$\text{Cs} = 2.92\left[\tanh\left(0.0284\Delta T_{\text{sk}} + 1.07\right) - 1\right]\Delta T_{\text{sk}} + 0.326\Delta T_{\text{sk}} \frac{\text{d}T_{\text{sk}}}{\text{d}t} \tag{6}$$

with ΔT_{sk} defined as:

$$\Delta T_{\text{sk}} = T_{sk} - T_{sk,0} \tag{7}$$

Table I: Parameters of the numerical model [15].

	Outer radius r [mm]	Conductivity k [W/m K]	Specific Heat c [J/kg K]	Density ρ [kg/m^3]	Metabolic Rate M [W/m^3]	Blood Flow ω [kg/m^3 s]
Brain	90.0	0.536	3643	1030	5370	5.37
Skull	96.5	0.650	1590	1520	0.0	0.06
Fat	97.5	0.217	2367	888	300	0.31
Skin (inner)	98.5	0.342	3662	1070	1800	1.8
Skin (outer)	99.5	0.342	3662	1070	0.0	0.0
Hair	100.5	0.026	1000	1.0	0.0	0.0
Cold Cap	110.5	0.500	4300	1000	0.0	0.0

Numerical Methods

The computer model consists of a typical head and a cold cap, both idealized with spherical elements representing brain, skull, fat, skin, hair and cold cap. The model is essentially one dimensional, which means that only radial conduction will be accounted for. Tissue layers are assumed to have homogeneous properties. Dimensions, thermal properties, basal blood flow and basal metabolic rate of each layer are taken from literature [15] and are shown in Table I.

Boundary conditions for head and cold cap include convective heat transfer and radiative heat transfer. Convective heat transfer from head or cold cap to the surroundings is modeled as

$$q'' = h\left(T - T_{\text{ambient}}\right) \tag{8}$$

in which h is the heat transfer coefficient. Its value was taken from literature as 4 W / K m^2 [15]. The thermo–neutral temperature distribution (i.e. no response of thermoregulation), was calculated with the ambient temperature (T_{ambient}) set to 20˚C.

Radiative heat transfer from the cap surface to the surroundings and between head and cold cap is modeled as

$$q'' = \sigma\varepsilon\left(T_1^4 - T_2^4\right) \tag{9}$$

in which σ is the Stefan Boltzmann constant (σ = $5.669 \cdot 10^{-8}$ W / m^2 K^4) and ε the emissivity. Emmisivity of both head and cold cap was taken as 1.0.

For cooling of a homogeneous sphere with constant material properties, temperature profiles in the sphere at various times during cooling matched the analytical solutions to within 0.06˚C [2]. Steady state temperatures of the model with heat generation and perfusion were also compared to the analytical solution [7] and the results are accurate to within $5 \cdot 10^{-3}$˚C.

Simulation of a scalp cooling procedure consisted of two steps. First, the temperature without a cold cap was calculated, keeping metabolism and perfusion constant. The resulting temperature profile was used as basal temperature profile for temperature dependent metabolism and skin blood flow. Then, a cold cap is added to the model. In practice, a cold cap can either be continuously cooled, or only be cooled before application. The first cold cap has an initial temperature of -5˚C and uses a cooling system that circulates fluid (temperature -5˚C) at 10 liters per minute (ω_{sk} = 119 kg/m^3 s). The second cold cap does not circulate fluid and has an initial temperature of -30˚C.

In a parameter study the influence of varying skin perfusion rates and different perfusion models on the temperature response was studied.

Results

Perfusion Models

First, the temperature development in time for different perfusion models was calculated for the pre–cooled cap. To indicate the boundaries of response, i.e. the minimum and maximum temperature responses, the constant model was used. For the constant model with α = 1, the scalp temperature dropped from 34.3˚C and reached a minimum of 16.0˚C after 476 seconds (Fig. 1A), after which it gradually returned to a normal value. With α = 0, minimum temperature was 14.5˚C, which was reached after 535 seconds.

Next, the Stolwijk and Fiala models were used (Eq. 4 and 5, respectively). The difference in minimum temperature between the Stolwijk model and the Fiala model was 0.2˚C (15.1˚C versus 14.9˚C, respectively). For the Stolwijk model, perfusion was reduced down to a relative value of 0.33 (Fig. 1B). After a strong decrease in the beginning of the simulation, the Fiala model shows a minimum relative value of 0.19.

Size of Hair Layer

In a parameter study, Van Lenthe [15] showed that the thickness of the hair layer is the most critical parameter in lowering the scalp temperature. To see the influence of this parameter on relative perfusion and scalp temperature, simulations were done using the cold cap with cooling system (T = -5˚C), to obtain stationary situations. The standard model uses a hair layer of 1mm, and resulted in a skin temperature of 17.2˚C. Doubling the hair layer thickness increases relative perfusion in the Stolwijk model from 0.37 to 0.49 (Fig. 2). For the Fiala model, the perfusion in the cooled state changes from 0.23 to 0.35. In addition, the minimum temperature of the

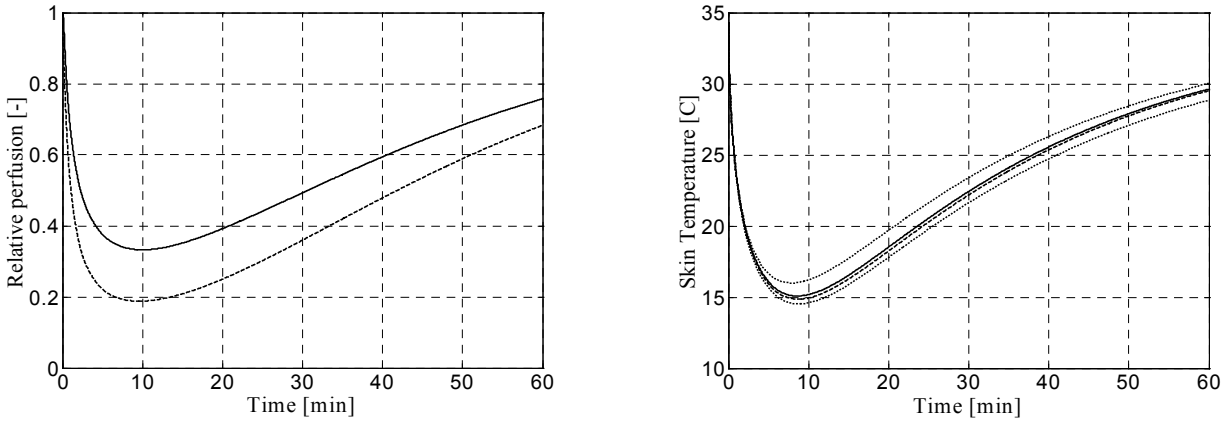

Figure 1: A: Development of the skin blood flow for the Stolwijk model (solid line) and the Fiala model (dashed line).
B: Development of the skin temperature for different perfusion models. Upper and lower dotted line are of the proportional model with α = 1 and α = 0, respectively. The solid line represents the Stolwijk model, and the dashed line the Fiala model.

skin is increased by 5.2˚C with respect to the standard model.

A hair layer of 0.5mm resulted in a minimum skin temperature that is 5.7˚C lower than that of the standard model. This temperature reduction decreases the perfusion from a relative value of 0.37 down to 0.27 for the Stolwijk model. The Fiala model showed a perfusion reduction from 0.23 down to 0.14.

Conclusions and Discussion

The perfusion models show a reduction in skin blood flow during cooling. For the Stolwijk model, this reduction is 67%. In the Fiala model, vasoconstriction is also modeled, resulting in a skin blood flow reduction of 81%.

The hair layer has a significant effect on both temperature and perfusion. An increase in hair layer from 1mm to 2mm results in an increase in minimum skin temperature of 5.4˚C. Relative perfusion increases from 0.37 to 0.49 (Stolwijk model). For the Fiala model, relative perfusion increases from 0.23 to 0.35. Decreasing the thickness of the hair layer resulted in a further decrease in relative perfusion. The Stolwijk model shows a decrease to 0.27 and in the Fiala model, perfusion is reduced to 0.14. To maximize the hair preserving potential, the cold cap should have a tight fit, to reduce temperature and perfusion as much as possible.

Decorti [6] showed that temperature is a very important determinant for uptake of doxorubicin (a type of chemotherapy–drugs). They performed experiments with healthy kidney epithelial cells, showing that drug uptake was considerably reduced when temperature was lowered from 37˚C to 4˚C (Fig. 3A). In addition, they studied the relationship between drug concentration and the initial doxorubicin uptake (15 min). At 4˚C, this relationship was linear. At 37˚C, uptake of doxorubicin was greater and showed a trend for saturation (Fig. 3B).

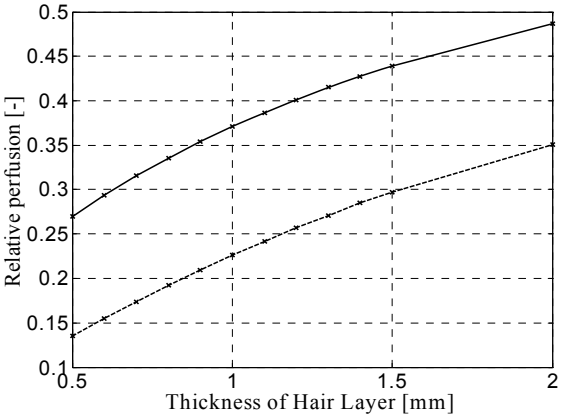

Figure 2: Influence of the thickness of the hair layer on relative perfusion. The solid line represents the Stolwijk model, the dashed line the Fiala model.

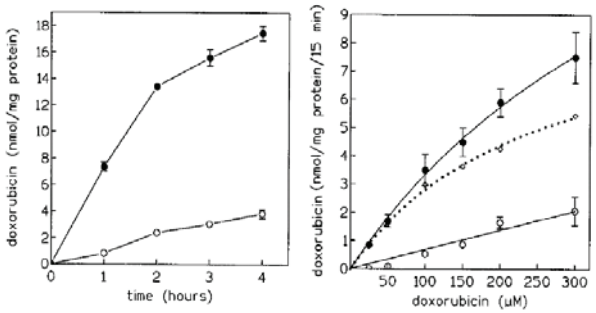

Figure 3: A. Effect of temperature on doxorubicin uptake at 37˚C (●) or 4˚C (○) [6].
B. Concentration dependence of doxorubicin uptake (15 min) at 37˚C (●) or 4˚C (○). The dotted line indicates the difference of doxorubicin uptake at 37˚C and 4˚C [6].

Although results from this study may not be generalized to other cell types, the above study indicates that reducing temperature during scalp cooling with 20˚C decreases the uptake of chemotherapy. In addition, the resulting decrease in perfusion of 60% to 80% leads to a diminished delivery of drugs to the hair follicle cell, lowering drug uptake. In total, the amount of damage done to the matrix cells will be lower, increasing the chances of preserving hair.

To understand the precise effect of reduced perfusion and temperature on cell death on a local level, studies are needed on drug uptake and cell death at different temperatures. In the future, these processes will be quantified by experiments on single hairs and by numerical modeling. Furthermore, the relationship between temperature reduction and perfusion will be studied using Laser Doppler Flowmetry.

References

[1] H. Arkin, L.X. Xu, K.R. Holmes, Recent Developments in Modeling Heat Transfer in Blood Perfused Tissues, IEEE Transactions on Biomedical Engineering 41 (2) (1994) 97-107.

[2] A. Bejan, Heat Transfer, John Wiley & Sons Inc, New York, 1993.

[3] W.P. Breed, What is wrong with the 30-year-old practice of scalp cooling for the prevention of chemotherapy-induced hair loss?, Support Care Cancer 12 (1) (2004) 3-5.

[4] T.F. Cash, The Psychology of Hair Loss and Its Implications for Patient Care, Clinics in Dermatology 19 (2001) 161-166.

[5] G. Cotsarelis, S.E. Millar, Towards a molecular understanding of hair loss and its treatment, TRENDS in Molecular Medicine 7 (7) (2001) 293-301.

[6] G. Decorti, I. Peloso *et al.*, Handling of Doxorubicin by the LLC-PK_1 Kidney Epithelial Cell Line, The Journal of Pharmacology and Experimental Therapeutics, 286 (1) (1998) 525-530.

[7] D. Fiala, Dynamic Simulation of human heat transfer and thermal comfort (thesis), De Montfort University, Leicester.

[8] A. Jemal, T. Murray *et al*., Cancer Statistics, 2003, CA A Cancer Journal for Clinicians 53 (2003) 5-26.

[9] P. Katsimbri, A. Bamias, N. Pavlidis, Prevention of Chemotherapy–induced alopecia using an effective scalp cooling system, European Journal of Cancer 36 (2000) 766-771.

[10] E.A. Olsen, Disorders of Hair Growth: Diagnosis and Treatment, McGraw-Hill, New York, 1994.

[11] H.H. Pennes, Analysis of Tissue and Arterial Blood Temperatures in the Resting Human Forearm, Journal of Applied Physiology 1 (2) (1948) 93-122.

[12] M. Ridderheim, M. Bjurberg, A. Gustavsson, Scalp Hypothermia to prevent chemotherapy–induced alopecia is effective and safe: A pilot study of a new digitized scalp–cooling system used in 74 patients, Support Care Cancer 11 (2003) 371-377.

[13] J.A. Stolwijk, J.D. Hardy, Partitional calorimetric studies of responses of man to thermal transients, Journal of Applied Physiology 21 (1966) 967-977.

[14] G.M. Van Leeuwen, J.W. Hand *et al.*, Numerical modeling of temperature distributions within the neonatal head, Pediatric Research 48 (2000) 351-356.

[15] G.H. Van Lenthe, J. De Hoogh, A.A. van Steenhoven, Numerical modeling of scalp cooling to prevent hair loss induced by chemotherapy, Heat Transfer; Proceedings of the Twelfth International Heat Transfer Conference, (2002) 555-560.

Strojniški vestnik - Journal of Mechanical Engineering 51(2005)7-8, 391-398
UDK - UDC 536.2
Izvirni znanstveni članek - Original scientific paper (1.01)

Thermal Characterisation of Rectangular Cooling Shapes in Heat Generating Mediums – A Three-Dimensional Investigation

Jaco Dirker[1], Arnaud G. Malan[2], and Josua .P. Meyer[2*]

[1]*Department of Mechanical Engineering, Rand Afrikaans University, Johannesburg, South Africa*
[2] *Department of Mechanical and Aeronautical Engineering, University of Pretoria, Pretoria, South Africa,*
** jmeyer@up.ac.za*

Abstract

The optimum aspect ratios of uniformly distributed embedded rectangular cross-sectioned solid cooling inserts in a heat-generating medium are investigated. Numerical investigations were performed to determine and characterise how various geometric and thermal parameters determine these optimum shapes.

Introduction

The current trend in power electronics is to increase the power conversion capability of circuits while reducing their size. One such a way is by means of three-dimensional integration of discrete components into multifunctional modules and the creation of standardized building blocks [1]. This can be done by using planar type structures or modules with various layers [2].

In order to satisfy future thermal demands associated with, for instance, integrated power electronic devices, the focus is starting to shift toward innovative design of the internal structure of power modules to assist in heat extraction, while maintaining high levels of electromagnetic performance and efficiency.

Such an integrated power electronics system requires advances in different technologies, which depend upon finding solutions to deal with the multi-disciplinary issues in materials, electromagnetic compatibility and thermal management.

Purpose

Due to the manufacturing method proposed for constructing the new type of integrated power electronic modules, the cooling inserts would need to have rectangular cross-sections. It is the aim of this paper to describe the optimum aspect ratio of the cooling insert's cross section such that the peak temperature within the heat-generating medium would be minimised. Little reference material was found in literature that describes the optimisation of such geometries. By characterising the influence of various parameters on the optimum cooling structure shape, the design of such embedded cooling systems are enabled.

Procedure

A numerical approach was followed in the study, as it would have been too time-consuming and costly to do the optimisation processes experimentally.

Consider Fig. 1 that gives a representation of a proposed method of assisting heat flow from within a heat-generating medium to the surroundings. The sectioned view shows a generalised distribution of evenly spaced identical rectangular cross-sectioned heat extraction inserts running parallel to the z direction. Arrows indicate the flow of heat from the heat-generating medium via the heat extraction inserts to the surrounding.

If such a set-up is large enough in the x and y directions, or insulated from the ambient, certain assumptions can be made. If each heat extraction structure is exposed to an isothermal uniform ambient in an identical way, rectangular regions drawn around each cooling structure such as those in Fig. 1 (dotted lines), would have identical temperature distributions.

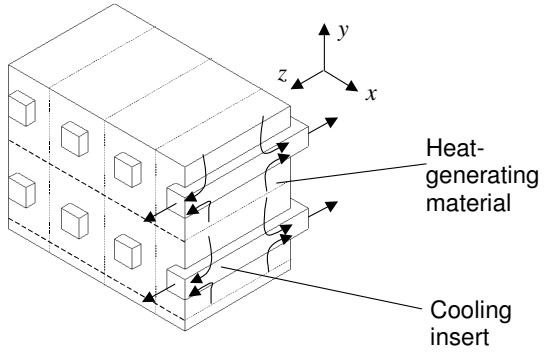

Figure 1 Cross-sectioned representation of a heat generating material with embedded cooling structures

Nomenclature

A x-y view cross-sectional area [m^2]
a x-y view aspect ratio [dimensionless]
$a_{C,rel}$ relative x-y view aspect ratio of cooling insert [dimensionless]
C heat equation coefficient
$\overline{C}_G$ vector of heat gain coefficients
G_M ration between volumetric heat generation and thermal conductivity [K/m^2]
k thermal conductivity [W/mK]
$\mathbf{M}$ matrix of heat equation coefficients
M_2 number of nodes in the x direction [dimensionless]
N_2 number of nodes in the y direction [dimensionless]
$\dot{q}''_C$ heat flux at exposed face of cooling insert [W/m^2]
$\dot{q}'''_M$ volumetric heat generation density [W/m^3]
R thermal interface resistance [m^{2}K/W]
T temperature [K]
x Cartesian coordinate
y Cartesian coordinate
z Cartesian coordinate

Greek and special symbols
α fraction of volume occupied by cooling inserts [dimensionless]
γ thermal conductivity ratio [dimensionless]
$\mathcal{A}$ half centre-to-centre x-directional offset of neighbouring cooling inserts [m]
a half x directional dimension of cooling insert [m]
$\mathcal{B}$ half centre-to-centre x directional offset of neighbouring cooling inserts [m]
b half y directional dimension of cooling insert [m]
$\mathcal{Z}$ half z directional dimension of structure [m]

Subscripts
B relative rear directional (negative z direction)
C cooling insert
D whole domain
E relative easterly direction (positive x direction)
F relative frontal direction (positive z direction)
G heat gain or heat loss
max maximum
min minimum
N relative northerly direction (positive y direction)
S relative southerly direction (negative y direction)
T relative current node indication
W relative westerly direction (negative x direction)
0 reference cooling insert temperature

Furthermore due to the even spacing of the cooling structures and the equal exposure to the surroundings in both sides in the z direction, the temperature field about one such cooling structure is symmetric in all three Cartesian directions. The rectangular region around such a heat extraction structure can thus be divided into quadrants, each of which would be sufficient to represent the temperature field about such a heat extraction structure. Such a three dimensional representative quadrant domain is shown in Fig. 2 where the heat extraction insert is exposed to the surroundings on its positive z side face.

In order to obtain the steady state three-dimensional temperature distribution in such a quadrant domain, a cell-centred finite volume numerical approach was used.

The schematic representation of the grid used for this is shown in Fig. 3 . The number of nodes shown here are not necessarily the number used during simulations. An important point to note is that no nodes were defined on the interface between the cooling structure and the heat-generating medium. This is due to discontinuities that appear in solutions for cases with small or no contact resistance at the interface.

The grid used was localised uniform, which means for each block shown in Fig.3 , the grid spacing was uniform, but not necessarily uniform across the entire mesh. Uniform grid spacing was also used in the z direction.

All boundaries were defined as being adiabatic, except the positive z side face of the heat extraction insert, which had a fixed reference temperature of T_0 at $x = 0$ and $y = 0$, and a uniform heat flux to the surrounding. By applying the principle of conservation of energy, the steady state heat flux, $\dot{q}''_C$ [W/m^2], on this surface can be obtained from the dimensions of, and volumetric heat generation density, $\dot{q}'''_M$ [W/m^3] within the representative domain:

$$\dot{q}''_C = -\frac{\dot{q}'''_M(\mathcal{A}\mathcal{B} - ab)\mathcal{Z}}{ab} \tag{1}$$

Here $\mathcal{A}$, a, $\mathcal{B}$, b, and $\mathcal{Z}$ are the dimensions of the representative domain as defined in Fig. 2 .

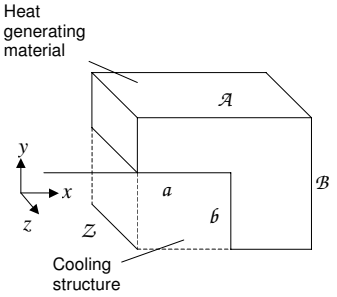

Figure 2 Schematic of the representative domain

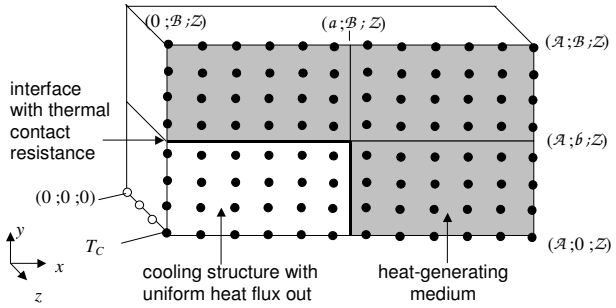

Figure 3 Meshing scheme used

Variable Definition

The aspect ratios of the overall domain and the cooling structure in the *xy*-plane were defined respectively as:

$$a_D = \frac{\mathcal{A}}{\mathcal{B}} \geq 1 \tag{2}$$

$$a_C = \frac{a}{b} \tag{3}$$

Only $a_D \geq 1$ were investigated, as the mirror behaviour for $a_D \leq 1$ is equivalent. For instance $a_D = 2$ would give the same results as $a_D = 0.5$ by just rotating the *x* and *y* axes by 90˚.

The cross-sectional area of the entire representative domain and cooling structure in the *xy* view can be written respectively as:

$$A_D = \mathcal{A}\mathcal{B} \tag{4}$$

$$A_C = ab = \alpha A_D \tag{5}$$

The fraction of the entire domain volume used for heat extraction purposes are denoted by α. Five variables namely A_D [m^2], a_D [dimensionless], a_C [dimensionless], α [dimensionless], and Z [m], define the geometry of the representative domain fully. Due to geometric constraints, the cooling insert aspect ratio, a_C, has maximum and minimum allowed values namely:

$$a_{C,\min} = \alpha a_D \tag{6}$$

$$a_{C,\max} = \frac{a_D}{\alpha} \tag{7}$$

The ratio between the thermal conductivity of the cooling structure, k_C [W/mK] and thermal conductivity of heat-generating material k_M [W/mK] was defined as:

$$\gamma = \frac{k_C}{k_M} \tag{8}$$

The ration between the volumetric heat-generation and thermal conductivity of the heat-generating material [K/m^2] can be written as:

$$G_M = \frac{\dot{q}'''_M}{k_M} \tag{9}$$

Numerical Method

Numerical simulation involves three separated stages namely pre-processing, processing or solution, and post-processing. Pre-processing include the definition of domain dimensions, thermal properties and conditions, mesh creation, and solution method specification. Due to the large number of anticipated simulation cases that would be needed to optimise cooling structure shapes and distribution, the conventional pre-processing stage would become very time consuming when using commercially available numerical simulation software packages. For this reason it was opted to create computer code that would automatically do the pre-processing functions and would then feed the problem information straight into a solution procedure or algorithm.

A fully implicit solution algorithm approach was followed. This approach has the advantage of being computational efficient in the case of relatively small meshing schemes, and highly predictable concerning the running time needed to solve the temperature field. It is only dependent on the number of nodes in the domain and is not influenced by the physical conditions of the domain, as would be the case if a fully explicit procedure were used.

In order to use an implicit method, it is necessary to express the temperature at a node in terms of its neighbouring temperature values by means of different coefficients [3]:

$$C_T T = C_F T_F + C_S T_S + C_W T_W + C_E T_E + C_N T_N + C_B T_B + C_G \quad \ldots(10)$$

Subscripts *F, S, W, E, N*, and *B* refer to the six reference directions namely “front”, “south”, “west”, “east”, “north”, and “back” respectively. Subscript *T* refer to temperature node under consideration, and *G* indicates the heat gain or heat loss of the particular node.

If there is N number of nodes, this will result in *N* number of equations. It is possible to express this system of equations as:

$$\mathbf{M}\overline{T} = \overline{C}_G \tag{11}$$

Here **M** is a *N*-by-*N* coefficient matrix, $\overline{C}_G$ is a vector containing the heat gain or loss coefficient for each node, and $\overline{T}$ is a vector containing the temperature values of all the nodes in the domain.

In order to construct such a matrix it is necessary to decide before hand on a numbering scheme for the nodes such that each node has a unique address. For a structured numbering scheme (shown in Fig. 4 for a 3x3x3 mesh) where there are M_2 number of nodes in the x direction and N_2 number of nodes in the y direction, **M** has a banded structure as shown in Fig. 5 with seven diagonals that contain non-zero entries. Each of these diagonals contains the relevant coefficients defined in Eq. (10).

The coefficient matrix is thus a very sparsely populated matrix with the majority of entries being zero. The conventional classic method of solving the temperature vector would be to use Gauss-Jordan elimination to obtain the inverse of the matrix, but due to the high density of zero-entries there are more efficient ways of solving the temperature vector.

One such a method is LU-decomposition of the coefficient matrix into an upper and lower triangular matrix. From this back- and forward-substitution can be used to obtain the temperature solution. Due to the banded structure of **M**, the traditional LU-decomposition algorithm can be adjusted to reduce the number of computations needed. This is done by only applying the decomposition algorithm within the band of **M** ranging from diagonals B to F. This is a valid adjustment as the entries of lower and upper triangular matrices corresponding to the regions outside this band only contain zero entries anyway.

The number of computations needed can further be reduced if the bandwidth of **M** is decreased. This can be done by using a different numbering scheme for the nodes in the domain according to the reverse Cuthill-McKee algorithm.

Refer to Fig. 6 for the percentage reduction in the bandwidth (compared with the structured numbering scheme) for three different size matrices at different number of nodes in the z direction after this algorithm was applied. It was found that for a structured two-dimensional mesh, where there is only one node in the z direction, there is no reduction in the bandwidth of the matrix. It is the most advantageous to apply the reverse Cuthill-McKee algorithm where the mesh has a width of two nodal point in the z direction. In the current study 10 nodes were used in the z direction. Using more than 10 nodes in the z direction, resulted in differences of less than 0.1% in solved temperature distributions.

Numerical Results

By running a sequence of simulations, the optimum cooling structure shape can be found for a particular representative domain geometry and thermal condition.

It was found that for $a_D \geq 1$, the lowest peak temperature is always associated with a cooling structure aspect ratio, a_C, in the range of $[a_D; a_{C,\max}]$. A convenient way of normalising a_C is by defining a new relative cooling aspect ratio, $a_{C,rel}$:

$$a_{C,rel} = \frac{a_c - a_D}{a_{C,\max} - a_D} \tag{12}$$

When $a_{C,rel} = 1$, it means that the cooling insert is at its maximum aspect ratio as shown in Fig. 7, while when $a_{C,rel} = 0$ the cooling insert has the same aspect ratio as the representative domain.

It was found that the maximum temperature in the domain, $T_{\max}$, is directly proportional to G_M and that an increase or decrease in the cooling structure temperature, T_C, is translated directly into an identical increase or decrease in $T_{\max}$. Mathematically this can be expressed as:

$$T_{\max} - T_C \propto G_M \tag{13}$$

This means that neither G_M nor T_C has any influence on the shape of the optimum cooling geometry.

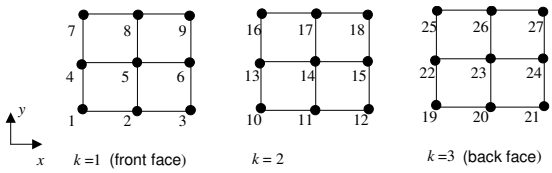

Figure 4 Structured numbering scheme used

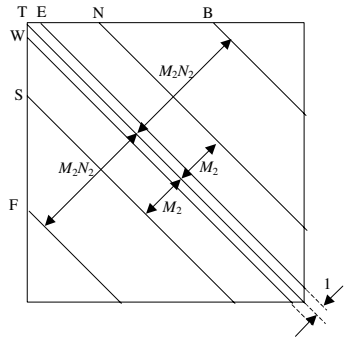

Figure 5 Banded structure of the coefficient matrix

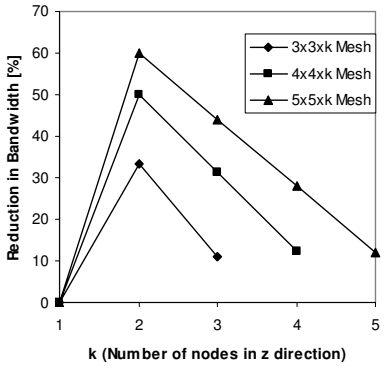

Figure 6 Reduction in matrix bandwidth after applying the Reverse Cuthill-McKee algorithm

Optimisation Results for $a_D = 1$

A domain with a square cross-sectional area is applicable to an arrangement where the cooling structure spacing in both Cartesian directions is identical.

Fig. 8 shows that for the case where there is no thermal contact resistance, the physical size of the cooling insert has little influence on its optimum shape. Similarly, in Fig. 9 , the same is shown to be true of the influence of the depth of the domain.

For cases where less than approximately 70% of the domain is occupied by cooling, the optimum cooling insert shape is found to be a flat continues "plate" as shown in Fig. 7.

Also, it was found for cases with no thermal interface resistance, that the actual values of the thermal conductivities did not play any role, but rather that the ratio between the thermal conductivities, γ, was of concern. In Fig. 10 the optimum cooling shapes for various ratios, where no thermal contact resistance is present, is given.

When however thermal contact resistance, R [m^2K/W] is introduced, it is found that none of the above mentioned trends are valid. From Figs. 11-13 it is shown that the presence of contact resistance results in the relative optimum aspect ratio deviating from the $a_{C,rel} = 1$ line at an earlier α value than in the case without the presence of contact resistance. This means that the optimum cooling shape for larger cooling fraction is no longer that of a flat continues plate. Also as is shown in Fig. 14 , that the physical sizes of the thermal conductivities influence the optimum cooling aspect ratio when interface thermal resistance is present.

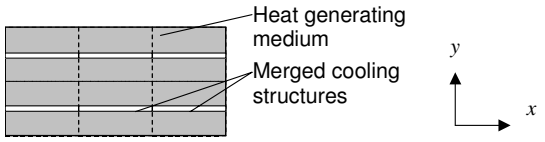

Figure 7 Physical meaning for the case where a_C is at its maximum

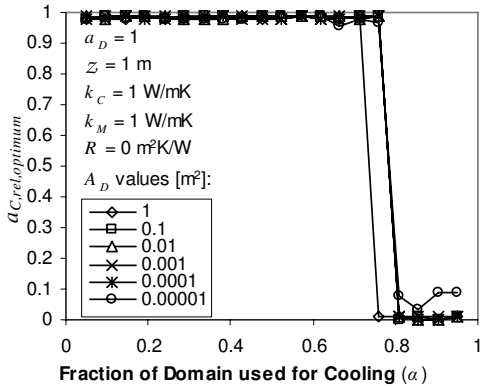

Figure 8 The influence of the physical size of the cooling structures on the optimum cooling insert shape for a mesh thickness of 1 m.

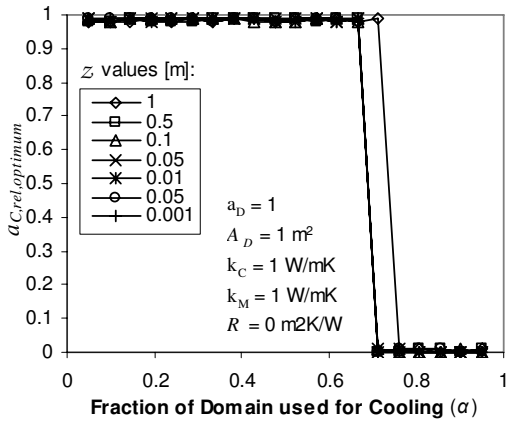

Figure 9 The influence of the z direction depth on the optimum cooling insert shape for a domain area of 1 m^2.

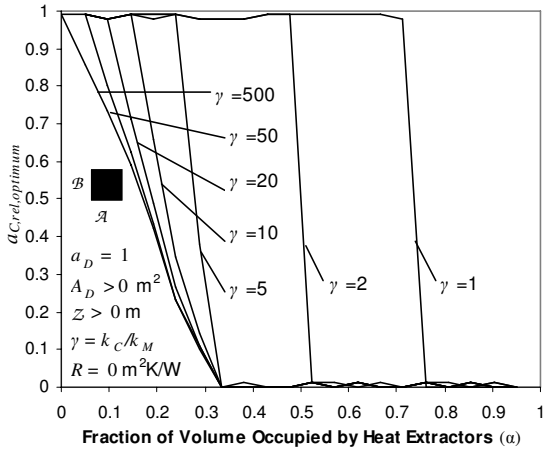

Figure 10 Influence of γ on $a_{C,rel,optimum}$ for $A_D = 1$ m^2, $Z = 0.001$ m, and $R = 0$ m^2K/W

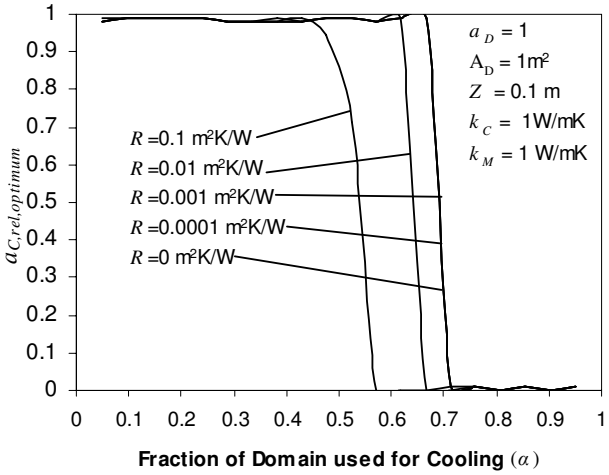

Figure 11 Influence of thermal contact resistance on the optimum cooling shape for $A_D = 1$ m^2 and $Z = 0.1$ m

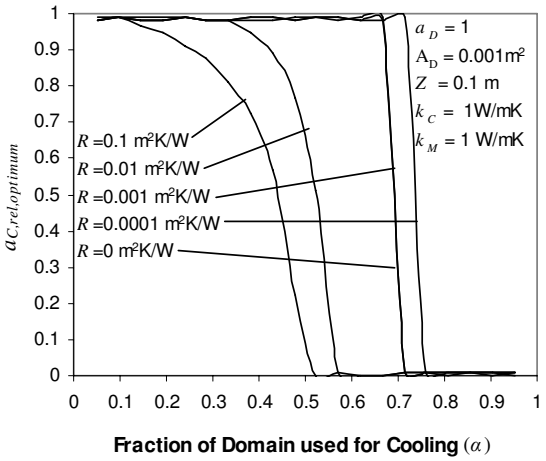

Figure 12 Influence of thermal contact resistance on the optimum cooling shape for $A_D = 0.001$ m^2 and $Z = 0.1$ m

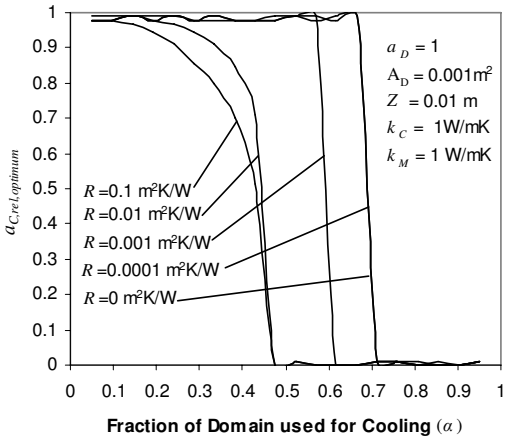

Figure 13 Influence of thermal contact resistance on the optimum cooling shape for $A_D = 0.001$ m^2 and $Z = 0.01$ m

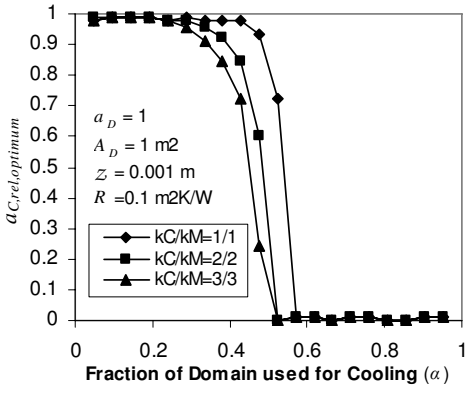

Figure 14 Non-zero R for a constant ratio of thermal conductivity for $A_D = 1$ m^2 and $Z = 0.001$ m

Optimisation Results for $a_D = 2$

A domain with an aspect ratio of 2 represents a situation where the centre-to-centre distance between two adjacent cooling structures in one Cartesian coordinate direction is twice the centre-to-centre distance of two neighbouring cooling structures in the other Cartesian direction.

Fig. 15 gives the behaviour of the optimum cooling shape for $a_D = 2$ at various R-values. It was found that as before the presence of thermal contact resistance influences the optimum shape. It was also found that unlike $a_D = 1$, the optimum cooling shape never has the same aspect ratio as the representative domain. It has a higher tendency to have a flat plate geometry as an optimum cooling shape.

For smaller cooling structures it was found that the optimum geometry graphs fan out a bit as indicated in Fig. 16 for different R values. The influence of the conductivity ratio was found to be small.

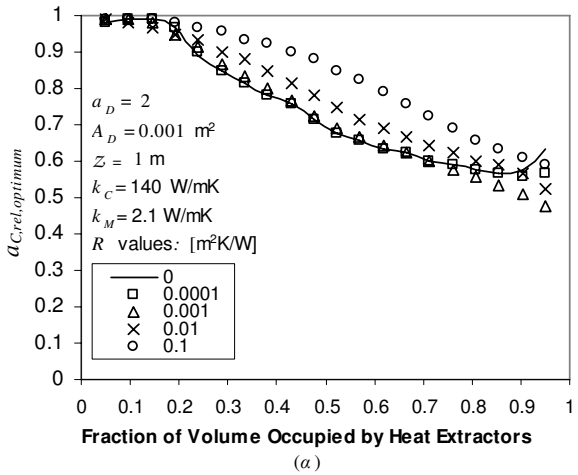

Figure 15 Influence of R on the optimum cooling shape for $a_D = 2$.

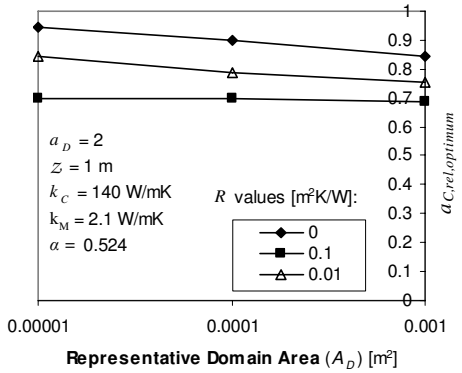

Figure 16 Influence of A_D for $a_D = 2$ at $\alpha = 0.524$

Optimisation Results for $a_D = 5$

As was found for $a_D = 2$, the case where $a_D = 5$, has an even higher tendency toward optimum cooling shapes of a flat plate. From Fig. 17 it can also be seen that the influence of the thermal contact resistance is also not as severe as before. Similarly the physical size of the cooling structure, A_D, has a lesser influence.

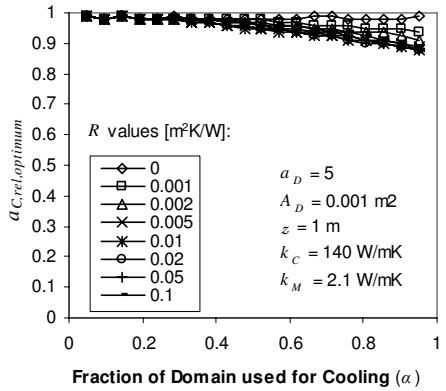

Figure 17 Optimum cooling shape aspect ratios for $a_D = 5$ and various R values.

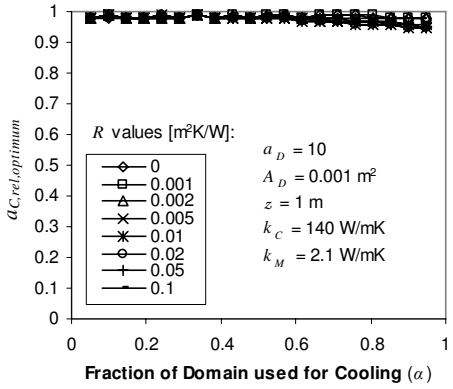

Figure 18 Optimum cooling shape aspect ratios for $a_D = 10$ and various R values.

Optimisation Results for $a_D = 10$

A similar trend is found to be true for higher representative domain aspect ratios as is shown in Fig. 18. In this case it was observed that almost through the entire spectrum of domain fractions used by cooling the optimum cross-sectional shape was that of a flat plate.

Dimensional Scaling

It is also important to determine when it is advantageous to optimise the cross sectional aspect ratio of the extractor inserts in order to accommodate higher heat generation densities while maintaining a certain maximum temperature within the representative domain. Fig. 19 shows, for a case with no internal interface thermal resistance, that the effectiveness of the heat extractor becomes less dependent on its cross sectional shape as the ratios of A_D to Z^2 decreases. For low ratios of A_D to Z^2, where the domain of a single insert becomes increasingly slender, the advantage of optimising the cross section in order to support higher heat-generation levels diminishes.

The advantage of inserting heat extractors however does not diminish, but rather the effectiveness thereof for slender domains are more dependent on the fraction of the total volume occupied by the heat extraction system α, rather than the cross sectional shape thereof. It would thus be sensible in such cases to use a cross-sectional geometry that is easier to manufacture or a geometry that would conform to possible other restrictions. Similar trends were obtained for beryllium oxide and synthetic diamond inserts. However, for the case where thermal contact resistance is present it was found that unlike the trend shown in Fig. 19, the influence of the cross-sectional shape remains present for low A_D to Z^2 ratios.

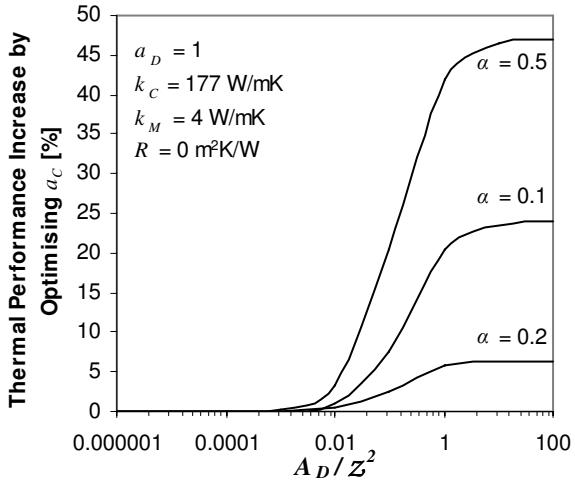

Figure 19 Additional allowable increase in heat generation density after geometric optimisation

Conclusions

It was found that there are 7 variables that determine what the optimum embedded cooling insert cross-sectional aspect ratio will be, namely a_D, A_D, α, Z, R, k_M, and k_C. When no thermal contact resistance is presents it seems as if this list can be reduced to a_D, α, and γ.

The actual temperature values within the heat-generating medium will however be dependent on all the above given parameters as well as the reference cooling temperature, T_0 and the volumetric heat generation, $\dot{q}_M'''$. The exact influence of the thermal contact resistance is difficult to describe from the presently available data, and more investigation will be needed in this regard.

Indications are that as the domain aspect ratio is increased, the tendency for the optimum cooling structure to be a continues flat plate increases.

References

[1]Van Wyk JD, Strydom JT, Zhao L, Chen R, Review of the development of high density integrated technology for electromagnetic power passives, Proceedings of the 2nd International Conference on Integrated Power Systems (CIPS), 2002, pp. 25-34

[2] Barbosa P., Lee F.C., Van Wyk J.D., Boroyevich D., Scott E., Thole K., Odendaal H., Liang Z., Pang Y., Sewell E., Chen J., and Yang B., An overview of IPEM-based modular implementation for distributed power systems, Center for Power Electronics Systems (CPES) Power Electronics Seminar, Virginia Tech, 674 Whittemore Hall, Campus Mail Code 0179, Blacksburg, VA 24061, 2002, pp 70-76

[3] Patankar S.V., Numerical heat transfer and fluid flow, Hemisphere (Washington D.C.) , 1980

Strojniški vestnik - Journal of Mechanical Engineering 51(2005)7-8, 399-404
UDK - UDC 536.2
Izvirni znanstveni članek - Original scientific paper (1.01)

Radiative water-cooling in maritime and moderate continental climatic conditions

Igor Balen*, Vladimir Soldo

Faculty of Mechanical Engineering and Naval Architecture
University of Zagreb, I. Lučića 5, Zagreb, Croatia
** e-mail: igor.balen@fsb.hr*

Abstract

In this paper, the analysis of a flat-plate radiative panels operation, using average hourly weather data, was conducted. Radiative panels, with high-emittance surface cover, were integrated in the space-ventilation system with air-cooling by means of a cold-water coil. The panels should prepare a sufficient quantity of cold water that is collected in a cold-water tank during the nighttime operation. The collected cold water is used for cooling of the air during daytime.

A simulation model for the parametric analysis of the system in summer operating conditions and the influence of its components on the system's operation was developed. The model includes the control of the system's operation, which prevents water circulation in the periods without cooling contributions.

The purpose of the research was to predict the system behaviour in the Irish and the continental Croatian climatic conditions, to enable sizing and design of the test rig that is to be built for experimental validation of the system. The results of simulation were obtained for the small cooling system with a total panel aperture area of 6 m^2 and a volume of tanks of 300 l.

The results were presented in the charts, where the influence of the main parameters on the system's operation was illustrated. The results showed that the radiative cooling system is more efficient in maritime than in moderate continental climatic conditions during summer.

Introduction

Passive, hybrid and low energy cooling, heating and ventilation techniques are being researched and implemented in a number of countries throughout the world. There are also ongoing collaborative efforts in this area, including the European Union Fifth Framework / Energy sub-programme "Evapcool" and the International Energy Agency Solar Heating and Cooling programme. There is currently a research project underway in the area of low energy cooling, heating and ventilation of buildings in Irish (maritime) climatic conditions.

Solar heating and radiative cooling systems have been studied in particular for the last 30 years. An extensive research of a radiative cooling system, consisting of unglazed flat plate radiators, water as a heat carrier, and storage tank was presented by Meir et al. [1-2]. The radiators were twin-wall sheets made of a modified PPO (polyphenylenoxid). The impact of a tilt angle, the aperture area and the reservoir volume on the system performance was simulated. The system performance has been investigated with a radiator aperture 5.3 m^2 and tank volume of 280 l in experiments for Norwegian (Oslo) climate. Argiriou et al. [3] have analyzed the combined effects of climate and radiator characteristics on cooling potential. Twelve years weather data set was used to assess radiative cooling potential in Athens. The dynamic performance of a radiative cooling system for buildings, using a metallic panels with covered by a polyethylene windscreen, for a location in northern Italy, has been analyzed by Mihalakakou et al. in [4]. Saenkhomvong [5] has developed the water heating system using flat-plate solar collectors. This author also developed a radiative cooling system. To use the same device, additional equipment for cooling water was designed and installed. This newly developed device, fixed to the flat-plate solar collector, was used to cool-off flat-plate surfaces in the night by self-radiation. The performance of a

Nomenclature

A_C	collector area	m^2
A_{TOT}	total panels area	m^2
c_p	specific heat capacity	J/(kgK)
F_R	collector heat removal factor	-
h_c	convection heat transfer coefficient	$W/(m^2K)$
I	global solar irradiation	W/m^2
m	mass of water in storage tank	kg
Q_C	heating capacity	W
Q_L	heating/cooling load	W
$Q_{l\text{-}g}$	heat loss/gain	W
Q_R	cooling capacity	W
U_L	overall heat loss coefficient	$W/(m^2K)$
t	time	s, h
T_a	ambient temperature	K
T_{dp}	dew point temperature	K
T_r	radiation panel temperature	K
T_s	water temperature in storage tank	K
T_{sky}	sky temperature	K
V	volume of water in storage tank	m^3
w	wind velocity	m/s
α	absorbtance	-
γ	panel tilt angle	°
ε_r	panel emissivity	-
ε_{sky}	sky emissivity	-
ϑ_{in}	temperature of water entering collector	°C
ϑ_a	ambient temperature	°C
τ	transmittance	-
σ	Stefan-Boltzmann constant	$5.67\ 10^{-8}\ W/(m^2K^4)$

thermosyphon water cooler with a parallel, flat-plate radiator has been studied theoretically and experimentally by Yeh and Tseng in [6]. Some theoretical predictions of water temperatures in the storage tank and of the cooling intensity have been obtained from energy and momentum balances. The results were used in assessing the combination of solar heating and radiative cooling with a single device. A radiator system using an infrared transparent windscreen that doubles as the structural envelope was proposed and supporting experimental results were presented in [7]. Analysis of flat-plate solar collectors, converted into cooling radiators, was performed by Erell and Etzion in [8, 9]. Primary factors determining the heat output were the global solar irradiation, wind velocity and temperature difference between the water and the air. An expression was derived linking these parameters to predict the system's performance with accuracy. Theoretical and experimental analysis of a radiative cooling system for Jordan climate was presented in [10, 11]. The results for the proposed models showed an acceptable qualitative agreement between simulations and measurements.

The purpose of the research, presented in this paper, was to develop and design the sustainable energy system that uses solar energy (solar panels) for the supply air-conditioning during the whole year for maritime climate. It was also necessary to compare the system operation in different climatic conditions in order to get more information about the system performance.

The panels are integrated in the space-ventilation system with air-cooling by means of a water coil. Their primary function is to prepare sufficient quantity of cold water, integrating radiative and convective cooling, that is collected in the cold-water tank during nighttime operation. That cold water is used for cooling of the air during daytime. The research objectives include analysis of solar system performance in cooling operating mode. The impact of the panel surface area, tank volume and panel surface emissivity on the cooling performance was studied in simulations. Hence, thermal analysis of water-cooling, including weather data analysis (temperatures, wind velocities, solar irradiation), together with design of the experimental rig were performed.

By small modification, solar panels could be turned into collectors and used to produce the hot water during daytime.

The aim of the research was to predict the system behaviour, to enable sizing and design of the test rig that is to be built for experimental investigation.

Mathematical model

The solar irradiation data presented in [12, 13] were used to estimate how much energy is likely to be available for the water heating at the observed location.

In the heating operating mode, the collector plates absorb as much of the irradiation as possible through the glazing, while losing as little heat as possible upward to the atmosphere and downward through the back of the casing. Collected heat is then transferred to the water. The performance of collectors was analyzed by Whillier's procedure [14-16]. The basic equation is:

$$\dot{Q}_C = A_C F_R[(\tau\alpha)I - U_L(\vartheta_{in} - \vartheta_a)] \quad (1)$$

where the collector heat removal factor F_R is the ratio of the heat actually delivered to that delivered if the collector plates were at uniform temperature equal to that of the entering water. F_R is affected by the collector characteristics, the fluid type and the flow rate thorough the collector, having a value less than 1.0.

The data of global solar irradiation on a horizontal surface, presented in [13], had to be converted into values for a tilted surface *I*. Determination of solar angles that describe the direction of incidence of the solar beams on a tilted surface was performed with the model that was developed and tested earlier [17].

Heat exchange between the panel and the surroundings, in the cooling operating mode during the night, is described with the following expression:

$$\dot{Q}_R = A_C[\varepsilon_r\sigma(T_r^4 - T_{sky}^4) + h_c(T_r - T_a)] \quad (2)$$

where the first term refers to radiation from the panel towards the atmosphere and the second term refers to convection between the panel and the ambient air. Because the radiation effect is the most obvious at night, it is often termed nocturnal radiation.

The most useful parameter for characterising the radiative heat transfer is the sky temperature, defined as the temperature of a black body radiator emitting the same amount of radiative flux as the sky. It is defined as:

$$T_{sky}^4 = \varepsilon_{sky} T_a^4 \quad (3)$$

Many correlations are reported in the literature for calculating the sky emissivity ε_{sky}. In this paper, the following relation [16] is used:

$$\varepsilon_{sky} = 0.8 + \frac{T_{dp} - 273.15}{250} \quad (4)$$

with the dew point temperature T_{dp} calculated from the psychrometric chart for moist air by the analytical procedure presented in [1-3].

Convective heat transfer depends on the ambient air temperature and wind velocity, which is expressed through the convection heat transfer coefficient h_c. In engineering practice, h_c is often represented by the simplified expression, as the first order linear function of the wind velocity [15]:

$$h_c = 2.8 + 3.0w \quad (5)$$

Sizing of water storage tanks is performed by using a simulation model developed for this purpose, that includes the heat balance between the charging energy Q_C (or Q_R) from the heat source/sink on one side and the heat removal by the load Q_L and the heat losses/gains (radiation + convection) $Q_{l\text{-}g}$ to/from the environment on the other side (Fig. 1):

$$(mc_p)_S \frac{dT_S}{dt} = \dot{Q}_C - \dot{Q}_L - \dot{Q}_{l-g} \quad (6)$$

where $(mc_p)_s$ is the heat capacity of the water in storage and dT_s is the change of water temperature in time *t*. Q_C (Q_R) is determined from Eqs. (1) or (2) when charging the water tank.

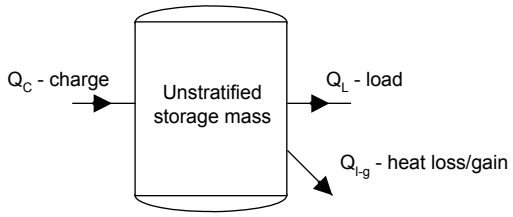

Fig.1 Schematic of the storage energy balance

After integration of Eq. (6) for a selected time interval, the change of storage temperature is calculated as a function of time. In Eq. (6) it is obvious that the storage mass and the water temperature in storage are indivisibly connected. Therefore, the storage mass (or volume) can be adjusted to the desired water temperature at the end of the heating/cooling process.

Solar thermal system (Fig. 2) is designed in order to supply the required amounts of energy for the heat exchanger, which is used for cooling of the supply air. The system is designed to satisfy completely cooling energy requirements.

Radiative panels are used for cooling of water by means of radiation towards sky (and convection to the outside air) during nighttime. Since the requirements on collectors and radiators operation are opposite to each other, it would be difficult to achieve good performance in both heat collection and heat dissipation with only one panel type (except, perhaps, in a warm climate – [18]). Therefore, the best approach would be to use one panel type for solar heat collection (i.e. standard flat-plate collectors) and to use different type for a nighttime water-cooling (could be done by using modified swimming pool absorbers [1, 2]). If the required total panels area is large, then the solution with two panel types becomes expensive. In this case, both operation modes could be covered with one panel type, but the adjustments of

standard panel designs are required. The easiest way to adjust a flat-plate collector for cooling operation is to substitute it's glazing with a high-radiative cover (i.e. PE/PPO) [10].

Results and discussion

Results presented in the following charts are based on average Irish and continental Croatian weather data for summer – solar irradiation, temperatures and wind velocities.

Continuous line presents the results for the Dublin climate (DUB). It can be seen that the end temperature in the tank can reach about 12°C in clear sky conditions in average outside temperature and wind conditions. Dashed line presents the results for the Zagreb climate (ZG). The end temperature in the tank can only reach about 16°C. The different outside weather conditions influence performance of the panels and change the temperature curve of water-cooling. Increase of the end temperature in continental climate conditions for about 4°C implicates that the radiative system would be more efficient in maritime climate. The reason is in significantly different

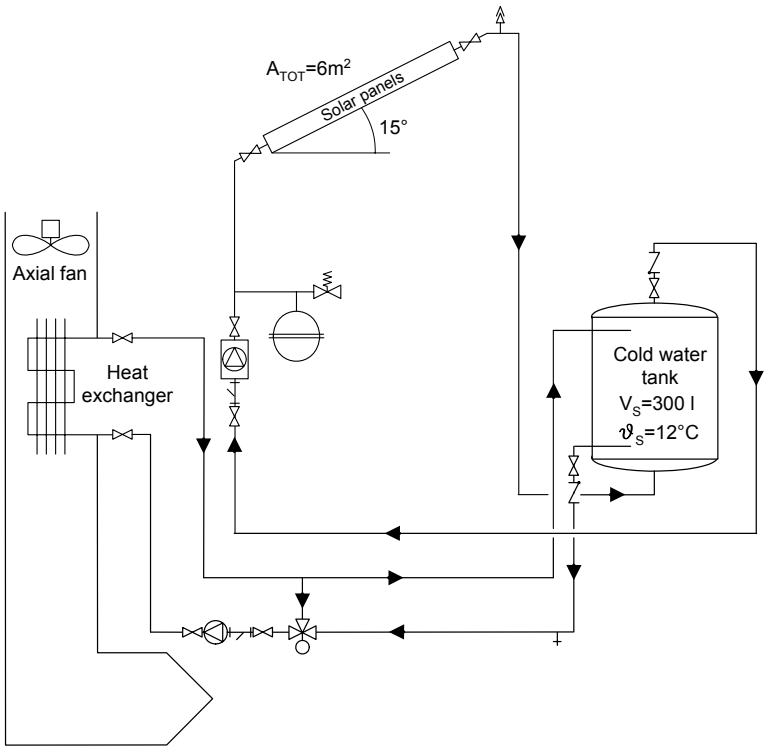

Fig.2 Radiative water-cooling system schematic

In Fig. 3, simulation of the change of water temperature in the cold storage tank during nighttime is presented.

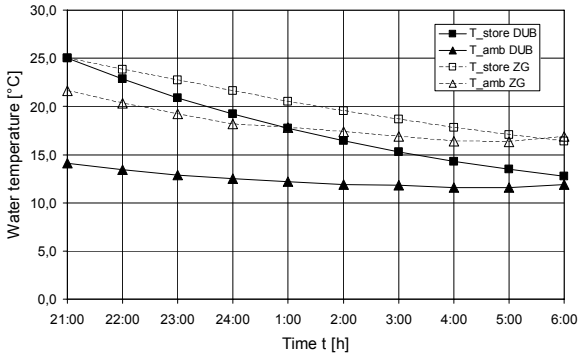

Fig.3 Water-cooling in the tank during the night

wind velocities and the sky temperatures during the night that are about 5.5°C higher in Zagreb compared to Dublin, in the average. The selection of initial water temperature 25°C is based on predicted summer room conditions. Placing the tank outside would cause heating of the water by the sun during the day. If the initial temperature were, for example, 30°C, the end water temperature would be about 1°C higher.

The temperature change in the tank, presented in Fig. 3, is calculated for the following design parameters:
- aperture area of the panels A_{TOT}=6m²
- volume of the tank V_S=300l
- tilt angle γ=15°
- panel emissivity ε_r=0.85

Presented parameters were also used for the experimental rig design (Fig. 2).

In Fig. 4, the change of water temperature in the tank for different emissivities of the panel surface is presented. This chart shows that the emissivity of panel surface ε_r has large impact on the cooling effect. In case when standard selective absorber plate is used (ε_r = 0.10), the end temperature in the tank rises significantly. This implies that standard absorbers used in solar collectors could not provide good cooling performance without the increase of their surface emissivity. The results for continental climate (dashed line) again show increased values of the water temperatures, compared to the maritime climate (continuous line).

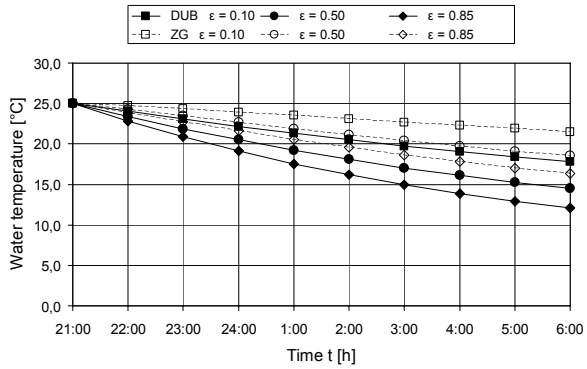

Fig.4 Water-cooling as function of panel emissivity

In Fig. 5, dependence of the change of water temperature in the tank for different sizes of panel surface area is presented. If the initial panel area is 6m^2, then decreasing of total panel area for 2m^2 causes about 2.8°C and 2.1°C higher water temperature in Dublin and Zagreb, respectively.

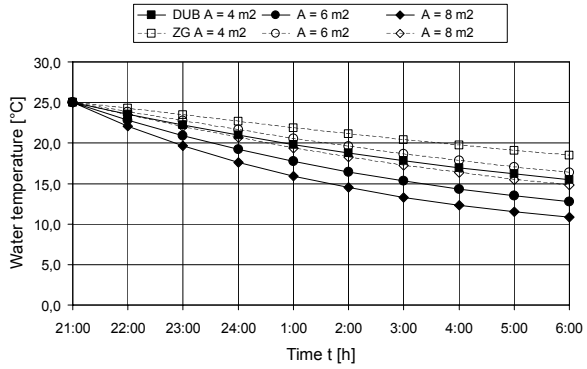

Fig.5 Water-cooling as function of panels' aperture area

On the other hand, increasing total area for 2m^2 would cause the temperature decrease for 1.8°C and 1.6°C, respectively. Further increasing of panel area would contribute even less in lowering the water temperature. Theoretically, with panel area of 12m^2 or more it would be possible to reach the water temperature in the tank equal to the dew point temperature of outside air.

The change of water temperature for different sizes of water storage is presented in Fig. 6. Increasing or decreasing the storage volume for 50 litres, would change the water temperature in the tank for about 1 °C in both climatic conditions.

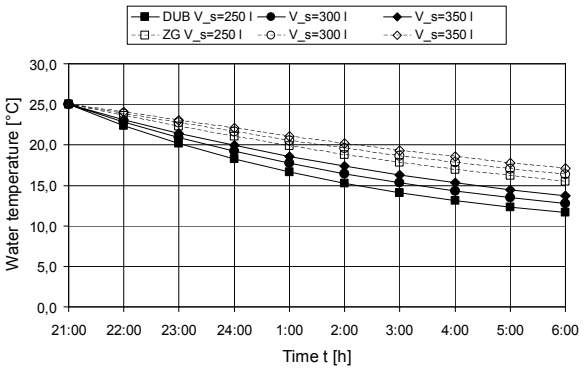

Fig.6 Water-cooling as function of tank volume

Conclusions

In this research, the mathematical model that describes the dynamic thermal performance of a radiative cooling system was developed and the test rig for the system experimental analysis was designed. Radiator panels are used for cooling of water by means of radiation towards the sky and convection to outside air during nighttime.

The results were obtained for a small solar cooling system with the total aperture area of 6 m^2 and tank volume of 300 litres (Fig.2).

The water temperature in the tank decreases for higher panel emissivity, which should be considered by panel design and material selection. Also, the temperature decreases for greater panels' area and smaller tank volume, which should be considered by system design in order to gain the optimal system sizing.

The radiative system is more efficient in maritime climatic conditions than in moderate continental climatic conditions. This is because, during summer, the sky temperatures are lower and wind velocities are higher in maritime climate, compared to continental climate. Hence, the cooling effect is more distinctive.

Future research will include analysis of parameters' influence on the system operation in more details, in different operating conditions and development of the experimental rig in order to validate the mathematical model.

References

[1] M.G. Meir, H. Storas, J.B. Rekstad, Combined Solar Heating and Radiative Cooling System, Proceedings of ISES 1999 Solar World Congress, Jerusalem, 1999.

[2] M.G. Meir, J.B. Rekstad, O.M. Løvvik, A Study of Polymer-Based Radiative Cooling System, Solar Energy 73 (6) (2002) 403-417.

[3] A. Argiriou, M. Santamouris, D.N. Assimakopoulos, Assessment of the Radiative Cooling Potential of a

Collector Using Hourly Weather Data, Energy 19 (8) (1994) 879-888.
[4] G. Mihalakakou, A. Ferrante, J.O. Lewis, The Cooling Potential of a Metallic Nocturnal Radiator, Energy and Buildings 28 (1998) 251-256.
[5] W. Saenkhomvong, The Study on Solar Collector for Diurnal Water Heating and Nocturnal Water Cooling, Dissertation, The King Mongkut's Institute of Technology, Bangkok, 1992
[6] H-M. Yeh, C-C. Tseng, A thermosyphon water cooler with a parallel, flat-plate radiator, Energy 15 (12) (1990) 1129-1141.
[7] T.E. Johnson, Radiation Cooling of Structures with Infrared Transparent Wind Screens, Solar Energy 17 (1975) 173-178.
[8] E. Erel, Y. Etzion, Analysis and Experimental Verification of an Improved Cooling Radiator, Renewable Energy 16 (1999) 700-703.
[9] E. Erel, Y. Etzion, Radiative Cooling of Buildings with Flat-plate Solar Collectors, Building and Environment 35 (2000) 297-305.
[10] M.A. Al-Nimr, Z. Kodah, B. Nassar, Theoretical and Experimental Investigation of a Radiative Cooling System, Solar Energy 63 (6) (1998) 367-374.
[11] M.A. Al-Nimr, M. Tahat, M. Al-Rashdan, A night cold storage system enhanced by radiative cooling – a modified Australian cooling system, Applied Thermal Engineering 19 (1999) 1013-1026.
[12] E. Lalor, Solar Energy for Ireland, National Science Council, Dublin, 1975.
[13] SESI/IHVE, Solar Energy and Irish Building, Trinity College, Dublin, 1976.
[14] ASHRAE, 1992 ASHRAE Handbook of HVAC Systems and Equipment, American Society of Heating, Refrigerating and Air Conditioning Engineers Inc., Atlanta, 1992.
[15] G.N. Tiwari, S. Suneja, Solar Thermal Engineering Systems, Narosa Publishing House, London, 1997.
[16] J.A. Duffie, W.A. Beckman, Solar Engineering of Thermal Processes, J. Wiley & Sons Inc., New York, 1980
[17] I. Balen, D. Dović, Comparison Between Different Models for Calculation of Solar Irradiation in Solar Thermal System Sizing, Proceedings of Interklima 2003 - 17th International Symposium of Heating, Refrigerating and Air-Conditioning, Zagreb, 2003, pp. 81-90.
[18] E. Erel, Y. Etzion, Heating Experiments with a Radiative Cooling System, Building and Environment, 31 (6) (1996) 509-517.

Strojniški vestnik - Journal of Mechanical Engineering 51(2005)7-8, 405-410
UDK - UDC 536.2
Izvirni znanstveni članek - Original scientific paper (1.01)

Energy consumption analysis of domestic oven

M. Penšek[1], N. Holeček[1], H. Gjerkeš[2], I. Golobič[2*]

[1]*Gorenje d.d., Partizanska 12, Velenje, Slovenia*
[2]*University of Ljubljana, Faculty of Mechanical Engineering, Askerceva 6, Ljubljana, Slovenia*
[*] *iztok.golobic@uni-lj.sil*

Abstract

For cookers with oven to be interesting for the market, they need to exhibit a high energy efficiency. On the basis of an analysis of individual influences on the energy efficiency of ovens, several solutions were proposed for improving oven operation. An analytical solution was made for describing the nonstationary temperature field within a test brick with convection at a constant heat transfer coefficient and a continuously variable temperature of the surrounding fluid using Green's functions. The influences of door sealing, vapor outlet slit, additional insulation, the oven regulation regime, door glazing and irradiation within the oven were experimentally analyzed. Because of the proposed improvements, the analyzed mass produced oven was moved to the A class of energy efficiency according to standard EN 50304:2001.

Introduction

Kitchen ovens consume large amounts of energy in households. By increasing their energy efficiency, it is possible to reduce greenhouse gas emissions via reduction of energy consumption. The energy efficiency of ovens is marked on energy labels. Oven manufacturers are increasingly forced to adjust their products to market requirements by developing ever more energy efficient ovens that fulfill Class A criteria [1-3]. Functionality, design and energy efficiency all need to be taken into account [4-6].

Standard EN 50304:2001 [7] prescribes measurement of energy consumption after the oven is switched on and once a Hipor test brick saturated with moisture is heated from 5 to 55 ^{o}C. Depending on the oven size, the electrical energy consumption in the given case should be below 800 Wh in conditions of natural air convection without the fan, or forced air convection with the oven fan switched on.

This paper focuses primarily on an experimental theoretical analysis of individual influential parameters that affect the energy efficiency of mass produced ovens.

Modeling of heat transfer within the oven

In order to be able to improve the energy efficiency of an oven, one must analyze the influence of the greatest possible number of parameters that affect it. However, a numerical approach in the form of 3D oven modeling does not enable the analysis of a greater number of parameters because of its complexity. Since the standard for determining the energy efficiency prescribes measurement of consumed energy for the required increase in the temperature inside a moist test brick while it is heated in the oven, we decided to approach the description of the nonstationary temperature field in the test brick analytically.

Fourier's equation for heat convection

$$\frac{\partial^2 T}{\partial x^2} + \frac{g(x,t)}{\lambda} = \frac{1}{a}\frac{\partial T}{\partial t} \qquad (1)$$

was solved analytically for a plate using Green's function (general solution) [1]:

$$T(x,t)=\int_{x'=0}^{L} G(x,t|x',0)F(x')\cdot dx' + a\sum_{i=1}^{s}\left[\frac{(\rho cL)_i}{\lambda_i} G(x,t|x',0)F(x')\right]_{x'=x_i} + \int_{\tau=0}^{t}\int_{x'=0}^{L}\frac{a}{\lambda} G(x,t|x',\tau)g(x',\tau)\cdot dx'\cdot d\tau +$$
$$+ a\int_{\tau=0}^{t} d\tau\sum_{i=1}^{s}\left[\left(\frac{f_i(\tau)}{\lambda_i} G(x,t|x_i,\tau)\right)\right] - a\int_{\tau=0}^{t} d\tau\sum_{i=1}^{s}\left[f_i(\tau)\frac{\partial G}{\partial n_i'}\bigg|_{x'=x_i}\right] \quad (2)$$

For the nonstationary continuous temperature variation of the surrounding fluid, we assumed that

$$T_\infty = (T_{\infty,maks} - T_{\infty,\infty})\cdot(k_1\cdot e^{k_2\cdot t} + k_3\cdot e^{k_4\cdot t}) + T_{\infty,\infty} \quad (3)$$

By using constants k1 through k4 under the following conditions:

$$k_1 > 0,\ k_2 > k_3,\ k_4 < k_2 < 0, \quad (4)$$

it is possible to capture the variation of temperature with time as can be seen in Figure 1.

This can serve as the basis for analyzing processes in the oven.

The maximum temperature is expressed as

$$T_{\infty,maks} = \frac{T_{\infty,0} - T_{\infty,\infty}}{k_1 + k_3} + T_{\infty,\infty} \quad (5)$$

Taking into account a constant heat transfer coefficient for heat transfer to the surrounding fluid and variable ambient temperatures according to equation (3), the nonstationary temperature field of a semiendless plate is in the form:

$$T(x,t) = 2\cdot T_0\cdot\sum_{m=1}^{\infty} e^{-\frac{\beta_m^2 at}{L^2}}\cdot\frac{\sin\beta_m}{\beta_m+\sin\beta_m\cdot\cos\beta_m}\cdot\cos\left[\beta_m\left(\frac{x}{L}\right)\right] + \sum_{m=1}^{\infty}\frac{4k_1aL\alpha\beta_m(T_{\infty,maks}-T_{\infty,\infty})\cdot\cos\left[\beta_m\left(\frac{x}{L}\right)\right]\cdot\cos\beta_m}{\lambda(k_2L^2+\beta_m^2a)\cdot(2\beta_m+\sin(2\beta_m))}\cdot\left(e^{k_2t}-e^{-\frac{\beta_m^2at}{L^2}}\right) +$$
$$+\sum_{m=1}^{\infty}\frac{4k_3aL\alpha\beta_m(T_{\infty,maks}-T_{\infty,\infty})\cdot\cos\left[\beta_m\left(\frac{x}{L}\right)\right]\cdot\cos\beta_m}{\lambda(k_4L^2+\beta_m^2a)\cdot(2\beta_m+\sin(2\beta_m))}\cdot\left(e^{k_4t}-e^{-\frac{\beta_m^2at}{L^2}}\right) + \frac{4\alpha L}{\lambda}T_{\infty,\infty}\sum_{m=1}^{\infty}\frac{\cos\left[\beta_m\left(\frac{x}{L}\right)\right]\cdot\cos\beta_m}{2\beta_m^2+\beta_m\sin(2\beta_m)}\cdot\left(1-e^{-\frac{\beta_m^2at}{L^2}}\right) \quad (6)$$

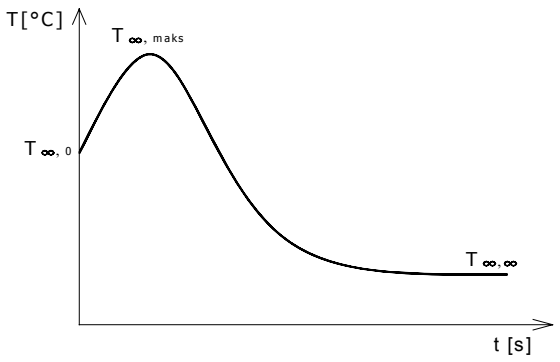

Figure 1 Example of variation of the surrounding fluid's temperature with time.

In order to determine the nonstationary temperature variation in a three-dimensional brick, the principle of superposition is used.

Experimental set up and test procedure

Figure 2 shows two cooker models that were used to perform oven measurements, namely Gorenje Pininfarina and Gorenje E774W. The model Gorenje E774W had an oven insulated with glass wool with a thickness of 3 cm, and Pininfarina had glass wool with a thickness of 5 cm. The oven door was double-glazed. Oven controls were set so as to allow temperature oscillations within the oven of about 10 K around the set temperature. When the oven operated with natural air convection only (switched off fan), two heaters were used – an upper and a lower one. During oven operation with forced air convection, the lower heater and the peripheral heater (which is installed around the fan) were switched on.

Figure 2 Gorenje E774W and Gorenje Pininfarina.

Figure 3 shows an oven schematic with the positions of the heaters and fan opening.

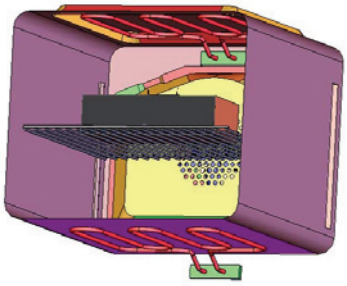

Figure 3 Schematic of oven in the Gorenje E774 W cooker.

The consumed energy was measured using a Siemens Simeas P power meter, which measures the input voltage and current, after which an integral processor calculates the desired values. The measurement accuracy of the power meter for the measurement of electric voltage and current is ±0.2 %, and for measuring power it is ±0.5 %.

The weight of the brick was measured using a Siemens Siwarex U balance. The balance was placed on top of the cooker. A bore with a diameter of 1 mm was drilled through the plate, insulation and the oven, and a thin wire was led through that connected the balance with a basket containing the test brick that was placed in the oven.

The temperature was measured using thermocouples Class 1 according to EN 60548-2 standard in a steel casing with an external diameter of 1 mm. The thermocouples were fit snugly inside the bores within the test brick. For all measurements according to standard EN 50304:2001, measurement of two temperatures is required. In our case, however, 10 were done to be able to analyze heat conduction within the test brick. A schematic of the measurement sites on the test brick and a picture of the thermocouples installed in the test brick are shown in Figure 4.

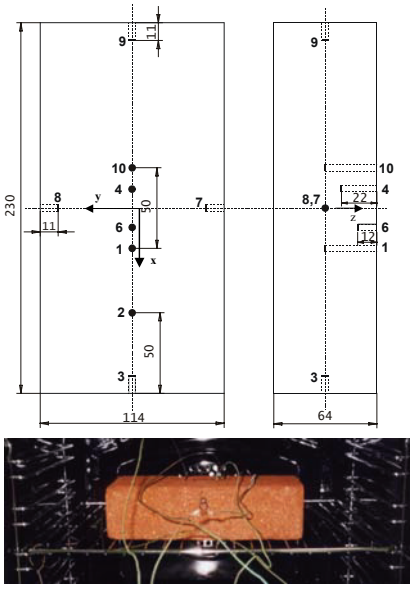

Figure 4 Measurement sites on Hipor test brick.

For the regulation of oven heaters, electronic elements were added to the oven with output relays for switching the heaters on, as well as power supply for external electronics that transformed the software PID controller data into an electric signal and sent it to the relays, which then switched oven heaters on or off. The PID controller was connected with the LABView PC program, via which the oven operation regime was determined for individual heaters and data were captured. The temperature profile was also set and it was determined which heaters should be switched on. Settings of the PID controller were also made.

The objective was to achieve Class A of energy efficiency for the oven according to standard EN 50304:2001. The standard for Class A prescribes that a Hipor test brick saturated with moisture should be heated from 5 to 55 ^{o}C after the NG 500 oven is switched on, whereby the total electrical energy consumption needs to be lower than 800 Wh, for both natural air convection and for forced air convection. A new test brick has to be dried in the oven before use for 3 hours with forced air circulation at a temperature of ≥175 °C. The weight of the dried brick without thermocouples has to be measured within 5 min after its removal from the oven. Then the brick can be used for up to 20 measurements to measure

the time and consumed energy that is necessary for an empty oven to be heated from the ambient temperature by 180 K in the case of natural convective air circulation, or by 155 K in the case of forced air circulation with the use of a fan. Two thermocouples required by the standard are fitted into the test brick such that the measuring sites are in the center of the brick, and the distance between the thermocouples is 50 mm (marks 1 and 10 in Figure 4).

Results and discussion

Figure 5 shows the influence of the rate of heating of the surrounding air on the increase in brick surface temperature in the middle of the test brick, as an example of using equation (6).

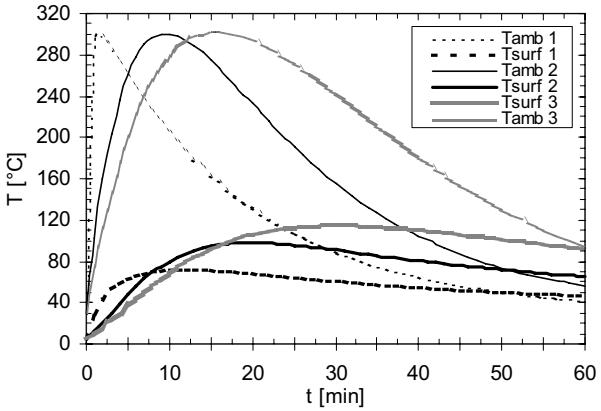

Figure 5 An example of using equation (6).

Figure 6 shows a comparison between the measured and calculated temperature curves during heating of dry brick at natural convection. The differences primarily resulted from inaccurate approximation of the temperature variation of the surrounding air, nonobservance of the irradiative share of heat transfer from the oven walls to the test brick, and a nonuniform initial temperature field in the test oven.

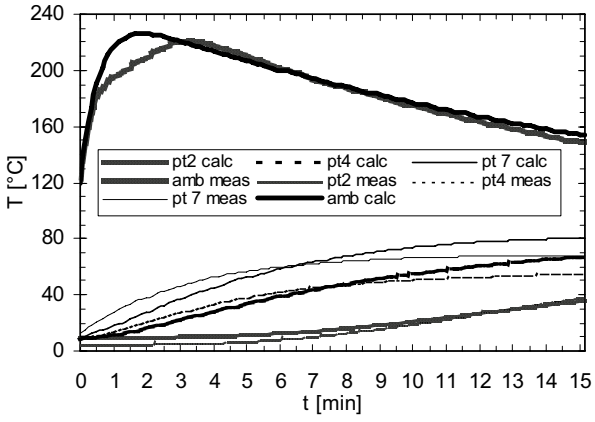

Figure 6 Comparison of the measured and calculated temperature profiles during heating of dry test brick at natural air convection, α = 16 W/m^{2}K.

Infrared camera ThermaCam S60 manufactured by Flir was used for thermographic measurements. Figure 7 shows IR photographs of the test brick and Figure 8 the time variation of the mass of moist test brick during drying, while it is heated with forced air convection and overheated to 155 K.

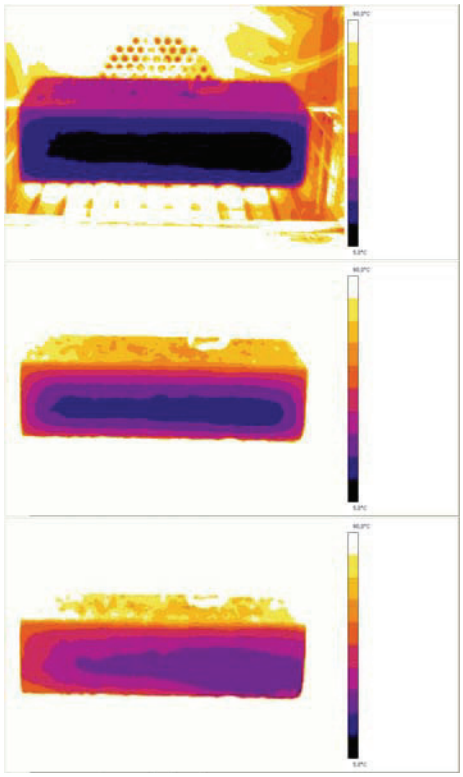

Figure 7 IR photographs of the test brick after 8, 16 and 32 min of heating with forced air convection and overheating of 155 K.

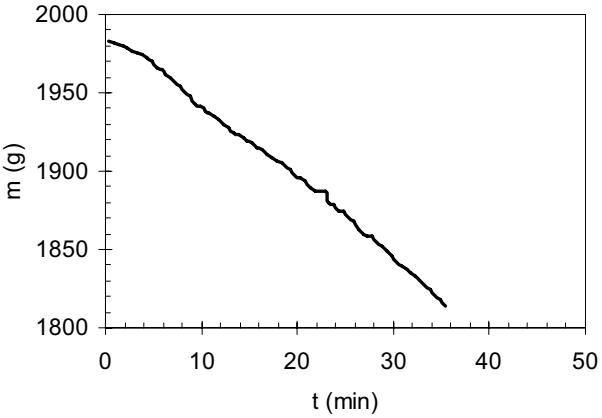

Figure 8 Time variation of the mass of moist test brick during heating with forced air convection with 155 K overheating.

The influences of sealing of the door, vapor outlet slit, additional insulation, the regulation regime, door glazing and irradiation in the oven were analyzed.

The sealing of door and gaps/slits on the oven was performed using an aluminum self-adhesive insulating tape. This measure reduced the energy consumption from the baseline of 917 Wh to 801 Wh.

The effect of the vapor outlet channel was tested by plugging the vapor outlet slit in addition to sealing all of the gaps and slits on the oven. After this, the oven's energy consumption decreased to 772 Wh.

When measuring the effect of glazing, the existing double-glazed door was replaced with a triple-glazed one. The measurements showed that an additional glass sheet on the door not only increases safety by lowering the temperature of the external glass surface, but also contributes to a higher energy efficiency of the oven. Figure 9 shows the temperature variations in the brick at position 1 (T pt1) and consumed energy (E) at a given air temperature in the oven (T amb) for double (2G) and triple (3G) door glazing. The energy consumption was 837 Wh.

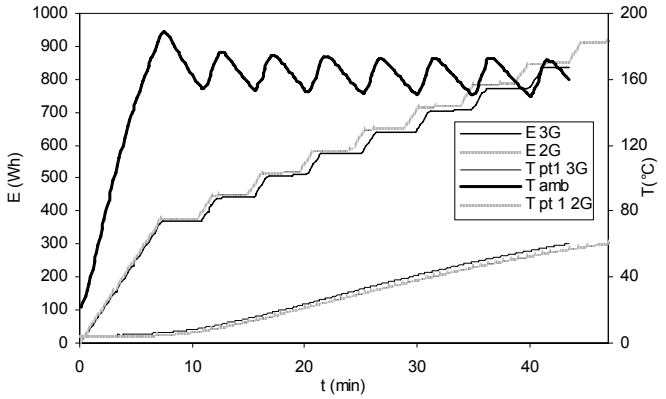

Figure 9 Effect of double (2G) and triple (3G) door glazing.

The influence of insulation layer thickness was analyzed by laying an additional glass wool layer on the sides and on the upper and lower external oven surface. On the rear, no insulation was added because of the vicinity of the electric heaters. A 3 cm layer of glass wool was added – a total of about 1300 g. Figure 10 shows a comparison of the basic oven and the additionally insulated oven (isol). The energy consumption of the oven with additional insulation was 846 Wh.

.

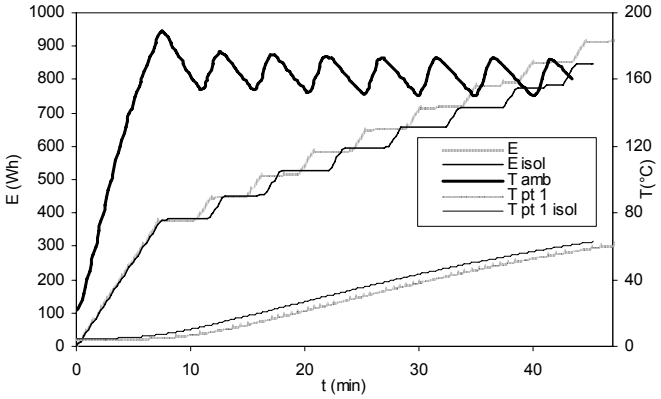

Figure 10 Effect of insulation.

The effect of irradiation inside the oven was tested by placing an aluminum foil onto the oven's inside walls, except for the upper and lower sections, where the heaters are. The foil was arranged in two layers at a distance of about 4 mm. The result for energy consumption is practically the same as the result for measurement with additional thermal insulation, i.e. 845 Wh.

The oven has an integral ON-OFF PID controller. The control regime was analyzed by setting different tolerances for the desired and actual air temperature in the oven. It turned out that small oscillations have a favorable effect on oven energy consumption. Figure 11 shows a comparison of energy consumption (E), temperature variation in the oven (T amb) and temperature in the test brick at measurement site 1 (T pt 1) between the standard control regime and a regime with smaller tolerances between the desired and actual oven temperature (E reg, T amb reg, T pt 1 reg). Energy consumption at improved regulation amounted to 745 Wh.

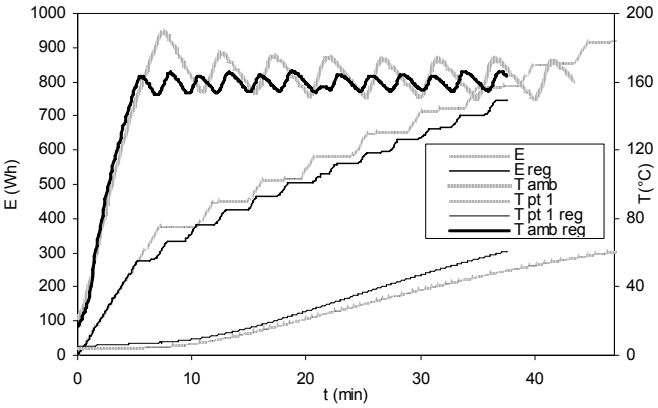

Figure 11 Effect of control.

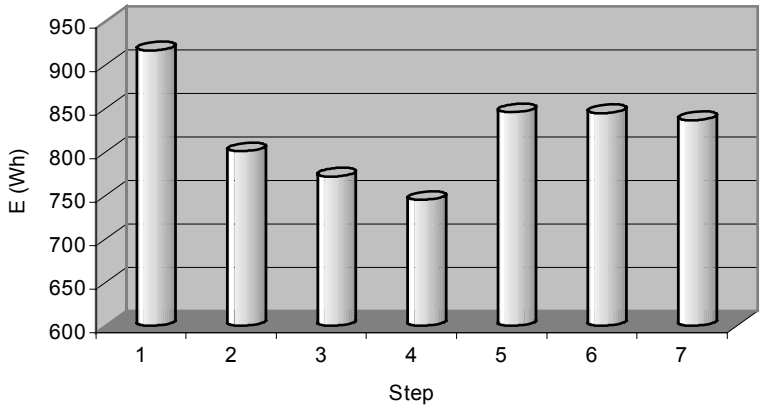

Step	Description	E (Wh)
1	Standard	917
2	Sealing of the door and gaps	801
3	Sealing of the door, gaps and vapor outlet	772
4	Control with smaller oscillations	745
5	The added 30 mm insulation layer around the oven	846
6	Aluminum foil glued over the interior oven surface	845
7	Triple glazed door	837

Figure 12 Quantitative comparison of measures.

On the basis of analysis of the influence of individual parameters on the energy consumption required for heating the test brick from 5 to 55°C, the above-mentioned measures were quantitatively compared. Figure 12 shows that the control method can contribute at most.

With a balanced combination of individual measures, it was possible to achieve a shift to a higher energy efficiency class for the studied oven. The acquired knowledge may be a good basis for designing ovens with a higher energy efficiency.

Conclusions

On the basis of an analysis of individual influences on the energy efficiency of ovens, several solutions were proposed for improving oven operation. An analytical solution was made for describing the nonstationary temperature field within a test brick with convection at a constant heat transfer coefficient and a continuously variable temperature of the surrounding fluid using Green's functions. The influences of door sealing, vapor outlet slit, additional insulation, the oven regulation regime, door glazing and irradiation within the oven were experimentally analyzed.

On the basis of the proposed improvements, the analyzed mass produced oven was moved to the A class of energy efficiency according to standard EN 50304:2001.

References

[1] B. Flipsen, J. Koot and G. Timmers, Design for energy efficiency as a basis for innovations in kitchen appliances, Energy Efficiency in Household Appliances and Lighting, Springer, pp. 182-191, 2001

[2] A.K. Meier and J.E. Hill, Energy test procedures for appliances, Energy and Buildings 26 (1), pp. 23-33, 1997

[3] T.M.I. Mahlia, H.H. Masjuki and I.A. Choudhury, Theory of energy efficiency standards and labels, Energy Conversion and Management 43 (6), pp. 743-761, 2002

[4] Efficient Domestic Ovens, Final report of the SAVE II Project 4.1031/D/97-047, Helsinki, 2000

[5] J.P. Clinch and J.D. Healy, Cost-benefit analysis of domestic energy efficiency, Energy Policy 29 (2), pp. 113-124, 2001

[6] B.M. Shaughnessy and M. Newborough, Energy performance of a low-emissivity electrically heated oven, Applied Thermal Engineering 20 (9), pp. 813-830, 2000

[7] Standard EN 50304:2001; CENELEC, Brussels, 2001

Strojniški vestnik - Journal of Mechanical Engineering 51(2005)7-8, 411-417
UDK - UDC 536.2
Izvirni znanstveni članek - Original scientific paper (1.01)

Numerical analysis of heat transfer and fluid flow in rotary regenerative air pre-heaters

Sandira Alagić[1], Nikola Stošić[2], Ahmed Kovačević[2], Indira Buljubašić[1]

[1]*Faculty of Mechanical Engineering, University of Tuzla, Univerzitetska 4, Tuzla, BiH, sandira.alagic@untz.ba*
[2] *School of Engineering and Mathematical Sciences, City University London, Northampton Square, EC1V 0HB, UK*

Abstract

The Ljungström rotary air pre-heater is a regenerative heat exchanger used for preheating the combustion air, mainly in steam boiler plant. The hot gas and cold air ducts are arranged to allow both the flue gas and the inlet air to flow simultaneously through the machine. The hot flue gas heats the rotor material and as the rotor rotates, the hot rotor section moves into the flow of the cold air and preheats it.

Existing simulations of regenerative air pre-heaters are mainly based on empirical approximations where some of the effects of the process are neglected. Although this usually gives reasonably acceptable results, it was thought that CCM analysis of such devices, which stands for Computational Continuum Mechanics, would result in a better understanding of the process features, such as the fluid-solid interaction.

A grid interface was developed to transfer the geometry of such a Ljungström air pre-heater to a finite volume numerical mesh which is later used for the calculation of unsteady fluid-solid interactions. Results were obtained by use of the commercial CCM solver "Comet" of Star CD. In this paper the results are presented in the form of diagrams of the velocity and temperature fields as functions of time and space. The results of both the one- and three-dimensional calculations and field measurements are compared and good agreement was achieved.

The result of this study is the development of an effective procedure for computer calculation of processes in a Ljungström air pre-heater to optimise its parameters, which can be used either for research and development or in everyday engineering practice.

Introduction

Much effort has been spent to maximise the efficiency of each stage of the transformation of the chemical energy of fuel to electrical power. In a steam boiler, the most significant loss is associated with the energy of the outgoing flue gas. This can be reduced by the use of an air pre-heater which transfers energy from the outgoing exhaust gases, to the incoming air, prior to combustion. The Ljungström air pre-heater, as shown in Figure 1, is a regenerative heat exchanger often used for this function in industrial power plant. In it, the hot gas and cold air are arranged to flow in opposite directions through parallel ducts, each of which, passes through a section of a rotor. The combustion products heat the rotor as it revolves through that section. Further rotation of the rotor brings it into contact with the incoming air, where it is cooled by it. The air is thereby preheated before passing to the boiler furnace, where it is used for combustion of the fuel. The rotor is divided into a number of sections, which are separated by seals, in order to prevent mixing of the flue gases and combustion air. These sections consist of small passages formed by profiled sheets, as shown in Figure 2, and the performance of the air pre-heater depends on the size and shape of these small cells.

A number of studies have already been published, which describe methods of estimating the performance of regenerative pre-heaters. However, all of them are based on dimensionless or one-dimensional models in which some significant effects are either neglected or estimated empirically. A three dimensional approach was therefore regarded as a useful tool to analyse heat and fluid flow within the cell elements more precisely and how varying their size and shape would affect the interaction between the rotor and the fluid.

Nomenclature

A	- area of contact between the solid body and gas, area	c	- specific heat
e	- internal energy	C	- turbulence model constants
h	- heat transfer coefficient, enthalpy	**f**	- body force
I	- unit tensor	**i**	- unit vector
m	- mass	k	- conductivity, kinetic energy of turbulence
P	- production of kinetic energy of turbulence	p	- pressure
s	- control volume surface	**q**	- source term
u	- displacement in solid	t	- time
V	- volume	**v**	- fluid velocity
z	- axial coordinate	x	- spatial coordinate
α	- temperature dilatation coefficient	Γ	- diffusion coefficient
ε	- dissipation of kinetic energy of turbulence	ϕ	- variable
λ	- Lame coefficient	μ	- viscosity
η	- Lame coefficient	ρ	- density
σ	- Prandtl number		

Indices

eff	- effective	g	- gas
in	- inflow	out	- outflow
s	- solid	T	- turbulent

The use of Computational Fluid Dynamics, CFD, to analyse the flow in a variety of thermal equipment has been widely reported, but there is no record in the open literature of its use and use of CCM for calculations of flows in Ljungström air pre-heaters. One possible reason for this is the complexity of the geometry and flow within these devices.

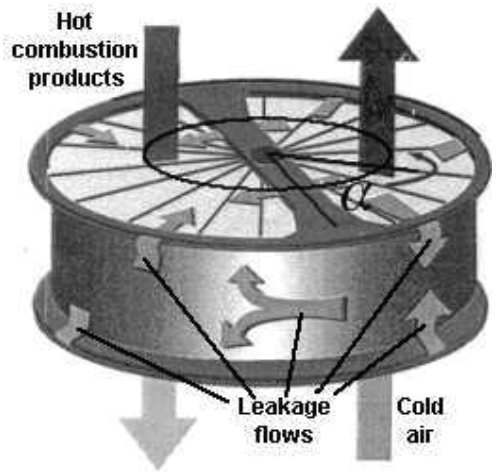

Figure 1 Fluid flows in rotary regenerator

A further complication of the analysis is that the flow processes involved are unsteady and their nature can only be properly understood by consideration of the interaction between the fluid flow and solid structure.

More recently, the use of continuum mechanics and a substantial increase in computer speed and capacity have made it possible to develop specialized computer codes for simultaneous application of finite volume numerical methods to both fluid flow and its surrounding solid structure in the form of commercial CCM codes.

In order to apply these advanced numerical methods to the calculation of rotary regenerator devices, the authors have developed a general and flexible grid generation procedure. An interface program written in FORTRAN enables an arbitrary geometry of a pre-heater to be automatically mapped with the discrete volumes and then used for calculation in a standard CCM code. By this means, a study was carried out on an existing pre-heater in "Tuzla" power station, using the commercial CCM solver "Comet". The results are displayed in the form of the temperature distribution within the pre-heater solid elements and fluid flow of both the hot combustion products and cold air as a function of both time and spatial position

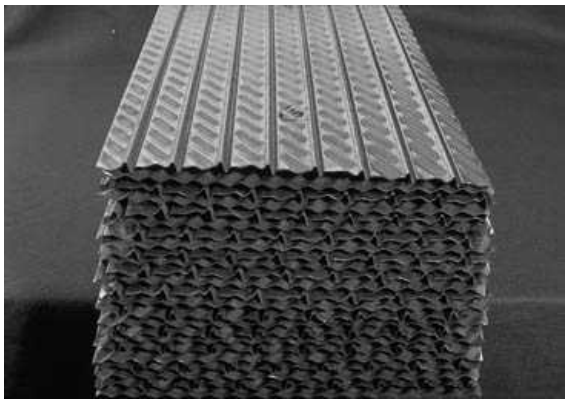

Figure 2 Filling of a rotary regenerator

One-dimensional energy balance of the pre-heater

A one-dimensional model is developed and described in this paper, which assumes that each control volume consists of solid and fluid parts connected via a common area surface. The solid and fluid components of the cell exchange heat through certain regions of the known surface area. As a result of the rotation of the device, the temperature within it changes continuously both in space and time.

In such a case, a one-dimensional numerical model of heat transfer between the hot combustion products and solid material on one side, and the cold air and solid body on another, can be applied to estimate the pre-heater performance reasonably well. [1]

The control volumes are positioned next to each other and a constant speed of rotation is assumed for all of them.

The mathematical model utilized here consists of two energy balance equations, one for the solid body, (1) and one for the fluid phase, (2). The interface between these two equations is the convective heat transfer between the fluid and the solid.

$$\underbrace{m_s c_s \frac{\partial T_s}{\partial t}}_{\substack{\text{accumulation}\\ \text{in solid body}}} + \underbrace{k_s A_i \frac{\partial^2 T_s}{\partial x_i^{\,2}}}_{\substack{\text{conduction}\\ \text{in solid}}} = \underbrace{hA\left(T_g - T_s\right)}_{\text{heat source}} \qquad (1)$$

$$\underbrace{m_g c_p \frac{\partial T_g}{\partial t}}_{\substack{\text{accumulation}\\ \text{in gas}}} + \underbrace{\dot{m}_g c_p \left(T_{in} - T_{out}\right)}_{\text{convection}} + \underbrace{k_g A_i \frac{\partial^2 T_g}{\partial x_i^{\,2}}}_{\text{conduction in gas}} = \underbrace{hA\left(T_g - T_s\right)}_{\text{heat source}} \qquad (2)$$

$$m_s c_s \frac{\partial T_s}{\partial t} + k_s A_z \frac{\partial^2 T_s}{\partial z^2} = hA\left(T_g - T_s\right) \qquad (3)$$

$$m_g c_p \frac{\partial T_g}{\partial t} + \dot{m}_g c_p \frac{\partial T_g}{\partial z} = hA\left(T_g - T_s\right) \qquad (4)$$

Since each flow passage is narrow and surrounded by thin material, the fluid temperature change in the direction perpendicular to the main flow can be regarded as small and neglected. Also, since it is assumed that heat is not exchanged with the surroundings in the radial direction, conduction in the solid body only occurs along the axial coordinate z. Heat transfer by conduction in the fluid is neglected because of the low fluid thermal conductivity. By means of these simplifications, the equations are reduced to those of unsteady 1-D flow, as shown in equations (3) and (4). These can be solved by a finite difference method.

Depending on the spatial position of the calculating domain, i.e. the angle of rotation, the fluid medium in these equations is either air or combustion products. The inlet temperatures and mass flow rates are assumed to be constant during the each half-period of the process and their assumed values are those obtained from industrial plant measurements. The spatial domain is discretised by assuming constant steps in the axial direction.

The time step is assumed to be constant. The resulting system of algebraic equations is then solved numerically by iterative procedure contained in the computer program written by the authors. The results obtained are in the form of instantaneous temperatures of the flue gas or air and solid, and the mass flows of the flue gas and air at every point along the axial coordinate z.

Three-dimensional analysis of the pre-heater

Both, the fluid flow and structural behaviour of the solid parts in a regenerative pre-heater are fully described by the mass averaged equations of continuity, momentum and energy conservation which are accompanied by equations of the turbulence model and state, as given, for example, in [4]. The solution of these equations is then made possible by inclusion of constitutive relations in the form of Stoke's and Fourier's law for the fluid momentum and energy equations respectively and Hooke's law for the momentum equations of the thermo-elastic solid body. The generic 3-D transport equation is then given as:

$$\frac{d}{dt}\int_V \rho\phi dV + \int_S \rho\phi \mathbf{v}\cdot d\mathbf{s} = \int_S \Gamma_\phi \operatorname{grad}\phi \cdot d\mathbf{s} + \int_S \mathbf{q}_{\phi S}\cdot d\mathbf{s} + \int_V \mathbf{q}_{\phi V}\cdot dV \qquad (5)$$

The terms in the equation which describe the pre-heater case are given in *Table 1*.

The resulting system of partial differential equations is then discretised by means of a finite volume method in a general Cartesian coordinate system. This method maintains the conservation of the governing equations, while at the same time enables a coupled system of equations for both, solid and fluid parts to be solved simultaneously. Connection between the solid and fluid parts is explicitly determined if the temperature on the solid body surface is a boundary condition for the fluid flow and vice versa. The numerical grid, as explained in the next section, is attached to the CCM solver to obtain the distribution of the fluid temperature and velocity throughout the fluid domain and the temperature of the solid elements.

This mathematical scheme is accompanied by the boundary conditions for both the solid and fluid parts. Whether the fluid part contains hot gas or cold air it is entirely surrounded by the walls. Cyclic boundary conditions are applied to all sides of the domain except to the top and bottom parts. These are represented either as inlet or outlet. The initial values for all physical variables are given at the centre of each numerical cell within the domain and preset to the values of the air inlet flow.

Table 1 Terms in the generic transport equation (5)

Equation	ϕ	Γ_ϕ	$\mathbf{q}_{\phi S}$	$\mathbf{Q}_{\phi V}$
Fluid Continuity	1	0	0	0
Fluid Momentum	v_i	μ_{eff}	$\left[\mu_{eff}\left(\operatorname{grad}\mathbf{v}\right)^{\mathrm{T}} - \left(\frac{2}{3}\mu_{eff}\operatorname{div}\mathbf{v} + p\right)\mathbf{I}\right]\cdot\mathbf{i}_i$	$f_{b,i}$
Solid Momentum	$\frac{\partial u_i}{\partial t}$	η	$\left[\eta\left(\operatorname{grad}\mathbf{u}\right)^{\mathrm{T}} + \left(\lambda\operatorname{div}\mathbf{u} - 3\alpha\Delta T\right)\mathbf{I}\right]\cdot\mathbf{i}_i$	$f_{b,i}$
Energy	e	$\frac{k}{\partial e/\partial T} + \frac{\mu_t}{\sigma_T}$	$-\frac{k}{\partial e/\partial T}\frac{\partial e}{\partial p}\cdot\operatorname{grad}p$	$\mathbf{T}$: grad $\mathbf{v} + h$
Turbulent kinetic energy	K	$\mu + \frac{\mu_t}{\sigma_k}$	0	$P - \rho\varepsilon$
Dissipation	ε	$\mu + \frac{\mu_t}{\sigma_\varepsilon}$	0	$C_1 P\frac{\varepsilon}{k} - C_2\rho\frac{\varepsilon^2}{k} - C_3\rho\varepsilon\operatorname{div}\mathbf{v}$

Grid generation

To solve the equations numerically, the spatial domain of the pre-heater has to be replaced by a numerical grid that contains discrete volumes. This process of replacing the spatial domain by a system of grid points is called numerical grid generation. Both, the type and the quality of a numerical grid play important role in the accuracy of the numerical solution and efficiency of the finite volume method [4].

A composite grid, made of several structured grid blocks patched together and based on a single boundary fitted co-ordinate system is used to transform the physical geometry of the selected part of an air pre-heater into discrete volumes. Grid blocks are then connected over the defined regions through their boundaries, which coincide with other elements of the entire numerical mesh. Boundary fitted and confirmed numerical meshes are generated for each part of both, the fluid and solid parts as in Figure 3, of ref [6].

In order to make the 3-D simulation and evaluation of the air pre-heater process faster and easier, only one cell of the accumulation mass in the radial and circumferential direction was considered for calculation.

The grid calculation method applied in this paper is based on algebraic transfinite interpolation with multi parameter adaptation of the boundaries. This includes stretching functions in order to ensure both grid orthogonality and smoothness.

More information about analytical grid generation methods can be found in refs [5] and [6].

The grid generation method is implemented in a pre-processor program developed by the authors in order to produce a numerical mesh suitable for analysis of a Ljungström rotary heat regenerator and to incorporate it into existing finite volume CFD and CCM software automatically.

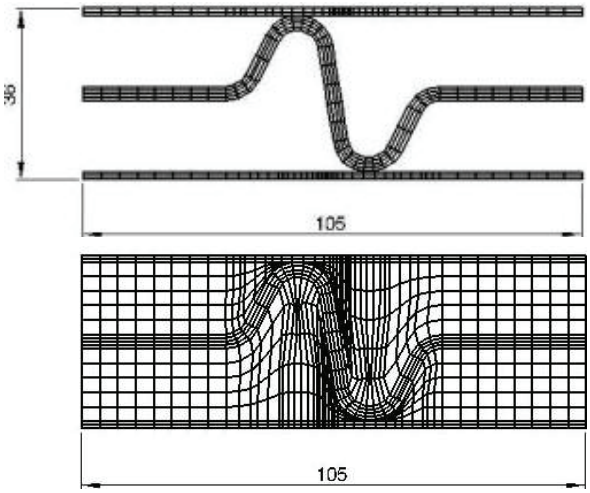

Figure 3 Cross section through the numerical mesh: Top – fluid part, Bottom - solid and fluid part

Comparison of 1-D and 3-D simulations

The analysis of processes in a rotary air pre-heater was performed for steam boiler No. V, Unit IV in Tuzla Power Plant.

A numerical solution was obtained for the working conditions specified in the operational documents [7]. These are: speed of rotation 1.76 rpm, air inlet temperature 313 K, gas inlet temperature 588 K, air inlet velocity 4.5 m/s and gas inlet velocity -8.0 m/s. The negative value means that gas enters the computational domain in the opposite direction to the air, as shown in Figure 1. Dimensions of the regenerator are: outer radius 3.8 m, inner radius 0.5 m, height 1.3 m.

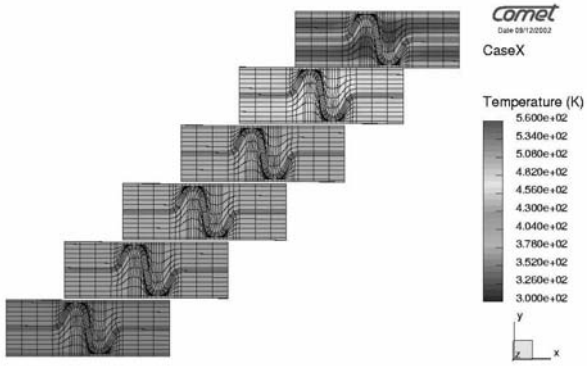

Figure 4 Time step 1, Rotor angle 3.36

Cold air enters the computational domain when the computational angles of rotation are between 0^o and 150^o. That is the angle range for which the pre-heater filling is exposed to the air channel. Similarly, the combustion products are in contact with the computation domain between $180\text{-}350^o$.

For other values of the rotational angle, both sides of the computational domain are closed and the velocities at their boundaries set at 0.

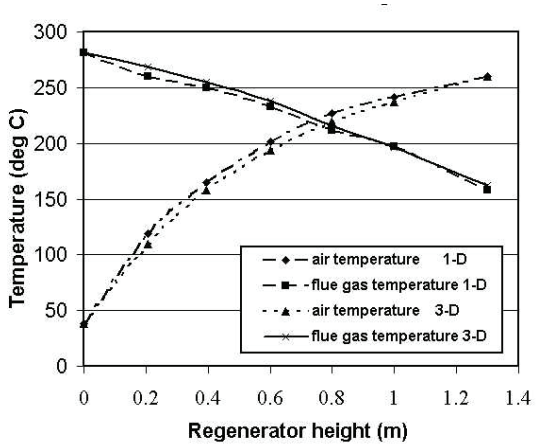

Figure 5 Comparison of temperatures calculated with 1-D and 3-D models

Figure 4 shows results of the 3-D analysis. The first time step, which is presented, corresponds to 3.36^o. This represents the position at which the control volume becomes exposed to the cold air stream. That part of the process ends at 150^o. In that period, heat is transferred from the solid part of the domain to the cold air, which, results in its temperature rise from 38^oC to about 263^oC.

During the second period, which finishes at the angle of 180^o, the gas contained in the computational domain tends to an average temperature along the height of the pre-heater. However, that time period is too short for such a process and the maximum gas temperature

remains at the level of 260°C. The computational domain then becomes open to the hot combustion products at 180°. During the following period, most of the heat is transferred to the cold metal sheets, which are heated to the highest temperature difference while the hot gas is cooled to about 177°C in the 62nd time step. A comparison between the results of the calculated air and gas temperatures obtained by both the 1-D and 3-D models is given in Figure 5. The temperature distribution is given along the complete height of the regenerator. Good agreement between the two models is achieved.

A comparison of both, the fluid flow and solid body temperatures at different heights as a function of the angle of rotation is shown in Figure 6. In the same figure, the variation in the temperature of the air, heated due to cooling of the metal sheets, as well as change in the temperature of the flue gas, which is cooled due to heating of the metal sheets, is shown. It can be concluded from these two diagrams that the 3-D results give good agreement with the corresponding results obtained by the 1-D model.

The results of this comparison between the 1-D and 3-D numerical results and experimental data confirm that the 1-D model is adequate for most purposes when using CCM procedures to estimate pre-heater performance, but the 3-D model increases a level of confidence of using numerical results.

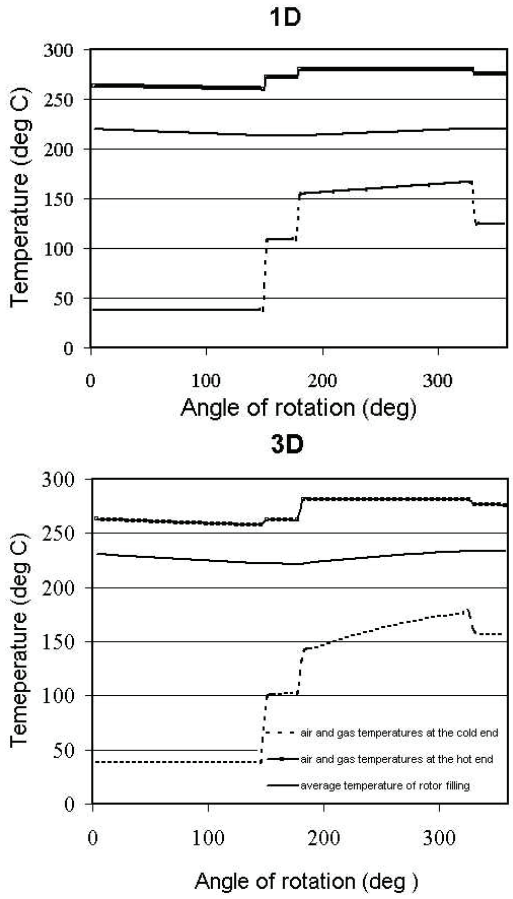

Figure 6 Temperatures of fluid and solid part obtained by 1-D and 3-D calculations

Experimental investigation and analysis

A further stage in the investigation was to determine how reliable the 1-D and 3-D models were in predicting real plant performance when compared with results obtained from power plant measurements.

Tests were therefore carried out on the regenerative heat exchanger of the pre-heater 3, steam boiler V, Unit IV at Tuzla Power Plant to obtain temperature measurements at the boiler hot and cold ends. Values of the flue gas temperature were taken at seven measuring points. A total of 28 temperature measurements were taken with thermocouple probes at depths of 0.5, 1, 1.5 and 2m in order to get temperature fields across the pre-heater cross section at four different depths.

The gas temperatures measured at the exit of the air pre-heater for one operational point at a rotational speed of 1.76 rpm are given in Table 2.

The results of the 1-D and 3-D models, shown in Figure 6 show reasonable agreement with the measured values, as shown in Table 3.

The relative error between the 3-D calculations and measurements for the flue gas side was 5.82 % while for the air side the error was 0.03 %. Relative error for the 1-D calculations and measurements was 6.41 % for flue gas and 0.81 % for air.

Table 2 Measured temperatures in °C for air pre-heater 3, steam boiler V, Unit IV, Tuzla Power Plant

Height	Measurement points						
(m)	1	2	3	4	5	6	7
0.5	161	168	168	158	178	179	183
1.0	162	167	167	168	178	181	183
1.5	161	167	171	168	175	182	181
2.0	162	168	169	168	176	182	180

Table 3 Comparison between measured and calculated values for the regenerator speed n=1.76 rpm

Model	Temperatures of flue gas at cold end (°C)	Temperatures of air at the hot end (°C)	Relative error gas/air (%)
1-D	160.80	262.13	6.41/0.81
3-D	161.82	260.10	5.82/0.03
Measured	171.82	260.00	-

Speed optimisation

Since the heat exchanged within the air pre-heater depends on the rotor speed, a thorrough numerical study was performed to find out the temperature behaviour of the Ljungström pre-heater with speed variation.

The gas outlet and air inlet temperatures in function of the rotor speed are presented in Fig 7. As it may be noticed, at low speeds air exits with lower temperature, while the flue gases leave the pre-heater with higher temperature because both, air and gas are in contact with the pre-heater walls for longer period. Therefore, the heat exchanged is small. At zero speed, for example, there virtually will be no heat transfer at all and the exit temperatures will be the same as the inlet ones. At higher rotor speeds, air and gas temperatures will tend to a single value which balances depending on heat capacity of both streams. At infinite speed for example, the heat transferred will be the same as in a parallel flow heat exchanger of infinte heat transfer surface. However, since a well designed Ljungstroem pre-heater performs beter than a parallel flow heat exchanger, there must exist a rotor speed for which the heat exchanged reaches its maximum. This was estimated at approximately 3 rpm for the pre-heater in question. It appeared that 3.2 % of increase in heat transfer was obtained for that speed in comparison with the pre-heater operational speed of 1.76 rpm.

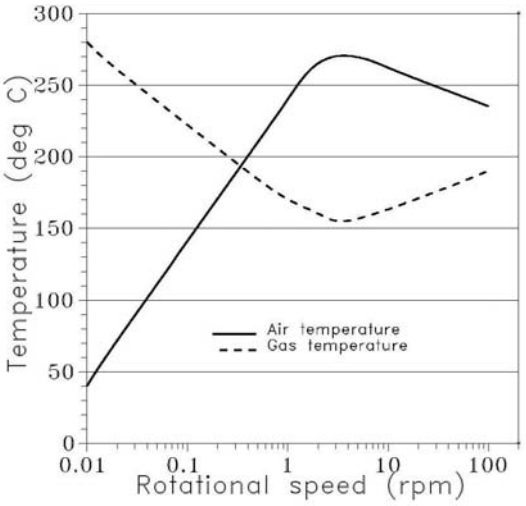

Figure 7 Exit air and gas temperatures in function of rotational speed

Conclusions

The aim of the investigation described in this paper was to obtain a better understanding of the processes in rotary air pre-heaters by the use of numerical estimation and experimental measurement of both the air and combustion product flows.

A convenient feature of rotary air pre-heater construction is that the entire machine can be analysed by consideration of only one gas and airflow path bounded by the filling metal material. The computational domain thus defined, can then be conveniently subdivided into a finite number of control volumes and analysed by the use of iterative procedures. The use of CCM, both in 1-D finite difference and 3-D finite volume methods, demonstrated that for most purposes, the 1-D model is adequate and demonstrated that this method both simplifies the problem statement significantly and speeds up the calculation procedure and that the 3-D model serves for better understanding of the pre-heater processes.

The experimental results confirm the validity of both the numerical analysis methods not only for calculation of the fluid flow temperatures but also for the temperatures of the pre-heater solid filling. By this means, a powerful tool was developed which allows a better understanding of the fluid flow and heat transfer process in rotary pre-heaters.

References

[1] E. Zafeiriou, D. Wurz: Numerical Simulation of Heat Transfer Processes in Rotating Regenerators, VGB Kraftwerkstechnik 76, Number 6, 1996.

[2] H. Klein, G. Eigenberger : Approximate solutions for metallic regenerative heat exchangers, International Journal of Heat and Mass Transfer 44, (3553 – 3563), 2001.

[3] B. S. Baclic, G. D. Dragutinovic: Operation of Counterflow Regenerators; Computational Mechanics Publications Southampton, UK and Boston, USA, 1998.

[4] J. H.Ferziger, M. Perić: Computational Methods for Fluid Dynamics, Springer, Berlin, 1996.

[5] J. F. Thompson, B. Soni; N. P. Weatherrill, "Handbook of Grid generation", CRC Press 1999.

[6] A. Kovačević, N. Stošić and I. K. Smith: Three Dimensional Numerical Analysis of Screw Compressor Performance, Journal of Computational Methods in Sciences and Engineering, vol. 3, no. 2, 2003, pp. 259- 284

[7] Documentation of the Power Plant Tuzla, Unit IV

Strojniški vestnik - Journal of Mechanical Engineering 51(2005)7-8, 418-425
UDK - UDC 536.2
Izvirni znanstveni članek - Original scientific paper (1.01)

Evaluation of Compact Heat Exchanger Technologies for Hybrid Fuel Cell and Gas Turbine System Recuperators

M. Ruhul Amin *, Joel D. Lindstrom

Department of Mechanical & Industrial Engineering, Montana State University, 220 Roberts Hall, Bozeman, Montana, USA, ramin@me.montana.edu*

Abstract

Hybridized Carbonate and Solid Oxide fuel cell power plants are currently under investigation to fulfill demands for high efficiency and low emissions. Selection of high performance, compact recuperators is essential for such applications. In this paper compact heat exchanger (CHEX) technology applicable to hybrid fuel cell and gas turbine technology has been extensively reviewed. Various compact heat exchanger designs pertinent to gas-gas recuperative duties for fuel cell and gas turbine (FCGT) hybrid systems are presented. The type of CHEXs considered in this study included: brazed plate-fin, fin-tube, microchannel, primary surface and spiral. Comparison of the candidate designs is performed by rating each exchanger with a set of desired criteria. Based on this rating procedure, two CHEX designs namely, plate-fin and microchannel were chosen for further review. Plain, strip, louver, wavy and semicircular surface geometries were then analyzed with a numerical CHEX sizing procedure ultimately to select the most suitable surface geometry for FCGT systems. The brazed plate-fin CHEX having the louver fin geometry was chosen, where numerical results show that this surface holds the greatest potential for CHEX size and cost reduction.

1. Introduction

Fuel cell technology has been identified to meet simultaneous demands for more electric power and less pollution. In particular, high temperature fuel cells can utilize existing natural gas infrastructures effectively. Carbonate and Solid Oxide fuel cells operate at high temperature and reject a significant amount of heat so that hybridized fuel cell and gas turbine (FCGT) power plants are under investigation. Ultra high fuel to electricity conversion efficiency (>70% LHV) of such designs is projected.

Recuperator design is instrumental to the success of a hybrid FCGT power plant. A recuperator with low effectiveness will have a large impact on system cost with only minimal impact on system output, and similarly, a recuperator with very high effectiveness will have a large size so that it will be too expensive to make the best overall impact, Utriainen and Sunden [1]. In addition, fuel cell systems have much lower power density than competing gas turbine systems. Therefore, component size is a principle issue for the FCGT hybrid design, especially since distributed power stations will likely have demand in areas where space is limited.

2. CHEX Technology Review

Compact heat exchangers offer the ability to transfer heat between large volumes of gas with minimum footprint. The degree to which an exchanger is considered compact can be characterized by the compactness parameter (β). A gas to fluid exchanger is considered compact if it has a heat transfer area to volume ratio (β) greater than 700 m^2/m^3 on at least one of the fluid sides, Shah [2]. Compactness is a good indication of performance, the higher the compactness generally the higher the effectiveness for a given pressure drop, Oswald [3].

2.1 Brazed Plate-Fin Exchangers

Compact brazed plate-fin exchangers (BPFE) have a long history in gas-gas heat transfer applications because of their ability to achieve high levels of compactness. An illustration of a generic counterflow plate-fin exchanger is shown in Fig. 1. There are numerous surface geometries that can be used in BPFEs. Offset strip-fins have more than 60 years of research behind them and are commonly employed. Louver fins are also widely used given their mass production manufacturability.

Nomenclature

a	Parting plate thickness, (m)
A	Total heat transfer area, $NTUC_{min}/U$, (m^2)
A_{fr}	Frontal area, A_o/σ, (m^2)
A_o	Minimum free flow area, m_{dot}/G, (m^2)
A_r	Fin area per total area, (---)
b	Plate spacing, (m)
C	Heat capacity rate, (W/K)
D_h	Hydraulic diameter, $4A_oL/A$,(m)
f	Fanning friction factor, (---)
g_c	Force-mass conversion constant
G	Mass velocity, (kg/m^2*s)
h	Convective heat transfer coefficient, $jGC_pPr^{(-2/3)}$, (W/m^2*K)
j	Colburn factor, (---)
k	Thermal conductivity, (W/m*K)
l	Fin length, (m)
L	Core length, $D_hA/4A_o$, (m)
m_{dot}	Mass flow rate, (kg/s)
NTU	Number of heat transfer units, (---)
ntu	Number of heat transfer units based on one fluid side, $\eta_o hA/C$, (---)
ΔP	Pressure drop, (kPa)
Pr	Prandtl number, (---)
Q	Exchanger heat duty, (kW)
Re	Reynolds number, GD_h/μ, (---)
TD	Exchanger thermal density, Q/V, (MW/m^3)
U	Overall heat transfer coefficient, (W/m^2*K)
V	Exchanger volume, A/α, (m^3)

Greek Symbols

α	Ratio of total heat transfer area on one side of an exchanger to the total volume of the exchanger, (m^{-1})
β	Compactness, ratio of heat transfer area on one side of a heat exchanger to the volume between the plates on that side, (m^2/m^3)
ε	Heat exchanger effectiveness
η_f	Fin efficiency, (---)
η_o	Extended surface efficiency, $1-A_r(1-\eta_f)$, (---)
ρ	Fluid density, (kg/m^3)
σ	Ratio of free flow area to frontal area, (---)
μ	Dynamic viscosity, (cp)

Subscripts

c	Cold fluid side
h	Hot fluid side
i	Inlet
o	Outlet
s	Scale
w	Wall
1	One section of the exchanger
2	Other section of the exchanger

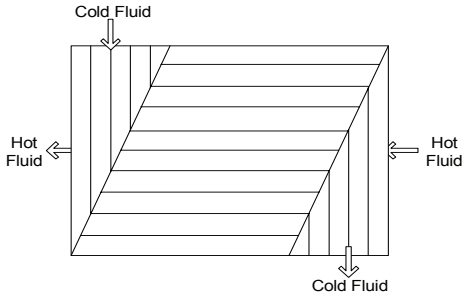

Fig. 1. Counterflow Plate Fin Heat Exchanger

A BPFE relevant to high temperature operation is available from Ingersoll-Rand. The design has a minimal need for preload and is modular, where cells and cores can be stacked together to meet a desired heat load. Five different cell sizes are available, including three different plate areas and two different fin heights, Kesseli et al. [4].

2.2 Fin-Tube Exchangers

Compact fin-tube exchangers (FTE) can consist of various tube, fin, and flow orientations where generally, small bore tubes are spaced closely together. Bare tube bundles in counterflow represent one of the first gas turbine recuperator designs manufactured over 40 years ago by Escher-Wyss, Ltd., Fraas and Ozisik [5]. The performance of this bulky design was improved by adding longitudinal fins; however, the improved design was still far from compact. Escher-Wyss used filler shapes to block gas flow through the interstices of the tube bundles and at the center of each tube in an attempt to provide fluids with sufficient proximity with exchanger surfaces.

Small bore, oval shaped tubes are good for pressure containment and can exhibit structural integrity in a cyclic environment. However, tubular structures are generally not amenable to a modular design approach. Tubes also have poor thermal density and are expensive compared to sheets. Use of tubes is rarely warranted for high temperature, low pressure, gas-gas operation.

2.3 Microchannel Exchangers

Microchannel exchangers are classified by having hydraulic diameter between 10 and 200 μm and minichannel exchangers having hydraulic diameter between 200 to 3000 μm, Kandlikar and Grande [6]. However, this work will consider microchannel exchangers (ME) as those fabricated from individual flat plates having high compactness. In addition, MEs fabricated specifically by chemical etching will be further classified and referred to as printed circuit heat exchangers (PCHE).

It has been reported that MEs can experience unexpectedly high heat transfer performance, Reid [7]. It is said that surface roughness is a main parameter of this,

which could represent an easily acquired and economical way to pursue CHEX performance enhancement. Despite this understanding there is still much difficulty in correlating numerical predictions with experimental data in MEs, so that uncharted and perhaps risky territory exists in this area. A commercial PCHE anticipated suitable for gas-gas exchange is fabricated by Heatric Ltd. Plates in Heatric's exchanger are diffusion bonded so that the connections are said to be as strong as the parent metal. However, it is yet to be seen how conducive this technology is with high temperature nickel alloys.

2.4 Primary Surface Exchangers

Primary surface exchangers (PSE) are characterized by having only a primary surface to transfer heat between fluid streams; there are no secondary surfaces (fins). Solar Turbines Inc. has developed this type of recuperator for over 30 years. They report that clamping cells together, instead of having a rigid cell structure, can permit enough movement between cell contacts to relieve concentrated stresses at weld locations. Sound suppression is also attributed to the damping characteristic of the clamped design, Solar Turbines [8].

However, stamped plate PSE designs are compactness limited and folded sheet PSE designs can suffer from exhaust flow blockage due to a lack of support structures between cells. The latter consideration is a very important aspect for high temperature (>650°C) operation. Another disadvantage of the PSE design is that they can require a significant preload mechanism which can result in complex and expensive manufacturing procedures, Kesseli [4].

2.5 Spiral Exchangers

Spiral exchangers (SE) have traditionally been used with particle laden or high viscosity fluids because of their self-cleaning nature. Scale is swept away from turbulence induced by swirling fluid paths. A fouling factor of one third that of shell and tube type exchangers is not unusual for SEs. Mechanical cleansing is also a desirable alternative available with some of the spiral designs. However, SEs generally have low compactness. In addition, the coiled design can require extensive manufacturing equipment. However, the SE is currently in development and has been proposed by Oswald [3] to withstand the structural problems of gas turbine recuperators.

2.6 CHEX Summary

Based on the emphasis that smaller core volume and increased performance can be obtained by increasing compactness, it was determined that this criterion is very important for the FCGT application. Therefore, an extensive literature review was conducted to estimate a range of compactness for each CHEX and tabulated in Table 1.

Table 1. Compactness Range

Exchanger Type	Compactness (m^2/m^3)
Plate-Fin	250 – 6560
Fin-Tube	190 - 3300 / Fin
	138 - 1150 / Tube
Microchannel	2000 - 10,000
Primary Surface	1640 – 3600
Spiral	120 – 1600

Complete detail of numerous BPFE and FTE surface configurations were found in the extensive work of Kays and London [9]. The BPFE was found to have compactness figures of up to 6560 m^2/m^3, given by Kraus et al. [10]. Compactness data for the FTE was found to have up to 3300 m^2/m^3 although for crossflow orientation. Data for counterflow FTEs with longitudinal fins could not be found since they are generally not even considered compact, Shah and Webb [11]. The tube side of the FTE displays rather low compactness, reaching only 1150 m^2/m^3, Shah [12]. The ME is discussed in Wadekar [13] and Hesselgreaves [14]. The PSE was found to have a compactness range of 1640 to 3600 m^2/m^3 by Utriainen and Sunden [15] and McDonald [16] respectively. The SE data was found to max out at 1600 m^2/m^3, Bacquet [17].

2.7 Durability

Historically, gas turbine recuperators have had very poor reliability due to fatigue and creep problems. Although, temperature ramping is expected to be much slower for FCGT systems, where high temperature fuel cells generally have a much longer start up time and more gradual transients than do traditional gas-fired turbine systems. However, some FCGT recuperators may be used for load leveling and or quick startup, where they could be subject to stringent temperature ramping rates. This scenario would most likely place durability as the primary design constraint as it is with traditional gas turbine recuperators. Despite this concern it is assumed that most FCGT systems will not operate in this manner, and that the temperature ramping rate in the recuperators will follow closely to that of the fuel cells. Therefore, durability requirements are considered not as severe for the present application.

2.8 Fouling and Corrosion

Fouling is one of the major potential problems in compact heat exchangers due to small hydraulic diameter and lack of cleaning ability. Fouling can reduce the heat transfer coefficient 5 to 10 percent in general, but can increase the pressure drop up to several hundred percent, particularly for compact heat exchangers with gas flow, Shah [2]. Fouling mechanisms are in general understood, but little success has been made in prediction and prevention. Effective cleaning techniques will be an increasingly important requirement for CHEX design.

It has been reported that water vapor has a deleterious role on the oxidative lifetime of metallic recuperators, Pint et al. [18]. This is important for FCGT recuperators

where process streams have relatively high steam content. Corrosion processes can be reduced by utilizing nickel bearing alloys which can provide general corrosion resistance and maintain sufficient mechanical properties. However, when a heat exchanger has to be made from an expensive nickel alloy, the cost of raw material generally dominates the cost of the exchanger, Deakin et al. [19].

2.9 Cost

High compactness is desired for FCGT recuperators, although increased compactness will generally reflect in increased capital cost. For a given pressure drop, the higher is the compactness, shorter is the flow length and larger is the frontal area. This implies that higher compactness yields smaller plate size, resulting in more plates and higher fabrication cost. However, higher compactness generally yields higher CHEX performance, so that a trade off is expected. Market availability is expected to be a heavy proponent for the high temperature (>650°C) application, where use of nickel alloys is usually warranted. BPFE cost has been well documented in Kesseli et al. [4].

3. Performance Comparison Method

The two step heat exchanger selection approach outlined by Wadekar [13] was used in this procedure. The first step consists of a coarse filter elimination, where CHEX types are compared and most of which eliminated. The second step consists of a fine filter elimination, where different surface geometries of the remaining CHEX types are evaluated, resulting in the selection of the single best performing surface geometry for the present application.

3.1 Mathematical Formulation - Coarse Filter

A numerical rating procedure was used to select the two most compatible CHEX types for three general FCGT process conditions: Fuel Preheater, Low Temperature Gas Turbine Recuperator, and High Temperature Gas Turbine Recuperator. The criterion used to make this selection include compactness, durability, material cost, manufacturability, availability, maintenance, and applicability. Each of these criteria was given a weight factor according to its importance for each FCGT process condition. The weighting scale was defined as a range from one to five, where five carried the most importance. The weights given to each criterion for each process condition consist of the following:

1. Compactness was assigned a weight factor of five for all three FCGT process conditions.
2. Durability was assigned a weight factor of four for the Fuel Preheater and five for both Low and High Temperature Recuperators.
3. Material Cost was assigned a weight factor of three for the Fuel Preheater and Low Temperature Recuperator assuming stainless steel is used. A weight factor of five was assigned for the High Temperature Recuperator assuming a nickel alloy is used.
4. Manufacturability was assigned a weight factor of two for the Fuel Preheater and Low Temperature Recuperator assuming stainless steel is used. A weight factor of 4 was assigned to the High Temperature Recuperator assuming a nickel alloy is used.
5. Availability, maintenance, and applicability were assigned a weight factor of three for all three FCGT process conditions.

3.2 Mathematical Formulation - Fine Filter

It should be noted that vendor manufacturing characteristics (available plate and fin sizes) should be considered at this point in order to proceed in an effective manner. As illustrated subsequently in section 4.1, the BPFE and ME were chosen for further review in the present elimination step. Thus, the fine filter was performed using the plate-fin heat exchanger sizing procedure outlined by Shah [2]. This procedure requires specification of all inlet and outlet fluid properties, NTU, and all surface properties being geometrical and thermal-hydraulic. From these inputs the CHEX volume necessary to meet the prescribed heat duty can be found, in which the fine filter elimination process is based.

The High Temperature Recuperator process condition was considered in the present CHEX sizing analysis since it generally requires high effectiveness (>90%). Therefore, the control volume for the mathematical formulation was taken as the counterflow heat exchange portion of Fig. 1. For space considerations, mathematical expressions for certain terms subsequently mentioned but not shown can be found in the nomenclature section. The assumptions made in this analysis are as follows:

1. Control volume is adiabatic
2. Longitudinal conduction is negligible
3. Radiation is negligible
4. Entrance effects need not be considered

With known process conditions, surface geometries, and estimated extended surface efficiencies, initial core mass flux terms are obtained for each fluid side using:

$$G = \sqrt{\frac{2\, g_c\, \Delta p}{\left[\frac{f}{j} \frac{ntu}{\eta_o} \frac{1}{\rho} Pr^{\frac{2}{3}} + 2\left(\frac{1}{\rho_o} - \frac{1}{\rho_i} \right) \right]}} \qquad (1)$$

Core Reynolds numbers are then obtained using the core mass flux terms and other known variables. With known surface geometries and Colburn data, heat transfer coefficients are calculated. Depending on the type of surface geometry, a particular relationship is used to determine the fin efficiency for each exchanger side,

followed by evaluating extended surface efficiencies. An initial overall heat transfer coefficient is then found based on known surface geometries and estimated values:

$$U_1 = \left(\frac{1}{\eta_{o.1}\, h_1} + \frac{1}{\eta_{o.1}\, h_{s.1}} + \frac{\frac{\alpha_1}{\alpha_2}}{\eta_{o.2}\, h_{s.2}} + \frac{\frac{\alpha_1}{\alpha_2}}{\eta_{o.2}\, h_2} \right)^{-1} \quad (2)$$

From this, the total heat transfer area on side 1 of the exchanger can be found. Given this area and known surface properties, the heat transfer area on the opposing side can be found. With the current mass velocity values the minimum free flow area can be found for each fluid side. Next, frontal area is obtained for both fluid sides. Because high effectiveness warrants counterflow orientation, both sides of the exchanger must have the same flow length. Therefore, a single frontal area must be agreed upon. It is recommended that the higher frontal area of the two fluid sides is assumed, Shah [20]. The minimum free flow area is then recalculated. Core flow length can then be obtained using parameters from either fluid side. From the estimated core length the core pressure drop can be estimated on both exchanger sides using:

$$\Delta p = \frac{G^2}{2\, g_c} \left[f \frac{4\, L}{D_h} \frac{1}{\rho} + 2 \left(\frac{1}{\rho_o} - \frac{1}{\rho_i} \right) \right] \quad (3)$$

Wall temperature effects are accounted for in the friction parameter of Eq. (3). Next, the mass flux terms are recalculated using the specified pressure drops and Eq. (3), followed by reevaluation of core Reynolds numbers and all subsequent steps described. For the second and subsequent iterations wall resistance is accounted for so that Eq. (2) becomes:

$$U_1 = \left(\frac{1}{\eta_{o.1}\, h_1} + \frac{1}{\eta_{o.1}\, h_{s.1}} + \frac{a\, A_1}{k_w\, A_w} + \frac{\frac{A_1}{A_2}}{\eta_{o.2}\, h_{s.2}} + \frac{\frac{A_1}{A_2}}{\eta_{o.2}\, h_2} \right)^{-1} \quad (4)$$

The specified and calculated pressure drops are then compared after each iteration, when they are within a desired tolerance the sizing procedure is complete. At this time the exchanger volume can be obtained, followed by thermal density.

3.3 Numerical Procedure

The commercial software Mathcad was used to carry out the fine filter numerical setup. Five surface geometries were considered: plain, louver, strip, wavy, and semicircular. The vast majority of surface information assessed with the code was taken from the extensive work of Kays and London [9]. The code remained identical for each surface analysis with exception to the heat transfer and friction characteristics unique to the given surface, which also bears distinct values for the following surface properties: hydraulic diameter, compactness, fin pitch, plate spacing, fin thickness, fin area per total area, and fin length. Optimization attempts such as using multiple fin layers or cross corrugated wavy patterns were ignored in this comparison. The fin layer for both hot and cold fluid sides was assigned identical. In general, this configuration would not yield a practical CHEX design, but this technique will show the thermal density of a particular surface geometry relative to another, given the present process condition. Eight iterations were carried out for each surface analyzed to obtain a consistent high level of convergence.

3.4 Code Validation

The numerical code was validated by reproducing data published by Wang [21], data of which was originally produced by Concepts Northern Research & Energy Corporation (Concepts NREC). This analysis sized a PCHE for a high temperature (helium) gas turbine recuperator, where multiple core and header dimensions (thus multiple pressure drops) were considered. The present numerical sizing procedure produced core dimensions that correlate well with the published data. Fig. 2 is a plot of PCHE thermal density (including distributor volume) versus header width. Discrepancy between the published and calculated data is also shown on Fig. 2 via the dashed lines, which lie roughly between 1.5 – 2.0 percent error.

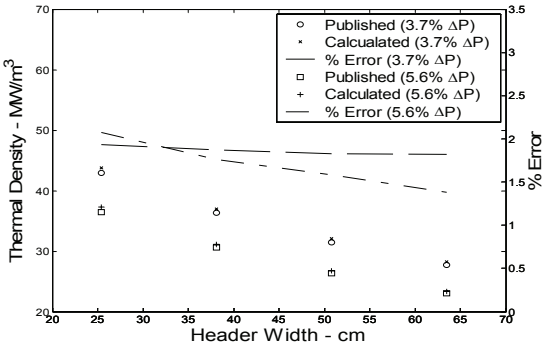

Fig. 2. Code Validation, TD versus Header Width

4. Results and Discussions

The results of the current study are divided into two categories, namely the coarse filter and fine filter. In the former case the heat exchangers are rated by using a set of predetermined design criteria such as compactness, durability, materials cost, etc. In the latter case, the performance of the heat exchangers is evaluated based on the heat transfer and fluid flow characteristics of the given surface of construction.

4.1 Coarse Filter

Each CHEX received a performance rating for each process condition and criterion. The rating scale was defined as a range from one to ten, where ten was the best score. Justification of the ratings given are the following:

1. With exception to the FTE, compactness ratings for all FCGT process conditions were directly proportional to the compactness data in Table 1. FTE ratings were effected by the expected flow orientation.
2. Durability ratings were assigned according to a CHEX's potential to overcome creep and fatigue. The assumptions made were as follows:
   - The BPFE can facilitate non-monolithic clamping as well as diffusion bonding.
   - The FTE can have problems with tube vibrations.
   - Diffusion bonding is used for ME assembly.
   - PSE durability decreases greatly above 650°C.
   - The SE is currently under investigation based in part on its rugged durability.
3. Material Cost ratings were assigned based on the cost of raw material necessary to transfer a unit of heat. The assumptions made were as follows:
   - Required material stock is relatively inversely proportional to compactness.
   - The FTE requires more expensive tube stock and its assembly can result in excessive material waste.
   - The ME requires relatively thick sheet stock for the flow channel etching process.
4. Manufacturability ratings were assigned based on the difficulties posed in fabrication. The assumptions made were as follows:
   - The BPFE and FTE have offsetting characteristics of high parts count and relatively inexpensive fabrication due to a long production history.
   - The ME has relatively expensive fabrication due to a short production history and sophisticated assembly.
   - The PSE and SE require significant investment in preload machinery.
5. Availability ratings were assigned based on market status. The assumptions made were as follows:
   - Competitive markets exist for The BPFE and FTE.
   - Nominal markets exist for the ME, PSE and SE.
6. With exception to the SE, Maintenance ratings were rated inversely proportional to Compactness data.
7. Applicability ratings were assigned based on CHEX attributes pertinent to the FCGT application. The assumptions made were as follows:
   - Ingersoll-Rand designed a BPFE in part for the FCGT application [22].
   - The FTE is better suited for gas-liquid or high pressure ratio applications.
   - The ME holds much promise for increased CHEX performance.
   - Most PSE designs were designed for high pressure ratio engines with operating temperatures at or below 650°C.
   - Low compactness SE designs may not be conducive with the inherently low power density, high temperature fuel cell stacks.

Total scores were tallied for each CHEX type for each process condition by summing the products of corresponding weights and ratings, see Tables 2-4.

Table 2 indicates the two best CHEXs for the Fuel Preheater process condition are the ME and BPFE, having a total score of 173 and 170, respectively. Despite the option of crossflow for the Fuel Preheater, it was not enough to make the FTE competitive. Similarly, the greatest attributes of the PSE and SE are durability, a less important criterion for the FCGT application.

Table 2. Fuel Preheater Selection

	Weight	BPFE	FTE	ME	PSE	SE
Compactness	5	7	3	10	4	2
Durability	4	8	8	10	10	10
Material Cost	3	8	4	9	10	6
Manufacturability	2	8	8	4	7	7
Availability	3	10	10	5	5	5
Maintenance	3	3	9	1	6	10
Applicability	3	10	5	10	7	8
	Total	**170**	**147**	**173**	**158**	**151**

Table 3 indicates the two best rated CHEXs for the Low Temperature Recuperator are the ME and BPFE, having a total score of 183 and 178, respectively. The FTE was rated even lower for this process condition given that high effectiveness is expected. The increase in durability requirements shortened the margin between the BPFE and the PSE, but not enough to offset emphasis on compactness.

Table 3. Low Temperature Recuperator

	Weight	BPFE	FTE	ME	PSE	SE
Compactness	5	7	1	10	4	2
Durability	5	8	8	10	10	10
Material Cost	3	8	4	9	10	6
Manufacturability	2	8	8	4	7	7
Availability	3	10	10	5	5	5
Maintenance	3	3	9	1	6	10
Applicability	3	10	5	10	7	8
	Total	**178**	**145**	**183**	**168**	**161**

Table 4 indicates the two best rated CHEXs for the High Temperature Recuperator process condition are the ME and BPFE, having a total score of 204 and 201, respectively. The margin at which the ME and BPFE are rated over the other CHEXs for this process condition is much greater than when stainless steel is the material of construction. This implies that the compactness criterion

Table 4. High Temperature Recuperator

	Weight	BPFE	FTE	ME	PSE	SE
Compactness	5	7	1	10	4	2
Durability	5	8	8	10	5	10
Material Cost	5	7	1	8	10	5
Manufacturability	4	8	8	4	7	7
Availability	3	10	10	5	5	5
Maintenance	3	3	9	1	6	10
Applicability	3	10	5	10	7	8
	Total	**201**	**154**	**204**	**177**	**182**

has a compounding effect when expensive alloys are used. In summary, the two CHEX types to be analyzed further in the fine filter selection process are the BPFE and ME.

4.2 Fine Filter

The thermal density of the counterflow CHEXs constructed out of the various fin geometries mentioned previously were plotted against their respective compactness values as shown in Figs. 3-6. It was taken from Figs. 3-5 that thermal density exhibits a relatively linear relationship with compactness. To determine the strength of this relationship, a squared correlation coefficient (r^2) was evaluated for each curve fit. The plain fin curve fit exhibited an r^2 value of 0.971, the louver fin curve fit a value of 0.904, and the strip fin curve fit a value of 0.872. It was assumed that these relationships could be extrapolated for a reasonable range of compactness values; hence, Fig. 6 presents a comparison of the general surface geometry performance correlations. There was enough data in the literature to obtain reasonable curve fits for the plain, louver, and strip fin geometries. However, this work is currently in progress and a sufficient amount of data for the wavy and semicircular geometries is yet to be obtained. Therefore, Fig. 6 has individual wavy and semicircular data points plotted with the plain, louver, and strip fin representations.

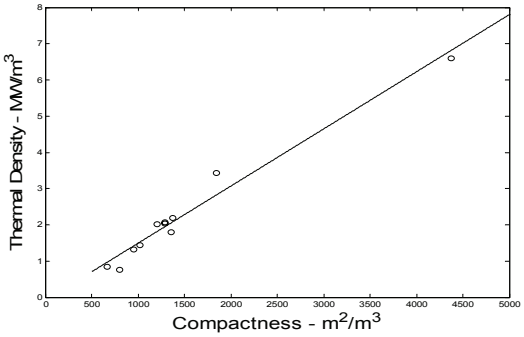

Fig. 3. Plain Fin TD versus β

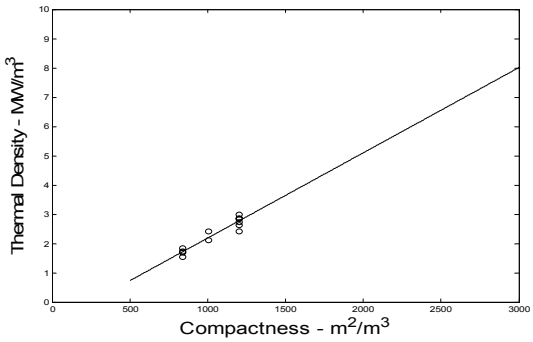

Fig. 4. Louver Fin TD versus β

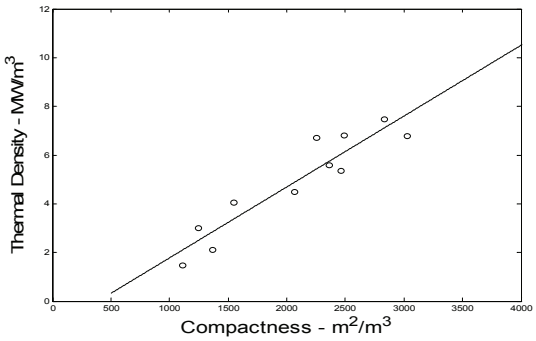

Fig. 5. Strip Fin TD versus β

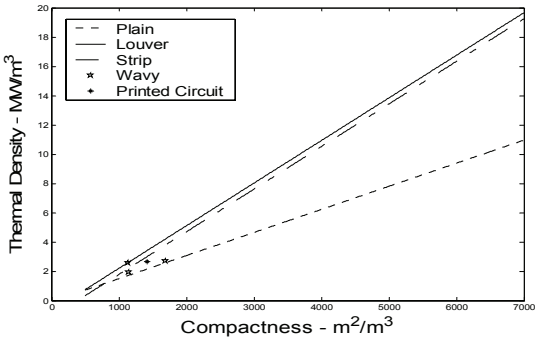

Fig. 6. Fin Comparison, TD versus β

Figs. 3-6 demonstrate the trivial concept that CHEX thermal density increases with increased compactness. More importantly, the results indicate which surface geometry will yield the highest thermal density for a given level of compactness. This is the basis for the fine filter elimination procedure. Fig. 6 indicates that the louver and strip fin geometries are very competitive, and that both of these surfaces clearly yield higher thermal density than the plain fin geometry for increased compactness. This figure also implies that the louver fin is superior to the strip fin for the present process condition.

It was assumed that the wavy and semicircular geometries also exhibit a linear relationship between thermal density and compactness, having a slope commensurate to that of the louver and strip fin geometry. If this assumption remains valid, then even the small amount of data in Fig. 6 implies that the louver fin generally yields the highest thermal density, or smallest core volume for a prescribed heat duty, of all surface geometries considered for the present process condition.

In addition to the numerical results, the louver fin geometry has other desirable characteristics. The louver fin is formed by a relatively inexpensive rolling process, instead of by a reciprocating press necessary for the strip fin, which makes it much cheaper to produce, Hesselgreaves [14]. Therefore, the louver fin surface geometry is currently found to be most compatible with hybrid FCGT process conditions.

5. Conclusion

Based on the literature review and coarse filter performed for this work, plate-fin and microchannel CHEXs were determined to have the most potential to meet the requirements placed forth by hybrid FCGT systems. To continue performance improvements in recuperator design, ability to increase cell compactness must remain. The plate-fin and microchannel have an advantage over competing CHEXs with respect to achieving high compactness.

Durability has been a recurring issue for gas turbine recuperators. However, it was concluded that both the plate-fin and microchannel designs have more than sufficient potential to successfully endure the structural demands expected from the present application. It was concluded that the primary concerns for FCGT system recuperators lie within their size and cost, especially for high temperature (>650°C) process conditions. Commercial availability will also play a crucial role for high temperature operation. If market conditions permit choice, then the results from this analysis indicate that a plate-fin heat exchanger constructed with a compact louver fin geometry is the most promising configuration for the hybrid FCGT process conditions.

Acknowledgements

This work was supported by US Department of Energy under a subcontract from FuelCell Energy, Contract No. 18297

References

[1] E. Utriainen, B. Sunden, Recuperators and regenerators in gas turbine systems, Investigation of Some Heat Transfer Surfaces for Gas Turbine Recuperators, Lund, Sweden, 2001.

[2] R. K. Shah, Compact Heat Exchangers, The CRC Handbook of Thermal Engineering, edited by Kreith, F., CRC Press, New York, 2000.

[3] J. Oswald, Personal Communication, Rolls Royce, 2003.

[4] J. Kesseli, T. Wolf, J. Nash, S. Freedman, Micro, industrial and advanced gas turbines employing recuperators, Proceedings of ASME Turbo Expo, Atlanta, Georgia, USA, 2003.

[5] A. P. Fraas, and M. Ozisik, Heat Exchanger Design, John Wiley & Sons, Inc., New York, 1965.

[6] S. G. Kandlikar, W. J. Grande, Evolution of Microchannel Flow Passages – Thermohydraulic Performance and Fabrication Technology, (2002) [Online]http://www.rit.edu/~taleme/77_imece2002_32043.pdf.

[7] G. Reid, A Numerical Investigation of Microchannel Heat Transfer, Masters Thesis, University of Seattle, Washington, 1998.

[8] Solar Turbines Inc., A Caterpillar Company, Recuperators (Brochure), Recuperator Development, Dept. 221, T-5, P.O. Box 85376, San Diego, CA. 92186-5376, 1995.

[9] W. M. Kays, A. L. London, Compact Heat Exchangers, 3rd Edition, McGraw-Hill Book Company, New York, 1984.

[10] A. Kraus, A. Aziz, J. Welty, Extended Surface Heat Transfer, John Wiley & Sons, Inc., New York, 2001.

[11] R. K. Shah, R. L. Webb, Compact and Enhanced Heat Exchangers, Heat Exchangers – Theory and Practice, edited by Taborek, J., Hewitt, G. F., and Afgan, N., Hemisphere Publishing Corporation, 1983.

[12] R. K. Shah, Classification of Heat Exchangers, Heat Exchangers – Thermal-Hydraulic Fundamentals and Design, edited by Kakac, S., Bergles, A., and Mayinger, F., Hemisphere Publishing Corporation, 1981.

[13] V. Wadekar, Compact Heat Exchangers, American Institute of Chemical Engineers. (2003) [Online] www.aiche.org/cep/.

[14] J. E. Hesselgreaves, Compact Heat Exchangers – Selection, Design, and Operation, Pergamon, New York, 2001.

[15] E. Utriainen, B. Sunden, Numerical analysis of a primary surface trapezoidal cross wavy duct, Investigation of Some Heat Transfer Surfaces for Gas Turbine Recuperators, Lund, Sweden, 2001.

[16] C. McDonald, Low-cost primary surface recuperator concept for microturbines, Applied Thermal Engineering, 20, 2000, pp. 471 - 479.

[17] N. Bacquet, The Spiral Heat Exchanger Concept and Manufacturing Technique, Compact Heat Exchangers and Enhancement Technology for the Process Industries, edited by Shah, R., Deakin, A., Honda, H., and Rudy, T., Begell House, Inc., 2001.

[18] B. Pint, R. Swindeman, P. Tortorelli, K. More, Materials Selection for High Temperature Metallic Recuperators for Improved Efficiency Microturbines, Microturbine Materials Program, Oak Ridge National Laboratory, 1999

[19] A. Deakin, P. Hills, T. Johnston, C. Adderley, R. Owen, T. Macdonald, E. Gregory, B. Lamb, N. Patel, L. Haseler, Guide to Compact Heat Exchangers, Energy Efficiency Enquiries Bureau, Oxfordshire, 1999.

[20] R. K. Shah, Plate-Fin and Tube-Fin Heat Exchanger Design Procedures, Heat Transfer Equipment Design, edited by Shah, R. K., Subbarao, E. C., and Mashelkar, R. A., Hemisphere Publishing Corporation, 1988.

[21] C. Wang, Design, Analysis and Optimization of the Power Conversion System for the Modular Pebble Bed Reactor System, Doctoral Thesis, Massachusetts Institute of Technology, Massachusetts, 2003.

[22] Ingersoll-Rand, Gas-Turbine Engine Manufacturers Consider the PowerWorks™ Recuperator for Long-Term Survival, Better Efficiency, and Low Life-Cycle Cost, NREC News, Volume 11, Issue 2, 1997.

Strojniški vestnik - Journal of Mechanical Engineering 51(2005)7-8, 426-430
UDK - UDC 536.2
Izvirni znanstveni članek - Original scientific paper (1.01)

Investigations of combustion process in stove fired on biomass

Dragoslava D. Stojiljković[1], Vladimir V. Jovanović[1], Milan R. Radovanović[1], Nebojša G. Manić[1], Ivo R. Radulović[1], Slobodan V. Perišić[2]

[1]Faculty of Mechanical Engineering, University of Belgrade, 27. marta 80, Belgrade, Serbia, Serbia and Montenegro, dstojiljkovic@mas.bg.ac.yu
[2]Milan Blagojević a.d. Smederevo, Đure Strugara 20, Smederevo, Serbia, Serbia and Montenegro

Abstract

The aim of the investigation was to make some reconstructions on the existing stove used for cooking and baking and to obtain the combined cooker–boiler which will fulfill the demands of European standard EN 12815. Implementation of modern scientific achievements in the field of combustion on stoves and furnaces fired on biomass was used. During the investigations four various constructions were made with different fresh air inlet and secondary air supply with the intention to obtain more complete combustion with increased efficiency and reduced CO emission. Three different fuels were used: firewood, coal, and wood briquette. A numerous parameters were measured: fuel weight changes during the combustion process, temperature of inlet and outlet water, flue gas composition (O_2, CO, SO_2, CO_2, NO_x), flue gas temperature, ash quantity ect. The result of the investigations is the stove with the efficiency of more than 75% - boiler Class 1 (according EN 12815) and CO emission of about 1 %v/v. The results obtained during the measurements were used as parameters for modeling of combustion process.

Introduction

Basic aim of the investigations was development of original domestic appliance fired on solid fuel that could be simultaneously used for cooking and heating the water for central heating system and heating the space in the room where it is installed. Original design of combined cooker and water heater – MBS 90KV was used as a base for further improvements. During the realization of the investigations several prototypes of combined cooker-boiler were tested and, based on the obtained results, appropriate reconstructions were made. Afterwards, the modified constructions characteristics (thermal and environmental) were tested.

Tests of the combined cooker-boiler MBS 90KV

The tests were based on definition of test program and choice of different fuels. Definition of listed parameters was necessary to provide the same test conditions for different constructions of combined cooker-boiler.

Test procedure

The tests of combined cooker-boiler MBS 90KV were made according to the demands of regulation EN 12815. Typical test cycle for lower grill position is foreseen by this standard, that comprise:

- startup and pre-test for reaching the steady state;
- minimum 1 hour testing for the nominal heat power when the firewood is used as a fuel, and minimum 3 hours when the coal or other fossil fuel is used for determination:
  a. total efficiency
  b. heat output.
- time required to reach the steady state.

The test rig was designed and constructed according to the demands of regulation EN 12815 (Figure 1).

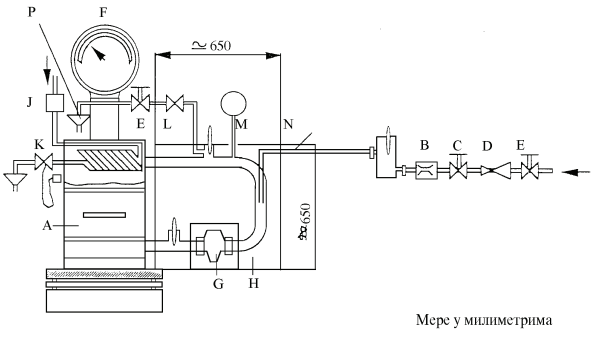

Figure 1: Test rig used for investigations

A-heating appliance, B-flowmeter, C-throttling valve, D-valve for pressure reduction, E-stop valve, F-weighing balance, G-circulating pump, H-steel reservoir, isolated with 120 mm thick mineral wool insulation or with cork

peaces, J-safety device, K-thermal safety overflow device, L-overpressure valve for pressurized systems, M-expansion vessel, N-flexibile junction, P-outflow
The combined cooker-boiler prepared for the test is shown on Figure 2.

Figure 2: Combined cooker-boiler MBS 90KV on the test rig

Test fuels

Three different fuels were used for tests:
- brown coal "Banovići" (letter "u" in the test marking),
- firewood - common beech (no letter in the test marking),
- briquette made of wood residues from furniture production (letter "b" in the test marking).

Proximate and ultimate analysis of all test fuels were made according to the regulation JUS B.H0.021.

Constructions of combined cooker-boiler MBS 90KV

During the investigations different constructions of combined cooker-boiler MBS 90KV were tested:

CONSTRUCTION 0 – Basic construction made by modification of classic solid fuel cooker MBS 90. Modification was primarily made on the firebox, which was increased in depth providing the space for insertion of heat exchanger in the upper zone. Other construction elements of the original cooker were not altered.
CONSTRUCTION 1 – The firebox grill was lowered related to the basic prototype. Air inlet from the front side was closed. Position and dimensions of the ashtray are such that in the working position it is completely blocking rear side air inlet (which is the only air inlet for both primary and secondary air). In this way the airflow is allowed only along the sidewalls of the ashtray providing the primary air to the grill. This construction is marked as Model 0.
CONSTRUCTION 2 – Ashtray height was reduced for 15 and 25 mm respectively, to allow air entrance in the air plenum beneath the firebox. The first modification was named Model 2 and the second one Model 1.
CONSTRUCTION 3 – The secondary air supply was modified in a such a way that the direct flow upwards was blocked and redirected under the firebox grill. This modification was named Model 1a.
CONSTRUCTION 4 – Firebox grill was moved backwards, to the rear wall, and the secondary air grill was placed on the front firebox wall instead on the back. This modification was named Model 1b.

Test results

Results obtained during the experiments were classified in 4 groups:
- fuel analysis,
- thermal characteristics,
- functional characteristics and
- environmental characteristics.

Fuel analysis

Analysis of all test fuels were made according to the regulation JUS B.H0.021. Proximate analysis was made in Fuel & Combustion Lab (University of Belgrade, Faculty of Mechanical Engineering) and ultimate analysis in the Institute for chemistry, technology and metallurgy – Center for chemistry. The results of proximate and ultimate analysis (only for as received mass) for all test fuels are given in the Table 1.

Table 1: Proximate and ultimate analysis of test fuels

	Fire-wood	Coal	Briqu-ette
PROXIMATE ANALYSIS			
Total moisture (%m/m)	8,23	12,42	9,76
Combustibles (%m/m)	91,00	78,05	89,87
Ash (%m/m)	0,77	9,52	0,37
Volatiles (%m/m)	75,07	38,93	76,06
Fixed carbon (%m/m)	15,94	39,12	13,80
High heating value (kJ/kg)	18031	21143	17420
Low heating value (kJ/kg)	16624	19724	15782
ULTIMATE ANALYSIS			
Carbon (%m/m)	43,43	56,47	46,05
Hydrogen (%m/m)	5,34	4,73	6,19
Nitrogen (%m/m)	0,45	1,35	0,67
Sulphur (%m/m)	-	1,40	0,21
Oxygen$^{\text{as the difference}}$ (%m/m)	41,79	14,10	36,73

Thermal characteristics

Thermal characteristics that were determined during the tests were:
- nominal total heat output;
- heat output to the central heating water;
- heat output to the ambient;
- total efficiency of the combined cooker-boiler.

Regulation EN 12815 doesn't have strict limits for the nominal heat output and ratio of heat output to the central heating system and ambient. However, total efficiency is strictly defined and, depending on it, all appliances are classified in 4 classes given in Table 2.

Table 2: Classes of appliances

Appliance class	Total efficiency (%)
Class 1	more than 75
Class 2	from 70 to 75
Class 3	from 65 to 70
Class 4	from 60 to 65

Nominal heat output, heat output to the water for central heating system, heat output to the ambient air and total efficiency are given in Table 3. Experimental results from the tests of final model (adopted for production) for different fuel types are given on Figure 3 (nominal heat output) and Figure 4 (total efficiency).

Based on the classification given in Table 2, combined cooker-boiler MBS 90KV is an appliance of Class 1 (efficiency grater than 75 %).

Table 3: Nominal heat output and efficiency for different models

Test	Nominal heat output (kW)	Heat output to the water (kW)	Heat output to the ambient (kW)	Total efficiency (%)
Firewood				
0	20,01	5,85	14,16	74,83
1	22,05	7,50	14,55	74,60
2	19,64	7,10	12,54	73,58
1a05	18,09	5,40	12,69	79,23
1a10	20,50	6,14	14,36	74,58
1b05	17,84	6,92	10,92	74,69
1b10	20,39	6,75	13,64	76,12
1b15	22,17	7,36	14,81	70,01
Coal				
1bu10	16,13	5,87	10,26	80,32
Briquette				
1bb05	15,70	5,79	9,91	80,85
1bb10	18,38	6,13	12,25	74,06

Note: first digit and first letter are model mark, second letter is mark of test fuel used (no letter – firewood, u – coal and b – briquette), last two digits are mark of draught in flue gas duct.

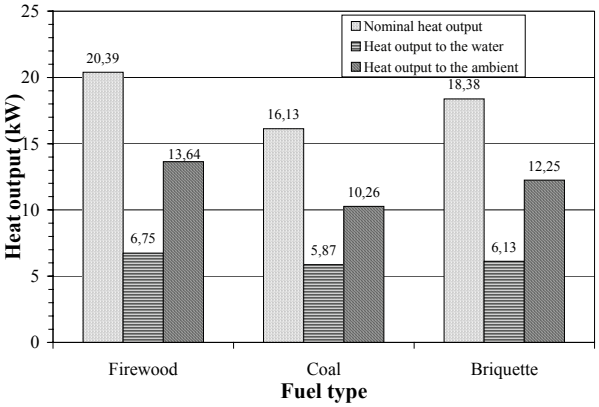

Figure 2: Heat outputs for all test fuels (final model)

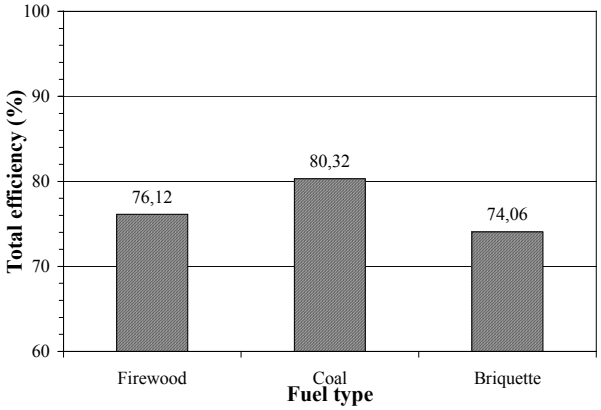

Figure 3: Total efficiency for different fuel types (final model)

Functional characteristics

Functional characteristics are defining heating of the water for central heating system. Determination of these characteristics comprised measurement of:

- water temperature at the outlet of the boiler,
- temperature difference between outlet and inlet.

Values for these temperatures defined in regulation EN 12815 are given in Table 4. Time period when those values are satisfied was just recorded as requested by this regulation.

Table 4: Requested values for temperatures

Requested water temperature at outlet (°C)	Requested temperature difference between outlet and inlet (°C)
80±5	from 10 to 25

Measurement results for different models and all three fuels are given in Table 5.

Table 5 Measurement results for the functional characteristics.

Test	Outlet water temperature (°C)	Temperature difference (°C)
Firewood		
0	78,6	13,3
1	88,2	16,9
2	83,5	14,6
1a05	76,3	13,1
1a10	71,9	11,5
1b05	80,5	14,5
1b10	78,0	14,4
1b15	87,2	15,7
Coal		
1bu10	78,7	12,4
Briquette		
1bb05	75,3	12,2
1bb10	76,3	13,1

Comparative values of outlet water temperature and temperature difference for all three test fuels are given on Figure 5.

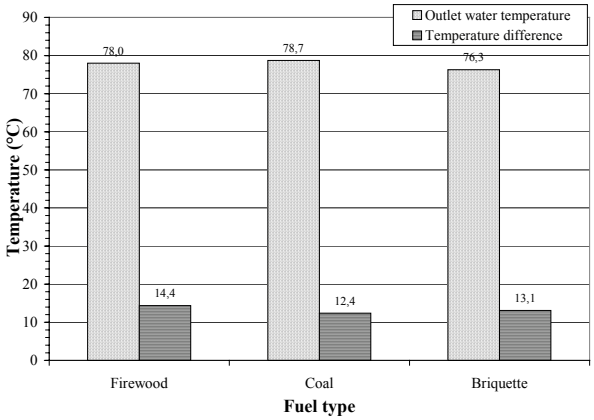

Figure 5: Outlet water temperature and temperature difference for different fuel types (final model)

Environmental characteristics

Under environmental characteristics only carbon monoxide (CO) emission level is defined. Based on the value of CO emission all appliances are, according to the EN 12815 classified in three classes given in Table 6.

Table 6: Classes of appliances based on CO emission

Appliance class	Maximum permitted CO content, calculated at 13 %v/v O_2 content in flue gas (%v/v)
Class 1	less than 0,3
Class 2	from 0,3 to 0,8
Class 3	from 0,8 to 1,0

Results of the CO emission measurements are given in Table 7, and comparative CO emissions (calculated on 13 %v/v O_2 content in flue gas) for all test fuels are given on Figure 6. The adopted final version was the best, fired on coal. It is Class 2 appliance based on classification given in Table 6 but it was slightly above the limit for the Class 1. Firing this appliance on firewood and briquettes from wood didn't reach even the limit of Class 3. This will be the principal target for further development of this appliance.

Table 7: Results of CO emission calculated at 13 %v/v O_2 content in flue gas

Test	CO emission (%v/v)
Firewood	
0	1,78
1	1,93
2	2,27
1a05	1,85
1a10	1,58
1b05	1,35
1b10	1,24
1b15	2,14
Coal	
1bu10	0,31
Briquette	
1bb05	1,71
1bb10	1,74

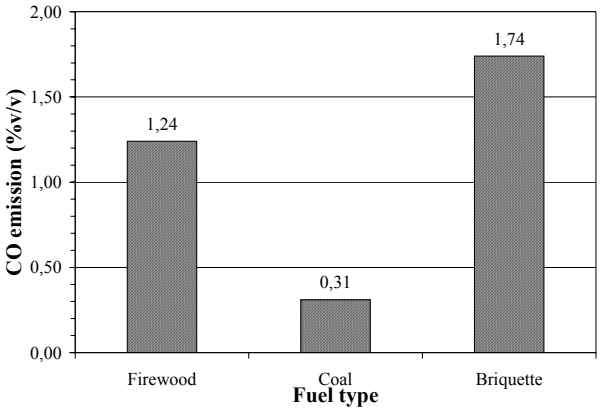

Figure 6: CO emission calculated at 13 %v/v O_2 content in flue gas for different fuel types (final model)

Conclusions

Heating appliances fired on solid fuel could be a part of past but definitely a part of the future, especially having on mind that the biomass is renewable energy source with zero CO_2 balance. The importance of this type of heating appliances is emphasized by the adoption of the latest European regulation in this field EN 12815. This regulation has brought clear test procedures and strict limits for heating appliances fired on solid fuel.
Combined cooker-boiler MBS 90KV produced by Milan Blagojevic a.d. Smederevo is one of the newest products on the Serbian market. The results from the tests made completely according to the demands of EN 12815 during its development are presented in this paper. Based on these results it can be concluded that:

- total efficiency required by Class 1 was achieved (more than 75 %) when fired on firewood and coal while slightly below this limit (Class 2) when fired on briquette made of wood residues from furniture production;
- nominal heat output of 16 kW was reached firing on coal, and even 20 kW fired on firewood;
- heat output to the water for central heating system was about 6 kW for all test fuels;
- CO emission of a Class 2 appliance was reached firing on coal (0,31 %v/v);
- CO emission was above the highest permitted limit when fired on biomass (firewood and briquette both);
- further improvements in biomass combustion (reconstruction of firebox) are needed to reduce the CO emission.

Acknowledgement

The investigations described in this paper are part of a project financed by Ministry of science, technology and development of Republic of Serbia. The authors hereby express their gratitude for financial support.

References

[1] ***, EN 12815 Residential Cookers fired by solid fuel – Requirements and test methods, Österreihsches Normuginstitut, Wien, 2002.
[2] D. Stojiljković, V. Jovanović, M. Radovanović, N. Manić, I. Radulović, Tests of heating appliance MBS 90KV Model 0, Report No. 12-29-12.01/2002, Faculty of Mechanical engineering, Belgrade, 2002.
[3] D. Stojiljković, V. Jovanović, M. Radovanović, N. Manić, I. Radulović, Tests of heating appliance MBS 90KV Model 1 and Model 2, Report No. 12-28-12.01/2002, Faculty of Mechanical engineering, Belgrade, 2002.
[4] D. Stojiljković, V. Jovanović, M. Radovanović, N. Manić, I. Radulović, Tests of heating appliance MBS 90KV Model 1bu, Report No. 12-54-12.01/2002, Faculty of Mechanical engineering, Belgrade, 2002.
[5] D. Stojiljković, V. Jovanović, M. Radovanović, N. Manić, I. Radulović, Tests of heating appliance MBS 90KV Model 1bb, Report No. 12-08-12.01/2003, Faculty of Mechanical engineering, Belgrade, 2003.
[6] D. Stojiljković, V. Jovanović, M. Radovanović, N. Manić, I. Radulović, Tests of heating appliance MBS 90KV Model 1b, Report No. 12-07-12.01/2003, Faculty of Mechanical engineering, Belgrade, 2003.

Strojniški vestnik - Journal of Mechanical Engineering 51(2005)7-8, 431-435
UDK - UDC 536.2
Izvirni znanstveni članek - Original scientific paper (1.01)

Modelling of Vertical Wall Influence on the Single Bubble Motion

Dariusz Mikielewicz, Jan Wajs

Department of Heat Technology, Gdansk University of Technology,
Faculty of Mechanical Engineering, Narutowicza 11/12, 80-952 Gdansk, Poland,
tel. +48 58 3472254; fax.+48 58 3472816; e-mail: dmikiele@pg.gda.pl

Abstract

In this paper authors would like to present the results of experimental investigations and modelling of repulsive force acting on the rigid sphere (representing the bubble) in its flow along the vertical wall. It has been found that such force has a periodical character and depends on the flow Reynolds number. Comparison between measured and calculated values has been made, which gives satisfactory agreement.

1. Introduction

From the point of view of thermodynamics and heat transfer the two-phase flows introduce into the processes an important feature that they intensify the heat transfer. The boiling process, particularly at a small content of vapour phase, enhances heat transfer in channels which is depicted in a significantly higher, compared to single phase flows, heat transfer coefficient. In the era of reduction of technical appliances sizes the idea of implementation of two-phase flows in the systems of semiconductor laser cooling, or microprocessors in electronics seem inevitable. Hence investigations of boiling in small diameter channels or microchannels as well as extended microsurfaces are conducted in several research centers in the world [1, 2]. Similar investigations have also commenced at the Heat Technology Department at Gdansk University of Technology. Also the two-phase flows without bubble generation, i.e. flows where bubbles coexists within liquid fins numerous practical applications. Here also the mathematical modeling presents serious shortcomings.

Issues connected with the presence of a vertical wall and bubble movement around it are important in two-phase flows analysis. Additionally, there is no sufficient experimental data on the flow resistance of gas bubbles near vertical walls as well as mathematical description of that problem is incomplete. According to experimental data [3], characteristic feature of two-phase flow is wall peaking and core peaking (Fig. 1), which means bubbles grouping near the wall or core of the flow, respectively. Such phenomenon still strikes difficulties and there is no unanimous explanation to that fact. Mikielewicz [4], for example, postulated that some additional angular velocity causes that phenomenon. He devised a model, which allows to determine the flow with void fraction distribution. Unfortunately, there is no experimental data confirming the details of that hypothesis apart from integral characteristics of the flow, i.e. velocity profile and void fraction distribution. Analysis of Eq. (1), a typical bubble diffusion equation, shows that in case of presence of void fraction maximum, α, the sign change of its derivative $\mathbf{d\alpha/dx}$ is expected. The diffusion equation of bubbles in the transverse direction, mentioned earlier, yields:

$$\alpha \vartheta_b = -D_b \frac{d\alpha}{dx} \tag{1}$$

where ϑ_b is transverse bubble velocity and D_b – bubble diffusion coefficient. In the case when the void fraction derivative changes its sign there is only one other remaining quantity, which can also alter its sign. That is the transverse velocity ϑ_b. It is associated with the change of the direction of action of the force acting on the bubble. Concluding, when the void fraction gradient is positive then the transverse velocity is directed to the wall. When the gradient is negative the transverse velocity is aimed to the core. The model due to Mikielewicz allows to model, at least qualitatively, such behaviour of the bubble. The model requires however some tuning to transverse velocity and flow around the groups of bubbles, where experimental data is yet available in the literature. One of other suggestions was that the presence of the wall influences the bubble

Nomenclature

α – angle, void fraction
A – projection area
c_D – drag coefficient
D_b – bubble diffusion coefficient
F_D – drag force
$\bar{F}$ – repulsive force
h – maximum deviation
m – mass
N – string force
ρ – density
Re – Reynolds number
t – time
t_c – time of maximum deflection
ϑ – transverse velocity
x – Cartesian coordinate
x_0 – initial distance between sphere and wall

motion. More details about hypothesis explaining that phenomenon have been presented in [4].

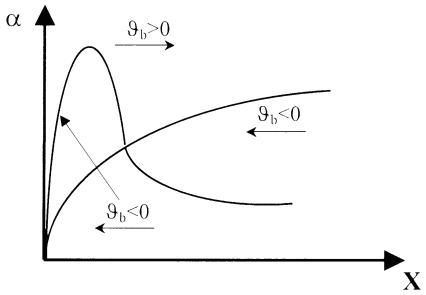

Fig. 1. A schematic depicting wall peaking and core peaking phenomenon

It is also expected, that the presence of the wall has a strong influence on the flow around a bubble, which becomes asymmetric. It leads to changes in drag force and appearance of transverse components of velocity. The aim of this work is investigation focused on accurate, experimental verification of forces effect on bubble flowing along the wall. The bubble is represented by a solid sphere suspended on a thin string. It is acknowledged that bubbles in such motion exhibit some specific patterns of motion, however, the authors are convinced that the model of a bubble considered in the present approach captures at least a qualitative behaviour of a bubble in the flow and will allow to determine the transverse force acting on the bubble.

2. Experimental rig

In order to measure the forces acting on the bubble an experimental rig, shown in Fig. 2, was designed and assembled at the Heat Technology Department of the Gdansk University of Technology. The rig consists of: 1 – vessel, 2 – sphere (the bubble model), 3 – steel string, 4 – velocity adaptor, 5 – frame, 6 – wheel, 7 – tensometric beam, 8 – mass, 9 – digital camera, 10– linear scale attached to vessel wall, 11– data acquisition set, 12– drain valve. Experimental rig is positioned in air-conditioned room with temperature 20 ± 1 °C. The vessel (0,5 x 0,5 x 1m), containing distilled water, is made of Plexiglas 8 mm thick. It is assumed that water properties are: density ρ = 998,2 kg/m^3, viscosity ν = 1,006 x 10^{-6} m^2/s, surface tension σ = 726,9 x 10^{-4} N/m, i.e. they correspond to temperature 20 °C. The wheel with negligible mass was located on stiff frame. The small mass of the wheel was obtained by selection of a special aluminium hoop with thin spokes and a light nave. The wheel is placed in two ball bearings with dimensions ∅6/10 mm, which results in insignificant movement resistance. The aluminium wheel was cut with 130 000 notches in order to determine the acceleration of the wheel and its angular velocity. The vessel has positioning system which gives the opportunity for measurements with varying distance from the wall. The sphere used in experiment is a physical model of gas bubble moving in vertical direction along the wall. The sphere movement was forced by the mass **m** falling down due to gravity on the opposite side of the wheel. The drag force was measured by means of tensometric force adapters of SCAIME type, measuring the tension in a steel string with the diameter of 0.35 mm. Tension on the perimeter of string is not taken into account, because of water environment (in author's opinion the viscous effect is negligible). The adapters were placed in the wheel bearing support. The sphere movement was also recorded by digital camera enabling taking 25 frames per second. This enables to observe a wall effect, it means deviation of the sphere trajectory.

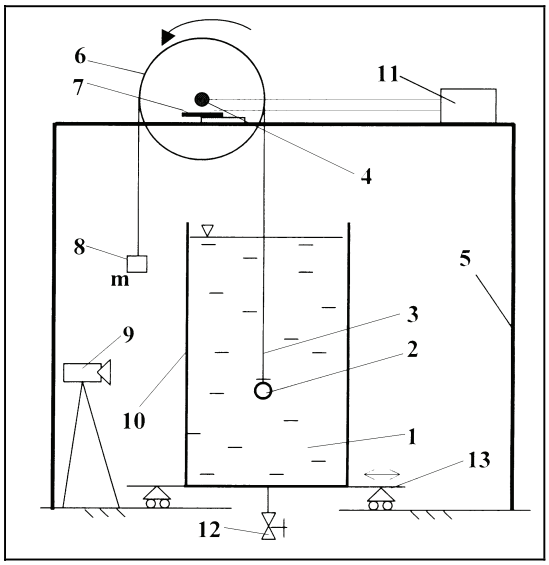

Fig. 2. Experimental rig

3. Model of wall forces acting on single bubble

Observations during experiments showed, that the sphere trajectory (the bubble model) depends on the bubble initial position, that is the distance in x direction (Fig. 3). If the sphere, in the initial time, is located very close to the wall, then the trajectory has significant deviation during the rising (Fig. 3). It is an evidence of repelling force from the wall. This effect lessens with increasing distance between the sphere and the wall and finally disappears.

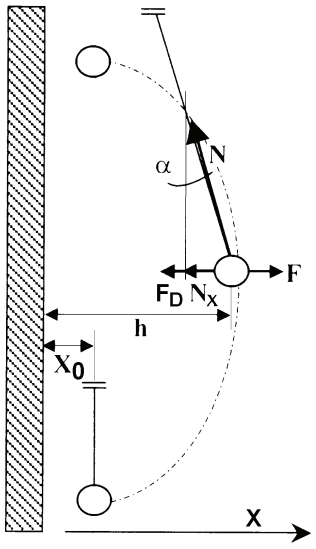

Fig. 3. A part of the sphere trajectory

The analysis range is placed between the moment when the repulsive force arises and when the repulsive force reaches its minimum. The drag force (F_D) and the horizontal component of the string force (N_x) is compensated by the repulsion force at each location. The largest repulsion force acts near the wall, $\bar{F}$ and our aim was to correlate it.

There is a possibility to determine values of $\bar{F}$ experimentally. The sphere motion equation in the direction perpendicular to the wall can be expressed in the form:

$$m\frac{d\vartheta}{dt} = \bar{F}(x) - N_X(t) - F_D(t) \tag{2}$$

$$\text{where} \quad \frac{d\vartheta}{dt} = \frac{d^2x}{dt^2} \quad \text{and} \quad N_X(t) = N(t)\cdot\sin\alpha(t), \tag{3}$$

The drag form can be expressed as:

$$F_D = c_D \cdot \rho \cdot \frac{\vartheta^2}{2} \cdot A \tag{4}$$

where ϑ is the lateral velocity, ρ - liquid density, A – projection area of a sphere. Drag coefficient (c_D) depends on the Reynolds number and in the range 0.5<Re<800 should be calculated from the expression:

$$c_D = \frac{24}{Re}\left(1 + 0.15\cdot Re^{0.687}\right) \tag{5}$$

The Eq. (2) should be solved, with different initial sphere and wall distance values to predict $\bar{F}$ values. In the first approximation it has been assumed that both forces $\bar{F}$ and N are independent of time and the angle α is a mean value of deviation from the vertical direction.

First integration of Eq. (2) leads to:

$$m\frac{dx}{dt} = (\bar{F} - N\sin\alpha - F_D)\,t + C_1 \tag{6}$$

and another integration yields:

$$mx = (\bar{F} - N\sin\alpha - F_D)\frac{t^2}{2} + C_1 t + C_2 \tag{7}$$

Constants C_1 and C_2 in equations (6) and (7) are estimated from the boundary conditions:

$$t = 0 \;\Rightarrow\; x = x_0 \tag{8}$$

$$t = t_c \;\Rightarrow\; x = h \tag{9}$$

Thus constants in Eq. (6) and Eq. (7) are:

$$C_1 = m\frac{h - x_0}{t_C} - (\bar{F} - N\sin\alpha - F_D)\frac{t_C}{2} \tag{10}$$

$$C_2 = m\,x_0 \tag{11}$$

Taking to account constants (10) and (11) Eq. (7) can be expressed:

$$m\left(x - \frac{h - x_0}{t_c}t - x_0\right) = (\bar{F} - N\sin\alpha - F_D)\left(\frac{t - t_C}{2}\right)t \tag{12}$$

The quantities appearing in Eq. (12), i.e. displacement **x**, force **N(t)**, maximum sphere trajectory deviation **h**, and time required to reach the maximum deflection $\mathbf{t_c}$ and finally angle $\boldsymbol{\alpha}$ between the steel string and vertical direction are measured directly in the experimental rig. The sphere mass **m** is also known. The force $\bar{F}$, related to initial sphere and wall position, is the one and only unknown value.

4. Experimental verification of the theoretical model

The sphere movement trajectory can be predicted by solving Eq. (12). The experiments where carried out with two spheres of different diameters: D = 40 mm and D = 30 mm. The experimental results showing the trajectories of spheres are presented in Fig. 4 and Fig. 5. In the presented cases the mass causing the sphere movement is m=2g. The experiments where also carried out with other loads, i.e. m=5g and m=10g. The repulsive force decreases when the initial distance from the wall increases, according to a schematic presented in Fig. 6. Experiments show that the effect connected with presence of the wall disappears when the initial distance between

the sphere and the wall exceeds about 1,5 sphere diameter in the case of excitation of m=2g. The comparison of proposed model predictions with experimental data are shown in Fig. 4. In Fig. 7 and Fig. 8 presented are mean values of the repelling force. Value of the force was determined for varying values of **x** and **t** in Eq. (12). Such force has an exponential character, however authors were yet unable to devise a general correlation describing such repelling force. Satisfactory consistency between measurements and the model has been obtained.

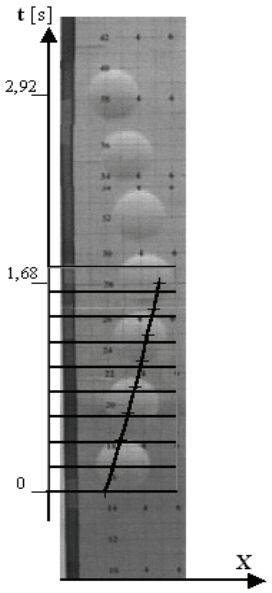

Fig. 4. Comparison between experimental and calculated values of repelling force (D=40mm, m=2g, x_0=8mm)

Fig. 5. Photograph of the sphere trajectory (D=30mm, m=2g, x_0=1mm)

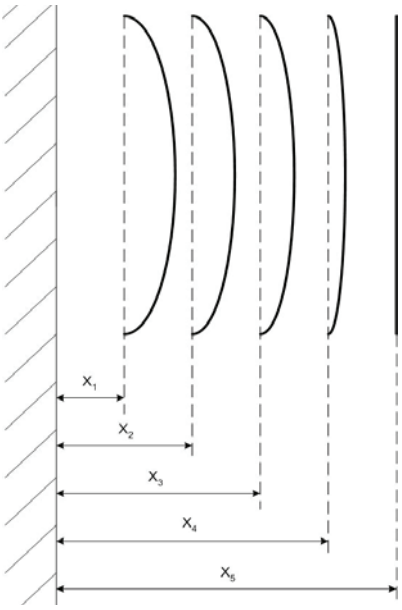

Fig. 6. Sphere trajectories for different initial distance between sphere and wall.

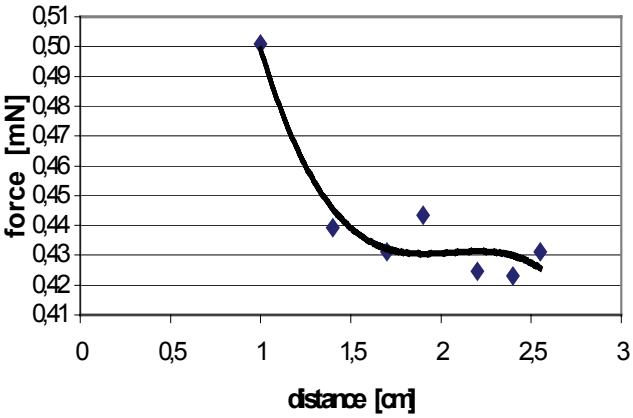

Fig. 7. Repelling force calculated for various values of distance between the sphere and the wall (D=40mm, m=2g, x_0=0,8cm)

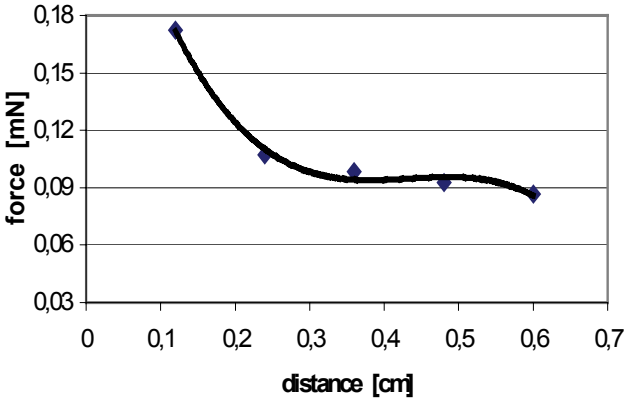

Fig. 8. Repelling force calculated for various values of distance between the sphere and the wall (D=30mm, m=2g, x_0=0,1cm).

5. Conclusion

The flow of a rigid sphere along the wall encounters deflection of its motion. This may be attributed to the non-uniform velocity distribution around the sphere. Authors own simple model explaining such behaviour has been presented to explain that phenomenon. Further analysis of experimental data will be conducted using the flow pattern recognition methods [5]. Analysed will be video recordings presenting the sphere trajectory of motion recorded with a digital camera during the experiment. Calculated time period, separating particular frames, as well as the decompression of the recording combined with the dimensional analysis of recorded space will enable authors calculation of velocities and acceleration of a sphere in the direction transverse to the wall. In effect, consideration of the equation of motion (2) in the direction vertical to the wall will become easier.

References

[1] Yan Y.Y., Lin T.F.: Evaporation heat transfer and pressure drop of refrigerant R-134a in a small pipe. Int. Journal of Heat and Mass Transfer, vol.41, 4183-4194, 1998.

[2] Huo X., Tian Y.S., Wadekar V.V., Karayiannis T.G.: Two-phase flow and boiling heat transfer in small diameter tubes. Raport South Bank University 1999.

[3] Marié, J.L.; Moursali, E.; Tran-Tong, S.: Similarity law and turbulence intensity profiles in a bubble layer at low void fractions. Int. J. Multiphase Flow, 23, 227-247, 1997.

[4] Mikielewicz D.: Hydrodynamics and heat transfer in bubbly flow in the turbulent boundary layer. Int. J. of Heat and Mass Transfer, vol. 46, 207-220, 2002.

[5] Stasiewicz A.: Recording and analysing physical phenomena. MIKOM Publishers, Warszawa 2003 (in Polish).

Strojniški vestnik - Journal of Mechanical Engineering 51(2005)7-8, 436-444
UDK - UDC 536.2
Izvirni znanstveni članek - Original scientific paper (1.01)

Simulation of Void Fraction Profile Evolution in Subcooled Nucleate Boiling in a Vertical Annulus with a Bubble-Tracking Model

Ivo Kljenak*, Borut Mavko

Reactor Engineering Division, Jozef Stefan Institute, Jamova 39, Ljubljana, Slovenia, ivo.kljenak@ijs.si*

Abstract

A three-dimensional bubble-tracking model of subcooled nucleate boiling flow in a vertical channel at low-pressure conditions is proposed, with specific application to the case of boiling in an annulus with a central heating rod. In the model, vapour is distributed in the liquid in the form of individually tracked bubbles. The overall behaviour of the liquid-vapour system results from motion, interaction, coalescence and boiling mechanisms prescribed mostly at the level of bubbles. The wall heat transfer coefficient and the wall temperature are calculated from one-dimensional correlations. The partitioning of the heat flux, which is consumed for bubble nucleation and heating of the liquid, varies along the flow and depends on bubble size as well as on local flow conditions. Bubbles are nucleated with constant frequencies at fixed nucleation sites randomly distributed over the heated surface. Liquid temperature profiles at different axial locations are determined from steady-state energy balances. The nucleation site density is determined from a balance between vapour generation rate, bubble departure sizes and nucleation frequencies. After nucleation, bubbles slide on the heated surface, detach and then gradually migrate into the low-temperature region away from the heated surface, where they eventually condense. Both bubble detachment and migration are modelled probabilistically. Bubble lateral migration is restricted by the lift force due to the liquid velocity gradient.

The proposed model was applied to experiments on subcooled boiling that were carried out at Purdue University (USA) by Bartel [1]. A good agreement between measured and calculated void fraction profiles at different axial locations was obtained.

Introduction

In the subcooled part of upward nucleate boiling flow in a vertical channel with a heated wall, the temperature near the wall and the bulk fluid temperature are respectively higher and lower than the saturation temperature. Subcooled boiling is thus characterized by a "higher-temperature" two-phase region near the heated surface and a "lower-temperature" single-phase liquid region away from the heated surface.

The evolution of void fraction in subcooled boiling flow may be modelled using various approaches with different time and length scales. One-dimensional two-fluid models with various degrees of empiricism may predict fairly well the void fraction, averaged over the channel cross-section (Hari and Hassan [2], Končar and Mavko [3]). On the other hand, models based on local instantaneous description of the flow are at present still computationally too demanding to be applied to boiling systems which may have a complex interface structure due to the presence of up to several thousand bubbles. "Intermediate-level" models, which may be applied to nucleate boiling flows, include multidimensional two-fluid models, based on ensemble and volume averaging of local instant conservation equations (Kurul and Podowski [4], Janssens-Maenhout et al. [5], Končar et al. [6], Lee et al. [7]), and so-called bubble-tracking models, in which gas is distributed in the liquid in the form of individually-tracked bubbles (Mortensen and Trapp [8]).

Among experimental results on subcooled boiling in channels, not many authors have measured the non-homogeneous radial distributions of two-phase flow parameters, such as void fraction and bubble size. Recently, these kinds of experiments have been carried out by Bartel [1] and Lee et al. [7].

In the present work, a three-dimensional bubble-tracking model of subcooled nucleate boiling flow in a vertical channel is presented. The behaviour of the bubble

Nomenclature

A	channel cross-section [m^2]
D_h	channel hydraulic diameter [m]
G	mass flux [kg/m^2·s]
R_o	radius of annulus outer wall [m]
R_i	radius of annulus inner wall [m]
T	temperature [K]
c	specific heat [J/kg·K]
d	bubble equivalent diameter [m]
f	bubble nucleation frequency [s^{-1}]
g	gravitational acceleration [m/s^2]
h	heat transfer coefficient [W/m^2·K]
	specific enthalpy [J/kg]
j	volumetric flux [m/s]
k	thermal conductivity [W/m·K]
l	bubble vertical chord length [m]
p	pressure [Pa]
	probability [-]
q''	heat flux [W/m^2]
r	distance from annulus inner wall [m]
t	time [s]
w	velocity in z-direction [m/s]
z	axial coordinate [m]
Pr_l	liquid Prandtl number = ν_l / υ_l
Re_b	bubble Reynols number = $w_{bl} \cdot d_b / \nu_l$

Greek letters

α	void fraction [-]
ρ	density [kg/m^3]
σ	surface tension [N/m]
	standard deviation of bubble diam. dist. [m]
υ	thermal diffusivity [m^2/s]
μ	viscosity [Pa·s]
ν	kinematic viscosity [m^2/s]

Subscripts

b	bubble
bl	bubble relative velocity
d	bubble departure equivalent diameter
g	gas
i	annulus inner wall
	i-th bubble
l	liquid
$l\infty$	undisturbed liquid velocity
o	annulus outer wall
p	constant pressure
sat	saturation conditions
w	heated wall

Other symbols

$< >$	average over channel cross-section

population is simulated by considering each bubble separately. The overall behaviour of the liquid-vapour system results from motion, interaction and boiling mechanisms prescribed mostly at the bubble level.

The proposed work represents a further development of a model, which has already been presented earlier. The model was first developed for subcooled boiling in a cylindrical tube (Kljenak [9]). It was later extended to annular channels, and calculated results were compared to experimental measurements at a single axial location (Kljenak et al. [10], Kljenak et al. [11]) which were obtained at Seoul National University (Lee et al. [7]).

In the present work, the model was used to simulate experiments with boiling water in a heated vertical annular channel at atmospheric pressure, which were performed by Bartel [1]. In these experiments, flow parameters at different axial locations along the flow were measured. Thus, experimental and simulated evolutions of radial void fraction profiles are compared.

Physical model

In the present work, the equations apply to boiling flow in an annular channel. However, the model may be applied to a cylindrical tube as well.

Bubble axial motion and interaction

In the proposed model, bubbles assume a rigid ellipsoidal shape and move upwards with their symmetry axis always vertical. The velocity of a bubble is calculated by first adding the bubble relative velocity (calculated from a correlation by Peebles and Garber, as cited by Wallis [12]) to the local hypothetical "undisturbed" liquid velocity, obtained from the 1/7th power law. Then, if some other (leading) nearby bubble is found to be present ahead of the bubble whose velocity is being calculated, an increase due to wake drift is added. The liquid velocity behind bubble *i,* which is increased due to wake drift, is described in, basically, the same form as suggested by Bilicki and Kestin [13]:

$$w_l(z,r,t) = w_{l\infty}(z,r,t) + \left[\frac{l_{b\max}}{2(z_i - z)}\right]^{2\varsigma/3} (w_{bi}(t) - w_{l\infty}(z_i, r_i, t)) \quad (1)$$

where $l_{b\ \max}$ denotes the bubble maximum vertical chord length (ellipsoid vertical axis) and ζ is an empirical attenuation factor, set equal to 3.0, which was introduced to obtain a weaker wake drift as the velocity in the wake decreases with distance from the wake axis.

A necessary condition for a bubble to be influenced by a leading bubble through wake drift and eventually collide with it is that bubbles overlap laterally (Fig. 1) by more than a certain critical fraction, called *minimum relative overlapping*. A similar approach was already proposed by Mortensen and Trapp [8]. If, following axial collision, bubbles *overlap in space*, the upper bubble is displaced laterally (sideways) for a fraction of its width if there is no other nearby bubble to prevent the movement. Otherwise, the upper bubble is displaced upwards so that bubbles barely stick. If bubbles still stick after collision (that is, if they were not separated due to a lengthy lateral displacement of the upper bubble), they remain sticking, move along together with the upper bubble's velocity and eventually merge if they do not separate earlier due to either turbulent dispersion, subsequent movements of either bubble or coalescence of either bubble with some other bubble.

If separate bubbles do not overlap laterally more than the critical fraction, the motion of the trailing bubble is not affected by the leading bubble and bubbles behave as if they would not overlap at all. This rule was prescribed to approximate the influence of bubble agitation, which occurs in real bubbly flow and allows tightly packed bubbles to overtake one another. The drawback of this approach is that bubbles may briefly overlap in space, which is not physically realistic.

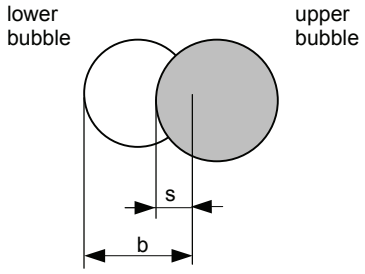

Figure 1. Relative overlapping between lower and upper bubble = s/b

The two-dimensional "undisturbed" liquid velocity profile causes bubbles located at different distances from the wall to move with different velocities, thus promoting bubble collisions and coalescence.

Bubble sliding, detachment and radial motion

In various experiments on subcooled nucleate boiling of water at low-pressure conditions, it has been observed that bubbles nucleated on a heated wall first slide along the wall and then tend to detach and migrate towards the tube region away from the heated surface (Bibeau and Salcudean [14], Zeitoun and Shoukri [15], Prodanovic et al. [16]). To the authors' knowledge, no consensus concerning bubble sliding distance has been reached yet. Prodanovic et al. [16] observed that bubbles usually slide a couple of diameters before detaching. In the proposed model, the following empirical approach was adopted, based on above-cited experiments: after nucleation, bubbles slide along the heated surface for some distance before attempting detachment. During sliding, the ellipsoidal bubble vertical axis is longer than the bubble horizontal axis to approximate the bubble inclination which was observed in experiments. Detachment, which may occur if no other bubble obstructs the radial motion away from the heated surface, is modelled probabilistically in the same way as bubble radial migration (see below). After detaching from the heated surface, bubbles tend to migrate towards the lower-temperature region (again, if other bubbles do not obstruct their motion), where they eventually condense. After detachment, the bubble shape changes and the horizontal axis is longer than the vertical axis.

In bubbly flow in general (that is, in boiling as well as in adiabatic flow), bubbles are distributed over the channel cross-section, supposedly as the result of interaction of different phenomena: liquid turbulent flow, transverse lift force, wall lubrication force and bubble interaction (Žun [17], Liu [18], Ohnuki and Akimoto [19], Okawa et al. [20]). Bubble transverse motion over the channel cross-section is presumably partly random, due to the interaction of bubbles with turbulent eddies. A probabilistic approach was thus implemented to model bubble radial motion (migration) towards the tube outer wall: the motion consists of finite steps that are equal to a fraction of bubble width, each displacement occurring with a certain probability. At present, the proposed model was developed for boiling systems in which all bubbles are located between the heated inner annulus wall and the middle of the annular gap. The lift force, which is related to the liquid velocity gradient, is assumed to represent a restraining force to bubble radial motion away from the heated wall. Thus, the probability of migration p_m was modelled to increase with decreasing velocity gradient over the channel cross-section:

$$p_m = 1.0 - C_r \left(\frac{\partial w_{l\infty}}{\partial r} \right)^{1/2} \tag{2}$$

where C_r is an empirical coefficient. As bubble lateral motion may be affected by turbulent eddies of a comparable size as the bubble, bubble migration is attempted every time a bubble moves axially a distance equal to its maximum vertical chord length.

Turbulent dispersion

The relative motion between bubbles is mainly influenced by eddy motion of the length scale of bubble size (Prince and Blanch [21]). The influence of turbulent eddies, which may affect wake drift or sticking bubbles, is modelled as a succession of random binary events. Thus, each event may have two possible outcomes: at a

given instant, bubble motion is or is not disturbed by turbulent dispersion. Higher turbulence intensity is simulated by prescribing a higher probability of dispersion. Intensities of turbulent dispersion are assumed to be constant over the channel cross-section. Disruption of wake drift and of sticking bubbles by turbulent eddies is related to the turbulence length scale and is simulated every time a bubble has moved in the axial direction a distance equal to 1/20 of the channel hydraulic diameter.

Bubble coalescence

Following axial collision and sideways or upwards displacement of the upper bubble, bubbles which still overlap more than the minimum relative overlapping stick together. Bubbles eventually merge after sticking together for a certain time interval (so-called "rest time") if they are not dispersed by liquid turbulence or do not move apart due to axial collisions with other bubbles. Bubble coalescence occurs instantly only if the leading bubble is sliding on the heated surface whereas the trailing bubble is not, as the impact between bubbles is presumably stronger due to larger velocity differences.

In the present work, it was assumed that the impact following bubble lateral collision is not strong enough to cause rupture of the vapour-liquid interface, so that coalescence following bubble lateral collision was not modelled.

Liquid temperature

In the proposed model, the liquid temperature T_l depends on the distance from the inner heated wall r and obeys the following law (Sekoguchi et al. [22]):

$$\frac{T_i - T_l}{T_i - T_o} = \left[\frac{r}{R_o - R_i} \right]^{1/m} \tag{3}$$

where the exponent m may depend on the flow rate. Namely, at higher flow rates, the temperature gradient near the wall is expected to be somewhat steeper due to more intense turbulent mixing. Liquid temperature profiles at different axial locations along the tube are obtained using steady-state values of the average cross-sectional enthalpy $<h>$. The liquid temperature profile must be such that the liquid specific enthalpy h_l fulfils the condition:

$$\langle h \rangle \int_A ((1-\alpha)\rho_l + \alpha\rho_g) dA = \int_A (1-\alpha)\rho_l h_l dA + \int_A \alpha\rho_g h_g dA \tag{4}$$

where α denotes the local void fraction and integrals are calculated over the channel cross-section. Steady-state values of $<h>$ at different axial locations are obtained from thermal energy balances. The gas phase is assumed to be at saturation conditions.

The temperature of the heated wall is assumed to increase until it reaches a value determined from a correlation by Shah (as cited by Kandlikar [23]):

$$q'' = \left(230 (G h_{lg})^{-0.5} h_{1\Phi} (T_w - T_{sat}) \right)^2 \tag{5}$$

where the single-phase heat transfer coefficient $h_{1\Phi}$ has to be calculated from the well-known Dittus-Boelter correlation (Collier [24]) and h_{lg} indicates the difference between vapour and liquid specific enthalpies at saturation conditions. Before reaching that value, the wall temperature is calculated from the relation:

$$q'' = h_{1\Phi} (T_w - < T_l >) \tag{6}$$

where $<T_l>$ denotes the liquid temperature, averaged over the channel cross-section.

Partitioning of wall heat flux

In the proposed model, the wall heat flux is partitioned as follows:

$$q'' = C_l h_{1\Phi} (T_w - < T_l >) + q''_{nucl} + q''_{slid} \tag{7}$$

The first term on the r.h.s. of Eq. (7) represents heat transfer due to single-phase forced convection. The factor C_l accounts for the portion of the heated surface not covered by bubbles. The term q''_{nucl} denotes the heat flux consumed for bubble nucleation. The term q''_{slid}, which denotes the heat flux consumed for growing of bubbles that slide on the heated surface, is determined as in the work of Tsung-Chang and Bankoff [25]:

$$q''_{slid} = \frac{2 k_l (T_w - T_{sat})}{(\pi v_l)^{1/2}} \tag{8}$$

The surface through which heat is transferred to the bubble is represented by a circular area with a diameter equal to the bubble vertical axis.

Bubble nucleation

In the proposed model, bubbles are nucleated at fixed nucleation sites randomly distributed over the heated surface, instantly reach *departure* size and assume an ellipsoidal shape. The bubble equivalent departure diameter d_d is constant at each site. Bubble diameters over nucleation sites are distributed according to Gaussian distributions and are randomly generated in intervals $[d_d - 3\sigma, d_d + 3\sigma]$, where d_d denotes the local mean bubble equivalent diameter and σ the local standard deviation. The mean bubble size was assumed to depend on local subcooling and was calculated in the same way

as in the work of Končar et al. [6], using Unal's [25] mechanistic model. Unal's model describes the bubble departure diameter d_d as a function of pressure, liquid subcooling, heat flux and liquid flow velocity:

$$d_d = C_{bw} \frac{2.42 \cdot 10^{-5} \cdot p^{0.709} a}{\sqrt{b\phi}} \tag{9}$$

where coefficients a, b and Φ are defined as:

$$a = \frac{(q'' - h_{l\phi} \cdot \Delta T_{sub})^{1/3} k_l}{2C^{1/3} h_{lg} \rho_g \sqrt{\pi k_l / \rho_l c_{pl}}} \sqrt{\frac{k_w \rho_w c_w}{k_l \rho_l c_{pl}}} \tag{10}$$

$$C = \frac{h_{lg} \mu_l \left[c_{pl} / \left(0.013 h_{lg} \, \mathrm{Pr}_l^{1.7} \right) \right]^3}{\sqrt{\sigma / (\rho_l - \rho_g) g}} \tag{11}$$

$$b = \frac{\Delta T_{sub}}{2(1 - \rho_g / \rho_l)} \tag{12}$$

$$\phi = \begin{cases} \left(\dfrac{v_l}{0.61} \right)^{0.47} & \text{for} \quad v_l \geq 0.61 \text{ m/s} \\ 1 & \text{for} \quad v_l < 0.61 \text{ m/s} \end{cases} \tag{13}$$

The range of applicability of the correlation is:
- pressure: $0.1 < p < 17.7$ MPa,
- wall heat flux: $0.47 < q'' < 10.64$ MW/m^2,
- liquid velocity: $0.08 < w_l < 9.15$ m/s,
- liquid subcooling: $3.0 < \Delta T_{sub} < 86$ K.

Since, in the present work, the heat flux in the considered experimental data is below the range of applicability of the correlation, the coefficient C_{bw} was added in Eq. (9) to describe relatively large bubbles at low-pressure conditions.

The frequency of bubble nucleation at individual sites is calculated from a correlation by Cole (1960, as cited by Ivey [27]):

$$f = \left[\frac{4g(\rho_l - \rho_g)}{3 d_d \, \rho_l} \right]^{1/2} \tag{14}$$

Bubble evaporation and condensation

In the proposed model, bubbles may further grow while part of them is still within the region near the heated wall where the temperature is higher than the saturation temperature. The interfacial heat transfer coefficient h_{int} is calculated from a correlation already used by Mortensen and Trapp [8]:

$$h_{int} = \frac{k_l}{d_b} \left(2 + (0.4 Re_b^{0.5} + 0.06 Re_b^{0.67}) Pr_l^{0.4} \right) \tag{15}$$

Bubbles that move laterally into the lower-temperature region collapse instantly if the liquid temperature at the bubble tip closest to the heated surface is lower than the saturation temperature.

Numerical model

Bubble behaviour

The proposed model was implemented as a computer code. Bubble axial motion is simulated with a simple discrete time-step method, neglecting inertial effects:

$$z_i(t + \Delta t) = z_i(t) + w_{bi}(t) \cdot \Delta t \tag{16}$$

As bubbles in the proposed model undergo significant accelerations only briefly before axial collision with a leading bubble or after radial migration to a higher liquid-velocity region, the added mass effect is not taken into account. After each axial displacement during a time step, bubbles, which overlap more than the minimum relative overlapping, are adjusted if they also overlap in space. Adjustments start at the tube entrance, and upper bubbles are adjusted with respect to lower bubbles. If possible, each upper bubble moves laterally (sideways) for up to a fraction of its width. If this is not possible due to the presence of other bubbles, the upper bubble is displaced upwards (see Section "Bubble axial motion and interaction"). This adjustment of bubbles simulates bubble collisions and subsequent displacements of upper bubbles.

Bubbles' cross-sectional coordinates assume discrete values, which correspond to points located on concentric circles, centred on the annulus axis (Fig. 2). The distance between neighbouring points along concentric circles is constant. The distance between any neighbouring points must be of the order of a fraction of the smallest bubbles' width (usually about few hundredths). Bubble lateral movements are modelled as instantaneous jumps to other points and occur between time steps. Mergers between bubbles, bubble condensations and bubble nucleations are also modelled as instantaneous events which occur between time steps.

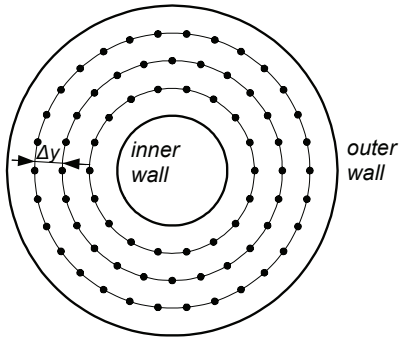

Figure 2. Schematic representation of bubble centres' discrete cross-sectional coordinates.

Volume fraction and energy coupling

The vertical channel is divided in the axial direction into control volumes. The partitioning of the heat flux into vapour generation and liquid heating is constant within each control volume. The total simulation time is divided into *time sub-intervals* during which passages of bubbles through control volume boundaries are recorded. At the end of each sub-interval, the liquid velocity profile corresponding to each boundary is adjusted to satisfy the following mass conservation condition (Kowe et al. [28]):

$$Aj_l = \int_A w_{l\infty}(1-\alpha)dA + C_m w_{bl} \int_A \alpha dA \qquad (17)$$

where α denotes the time-averaged local void fraction obtained from recordings of bubble passages at the control volume boundary and integrals are calculated over the channel cross-section. The coefficient of added mass C_m was set equal to 0.5. In the same way, the liquid temperature profile is set so that the cross-sectional enthalpy at each boundary assumes the steady-state value (Eq. 4), obtained from the total heat input below the boundary. These liquid velocity and temperature profiles are then used in calculations during the next time sub-interval.

Within each control volume, local liquid velocities and temperatures are calculated by linear interpolation between values, which correspond to the control volume lower and upper boundaries. These values are needed when calculating liquid velocities and temperatures corresponding to bubble centres.

For each control volume, the partitioning of the heat flux into vapour generation and liquid heating is based on conditions at the control volume upper boundary and is determined periodically after each time sub-interval. The nucleation site density at a given axial location is determined by an iterative calculation so that the sum of all the heat flux components equals the imposed heat flux. Nucleation sites on the tube wall are placed randomly and used to generate bubbles during the next time sub-interval.

Results

Experimental conditions

Experiments on subcooled nucleate boiling at atmospheric pressure were performed at Purdue University (USA) by Bartel [1]. The experiments were carried out in a vertical annulus with a heated inner rod. The diameter of the rod was 19.1 mm, whereas the inner diameter of the outer tube was 38.1 mm. The length of the heated part of the annulus was 1.5 m. Local void fraction was measured using an electrical conductivity probe technique. The data were collected simultaneously at different axial locations. Thus, the axial evolution of radial distribution of flow parameters was observed. Experimental conditions for runs, which were simulated with the proposed model, are presented in Table 1. The inlet subcooling refers to conditions at atmospheric pressure.

Table 1. Experimental conditions

Run	ΔT_{sub} [°C]	q'' [kW/m^2]	G [kg/m^{2}s]
1	8.9	105	470
2	6.1	128	701
3	4.8	128	701
4	5.2	145	700

Model parameters

At each nucleation site, the bubble departure diameter was constant but generated as a random variable with a Gaussian distribution (see section "Bubble nucleation"). It was assumed that the smallest bubble diameter (lower boundary of the interval: d_d - 3σ) was always 0.0005 m, from which the interval upper boundary was calculated.

The value of the coefficient C_{bw} in Eq. (9) was set to 1.5. The ratio of horizontal to vertical bubble axis before bubble detachment from the wall was set to 0.8, to approximate the inclination of bubbles while they are sliding on the walls. After detachment, the ratio was set to 1.2.

All simulations were carried out with identical values of bubble minimum relative overlapping (0.3) and rest time during which bubbles stick together before merging (0.02 s). There is a lack of information on rest times in turbulent flows, necessitating the use of what is in effect an adjustable parameter (Prince and Blanch [21]). Bubble radial motion (including detachment from the heated wall and sideways displacement of the upper bubble after axial collision) consisted of finite steps of 1/20 bubble width. The factor C_r in Eq. (2) was set equal to 0.03 for all runs.

The probabilities of turbulent dispersion were set to 0.09 for G=470 kg/m^2·s and 0.13 for G=700-701 kg/m^2·s.

The ratios of probabilities of turbulent dispersion correspond to the ratios of bulk Reynolds numbers.

The factor *m* in Eq. (3) (liquid temperature profile) was set to 4.0 for all runs.

For G=470 kg/m^2·s, it was assumed that bubbles slide along the wall for a distance equal to twice their maximum vertical chord length (that is, twice the ellipsoid vertical axis) before attempting detachment. For G=700-701 kg/m^2·s, it was assumed that the "sliding distance" is equal to one vertical axis. The rationale for the difference is that bubble detachment is more likely to occur sooner at higher mass flow rates due to the influence of turbulent eddies.

Simulation results

Figures 3-6 show experimental and simulated time-averaged void fraction radial profiles at different experimental conditions and different axial locations along the channel. The coordinate *z=0* corresponds to the beginning of the heated section. In general, the overall agreement between simulations and experiments is good.

As bubbles instantly assume the shape of ellipsoids, which have their axis always vertical and touch the wall only with their tip, void fraction assumes zero values at the heated wall.

Due to the assumption of *rigid* ellipsoidal bubbles, whose axis always remain vertical, the proposed approach is necessarily limited to relatively low void fraction values. Namely, at higher void fractions, bubbles in actual flows are packed more closely, so that their shape is probably somewhat distorted and their axis do not always remain vertical.

In the proposed model, parameters that were adjusted either assume a constant value or their variation may be justified on physical grounds. Thus, the presented simulations of experiments, performed with different combinations of boundary conditions (subcooling, mass flux and heat flux), augur that the model should be applicable to subcooled boiling in vertical annular channels of similar dimensions and over a range of experimental conditions.

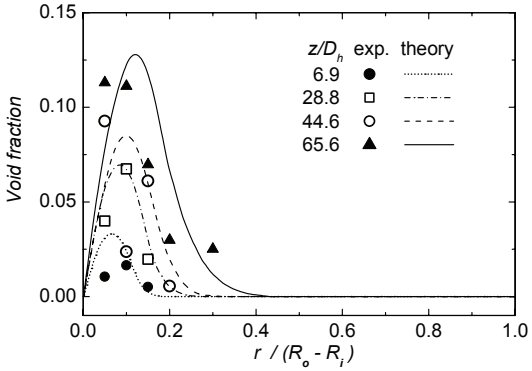

Figure 3. Simulated and experimental void fraction profiles (G=470 kg/m^{2}s, q''=105 kW/m^2, ΔT_{sub} =8.9 °C)

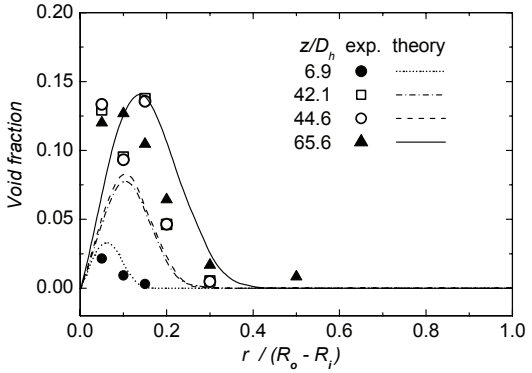

Figure 4. Simulated and experimental void fraction profiles (G=701 kg/m^{2}s, q''=128 kW/m^2, ΔT_{sub} =6.1 °C)

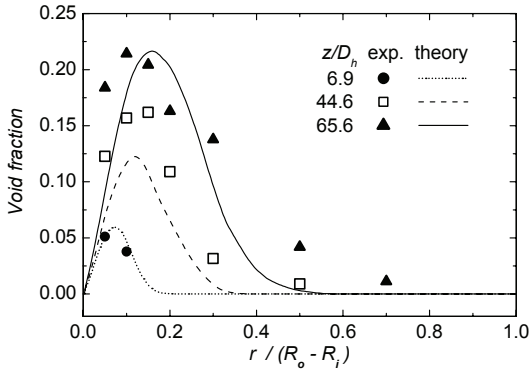

Figure 5. Simulated and experimental void fraction profiles (G=701 kg/m^{2}s, q''=128 kW/m^2, ΔT_{sub} =4.8 °C)

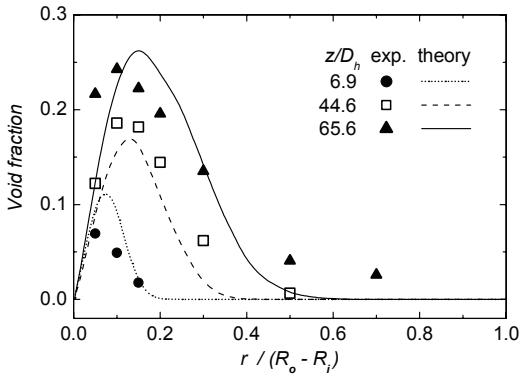

Figure 6. Simulated and experimental void fraction profiles ($G=700$ kg/m^{2}s, $q''=145$ kW/m^2, $\Delta T_{sub}=5.2$ °C)

Conclusions

A three-dimensional bubble-tracking model, in which empiricism is included at a "more fundamental" level, was developed to simulate upward subcooled nucleate boiling flow in a vertical annular tube with a central heating rod. Bubble collective behaviour results from motion, interaction and heat transfer mechanisms prescribed at the level of individual bubbles.

The model was used to simulate experiments performed with water at near atmospheric pressure. A good overall agreement between calculated and measured radial profiles of void fraction at different axial locations along the channel was obtained. Although the model contains a number of adjustable parameters, the comparison of simulated results with experimental data indicates that the proposed approach captures the basic mechanisms that govern the development and evolution of subcooled nucleate boiling along a heated channel at near atmospheric pressure and relatively low void fraction.

References

[1] M.D. Bartel, Experimental Investigation of Subcooled Boiling, M.Sc.Thesis, Purdue Univ., West Lafayette, IN, USA, 1999.

[2] S. Hari, Y.A. Hassan, Improvement of the subcooled boiling model for low-pressure conditions in thermal-hydraulic codes, Nuclear Engng. Design 216 (2002) 139-152.

[3] B. Končar, B. Mavko, Modelling of low-pressure subcooled flow boiling using the RELAP5 code, Nuclear Engng. Design 220 (2003) 255-273.

[4] N. Kurul, M.Z. Podowski, On the modeling of multidimensional effects in boiling channels, Proc. 27th National Heat Transfer Conf., Minneapolis, USA, 1991.

[5] G. Janssens-Maenhout, J.U. Knebel, U. Mueller, Subcooled nucleate boiling at low pressure and low heat flux, Proc. 3rd Int.Conf. Multiphase Flow ICMF'98, Lyon, France, 1998.

[6] B. Končar, I. Kljenak, B. Mavko, Modelling of local two-phase flow parameters in upward subcooled flow boiling at low pressure, Int.J. Heat Mass Transfer 47 (2004) 1499-1513.

[7] T.H. Lee, G.C. Park, D.J. Lee, Local flow characteristics of subcooled boiling flow of water in a vertical concentric annulus, Int. J. Multiphase Flow 28 (2002) 1351-1368.

[8] G.A. Mortensen, J.A. Trapp, Two-phase flow modeling with discrete particles, Proc. ASME Heat Transfer Div., Two-Phase Flow in Energy Exchange Systems, vol. 220, 1992, pp. 73-85.

[9] I. Kljenak, Modeling of void fraction and liquid temperature profiles evolution in vertical subcooled nucleate boiling flow, Proc. ASME-ZSITS Int.Thermal Science Seminar, Bled, Slovenia, 2000.

[10] I. Kljenak, G.C. Park, B. Mavko, T. Lee, Bubble-tracking modeling of subcooled nucleate boiling in a vertical annulus, Proc. 4th Int. Conf. Multiphase Flow, New Orleans, USA, 2001.

[11] I. Kljenak, G.C. Park, B. Mavko, T. Lee, Bubble-tracking modeling of subcooled nucleate boiling in a vertical annulus, Proc. 12th Int. Heat Transfer Conf., Grenoble, France, 2002.

[12] G.B. Wallis, One-Dimensional Two-Phase Flow, McGraw-Hill, 1969, pp. 248-251.

[13] Z. Bilicki, J. Kestin, Transition criteria for two-phase flow patterns in vertical upward flow, Int.J. Multiphase Flow, 13 (1987) 283-294.

[14] E.L. Bibeau, M. Salcudean, Subcooled void growth mechanisms and prediction at low pressure and low velocity, Int.J. Multiphase Flow, 20 (1994) 837-863.

[15] O. Zeitoun, M. Shoukri, Bubble behavior and mean diameter in subcooled flow boiling, Trans. ASME, J. Heat Transfer 118 (1996) 110-116.

[16] V. Prodanovic, D. Fraser, M. Salcudean, Bubble behavior in subcooled flow boiling of water at low pressures and low flow rates, Int.J. Multiphase Flow 28 (2002) 1-19.

[17] I. Žun, The mechanism of bubble non-homogeneous distribution in two-phase shear flow, Nuclear Engng. Design 118 (1990) 155-162.

[18] T.J. Liu, Bubble size and entrance length effects on void development in a vertical channel, Int.J. Multiphase Flow 19 (1993) 99-113.

[19] A. Ohnuki, H. Akimoto, Prediction of phase distribution under bubbly flow in a large vertical pipe by multidimensional two-fluid model, Proc. 3rd Int. Conf. Multiphase Flow ICMF'98, Lyon, France, 1998.

[20] T. Okawa, I. Kataoka, M. Mori, Numerical simulation of lateral phase distribution in turbulent upward bubbly two-phase flows, Nuclear Engng. Design 213 (2002) 183-197.

[21] M.J. Prince, H.W. Blanch, Bubble coalescence and break-up in air-sparged bubble columns, AIChE J. 36 (1990) 1485-1499.

[22] K. Sekoguchi, O. Tanaka, S. Esaki, T. Imasaka, Prediction of void fraction in subcooled and low quality boiling regions, Bull. Japan Soc. Mechanical Engineers 23 (1980) 1475-1482.

[23] S.G. Kandlikar, Heat transfer characteristics in partial boiling, fully developed boiling and significant void flow regions of subcooled flow boiling, Trans. ASME, J.Heat Transfer 120 (1998) 395-401.

[24] J.G.Collier, Convective Boiling and Condensation, McGraw-Hill, 1981.

[25] G.Tsung-Chang, S.G. Bankoff, On the mechanism of forced-convection subcooled nucleate boiling, Trans. ASME, J.Heat Transfer 112 (1990) 213-218.

[26] H.C. Unal, Maximum bubble diameter, maximum bubble-growth time and bubble-growth rate, Int.J. Heat Mass Transfer 10 (1967) 1023-1040.

[27] H.J.Ivey, Relationships between bubble frequency, departure diameter and rise velocity in nucleate boiling, Int.J. Heat Mass Transfer 10 (1967) 1023-1040.

[28] R. Kowe, J.C.R. Hunt, A. Hunt., B. Couet, L.J.S. Bradbury, The effects of bubbles on the volume fluxes and the pressure gradients in unsteady and non-uniform flow of liquids, Int.J. Multiphase Flow 14 (1988) 587-606.

Strojniški vestnik - Journal of Mechanical Engineering 51(2005)7-8, 445-450
UDK - UDC 536.2
Izvirni znanstveni članek - Original scientific paper (1.01)

Modelling of Flow Boiling Process in Small Diameter Tubes

Dariusz Mikielewicz[1], Jarosław Mikielewicz[2]

[1]*Gdańsk University of Technology, Faculty of Mechanical Engineering*
Heat Technology Department, Narutowicza 11/12, 80-952 Gdańsk, Poland
tel. +48 58 3472254; fax. +48 58 3472816; e-mail: dmikiele@pg.gda.pl
[2]*Institute of Fluid-Flow Machinery, Polish Academy of Sciences*
Fiszera 14, 80-952 Gdańsk, Poland, e-mail: jarekm@imp.gda.pl

Abstract

In the paper presented is application of a correlation describing flow boiling data, developed for conventional tubes, to small diameter tubes. Comparison between data from literature and calculated values has been made, which gives poor agreement and indicates that substantially more research is required to develop correlations with theoretical foundations to predict heat transfer in small diameter channels.

1. INTRODUCTION

Heat transfer during boiling is one of the most effective techniques for the removal of large heat fluxes from the heated wall. Its industrial applications are widespread, but originally applications can be found in energy conversion systems such as petrochemical industry, power engineering, chemical engineering, refrigeration and air-conditioning and other large-scale installations. With respect to such applications investigations into boiling heat transfer have been focused on large diameter tubes. Presently, a great progress in implementation of boiling heat transfer in mini or microscale can be observed, for example in compact heat exchangers, micro-heat pipes of large efficiency, cooling of electronic equipment and others. The increased interest is observed in better understanding of small-scale or micro-scale heat transport phenomena during intense heat transfer processes. For example, integrated computer processors can generate very high heat fluxes and therefore the accurate control of their temperature is of paramount importance with respect to their reliable operation. Single phase heat transfer proved to be insufficient in the removal of such high heat fluxes due to relatively smaller heat transfer coefficients. The last decade of the past century can confirm fast developments in the research into micro and nanoscale, which find applications in numerous technologies. According to Kandlikar [1], 3 mm tube hydraulic diameter can be regarded as a lower limit of the conventional evaporator tubes. Following his suggestions the minichannels fall into the range of hydraulic diameters between 600 μm and 3 mm, whereas the microchannels into the range between 50 μm and 600 μm, respectively.

Flow boiling in channels is probably the most complicated mechanism of convective heat transfer, which can be found in various applications. It has been the topic of significant interest for several years now, but the contributions into the subject are merely very specific and does not enable a more general analysis.

There is a considerable number of correlations that can be employed in determination of the heat transfer coefficient for flow boiling of freons in channels. Only very few of them, however, enable analysis within a full variation range of the quality, x=0÷1. Remarkably, none of the known correlations features theoretical foundations. This paper is aimed at presentation of a correlation developed some time ago, but yet to be published properly. The following issued should be considered in evaluation of applicability of correlations:

- theoretical foundations,
- high reliability of reproduction of heat transfer coefficients (considering experimental investigations for different freons, tube diameters and boiling parameters),
- generality to such an extent that it might be used to predict the heat transfer coefficient for new refrigerants or dimensions not considered hitherto, i.e. such that have not yet been applied in technical use or small diameter channels.

Nomenclature

C - specific heat
d - channel inner diameter
E - dissipation energy
g - gravity, exponent
G - mass flowrate
l - bubble characteristic length
p - pressure
q - heat flux density
S - limiting heat flux
R_G - two-phase flow resistance coefficient
R_{GM} - modified two-phase flow resistance coefficient
h_{fg} - latent heat of evaporation
C - specific heat at constant pressure
t - temperature
x - quality
w - velocity
α - heat transfer coefficient
λ - thermal conductivity
μ - dynamic viscosity
σ - surface tension
ξ - friction factor

Subscripts:

PB - pool boiling
TP - two-phase flow
L - saturated liquid
G - saturated vapour
TPB - two-phase boiling
n - saturated state, exponent

So far the Chen's [2] correlation has quite commonly used in a variety of applications. He divided the heat transfer into two parts namely, the nucleate boiling contribution and non-boiling forced convection. There are numerous modifications of this correlation depending mainly on the employed in it formula to determine the "pool-boiling" coefficient. Shah [3] proposed a correlation in a graphical form introducing to it the convective number, Co, and the boiling number, Bo. Instead of taking the sum of two above mentioned contributions he recommends to pick the higher value of heat transfer coefficient. In the development of correlation approximately 800 experimental points have been used. In some later publications, [4], Shah supplemented his correlation with the relations enabling analytical calculation of constituent coefficients. Shah's correlation has been widely used in engineering practice. Kandlikar and Thakur [5] put forward another widely acknowledged correlation, which included both the bubble boiling and the convective evaporation process, taking advantage for its construction of the same data as Shah did. A later publication by Kandlikar [6] presented a correlation for a number of agents. In effect, the heat transfer coefficient is expressed in terms of the parameter dependent on the type of refrigerant. A large bank of data amounting to over 5000 testing points for water, R11, R12, R114, R13B1, R22, R113, R152a, nitrogen and neon has been used in development of correlation. As it follows from the construction of the Kandlikar's correlation, it does not provide accurate values for liquid-only or vapour-only flow of fluid in a channel. The correlation proposed by Gungor and Winterton [7] is a modification of Chen's correlation. The correlation is based on the same parameters used by Shah and Kandlikar. Bjorge [8] suggests superposition of heat flux as the base for elaborating the correlation. The constants of Bjorge's correlation depend also on the type of refrigerant. As can be deduced from the above survey none of the above correlations, despite their wide acceptance, does not feature theoretical foundations. They have been tuned to selected amount of experimental data and require constant validation against new flow parameters. Another difficulty is represented by the fact that flow boiling occurs in practice at small mass flowrate and small to moderate heat fluxes (refrigeration, air-conditioning) and large mass flowrates and moderate to high heat fluxes (power engineering). Capturing all these trends with one only correlation is a very difficult task. The research went in two directions to devise suitable tools for the first and the latter case. On the brink of application of boiling heat transfer to miniscale and microscale it seems that reliability of predictions must be sought in the correlations describing the moderate to small flowrates and small to moderate heat fluxes.

Since a few correlations are already available some justification would be desirable to propose a new one. First of all it would be desirable for a new correlation to lay some theoretical basis for the flow boiling process, secondly, be relatively simple to use without recourse to obscure functions, be applicable to subcooled and saturated flow conditions, be tested against a significant amount of data. In authors opinion the correlation due to J. Mikielewicz [9], with later modifications [10], tested in the present paper satisfies all these requirements.

2. A GENERAL CORRELATION DESCRIBING FLOW BOILING IN CHANNELS

J. Mikielewicz [9] has made use of a generalization of investigations by various authors as well as his own to devise a semi-empirical method of determining the heat transfer coefficient for boiling flow. The correlation is based on the knowledge of heat transfer coefficients for simpler cases of pool-boiling and convective single-phase flow, as well as on the knowledge of hydrodynamical resistance coefficients for two-phase vapour-liquid adiabatic flow conditions. Such conditions are acknowledged to be fairly well investigated and by means of them it was possible to determine the heat transfer for

the complex problem of boiling flow. The correlation was further modified by Bilicki [11] and then further by Mikielewicz et al. [10,12]. The following issues were subject to additional analysis to obtain the latter form of correlation of higher accuracy:

- experimental flow conditions, the analysis was aimed at determination whether experimental data represents the boiling process or fluid convection, or flow beyond the critical heat flux.
- selection of the function describing the two-phase flow resistance; attempts have been made to search for the specific function which describes the flow resistance of two-phase freons.

The generalized correlation was worked out on the basis of the available data base for R12, R11 and R22. Selected data has been excluded from the analysis, where it was tested that the data correspond to a heat flux below which the boiling process does not occur, i.e. vapour bubbles are not generated on the channel wall. In such situation the heat exchange takes place between the overheated fluid and the channel wall. The correlation has been devised taking advantage of the linear regression theory fit to the experimental data using multiple regression theory. The details of the method can be found in [12], and here only the general outline is recalled.

2.1. Heat transfer in two-phase flow without bubble generation

Transformation of a two-phase flow onto an equivalent liquid flow enables to assume that heat transfer in the considered case can be described by means of relations applicable to equivalent single phase flow. The convective heat transfer coefficient is usually described with the aid of the Dittus-Boelter, which leads to the relation [12]:

$$\frac{\alpha_{TP}}{\alpha_O} = R^{0.4} \tag{1}$$

where α_O is the liquid- or vapour only heat transfer coefficient depending on the chosen two-phase flow resistance coefficient R. In the two-phase flow the following holds [12]: $Re_{TP}=R^{0.5}Re_0$. The result (1) allows to consider a more general case with bubble generation.

2.2. Heat transfer in two-phase flow with bubble generation

It has been assumed that the heat transfer during flow boiling can be characterized by a sum of dissipation of a convective two-phase flow E_{TP} and bubble generation in the flow, E_{PB}, in the form:

$$E_{TPB} = E_{TP} + E_{PB} \tag{2}$$

The rate of energy dissipation in steady-state conditions can be approximated by dissipation in the laminar boundary layer. Similarly it can be assumed that there exists the friction factor for the bubble generation in the flow itself. In the same manner a total energy dissipation in the equivalent two-phase flow with bubble generation can be presented. Substitution of the above statements to (2) enables to obtain the following relation:

$$\xi_{TPB}^2 = \xi_{TP}^2 + \xi_{PB}^2 \tag{3}$$

The above result can be generalized using the analogy between the exchange of momentum and heat to obtain a similar relation linking the corresponding heat transfer coefficients:

$$\alpha_{TPB}^2 = \alpha_{TP}^2 + \alpha_{PB}^2 \tag{4}$$

Substituting (1) into (4) we arrive at a final form of correlation obtained by J. Mikielewicz [9]:

$$\frac{\alpha_{TPB}}{\alpha_{GO}} = \sqrt{R^{0.8} + \left(\frac{\alpha_{PB}}{\alpha_{GO}}\right)^2} \tag{5}$$

Further modification of J. Mikielewicz's correlation was based on devising an experimental correction, which provided a better fit to considered data points and enabled to extend the generality of correlation. The correlation form obtained after modification looks as follows:

$$\frac{\alpha_{TPB}}{\alpha_G} = \sqrt{R_{GM}^n + p\left(\frac{\alpha_{PB}}{\alpha_G}\right)^2} \tag{6}$$

where

$$p = aCo^b\, Re_L^c\, Bo(l/d)^e \left(\frac{P_n \cdot l}{4\sigma 10^4}\right)^f Fr^g\, Pr_L^{1/3};$$

$R_G = [f_l + 2(1-f_l)x]\cdot(1-x)^{1/3} + x^3$ is the Muller-Steinhagen and Heck relation [13] describing the flow resistance. Function f_l has a following definition $f_l = \left(\frac{\mu_L}{\mu_G}\right)^{0,25} \cdot \frac{\rho_G}{\rho_L}$ and finally the vapour-only heat transfer coefficient is calculated from the relation $\alpha_G = 0{,}023\frac{\lambda}{d} Re_G^{0,8}\, Pr_G^{1/3}$, where $Re_G = \frac{w_G \rho d}{\mu_G}$.

Much attention was paid to the right selection of the non-dimensional numbers present in the correction, namely the convective number, Co, and the flow resistance formulae, R_G. In the course of development of the correlation different variants of these numbers have been tested. Many of them did not meet the boundary conditions, i.e. for x=0 values of the heat transfer coefficient for liquid were not obtained, nor in the case of x=l it was possible to obtain the value of heat transfer coefficient for vapour. The data bank available to authors at the time did not include any heat transfer coefficients for flow quality approaching zero or unity. Therefore, only the values of heat transfer coefficients for fluid and vapour were known. The point was to find out a compatibility for boundary values of flow quality so as not to depreciate the simplicity of the analytical correlation. To determine the formulae describing the

flow resistance coefficient R_G there was made use of an analogy between flux resistances and the heat transfer through application of the ratio of appropriate heat transfer coefficients in an equivalent power instead of the pressure ratio. The obtained result was named a modified coefficient R_{GM} describing the convection process of heat exchange in the boiling mixture flow:

$$R_{GM} = [f_{lz} + 2(1 - f_{lz})x] \cdot (1 - x)^{1/3} + x^3 \quad (7)$$

where $f_{lz} = \frac{\mu_G}{\mu_L} \cdot \frac{C_L}{C_G} \cdot \left(\frac{\lambda_L}{\lambda_G}\right)^{1,5}$.

Having introduced R_{GM} to the correlation we obtain the compatibility of heat transfer coefficient for limiting boundary cases. To obtain compatibility also for boiling with vapour generation in flow it was necessary to assume such a form of the correction function which assumes zero values for limiting boundary conditions. This requirement was found to best met by the convective number Co. It has been constructed in the following form:

$$Co = R_G - (1 - f_l)x - f_l \quad (8)$$

3. COMPARISION OF CORRELATION WITH EXPERIMENTAL DATA

Physical properties of considered fluids have been determined by means of application of spline approximation to the physical property data provided by Hirschberg [14]. The pool-boiling heat transfer coefficient has been obtained from the fluid-specific relations of the heat flux – temperature form. The Dittus-Boelter equations was used to compute the liquid-only and gas-only heat transfer coefficients. The input data for the computing program were: mass flow rate G (kg/m^2s), saturation temperature - t_s (°C), flow quality - x(-), flow boiling heat transfer coefficient - α_{TPB} (W/m^2K) and the tube diameter - d(m). Using the method of multiple regression calculated have been coefficients a, b, c, d, e, f, g and n which were compared with the experimental values taken from the data base. The acquired data bank consisted of over 2000 points and the entire data were utilized in elaborating of the correlation. As a result of the calculations for the whole data bank, i.e. for over 2000 points it was possible to obtain the coefficients which appear in the correlation. These are: a=0.024, b=0.639, c=1.524, d=-0.907, e=2.727, f=-1.339, g=0.029 and n=0.76. The experimental data correlate with the coefficient r=0.97. The obtained result, should be regarded as a very good, taking into account that the correlation is of a general character and its coefficients do not. depend on the kind of fluid. From the histogram in Figure 1 it is evident, that 49.3% of the predictions fall in the range within ±20% of deviations, while 63.3% of predictions within ±30% of deviations. It must be borne in mind that considered data come from a variety of authors and each containing its own statistical error.

4. APPLICATION OF CORRELATION TO SMALL DIAMETER TUBES

Recent developments in heat transfer in small diameter passages bring about the question how good are the correlations developed for conventional tubes in predicting heat transfer coefficient and friction coefficient in small diameter passages.

Flow boiling in small diameter passages raises few questions, namely:

1. How does the small passage dimension affect the bubble dynamics and the two-phase flow?
2. How is the heat transfer and pressure drop affected in these channels?
3. What is the performance of best flow boiling models in predicting heat transfer and pressure drop in small diameter passages?
4. Are there any other additional effects influencing heat transfer, which are more pronounced in small diameter channels, such as for example axial heat conduction (small Peclet numbers), conjugate heat walls (relatively thick walls), temperature dependent properties (large axial temperature gradients), pressure dependent properties (large axial pressure gradients) or the wall roughness, Herwig & Hausner [15].

A very good review has appeared recently by Bergles et al. [18], where the recommendations for further research include development of experimental data and correlations for the hydraulic diameters smaller than 300 μm to predict heat transfer, pressure drop and critical heat transfer.

In order to perform comparisons some selected data from literature has been collected and the presented earlier correlation run to predict such cases. In Figures 2-4 presented are the results of calculation for three different refrigerants. The results show a good qualitative character, however quantitatively they require more accuracy of predictions. This means that the correlations developed earlier for larger diameters cannot be blindly used in predictions of data for smaller diameters, even in the light of the fact that the phenomena should only be scaled down in the considered cases.

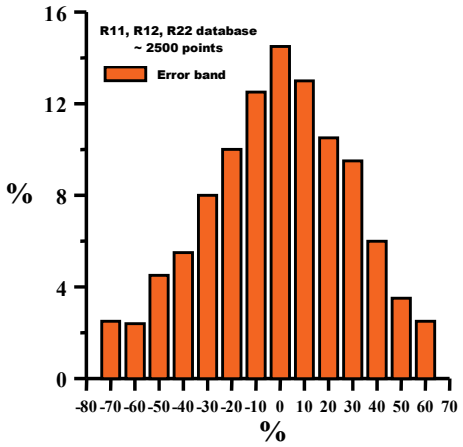

FIG. 1. Histogram of deviations for the entire data bank [12].

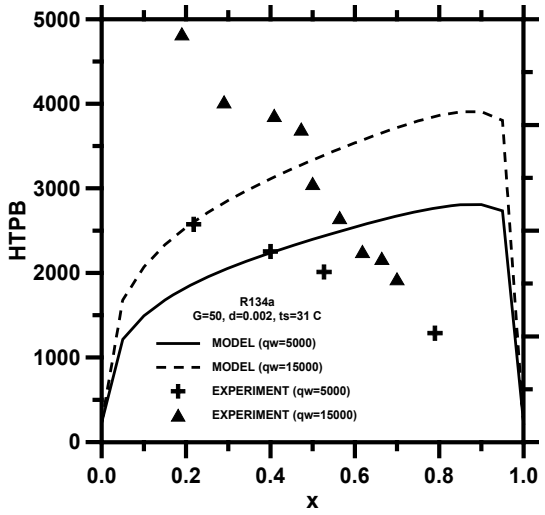

FIG. 2. Dependence of heat transfer coefficient with quality for R134a. Data due to Yan and Lin [16]. G=50 kg/m^{2}s, d=2mm.

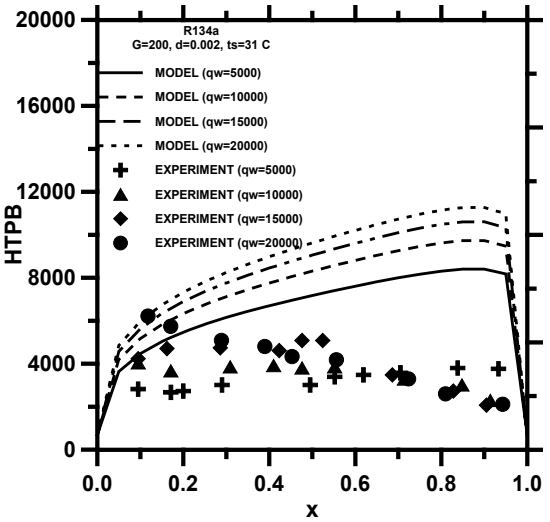

FIG. 3. Dependence of heat transfer coefficient with quality for R134a. Data due to Yan and Lin [16]. G=200 kg/m^{2}s, d=2mm.

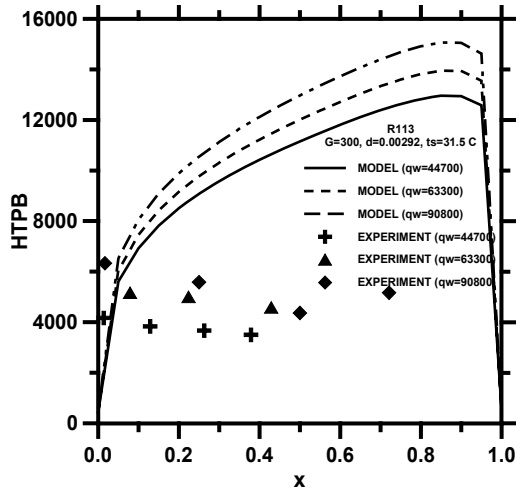

FIG. 4. Dependence of heat transfer coefficient with quality for R113. Data due to Wambsganss et al. [17]. G=300 kg/m^{2}s, d=2.92mm.

5. CONCLUSIONS

According to the theory of similarity the presented correlation can also be applied to new refrigerants as far as the investigated range of the similarity numbers is concerned. The use of correlation is very simple on account of its analytical form which is its fundamental advantage. Moreover it satisfies the requirements of the experimental correlation accuracies describing the boiling flow process. In view of the latest investigation by Kandlikar [1], it may occur that the heat transfer coefficient deteriorates with the flow quality in some cases. Such a case cannot be described by the majority of correlations known from literature on account, of their structure. The correlation under investigation possesses; such a capability which raises its quality. It is coded within the relationship of the flow resistance coefficient and the correction p. The mutual relationship between these functions makes it. possible to obtain a rising or falling dependence of heat transfer coefficient, during the boiling flow upon flow quality x. The accuracy of the proposed correlation, in the common range of parameters, is comparable with the best correlations known today. The presented correlation is of general character, and its coefficients do not depend on the type of freon. Further work on fitting of that correlation into a larger database including the small passages is required.

ACKNOWLEDGEMENTS

Financial support from the Polish State Committee for Research grant 4 T10B 054 23 is greatly acknowledged by the first author.

REFERENCES

[1] Kandlikar S.G., Fundamental issues related to flow boiling in minichannels and microchannels, Proc. Experimental Heat Transfer, Fluid Mechanics and Thermodynamics, pp. 129-146, Thesalloniki 2001.

[2] Bennet D.L. i Chen J.C., Forced convective boiling in vertical tubes for saturated pure components and binary mixtures, AIChE J., Vol. 26, 454-461, 1980.

[3] Shah M.M., A new correlation for heat transfer during boiling flow through pipes, ASHRAE Trans., Vol. 82, część 2, 66-86, 1976

[4] Shah M.M., Chart correlation for saturated boiling heat transfer: Equations and further study, ASHRAE Trans., Vol. 88, część 1, 185-196, 1982

[5] Kandlikar S.G., A General Correlation for Saturated Two-Phase Flow Boiling Heat Transfer Inside Horizontal and Vertical Tubes. J. Heat Transfer, Vol. 112, 219-228, 1989.

[6] Kandlikar S.G., A general correlation for saturated flow boiling heat transfer inside horizontal and

vertical tubes, The winter annual Meeting of the ASME Boston, Mass., December 13 - 18, 1987.
[7] Gungor K.E. i Winterton R.H.S., A general correlation for flow boiling in tubes and annuli, Int. J. Heat Mass Transfer, Vol. 29, 351-358,1986.
[8] Bjorge R.W., Hall G.R. i Rohsenow W.M., Correlation of forced convection boiling heat transfer data, Int. J. Heat Mass Transfer, Vol. 25, 753-757,1982.
[9] Mikielewicz J., Semi-empirical method of determining the heat transfer coefficient for subcooled saturated boiling in a channel, Int. J. Heat Transfer, 17, 1129 1134, 1973.
[10] Mikielewicz J., Iwicki J., Mikielewicz D., A general correlation for saturated freon flow boiling in a horizontal tube, Proc. 1st Baltic Heat Transfer Conference, Recent Advances in Heat Transfer, Ed. B. Sunden and A. Zukauskas, Elsevier Science Publishers, Goteborg 1992.
[11] Bilicki Z., Analysis of boiling heat transfer in a channel, Ph.D. Thesis, IFFM PAS, Gdansk, Poland, 1979 (in Polish).
[12] Mikielewicz D., Mikielewicz J., Flow boiling heat transfer in tubes, submitted for consideration to publish in International Journal of Heat and Mass Transfer, 2003.
[13] Muller-Steinhagen R., Heck K., A simple friction pressure drop correlation for two-phase flow in pipes, Chem. Eng. Progress, 1986, No.20.
[14] Hirschberg H.G., Kaltemittel, Verlag G.F. Muller Karlsruhe,1966.
[15] Herwig H., Hausner H., Critical view on „new results in micro-fluid mechanics“: an example, Int. J. Heat and Mass Transfer, vol. 46, 935-937, 2003.
[16] Yan Y., Lin T., Evaporation Heat Transfer and Pressure Drop of Refrigerant R-134a in a Small Pipe, Int. J. of Heat and Mass Transfer, vol. 41, 4183-4194, 1998.
[17] Wambsgans G.R. et al., Boiling Heat Transfer in a Horizontal Small-Diameter Tube, Journal of Heat Transfer, vol 115, 963-972, 1993.
[18] Bergles A.E., Lienhard V J.H., Kendall G.E., Griffith P., Boiling and Evaporation in Small Diameter Channels, Heat Transfer Engineering, vol. 24 (1), 18-40, 2003.

Strojniški vestnik - Journal of Mechanical Engineering 51(2005)7-8, 451-455
UDK - UDC 536.2
Izvirni znanstveni članek - Original scientific paper (1.01)

Analysis of loop heat pipe performance under varying wick load

A. Heitor Reis[1,2], António F. Miguel[1,2] and Murat Aydin[2,3]

[1]*Physics Department, University of Évora, R. Romão Ramalho, 59, 7000-671 Évora, Portugal*
[2]*Évora Geophysics Center, R. Romão Ramalho, 59, 7000-671 Évora, Portugal*
[3]*Dep. of Mech. Engineering, Istanbul Technical University, 34439 Gumussuyu, Istanbul, Turkey*
e-mail:ahr@uevora.pt

Abstract

Loop heat pipes (LHP) are heat transfer devices used to enhance cooling of small spaces and basically consist of sealed tubes connecting a heat source, the evaporator, whose major part is a porous wick, with a condenser that operates as heat sink. In this paper we analyse the effect of curvature of the liquid vapor interface upon the vapor pressure within wick pores. We show how this effect affects start-up by requiring a difference between wick and condenser temperatures as higher as wick pore width becomes smaller. We analysed also transient operation and found that idealy LHP are self-adjusting systems that tend to stable operation. We present a formula to describe the transient regime. The analysis provides also optimization of wick pore width for maximum heat transfer. Optimal pore width is shown to vary with temperature difference between wick and condenser. It is envisaged how this feature may help in LHP design.

Introduction

Loop heat pipes (LHP) are heat transfer devices in which a working fluid transfers continuously heat from the evaporator to the condenser. LHP operate under a pressure difference generated at a porous wick (the evaporator) and that drives the working fluid within the loop (see Fig.1). The pressure difference is due to the capillary forces drives the liquid from the condenser into the evaporator while the difference between the saturation pressures corresponding to the evaporator and condenser temperatures drive the vapor back into the condenser.

LHP have been broadly used in electronics cooling, spacecraft and other areas. Numerous papers dealing with various aspects of LHP performance characteristics have been published so far [1-12]. Our purpose is not to review this abundant literature extensively but just to focus on a feature whose complete comprehension remains rather elusive: LHP require a pressure difference across the wick in order to start properly. This is usually overcome through the use of active devices to assist in the start-up. Although some structural aspects of LHP may contribute to start-up problems, we believe that thermodynamics play here the major role.

When analyzing LHP cycles it is commonly assumed that wick pressure follows Clausius-Clapeyron equation that relates pressure to temperature at an equilibrium planar liquid-vapor interface. However liquid-vapor interfaces in the wick pores are far from being planar. In fact such interfaces are in a shape of meniscus which implies that the equilibrium vapor pressure P follows Kelvin's equation [13,14]:

$$\frac{P}{P_s} = \exp\left(-\frac{4\gamma\cos\theta}{d\rho_L R_g T}\right) \tag{1}$$

where P_s is the saturation pressure corresponding to a planar interface, γ is surface tension, θ is solid/liquid contact angle, d is pore width, ρ_L is density of liquid, R_g is the specific gas constant and T is temperature. Eq. (1) indicates that liquid can boil in the wick pores even if pressure in the overlying vapor is well bellow the saturation pressure corresponding to a planar interface that is given by Clausius-Clapeyron equation:

$$P_s = P_0 \exp\left[-\frac{h_{LV}}{R_g}\left(\frac{1}{T}-\frac{1}{T_0}\right)\right] \tag{2}$$

where h_{LV} stands for the enthalpy of evaporation and the subscript 0 for reference values.

By defining the dimensionless temperature $T^* = (R_g/h_{LV})T$ and dimensionless pore diameter

Nomenclature

D – duct diameter (m)
d – pore width (m)
h_{LV} – enthalpy of evaporation (J kg^{-1})
L – duct lenght (m)
$\dot{m}$ – mass flow rate (kg s^{-1})
n – number of wick pores
P – pressure (Pa)
P_s – saturation pressure (Pa)
$\dot{Q}$ – heat current (W s^{-1})
R_g – specific gas constant (J kg^{-1} K^{-1})
T – temperature (K)
t – time (s)
ϕ – wick load (liquid)
γ – surface tension (N m^{-1})
ν – kinematic viscosity (m^2 s^{-1})
ρ – density (kg m^{-3}
θ – solid/liquid contact angle (rad)

Superscript
* – non-dimensional

Subscripts
C – condenser
eq – equilibrium
L – liquid
max – maximum value
op – optimal
V – vapor
W – wick
0 – reference value

$d^* = (\rho_L h_{LV}/\gamma\cos\theta)d$, and combining Eqs. (1) and (2) we obtain:

$$P=P_0 \exp\left[-\frac{1}{T^*}\left(1+\frac{4}{d^*}\right)-\frac{1}{T_0^*}\right] \tag{3}$$

For difference in temperature such that $\Delta T^*/T^* << 1$, the vapor pressure difference between two successive menisci α and β (see Fig. 2 and [13] for details) is:

$$\frac{P_\alpha - P_\beta}{\langle P\rangle} \approx \frac{1}{T_\beta^*}\left(1+\frac{4}{d_\beta^*}\right)-\frac{1}{T_\alpha^*}\left(1+\frac{4}{d_\alpha^*}\right) \tag{4}$$

where <P> represents the average pressure of the vapor between the menisci.

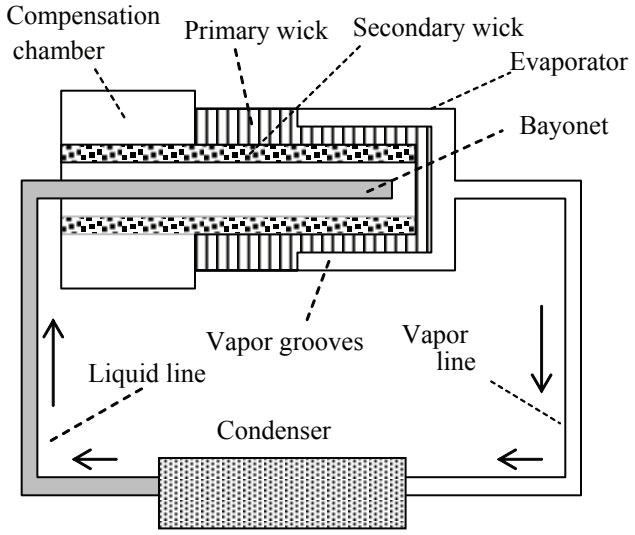

Fig. 1. Schematic representation of a LHP (major parts).

When $d^* \to \infty$ (planar interface) Eq. (3) reduces to Clausius-Clapeyron equation. However, when d* is finite the vapor pressure is lower than saturation pressure at the same temperature. This effect is as much important as the pore width becomes smaller. As a consequence when both the evaporator and condenser are at the same temperature T^*, vapor pressure in the wick is lower than that in the condenser (see Eq. (4) and [13] for details):

$$\frac{P_W - P_C}{\langle P\rangle} \approx \frac{4}{T^*}\left(\frac{1}{D_C^*}-\frac{1}{d^*}\right) < 0 \tag{5}$$

where $D_C^* >> d^*$ are the curvature radiuses of the liquid-vapor interfaces in the condenser and the wick, respectively. To start LHPs one has to surpass this negative pressure difference by increasing the wick temperature. By using Eq. (4) again, we see that LHP start-up can only occur for values of the ratio of wick temperature to condenser temperature higher than:

$$\frac{T_W^*}{T_C^*} \approx 1 + \frac{4}{d^*} \tag{6}$$

This is one of the reasons why LPHs require a significant

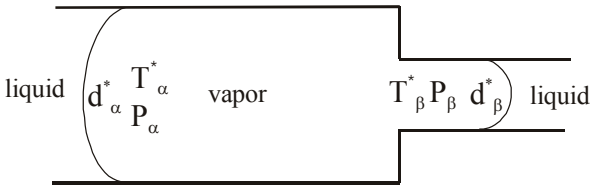

Fig. 2. Liquid/vapor interfaces of different curvature radiuses. Pressure and temperature of the vapor in equilibrium with the liquid depends upon the radius of curvature of the interface.

difference of wick to condenser temperature in order to start properly. Otherwise LHPs can even start with vapor condensation in the wick, which is recognized as "the ability to occasionally start in the reverse direction" [12].

Authors of recent LHP literature [1-12] do not consider the effect of the curvature of the interface upon the vapor pressure and usually restrict the explanations of start-up difficulties to features of LHP operation.

In this paper we address the problem LHP operation under varying heat load by taking into account the effect of interface curvature upon pressure of the vapor in the wick.

Analysis of transient LHP operation

The sum of the pressure heads and drops along a closed path within a LHP must be zero. Therefore for a LHP in a horizontal plane if ΔP_W, ΔP_V, ΔP_C and ΔP_L denote the pressure differences across the liquid-vapor interface at the wick, between vapor at the condenser and the wick, across the liquid-vapor interface at the condenser and between liquid in the wick and the condenser, respectively (see Fig. 3), this condition reads:

$$\Delta P_W + \Delta P_V + \Delta P_C + \Delta P_L = 0 \tag{7}$$

The pressure difference across the liquid-vapor interface in the wick is given by the Young-Laplace equation as [13]:

$$\Delta P_W = \frac{4\gamma\cos\theta}{d} \tag{8}$$

The vapor pressure difference between condenser and wick is the sum of the pressure head given by Eq. (4) with the pressure drop due to vapor flow (see Fig. 3):

$$\Delta P_V = \langle P \rangle \left[\frac{1}{T_C^*} - \frac{1}{T_W^*}\left(1+\frac{4}{d^*}\right)\right] + -32\dot{m}_V \nu_V \left(\frac{L_W(1-\phi)}{nd^4} + \frac{L_V}{D_V^4} \right) \tag{9}$$

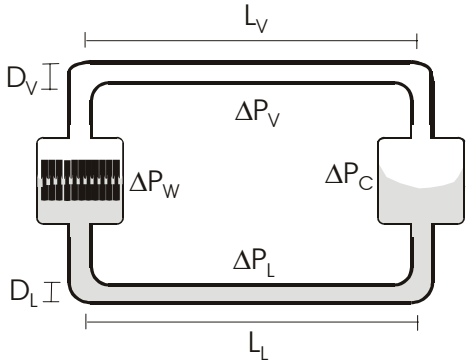

Fig. 3. Schematic representation of the liquid and vapor phases within the LHP as well as pressure differences and diameter and length of the liquid and vapor lines.

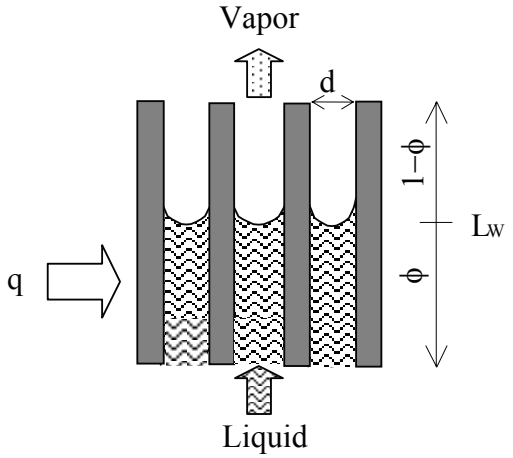

Fig.4 Schematic representation of the liquid vapor interface in the wick. Wick load is represented by ϕ that is the wick's pore filling level.

In Eq. (9) both dimensional and dimensionless variables coexist as an intermediary step towards a final dimensionless equation to be presented further on. Also in Eq. (9) $\dot{m}_V$ is vapor flow rate, d and d^* are pore width and dimensionless pore width, n is the number of wick's pores and the subscripts C, V, W represent condenser, vapor and wick.

We assume planar liquid-vapor interface in the condenser and therefore

$$\Delta P_C = 0 \tag{10}$$

By assuming Hagen-Poiseuille flow along the liquid line, the pressure drop is given by:

$$\Delta P_L = -32\dot{m}_L \nu_L \left(\frac{L_W \phi}{nd^4} + \frac{L_L}{D_L^4} \right) \tag{11}$$

where $\dot{m}_L$ is liquid flow rate and the subscript L stands for liquid.

In the wick, heat $(\dot{Q})$ is absorbed almost totally by the liquid phase (see Fig. 4) therefore we assume that

$$\dot{Q} = \phi \dot{Q}_0 \tag{12}$$

where $\dot{Q}_0$ represents the heat current absorbed by the wick at maximum load (ϕ=1).

We define wick's varying load $\dot{\phi}$ as:

$$\dot{\phi} = \frac{\dot{m}_L - \dot{m}_V}{n\rho_L d^2 L_W} \tag{13}$$

By combining Eqs. (7)-(13) and adding to the already defined d^* and T^* the following dimensionless variables:

- $P^* = P/(\rho_L h_{LV})$
- $t^* = t(\dot{Q}/(n\rho_L d^2 L_W h_{LV})$
- $\dot{Q}^* = \dot{Q}\left(32\nu_L/(\rho_L d^2 L_W h_{LV}^2)\right)$

we arrive at the following equation:

$$\frac{4}{d^*}+\left\langle P^*\right\rangle\left[\frac{1}{T_C^*}-\frac{1}{T_W^*}\left(1+\frac{4}{d^*}\right)\right]+$$
$$-\dot{\phi}^*\dot{Q}_0^*\left[\phi\left(\frac{L_W^*}{d^*}\right)^2-\frac{nL_W^*L_L^*d^{*2}}{D_L^{*4}}\right]+$$
$$-\phi\dot{Q}_0^*d^{*2}L_W^*\left[\frac{L_W^*}{d^{*4}}\left(\phi+\frac{\nu_V}{\nu_L}(1-\phi)\right)+\frac{nL_L^*}{D_L^{*4}}+\frac{n\nu_VL_V^*}{\nu_LD_V^{*4}}\right]=0 \quad (14)$$

In Eq. (14) the first and second terms represent liquid and vapor pumping heads, respectively while the remaining terms represent pressure drops due to fluid flow. Since $\dot{D}_V^*;\dot{D}_V^*>>d^*$ and $\nu_V<<\nu_L$ Eq. (14) can be simplified to:

$$H^*-\dot{\phi}^*\phi-\phi^2=0 \quad (15)$$

where

$$H^*=\frac{1}{\dot{Q}_0^*}\left(\frac{d^*}{L_W^*}\right)^2\left\{\frac{4}{d^*}+\left\langle P^*\right\rangle\left[\frac{1}{T_C^*}-\frac{1}{T_W^*}\left(1+\frac{4}{d^*}\right)\right]\right\} \quad (16)$$

is the dimensionless total pumping head.

The general solution of Eq. (15) is

$$H^*-\phi^2=A\exp(-2t^*) \quad (17)$$

where A is a constant to be determined from initial conditions. At $t^*=0$, $H^*-\phi_0^2=A$ and when $t^*\to\infty$, the dimensionless pumping head equals equilibrium wick load, i.e.

$$H^*=\phi_{eq}^2 \quad (18)$$

which implies that for reaching stable (equilibrium) operation the total pumping head H^* cannot be negative. This equilibrium condition also follows from Eq. (17) with $\dot{\phi}^*=0$ that corresponds to liquid flow rate being equal to vapor flow rate. Therefore rearranging Eq. (17) one obtains:

$$\frac{\phi_{eq}^2-\phi^2}{\phi_{eq}^2-\phi_0}=\exp(-2t^*) \quad (19)$$

which by taking into account Eq. (12) and the definitions of $\dot{Q}^*$ and t^* may be also expressed in terms of the heat current absorbed at the wick as

$$\frac{\dot{Q}_{eq}^2-\dot{Q}^2}{\dot{Q}_{eq}^2-\dot{Q}_0}=\exp\left(-\frac{2\dot{Q}_0}{n\rho d^2L_Wh_{LV}}t\right) \quad (20)$$

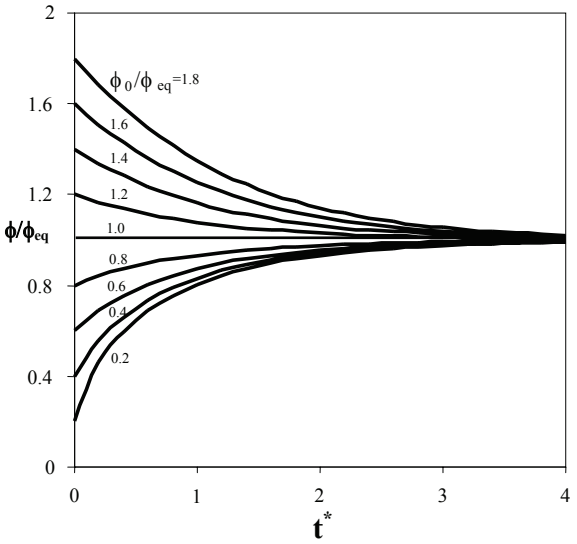

Fig. 5. Variation of wick load with time. Lines correspond to different ratios of start-up loads to equilibrium wick load. Stable operation may be reached by starting either from above or from bellow equilibrium load ($\dot{\phi}=0$) that matches stable operation.

The variation of wick load ϕ, with time is shown in Fig. 5. We see that stable operation (equilibrium) may be (ideally) reached either from above or from bellow the equilibrium wick load. In practice, often the wick is not in equilibrium itself what may lead to additional troubles in LHP operation [12]. However as Fig. 5 shows, LHPs have a self-adjusting capacity that enable them to reach stable operation.

As $H^*=\phi_{eq}^2>0$, (see Eq. 18) the total pumping head has to be always positive in order LHP to start and keep on functioning. From Eq. (16) this implies that start-up must comply with the following inequality:

$$T_W>T_C\frac{1+d^*/4}{T_C^*/\langle P^*\rangle+d^*/4} \quad (21)$$

For a planar surface, as $d^*\to\infty$ the start-up condition would be $T_W>T_C$ simply.

By considering the definitions of T^* and P^* we conclude that $T_C^*/\langle P^*\rangle$ is of order $\rho_V/\rho_L\approx10^3$ what enables us to consider that the general condition expressed by Eq. (21) is not impeditive of LHP functioning. Although Eq. (21) is a necessary condition for LHP start-up it does not represent a sufficient condition. In fact, by Eq. (16) H^* is the sum of the liquid and the vapor pumping head. Since the first, $4/d^*$, is always positive the second one may be negative. Nevertheless it is sufficient for LHP start-up that wick and condenser temperatures additionally comply also with Eq. (6). From Eq. (6) we conclude that curvature effects of the wick's liquid-vapor interface become important for $d^*=(\rho_Lh_{LV}/\gamma\cos\theta)d$ smaller than 10^3 (see Eq. 6). Since $(\rho_Lh_{LV}/\gamma\cos\theta)\approx10^{10}$ m^{-1} significant difference between wick and condenser temperatures is

required to start LHPs with wick pore widths smaller than 0.1μm.

Optimization of wick's pore width for LHP design

The analysis of the preceding section may become useful in LHP design as it allows for the optimization of wick pore width. By combining Eqs. (12) and (18) one obtains:

$$\dot{Q}^*_{eq}=\frac{d^*}{L^*_W}\left[\dot{Q}^*_0\left(\frac{4}{d^*}+\left\langle P^*\right\rangle\left(\frac{1}{T^*_C}-\frac{1}{T^*_W}\left(1+\frac{4}{d^*}\right)\right)\right)\right]^{1/2} \qquad (22)$$

By analyzing Eq. (22) we can see that heat absorbed at stable operation $\dot{Q}^*_{eq}$, can be maximized with respect to wick's pore diameter d^*. The optimal pore diameter is a function of wick and condenser temperatures of the form:

$$d^*_{op} = 2\left(\frac{T^*_C}{\langle P^*\rangle}+\frac{T^*_C}{T^*_W}\right)\frac{T^*_W}{T^*_W - T^*_C} \qquad (23)$$

which in dimensional form reads:

$$d_{op} = \frac{2\gamma\cos\theta}{\rho_L h_{LV}}\left(\frac{\rho_L R_g T_C}{\langle P\rangle}+\frac{T_C}{T_W}\right)\frac{T_W}{T_W - T_C} \qquad (24)$$

Eq. (24) shows that wick pore diameter that allows for maximum heat transfer is as smaller as the difference between wick and condenser temperatures gets higher. On the other end we see that $d_{op}\rightarrow\infty$ (planar surface) as $T_W\rightarrow T_C$.

In Eq. (24) the term within brackets is of order $\rho_V/\rho_L\approx 10^3$ while $(2\gamma\cos\theta/\rho_L h_{LV}) \approx 10^{-10}$ m^{-1}. Therefore for $T_W - T_C \approx 10$ K and $T \approx 300$K, d_{op} is of order 3μm.

Therefore Eq. (24) may help LHP manufacturers in choosing the wick pore diameter that matches optimal performance at prescribed wick and condenser temperatures.

Conclusions

The analysis of loop heat pipe (LHP) carried out in this paper shows that curved liquid vapor interfaces may change significantly equilibrium vapor pressure in wick pores of widths of order 1 μm. and smaller. This affects LHP start-up by requiring significant difference between wick and condenser temperatures for start-up to occur. This difference in temperature gets higher as the wick pore width becomes smaller.

Solution of a differential equation describing transient functioning shows that LHP are self-adjusting systems that ideally tend to stable operation either if started from above or from below stable operation points. However LHP start-up from below stable operation points are unlikely to occur in LHP whose wick pores are of order 1 μm and smaller due to the above mentioned difference between wick and condenser temperatures required to start-up.

Optimization of performance of LHP with respect to wick pore width shows that optimal pore width can be related to wick and condenser temperatures and vary linearly with the Carnot coefficient of performance of heat pumps. This aspect may help in choosing the appropriate wick structure for prescribed LHP operating conditions.

References

1. Ku, J. Operating characteristics of loop heat pipes, Proc. 29th Int. Conf. Of Environ. Systems, paper No. 981212, (1999) Denver, USA.
2. Kamotani, Y,Thermocapillary flow under microgravity – Experimental results, Adv. Space Res. **24**, 10 (1999). 1357-1366.
3. T. Kaya and T. Hoang, Mathematical modeling of loop heat pipes and experimental validation, J. of Thermophysics and Heat Transfer **13**, 3, (1999) 314-320.
4. I. Muraoka, F. M. Ramos, V. V. Vlassov, Analysis of the operational characteristics and limits of a loop heat pipe with porous element in the condenser, Int. J. of Heat and Mass Transfer **25**, 8 (2001) 2287-2297.
5. R. Chandratilleke., H. Hatakeyama, and H. Nakagome, Development of cryogenic loop heat pipes, Cryogenics **38**, (1998) 263-269.
6. N. Zhang, Innovative heat pipe systems using a new working fluid. Int. Comm. Heat Mass Transfer, **28** (2001) 1025-1033.
7. H. F. Smirnov and B. V. Kosoy, Refrigerating heat pipes, Appl. Therm. Eng. 21 (2001) 631-641.
8. Q. Liao. and T. S. Zhao, Evaporative heat transfer in a capillary structure heated by a grooved block, J. of Thermophysics and Heat Transfer **13,** No**.** 1 (1999) 126-133.
9. J. S. Allen, K .P.Hallinan and J. Lekan, A study of the fundamental operations of a capillary driven heat transfer device in both normal and low gravity, AIP Conference Proceedings **420**, (1998) 471-477, Ed. American Institute of Physics, Woodbury, New York.
10. C. Figus, Y. Le Bray, S. Bories, and M. Prat Heat and mass transfer with phase change in a porous structure partially heated: continuum model and pore network simulations, Int. J. of Heat and Mass Transfer **42** (1999) 2557-2569.
11. J. Ku, Operating characteristics of loop heat pipes, Int. Conf. on Env. Syst., paper 1999-01-2007.
12. J. Baumann, B. Cullimore; J. Ambrose, E. Buchan and B. Yendler, A methodology for enveloping reliable start-up pf LHPs. Paper nº 2000-2285, (2000) Am. Inst. of Aeronautics and Astronautics, Inc.
13. A. H. Reis, Thermodynamics of fluids in mesoporous media, in D. B. Ingham (Ed.) Proc. of NATO Adv. St. Inst. on Porous Media, 9-20 June 2003, Ovidius Un. Press (2003).
14. A. H. Reis and R. Rosa, Sorption isotherms as a fundamental tool for the analysis of coupled heat and mass fluxes in porous media, J. of Porous Media (to appear in 2004).

Strojniški vestnik - Journal of Mechanical Engineering 51(2005)7-8, 456-461
UDK - UDC 536.2
Izvirni znanstveni članek - Original scientific paper (1.01)

A Numerical Study of Thermosolutal Melting

Thomas J Scanlon[1] and Matthew T Stickland[1]

[1]*Department of Mechanical Engineering, University of Strathclyde, Glasgow, G1 1XJ, Scotland*
** e-mail tscanlon@mecheng.strath.ac.uk*

Abstract

This paper describes the numerical investigation into the melting of a pure ice block into an aqueous solution of sodium carbonate (Na_2CO_3). The numerical study is concerned with capturing the evolving solid-fluid interface during phase change while solving sequentially the double-diffusive conditions resulting from the combined effects of thermal and solutal buoyancy in the flow field. The results show that, with a relatively simple phase change model incorporated into a fixed grid, finite volume numerical formulation, reasonable concurrence may be obtained in comparison with published experimental data.

Introduction

The melting of ice in mixtures began as a problem for the melting of glaciers in sea water motivated by oceanographers. The melting of glaciers in sea water has assumed further importance recently because of the apparent increasing temperature in the earth's environment. Therefore, it is important to analyse correctly the characteristics of the melting of ice in mixtures.

Such natural convection phenomena, driven by the twin competing buoyancy forces due to concentration and temperature gradients, have been of interest to many authors during the latest decades. The thermosolutal natural convection is seen to play an important role in controlling the characteristics of solid-liquid phase change in mixtures [1-2]. It has been found that the time evolution of the solid-liquid interface and the local equilibrium conditions existing at the interface are strongly coupled to the interface heat and mass transfer due to thermosolutal convection. In solidification processes, changes in the time evolution of this coupling is one of the principal criteria which governs the front velocity and any micro or macro segregation effects. Such effects are thus considered to impinge directly on the homogeneity of the forming solid [3-8].

A significant number of experimental and numerical studies have been devoted to double-diffusive convection associated with melting or solidification. In the case of solidification, the existence of a mushy zone adjacent to the solid-liquid interface is a specific problem that will not be considered in this paper. In the context of melting, a series of fundamental experimental and theoretical studies have been executed concerning buoyancy-induced flows driven by combined thermal and solute transport near a vertical melting ice surface in saline water [9-12]. Considering melting in a cavity [13-21], an analytical and experimental study has been carried out [13] which focused upon the different modes of double-diffusive convection arising from a horizontal melting interface. Using the same configuration, a quantitative model and scaling analyses of melting or dissolving driven by compositional convection has also been developed [14-16]. When the phase change interface is vertical, multicellular flow structures are seen to arise in the cavity that strongly influence the melting characteristics [17-21].

Numerical Methodology

The aim of the computational is to develop, as far as possible, a reliable model of the thermo-fluid behaviour of a block of pure ice melting into an aqueous solution of sodium carbonate under conditions of natural convection as detailed in figure 1. The computational model would be based on a coupled thermo-fluid system with laminar natural convection heat and mass transfer with phase change occurring. The aim would be to establish the critical modelling parameters encountered in such flows. The computational model is undertaken within the framework existing commercial computational fluid dynamics analysis software FLUENT which

Nomenclature

$Ra_T = \dfrac{g\beta_T \Delta T H^3}{\alpha \upsilon}$ = thermal Rayleigh number

α = thermal diffusivity of the fluid (m^2/s)
υ = kinematic viscosity of the fluid (m^2/s)

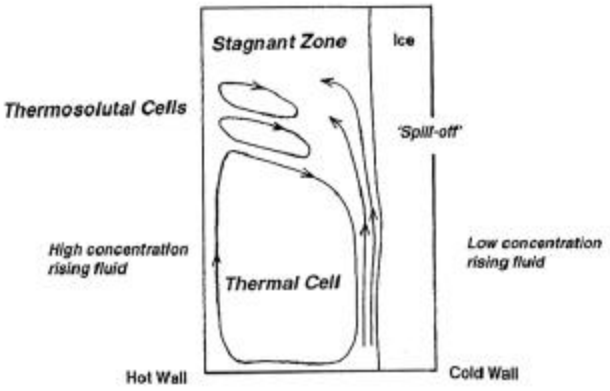

Figure 1 Tyical flow structures involved in thermosolutal melting.

offers current capabilities for coupled thermal and fluid analysis but cannot address the details of the thermo-physical modelling being required here. Such features need to be incorporated using user subroutines. Such work has recently been described by Scanlon and Stickland [22-27].

This numerical methodology proposes that the governing equations are solved in a manner such that if the temperature falls below the freezing isotherm then the convection terms in the equations of motion are effectively disengaged. Variations in the specific heat of the material are incorporated in order to account for the phase change according to the graph shown in figure 2, where Δh_{fus} is the latent heat of fusion of ice, ΔT is the finite temperature bandwidth over which phase change is assumed to occur and *PCZ* is an acronym for the phase change zone.

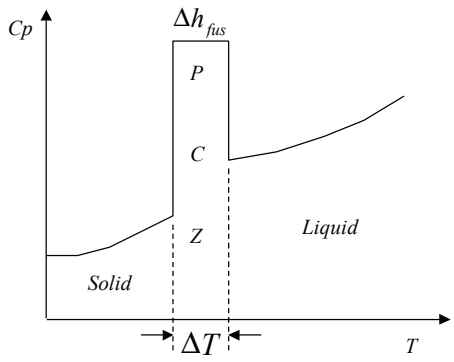

Figure 2 Variation in specific heat with temperature

The model of Scanlon and Stickland [22-27] has been shown to be a stable, computationally efficient, uncomplicated numerical technique that provides reasonable solutions to complex problems involving natural convection with phase change, as shown in figures 3 and 4.

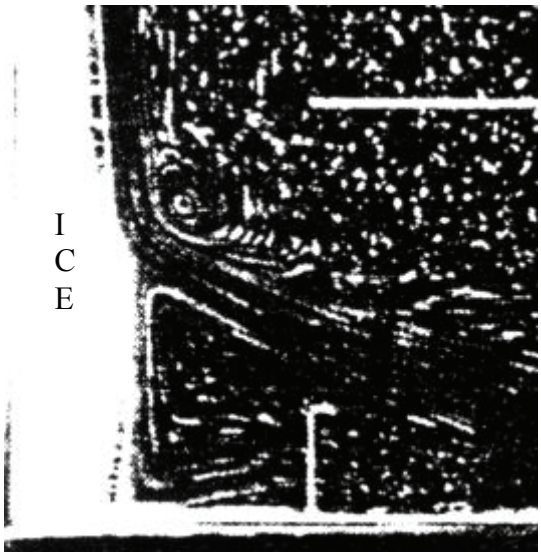

Figure 3 Experimental results (particle tracers) for the freezing of pure water on a vertical wall [24].

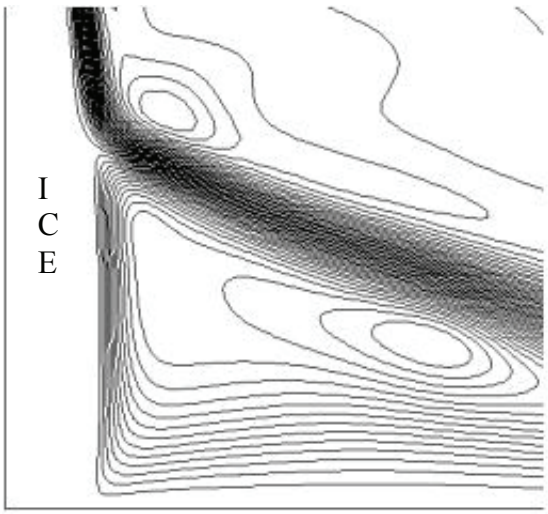

Figure 4 Numerical prediction (streamlines) for the freezing of pure water o a vertical wall [24].

The experimental work of Bénard *et al* [20], to which the numerical solution will be compared, is detailed in figure 5

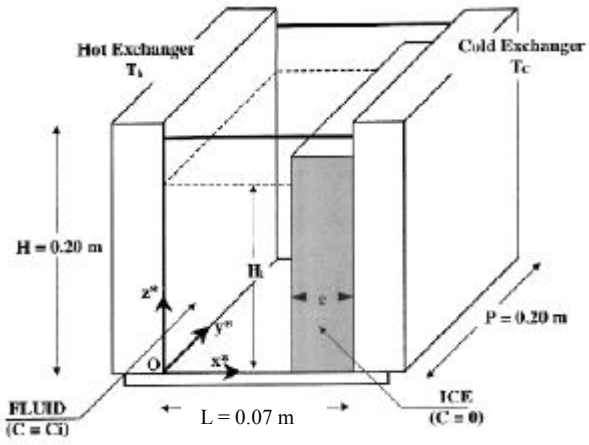

Figure 5 Experimental set up of Bénard *et al* [20].

The experimental cell consists of a rectangular cavity (height H = 20 cm, width L = 7 cm and depth P = 20 cm) designed to generate a two-dimensional flow. The two opposing walls are heat exchangers which are differentially heated at constant and uniform temperatures controlled by two independent thermal loops where a water-glycol mixture is circulated.

For the experimental conditions considered in this paper, pure water (concentration C = 0) is contained within distance *e*. the rest of the cell contains a still solution of Na_2CO_3 of concentration C_i = 2 % by mass. This aqueous solution is separated from the pure water by a thin metal plate. Initially, the whole experimental system is maintained a few tenths of a degree under 0 °C after which a rectangular block of pure ice will have formed and is attached to the cold wall.

The initial dimensions of the ice block are 3 cm thickness (distance *e*) and height H_i = 14 cm. This implies an initial length for the aqueous solute of 4 cm. For an initial solute concentration of 2 % (by mass), the corresponding equilibrium liquidus temperature is –0.66 °C, so the solute mixture remains in its liquid phase. At time t = 0 the metal barrier is removed very slowly such that the fluid is not disturbed and the hot exchanger is raised quickly to a temperature of T_h = 10 °C which is maintained throughout the experiment. The cold exchanger temperature is kept at Tc = 0 °C. For the numerical solution the bottom wall is considered to be adiabatic while at the top surface symmetric solutions are assumed.

Thermosolutal convection is characterized by five dimensionless parameters; the Prandtl number *Pr*, the Lewis number *Le*, the thermal Rayleigh number Ra_T, the buoyancy ratio N and the aspect ratio A ($A = Hi/e$ in Figure 5). This leads to the conditions outlined in Table 1 which are considered in this study. Such a range of parameters may be varied through the initial concentration of the liquid and the temperature difference

Table 1 Parameters considered in the numerical study

Pr	11
Le	190
Ra_T	3.8×10^8
N	-8
A	4.667

between the heat exchangers. The buoyancy ratio N represents the effects of solutal buoyancy to thermal buoyancy where N is defined as:

$$N = \frac{\beta_S C_i}{\beta_T \Delta T} \tag{1}$$

For an initial concentration C_i = 2 % by mass, a temperature difference $?T$ = 10 K and a thermal expansion coefficient $ß_T = 3.275 \times 10^{-4}$ K^{-1} this produces a solutal expansion coefficient $ß_S$ = -1.31002 wt percent^{-1}. The experimental conditions are such that the initial solute mass fraction ranges between 2 % and 5 %. Under such conditions, the density is observed to be a linear function of temperature and concentration such that the standard linear Boussinesq approximation can be applied and the density inversion effects found in pure water are negated. In this manner the density may be considered as a linear function of temperature and concentration according to [20]:

$$\rho = \rho_0 \left(1 - \beta_T \delta T - \beta_S C\right) \tag{2}$$

where $?_0$ = 999.8 kg/m^3 is the density of pure water at T = 0.01 °C. In order to incorporate mass transfer an additional transport equation is required for the solute transport with appropriate initial and boundary conditions. For the initial solute conditions a concentration is applied to the ice (C = 0) and solute (C_i = 0.02) regions respectively. As the numerical solution progresses, it is only when melting of an initially solid cell in the ice zone occurs that the nascent fluid cell will allow the solute to be advected into the melt flow.

For the numerical solution a computational mesh of 180000 rectangular cells was employed and a time step of 4 s was adopted. For the pressure-velocity coupling the conventional SIMPLE scheme was used. Temporal discretisation was based on an implicit method and for convective discretisation the QUICK scheme was employed. This led to total computational times of approximately 30 hours on a Pentium4 3GHz PC with 512 Mb RAM.

Results and Discussion

The following results show the comparison between the numerical work (contours of solute concentration) and the experimental results of Bénard *et al* [20] (observations by fluorescence – lighter regions = lower concentration):

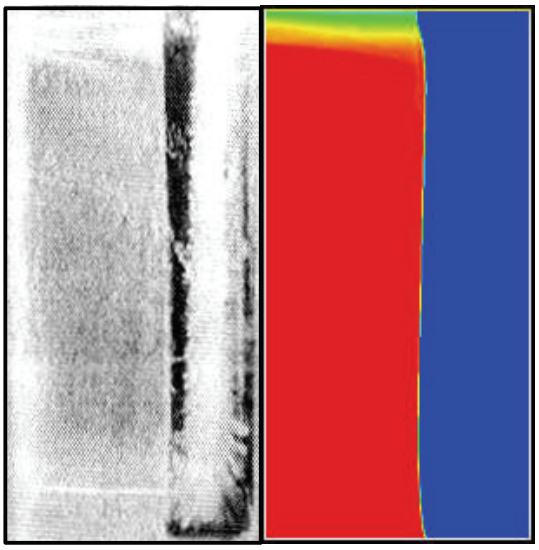

Fig. 6 Experiment (left), Numerical (right), t = 7 min

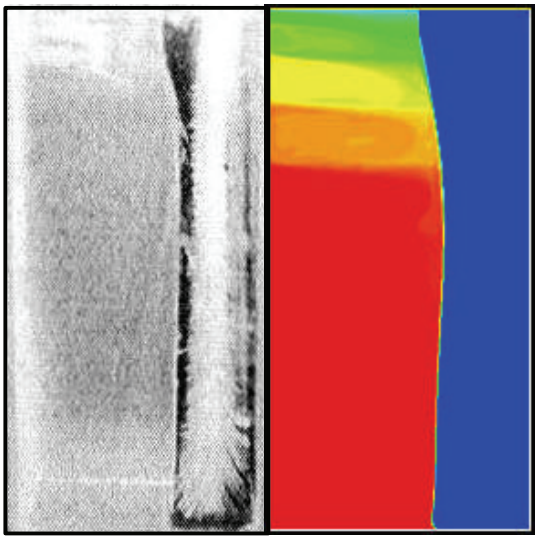

Fig. 7 Experiment (left), Numerical (right), t = 15 min

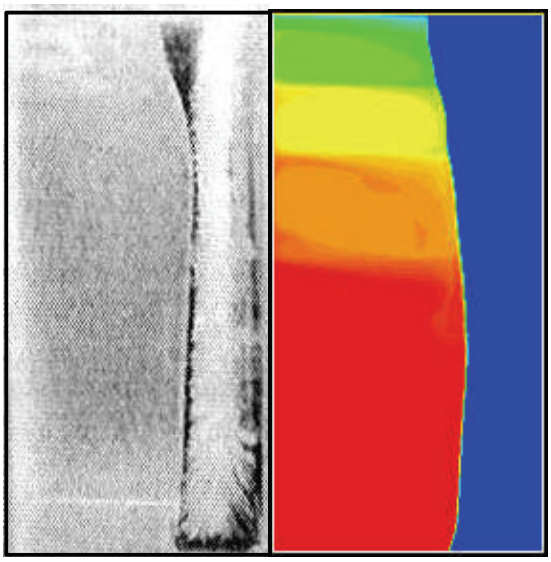

Fig. 8 Experiment (left), Numerical (right), t = 20 min

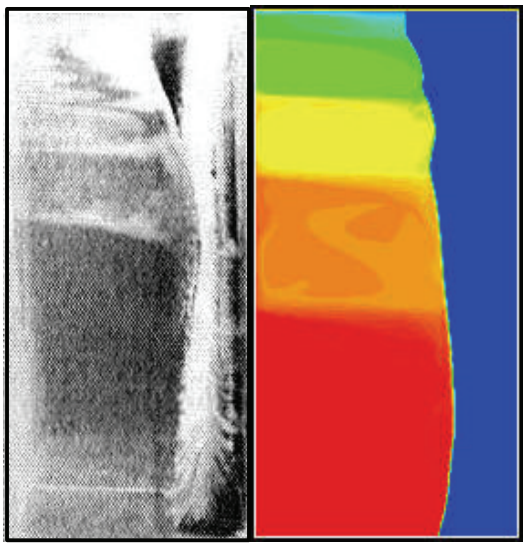

Fig. 9 Experiment (left), Numerical (right), t = 25 min

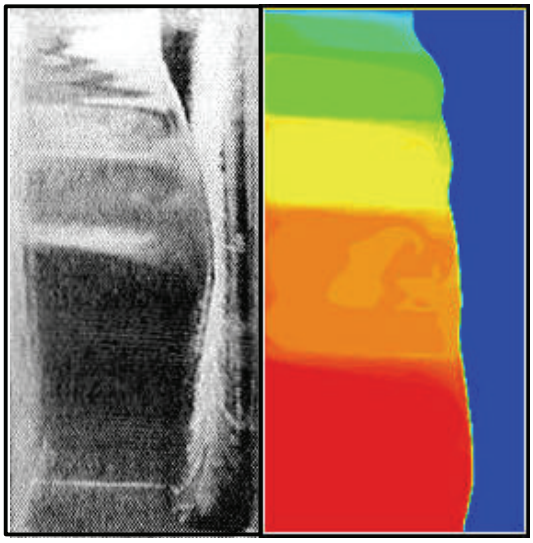

Fig. 10 Experiment (left), Numerical (right), t = 30 min

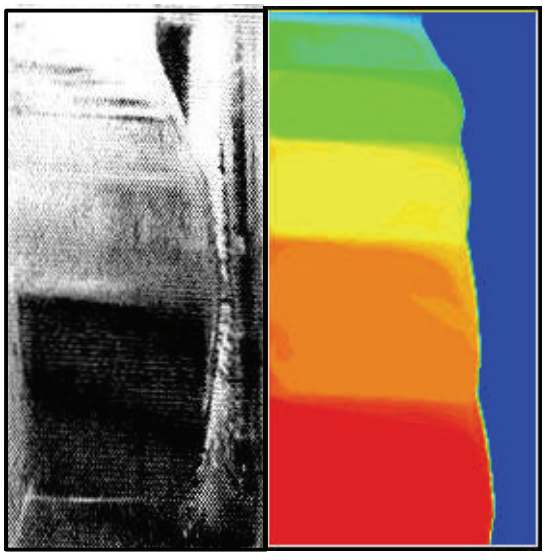

Fig. 11 Experiment (left), Numerical (right), t = 35 min

In figures 6-11 we can observe the temporal evolution of the thermosolutal melting process over a period of 35 minutes. It is evident that the competing effects of thermal and solutal buoyancy in the melt flow result in the non-linear solid-fluid interface profiles observed. The general form of this interface is of a progressive 'waisting' effect around the central core of ice with thicker upper and lower solid regions.

From the numerical study it was observed that horizontal fingers of warmer fluid existed which traversed the fluid region and effectively 'bit' into the ice via the melting process. Such multicellular regions of varying concentration appear to have been captured qualitatively by the numerical techniques employed in this study.

Conclusions

A numerical study of thermosolutal melting has been carried out. The numerical techniques employed have attempted to capture the time-evolving interface of pure ice melting into an aqueous solution of Sodium Carbonate and the resulting double-diffusive flow with its competing influences due to thermal and solutal buoyancy.

The numerical results show a reasonable qualitative concurrence with published experimental work with the general trends of solid-fluid interface evolution and thermosolutal melt flow characteristics being captured.

References

[1] Huppert, H. E. and Turner, J. S., Ice Blocks Melting into a Salinity Gradient, *Journal of Fluid Mechanics*, Vol. 100, pp. 367-384, 1980.

[2] Huppert, H. E., The Fluid Mechanics of Solidification, *Journal of Fluid Mechanics*, Vol. 280, pp. 287-302, 1990.

[3] Prescott, J. P. and Incropera, F. P., Convective Transport Phenomena and Macrosegregation During Solidification of a Binary Metal Alloy: I-Numerical Predictions, *ASME J. Heat Transfer*, 116, pp. 735-741, 1994.

[4] Prescott, J. P. and Incropera, F. P., Convective Transport Phenomena and Macrosegregation During Solidification of a Binary Metal Alloy: II- Experiments and Comparisons with Numerical Predictions, *ASME J. Heat Transfer*, 116, pp. 742-749, 1994.

[5] Campbell, T. A. and Koster, J. N., Visualizations of Liquid-Solid Interface Morphologies in Gallium Subject to Natural Convection, *J. Cryst. Growth*, 140, pp. 414-425, 1994.

[6] Yin, H. and Koster, J. N., Double Diffusive Convective Flow and Interface Morphology During Transient Ga-5 percent in Alloy Melting, *J. Cryst. Growth*, 217, pp. 170-182, 2000.

[7] Tanny, J., Experimental Study on the Crystallization of a Binary Melt at the Vertical Boundary of an Enclosure, *Int. J. Heat Mass Transf.*, Vol. 38, pp. 1141-1150, 1995.

[8] Wettlaufer, J. S. and Worster, M. G., Natural Convection During Solidification of an Alloy from Above with Application to the Evolution of Sea Ice, *Journal of Fluid Mechanics,* Vol. 111, pp. 291 – 316, 1997.

[9] Joseberger, E. G. and Martin, S., A Laboratory and Theoretical Study of the Boundary Layer Adjacent to a Vertical Melting Ice Wall in Water, *Journal of Fluid Mechanics*, Vol. 111, pp. 439-473, 1981.

[10] Carey, V. P. and Gebhart, B., Transport Near a Vertical Ice Surface Melting in Saline Water: Some Numerical Calculations, *Journal of Fluid Mechanics,* Vol. 117, pp. 379 – 402, 1982.

[11] Carey, V. P. and Gebhart, B., Transport Near a Vertical Ice Surface Melting in Saline Water: Experiments and Low Salinities, *Journal of Fluid Mechanics,* Vol. 117, pp. 403 – 423, 1982.

[12] Sammakia, B. and Gebhart, B., Transport Near a Vertical Ice Surface Melting in Water of Various Salinity Levels, *Int. J. Heat Mass Transf.,* Vol. 26, pp. 1439-1452, 1983.

[13] Woods, A. W., Fluid Mixing During Melting, *Phys. Fluids* A, 3, pp. 1393-1404, 1991.

[14] Woods, A. W., Melting and Dissolving, *Journal of Fluid Mechanics*, 239, pp. 429-448, 1992.

[15] Kerr, R. C., Melting Driven by Vigorous Compositional Convection, *Journal of Fluid Mechanics*, 280, pp. 255-285, 1994.

[16] Kerr, R. C., Dissolving Driven by Vigorous Compositional Convection, *Journal of Fluid Mechanics*, 280, pp. 287-302, 1994

[17] Sugawara, M. and Irvine, T. F., The Effect of Concentration Gradient on The Melting of a Horizontal Ice Plate From Above, *Int. J. Heat Mass Transf.*, Vol. 43, pp. 1591-1601, 2000.

[18] Beckerman, C. and Viskanta, R., Double-Diffusive Convection Due to Melting, *Int. J. Heat Mass Transf.*, Vol. 31, pp. 2077-2089, 1988.

[19] Beckerman, C. and Viskanta, R., An Experimental Study of Melting of Binary Mixtures With Double-Diffusive Convection in the Liquid, *Exp. Therm. Fluid Sci.*, Vol. 2, pp. 17-26, 1989.

[20] Benard, C., Benard, R., Bennacer, R. and Gobin, D., Melting Driven Thermohaline Convection, *Physics of Fluids*, Vol. 8, pp. 112-130, 1996.

[21] Mergui, S., Geoffroy, S. and Benard, C., Ice Block Melting Into a Binary Solution: Coupling of the Interfacial Equilibrium and the Flow Structures, *ASME Journal of Heat Transfer*, Vol. 124, pp. 1147 – 1157, 2002.

[22] Scanlon, T.J., Stickland, M.T. and Robertson, N.A., A Numerical and Experimental Analysis of Natural Convection Ice Melting. *Presented at*

the 6th UK National Conference on Heat Transfer, Heriot-Watt University, 15-16 September 1999. Published in IMechE Conference Transactions 1999-7-C565/064, pp. 443-452, 1999.

[23] Scanlon, T.J., and Stickland, M.T., An Experimental and Numerical Investigation of Natural Convection Melting. *Int. Comm. Heat Mass Transfer*, Vol. 28, No. 2 (01), pp. 181-190, 2001.

[24] Scanlon, T.J. and Stickland, M.T., A Numerical Analysis of Buoyancy-Driven Melting and Freezing , *Int. J. Heat Mass Transf.,* 47, pp.429-436, 2004.

[25] Stickland, M.T., Scanlon, T.J., Oldroyd, A. and Waddell, P. An Experimental and Computational Analysis of Buoyancy Driven Flows by LaserSheet Tomography, Particle Image Velocimetry and Computational Fluid Dynamics. *Proceedings of the 1st Pacific Symposium on Flow Visualisation and Image Processing*, Honolulu, USA, February 23-26, Vol. 1, pp.203-208, 1997.

[26] Scanlon, T.J. A Numerical Model of the Ice Melting Process. Presented at the *3rd International Conference on Advances in Heat Transfer,* Montreal, Canada, May 2000. Published in Advances in Fluid Mechanics III, Ed. M. Rahman and C. A. Brebbia, pp. 313-322, 2000.

[27] Scanlon, T.J., Stickland, M.T. and Lacombe, M., A PIV Analysis of Natural Convection Ice Melting, *European Association of Laser Anemometry Conference*, September 2001, Limerick, Eire.

Strojniški vestnik - Journal of Mechanical Engineering 51(2005)7-8, 462-469
UDK - UDC 536.2
Izvirni znanstveni članek - Original scientific paper (1.01)

The Use of a Phase Change Material within a Cylinder Wall in order to Detect Knock in a Gas SI Engine

Jérôme Bellettre*, Eric Ollivier, Mohand Tazerout

Department of Energetics and Environmental Engineering, Ecole des Mines de Nantes, La Chantrerie 4 rue Alfred Kastler BP 20722 44307 Nantes cedex, France, *Jerome.Bellettre@emn.fr

Abstract

The present paper studies the possibility to develop a new method of knock detection in a gas SI engine. This method is based on the increase in the wall heat flux when knock occurs. It also must be simple enough to be used by industry. In order to achieve this goal, a metallic Phase Change Material is put within the wall cylinder. The melting of the PCM means that knock has occurred and is persistent. The melting of such a phase change material would be easy to detect using industrial measurement tools.

In this paper, numerical simulations of unsteady heat transfer across the cylinder wall are presented. Unsteady heat transfer from the hot gas to the wall chamber is simulated by a self-developed program. This program allows fixing instantaneous local heat flux values deduced from the literature in case of both normal and knocking combustion. Heat transfer across the cylinder wall is solved by the finite volume technique. Grid is validated by comparison with analytical results. Melting is treated by the Voller and Prakash model and Sodium is chosen as PCM. Among all the results, we can notice that an increase in the knock intensity changes the shape of the isothermal curves around and inside the PCM. This leads to an increase in the melting velocity with a higher rate than the increase in the heat flux.

Introduction

Knock is due to an unexpected combustion in Spark Ignition (SI) engines. It is a result of spontaneous ignition of a portion of end gas in the engine chamber, ahead of the propagating flame. The very rapid heat release implied by this abnormal combustion generates shock waves that can lead to the decrease in output, the increase in some pollutants and the destruction of the engine. Although knock has been more or less overcome in gasoline engines by controlling the fuel quality, gas engines are not safe from knock. Natural gas contains different gases (CH_4, C_2H_6, etc.) with variable knock-resistance. Its composition varies widely with time and place. Consequently, an engine can start to knock if the gas reaches too low anti-knocking properties. A reliable method for the detection of knock in gas SI engine is then of high interest.

The knock detection is currently based on data generated by accelerometers or cylinder pressure sensors [1, 2]. Due to its simplicity, accelerometry (vibration measurement) is largely employed in industry. Nevertheless, parasitic noises relative to engine operation often affect the quality of knock detection in this method. On the other hand, cylinder pressure data provide a direct and reliable way to analyze knock. The major disadvantage is that a suitable probe has to be provided in the engine cylinder that may reduce the engine lifetime [3].

Knock occurrence is accompanied by an important increase (up to 4 times higher) in the wall heat transfer inside the combustion chamber [4-6]. Thus, an alternative to the current methods could be the detection from analysis of the thermal signal measured near the outer side of the cylinder. However, the deadening effect of the cylinder wall makes such detection difficult [7-9]. Moreover even low knock intensity (with low increase in heat transfer) should be detected in order to protect reliably the engine. The use of a Phase Change Material (PCM), placed within the wall cylinder, can make this target reachable because the phase change is easy to detect with industrial tools.

The present paper treats numerically the melting of a metallic PCM. It is divided into three main parts. Firstly, the background in the field of knock detection deduced from heat transfer analysis is presented. Secondly, the

Nomenclature

c_p	specific heat capacity, J/kg.K
d	depth of the slot, m
e	wall thickness, m
h	enthalpy, J/kg
k	thermal conductivity, W/m.K
l	connecting rod length, m
r	crankshaft radius length, m
T	temperature, K
t	time, s
w	width of the slot, m
w/d	width to depth ratio, -
x	horizontal coordinate, m
y	vertical coordinate, m

Greek letters

α	thermal diffusivity, m^2/s
Δh	latent heat of melting, J/kg
θ	crank angle, rad
ω	angular frequency, rad/s
ρ	density, kg/m^3

Subscript

e	on the outer side of the wall
i,	i direction
m	time averaged
ext	external
w	on the inner side of the wall

modeling assumption and the validation of the model are detailed. Finally, model is exploited and main results are then exposed and discussed.

Background

In previous studies [7-9], we studied numerically the thermal signal in the coolant flow close to the outer side of the cylinder wall. A rib or a slot was made on the external surface in order to enhance the temperature variations. An example of sketch of those studies is presented in Fig. 1. We treated the case of a water-cooled engine running at 1500 rpm and full load. Its stroke is 170 mm and bore is 152 mm.

The computational domain (Fig. 1) includes the cylinder liner, (made of cast iron), the water jacket (10 mm wide) and the cylinder head (made of aluminum). The representation of the latter is very simplified because only its contribution to the vertical heat flux in the cylinder liner has to be taken into account. A cavity [8] or a rib [9] was machined at the top dead center on the outer surface of the cylinder liner. The coolant flow is vertical and extents from the bottom to the top of the cylinder liner along the external side of the cylinder. Calculations have shown that a two-dimensional plane representation was equivalent to a 2D asymmetric one so the coolant is assumed to flow in a 10 mm wide rectangular duct.

The heat transfer from the hot burnt gas to the chamber walls is simulated by a self-developed program that allows fixing instantaneous heat flux values deduced from the literature in case of both normal and knocking combustion. An example of heat flux is plotted in Fig. 2. In all the studied case, knock occurs one time every two cycles. The combustion starts when the piston reaches top dead center and its duration is 0.033s (corresponding to 30° Crank Angle at 1500 rpm). The equation of the piston movement (Eq. 1) is given by:

$$y = \left[r \times \cos\theta + l \times \sqrt{1 - (r/l)^2 \times (\sin\theta)^2} \right] \quad (1)$$

where y is the vertical position of the piston, θ the crankshaft angle and r and l the lengths of the crankshaft radius and of the connecting rod.

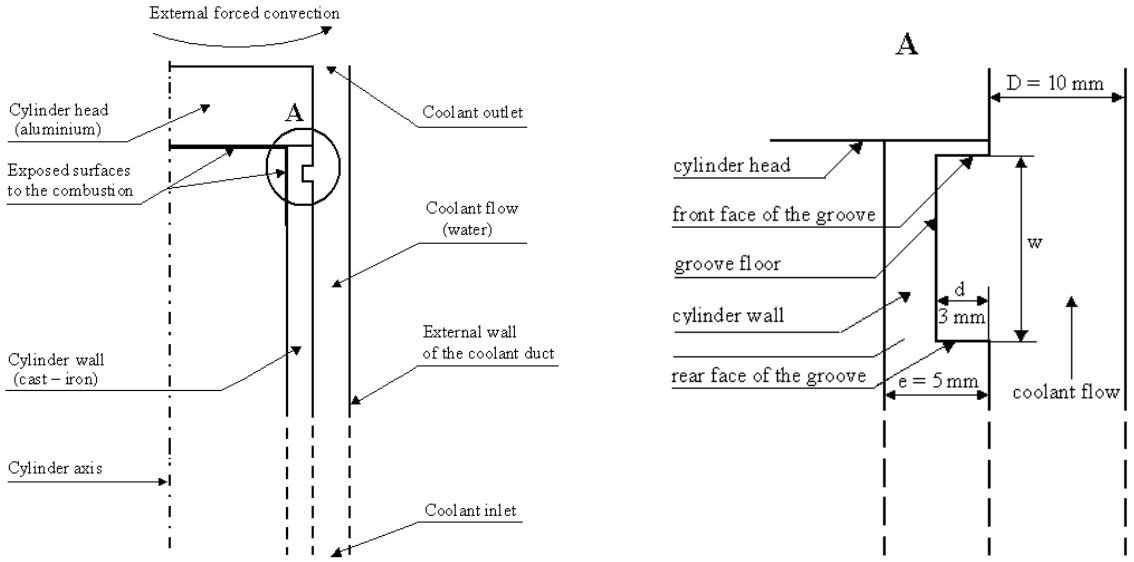

Fig. 1 Sketch of a previously studied configuration [8]

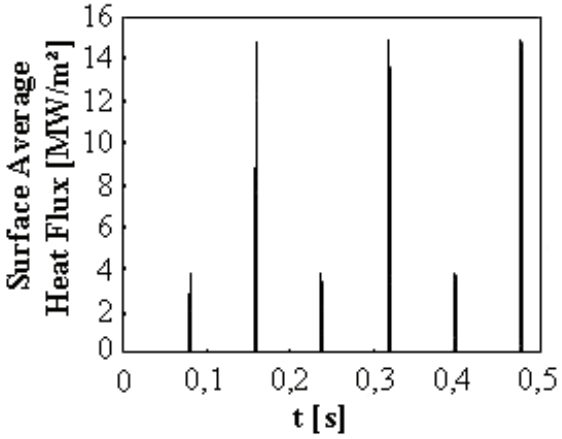

Fig 2. Unsteady heat flux imposed for a semi knocking combustion (50%) [8]

According to Eq. (1), only 31.64 mm of the wall height can face the combustion, during the combustion period. This distance is divided into five parts. The heat flux received by each one is a function of the time they are exposed to the combustion. The associated heat flux is assumed to have sinusoidal variation with time during the combustion period.

The two previously obtained main results are summarized here. More details can be found in reference [7-9]. Firstly, in the case of a square slot machined on the outer wall surface, Fig. 3 shows the resulting temporal variations of temperature in the coolant, 0.5 mm above the floor. Only variations due to knocking combustion can be seen. Those variations are the highest in point 1 (see Fig. 3a) which is situated in the upstream corner of the groove. At this location, they are 3 times higher than for a 2 mm thick smooth plane wall (Fig. 3b). This is due to the low velocity of the flow that makes the fluid stagnant. The passage of the fluid in this location of the groove occurs after a larger residence time along the cavity floor compared to other points. Moreover, the location of point 1 coincides with streamlines that skim the cavity floor.

Loubar et al. [9] studied the effect of a rib placed in the outer side of the wall. They found a similar result. A surface roughened gives good results in terms of amplitude amplification. The temperature variations are approximately 20 times those obtained with smooth surface at the same location (Fig. 4). The presence of recirculation in downstream of the rib (Fig. 4) makes the residence time of the fluid in contact of the wall more important. Consequently, the fluid has got more time to collect the thermal signal. As in Ollivier et al. [8], they found that the best location regarding amplification is located in the upstream left corner of the recirculation.

Even if thermal signal amplitude inside the coolant may be significantly increased compared to a smooth wall case, we must notice that temperature variations are always weak within the water (around 0.2 K in the best case). This is due to the important deadening effect of the metallic wall. Consequently, it would be difficult to detect knock by measuring such variations using industrial measurement tools.

The use of the phase change phenomena in order to detect knock occurrence can lead to the development of method that requires less accuracy regarding the thermal sensors. Thus, the melting of PCM placed within the wall cylinder is now going to be numerically treated.

Modeling assumption

The principle of the proposed technique is illustrated in Fig. 5. A cavity filled with a Phase Change Material (PCM) is placed within the cylinder wall. The melting temperature of the PCM should be chosen in order to be solid in the case of normal combustion.

In the chosen configuration, there is no need to simulate the heat transfer within the coolant flow. The computational domain is then reduced to the cylinder wall (made in cast iron) and the cylinder head (made in aluminum, cf. Fig. 5).

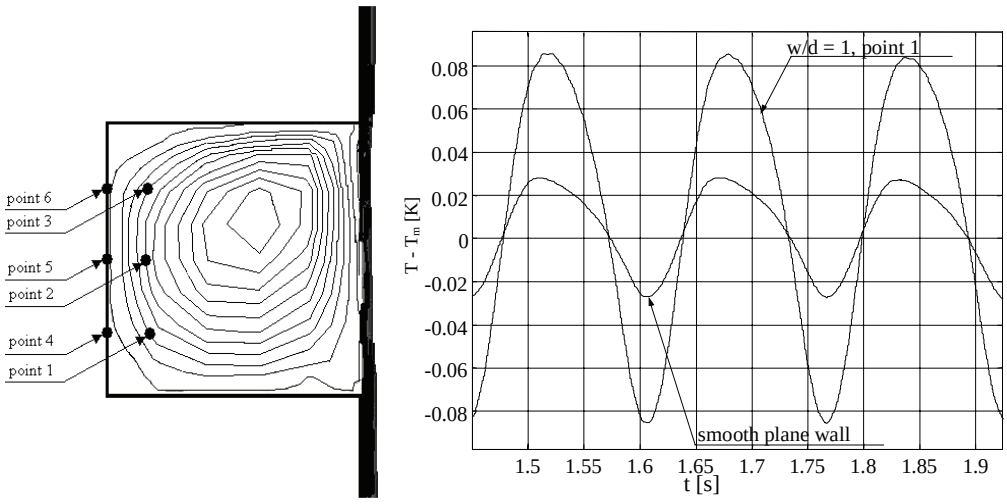

a) b)

Fig. 3 a) Recording points in the square slot ($w/d = 1$)[8] b) Temporal temperature variations for a 2 mm thick smooth plane wall and in point 1 of the square slot [8]

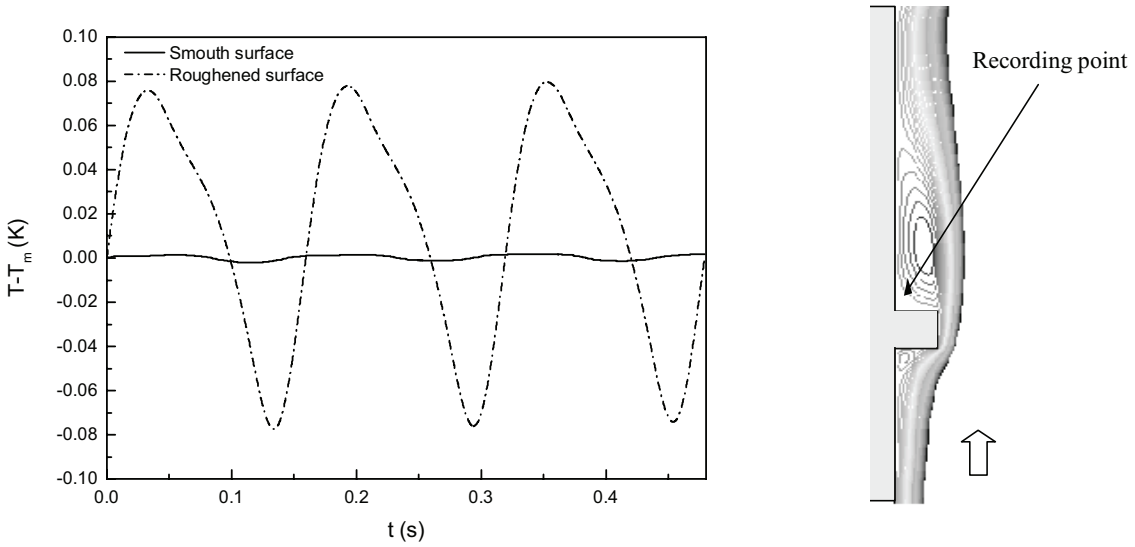

Fig. 4 Temporal variation of temperature in the fluid (0.5 mm from the wall) and recirculation zone downstream the rib [9]

Eq. (2) governs the heat transfer in the whole computational domain:

$$\frac{\partial \rho h}{\partial t} = \frac{\partial}{\partial x_i}\left(k\frac{\partial T}{\partial x_i}\right) - S_h \qquad (2)$$

where h and T are respectively the enthalpy and the temperature of the material; c_p its specific heat, ρ the density and k the thermal conductivity. S_h is a source term.

The thermal properties ρ, c_p, and λ depend only on the material nature because of the low temperature gradients observed outside the combustion chamber [4-10].

Moreover, the mesh is structured and has got 20 cells in the thickness of the cylinder wall.

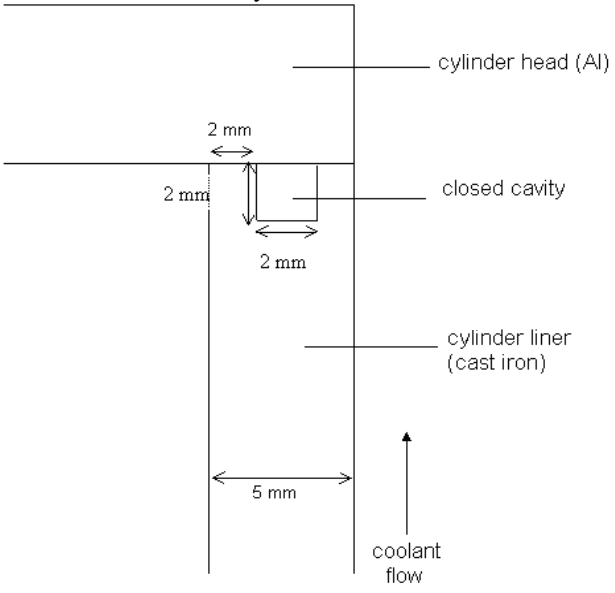

Fig 5. Studied configuration

The melting of the PCM is treated by the Voller and Prakash [10] model. Its allows to calculate the source term of Eq. (2), S_h. It uses an enthalpy formulation methodology and a fixed grid to solve mushy region phase change problems.

Boundary conditions

The cylinder head and the cylinder wall cooling is taken into account by "external convection" boundary conditions. The external heat transfer coefficient and temperature are respectively: h_{ext} = 2500 W/m²K (corresponding to forced convection with liquid) and T_{ext} = 353 K (corresponding to the temperature regulation of coolant in an actual engine).

Unsteady heat transfer from the hot burnt gases to the chamber wall is simulated by the previously presented self-developed program. Four types of combustion are simulated: a normal combustion and knocking combustion with three levels of knock intensity. In case of knocking combustion, cyclic variations (generally met in engine operation) are taken into account by imposing successively a high and a low peak heat flux value. Table 1 summarizes all the peak heat flux values that are used in this study. Their are deduced from literature [6].

Table 1. Peak heat fluxes for the four different types of combustion [6]

Type of combustion	**Peak Heat Flux (MW/m²)**	
	Low Value	**High Value**
Normal	2.5	2.5
Knocking (low intensity)	2.5	3.5
Knocking (moderate intensity)	3.5	5
Knocking (high intensity)	5	8

Numerical technique

The energy equation (Eq. (2)) is solved by the finite volume technique. The time dependent term is integrated using a 1st order implicit scheme. The time step is fixed at 10^{-4} s (corresponding to 30 steps during one combustion period with engine cycle period of 0.08 s).

Four iterations per time step were adopted because more iterations do not improve the convergence of computations. This choice gives good results while preserving a reasonable calculation time.

Mesh validation

The accuracy of the model has to be checked before being used for the simulation of the PCM melting. Thus, the numerical results are confronted to an analytical solution in a simplified 1D case without cavity.

The combustion chamber wall constitutes a frontier between hot gases and water coolant flow. Its thickness is *e*. It is assumed to be isotropic and can be considered, in this step, as a semi-infinite plan in order to make the problem mono-dimensional. On one side, the temperature varies periodically (combustion chamber), on the other it remains constant (coolant flow).

The mesh validation for the conduction problem consists in the confrontation of the calculated temperature field within the wall thickness with analytical solutions deduced from the resolution of the unsteady heat conduction equation in an one dimensional case (Eq. (3)):

$$\frac{\partial T(x,t)}{\partial t} = \alpha \cdot \frac{\partial^2 T(x,t)}{\partial x^2} \tag{3}$$

where α is the thermal diffusivity of wall material (cast-iron in the present case) and x the position from the internal side of the wall.

The boundary conditions can then be written as:

- $T(0,t) = T_w(t)$, at x=0
- $T(e,t) = T_e$ = const, at $x = e$

The periodic variations of temperature on the inner side of the wall can be expressed as a Fourier Series in the following form (Eq. (4)):

$$T_w(t) = T_0 + \sum_{n=1}^{n=\infty} A_n \cdot \cos(n \cdot \omega \cdot t) + B_n \cdot \sin(n \cdot \omega \cdot t) \tag{4}$$

where ω is the angular frequency of temperature variation (in the case of a four-stroke engine, ω is half the engine angular speed).

The temperature at any point of the wall can take the form of Eq. (5).

Fig. 6 represents the instantaneous temperature in different points of the cylinder wall thickness. Good agreement is found between numerical and analytical results. The difference between the numerically and analytically calculated temperatures is less than 0.1 K. The phase shift between the thermal signals is also well predicted. Moreover the numerical results appeared to be independent of the mesh within the range 20-40 cells in the wall width.

$$T(x,t) = T_0 - (T_0 - T_e) \cdot \frac{x}{e} + \sum_{n=1}^{n=\infty} e^{-x \cdot \sqrt{\frac{n \cdot \omega}{2 \cdot \alpha}}} \left(A_n \cdot \cos\left(n \cdot \omega \cdot t - x \sqrt{\frac{n \cdot \omega}{2 \cdot \alpha}}\right) + B_n \cdot \sin\left(n \cdot \omega \cdot t - x \sqrt{\frac{n \cdot \omega}{2 \cdot \alpha}}\right)\right) \tag{5}$$

Choice of the PCM

As previously explained, the PCM placed within the wall should melt if knock occurs. Thus, the melting temperature of the PCM must be slightly higher than the coolant one (363 K) in order to melt only if the thermal load increases. Among the different possibilities, the sodium was chosen because of its thermal diffusivity (5.6 10^{-5} m^2/s at 371 K) which is much more close to cast iron than the thermal diffusivity of non metallic PCM. Thus, isothermal curves around the top of the cylinder are not much changed in comparison with the situation without the PCM. Otherwise, the use of the Voller and Prakash [10] model requires that the thermal properties of the material must be assumed constant with temperature and phase. Finally, Table 2 summarizes the thermal properties used to simulate the Sodium melting.

Results

A reference test is initially performed. In this test, heat flux corresponding to a normal combustion is imposed. In these conditions, once the thermal regime is established, the melting temperature in the cavity is slightly under the melting temperature of the PCM. The gap between cavity and melting temperature is comprised between 0.5 and 1.5 K depending on the location within the cavity. Starting from this reference situation, each knocking combustion is simulated.

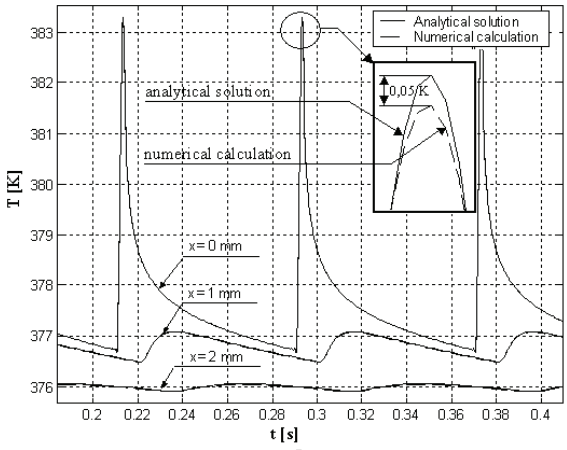

Fig. 6 Validation of the mesh (cast iron wall, normal combustion: Peak Heat Flux = 2.5 MW/m²)

Table 2. Thermal properties of the sodium

$T_{melting}$ (K)	ρ (kg/m^3)	k (W/m.K)	Δh (J/kg)	c_p (J/kg.K)
371	930	85	113000	1380

The average liquid fraction in the cavity is plotted as a function of the time in Fig. 7. In each case, the PCM totally melts. Of course, the melting process is much slower with the low knock intensity.

In Fig. 8, we compare the number of engine cycles that separate the knock occurrence from the end of the melting for the three studied knock intensity. If we assume that melting would be detected as soon as it has ended (using a probe located on the outer side of the cavity, for example), we can notice that the detection of knock occurrence would be done after 17 to 120 engine cycles depending on the knock intensity. So the knock must appear and be persistent to be detected. On the other hand, wall heat flux can also change because cyclic variation always present in engines (see ref. [4] for examples that show changes in peak heat flux generated by cyclic variations). Thus, one of the advantages of the proposed technique is that a non persistent heat flux increase due to cyclic variations would not totally melt the PCM. This can be seen as a protection against wrong detection of knock occurrence.

The results plotted in Fig. 8 show that the melting speed is not proportional to the increase in wall heat transfer due to knock. The raison for such a behavior can be found by observing the shape of the melting front. Figs 9 and 10 represent the liquid fraction curves when respectively 5 % and 10 % of the PCM has melt. In the case of the low knock intensity, the vertical heat transfer near the top of the wall cylinder is quite significant compared to the radial heat transfer. This is confirmed by the direction of the isothermal curves close to the cavity (Fig. 11 a). Thus, the mushy region is diagonally moving. In this case, an important part of the heat flux from the combustion chamber crosses the PCM by heat conduction without contributing to the melting process.

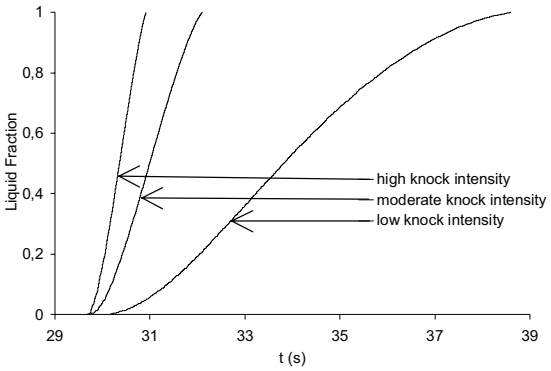

Fig. 7 Average liquid fraction in the cavity as a function of time

If the knock intensity is high, the heat transfer becomes more horizontal close to the top of the cylinder (as shown by the isothermal curves plotted in Fig. 11 b)). Thus, the mushy zone tends to become vertical. In this situation all the heat coming out from the combustion chamber is utilized in order to melt the material. This explains that, when knock intensity is increased, the melting velocity is increased in a higher rate than the wall peak heat flux.

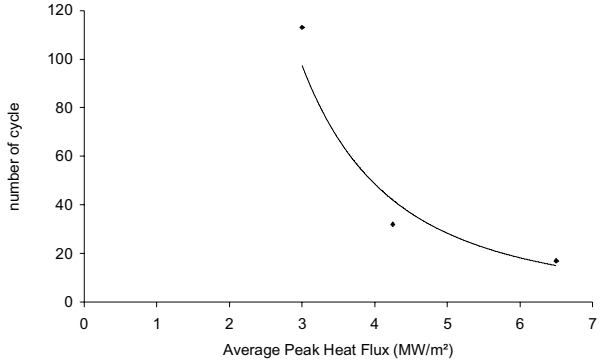

Fig. 8 Number of engine cycles between the knock occurrence and the end of the melting

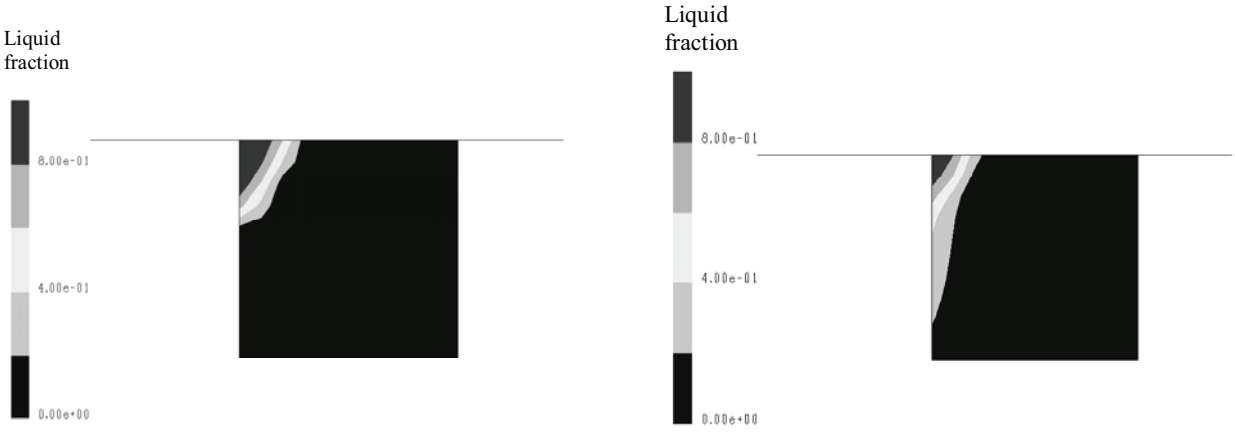

a) b)

Fig 9 Melting fronts at 5 % a) low knock intensity b) high knock intensity

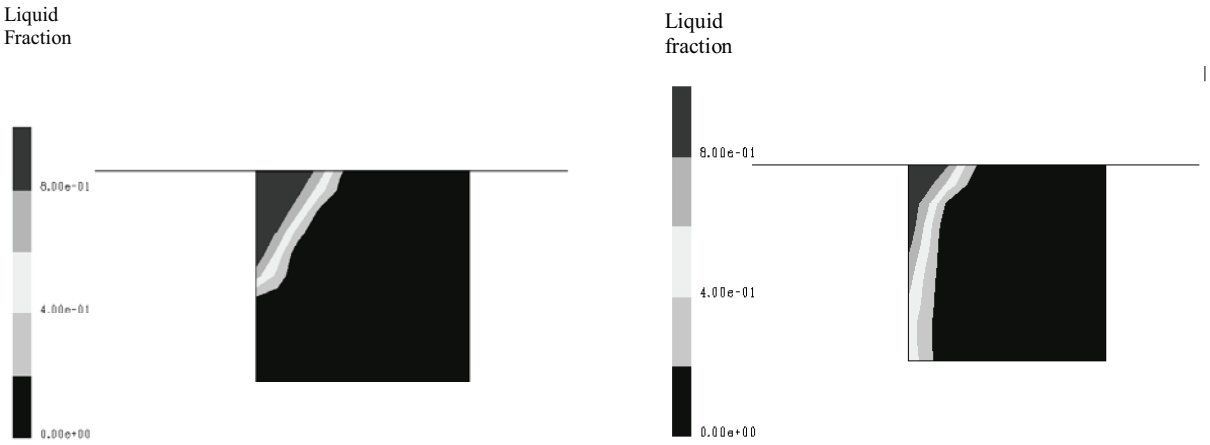

a) b)

Fig. 10 Melting fronts at 10 % a) low knock intensity b) high knock intensity

Conclusions and perspectives

The present paper proposed a new technique for knock detection in a gas SI engine. It is based on the increase in heat transfer between the combustion chamber and the wall cylinder when knock occurs. The melting of a metallic Phase Change Material is proposed to detect knock occurrence because melting is easy to detect with industrial sensors. The feasibility of this new method was numerically investigated. From the different results, we can especially retain:

- if the knock is persistent, the PCM totally melts even if the knock intensity is low,
- in the studied configuration, the duration of the melting process is included in a range 17-120 engine cycles depends on the knock intensity,
- small increase in the wall heat flux due to cyclic variation should not be interpreted as knock occurrence because they are not persistent,
- Melting velocity increases with a higher rate than the peak heat flux when knock intensity is increased. This is due to the change in the melting front shape.

However, this new technique can be used only if the engine is at full load. In an other case, melting of the PCM could occurs because of an increase in the engine load and not because of knock occurrence. Consequently, further work is now carried out by analyzing the effect of knocking combustion on the exhaust gas temperature. This temperature is decreased when knock occurs. This would certainly complete usefully the information obtained from the wall heat transfer study in order to develop a new method for the knock detection in a large range of engine tunings.

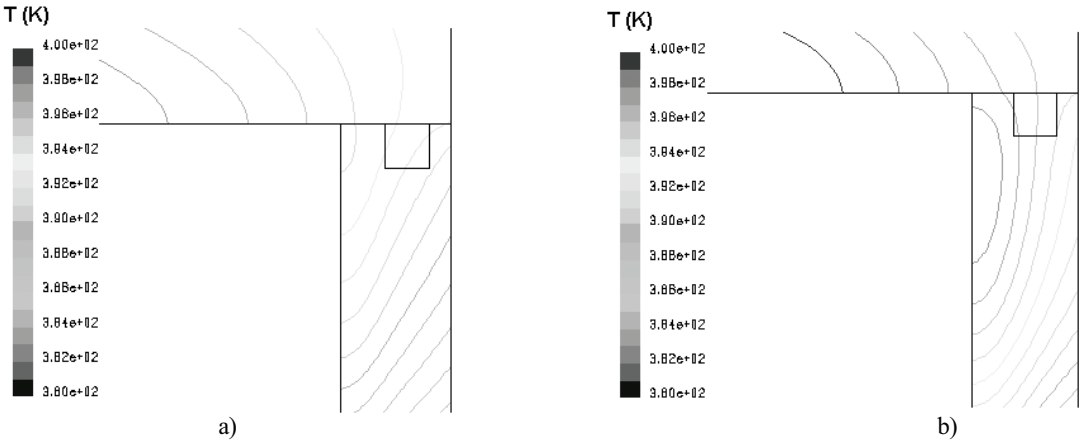

a) b)

Fig. 11 Isothermal curve at the end of a knocking cycle a) low knock intensity b) high knock intensity

References

[1] G. Brecq, M. Tazerout, O. Le Corre, A comparison of experimental indices to determine knock limit in CHP SI engines, in: Proceedings of the 5th World Conference on Experimental Heat Transfer, Fluid Mechanics and Thermodynamics – ExHFT, Thessaloniki (Greece), 2001, vol. 1, pp. 517-521.

[2] G. Brecq, J. Bellettre, M. Tazerout, A new indicator for knock detection in gas SI engines, International Journal of Thermal Sciences 42 (5) (2003) 523-532.

[3] G. Brecq, Contribution à la caractérisation thermodynamique du cliquetis dans les moteurs à gaz : application à de nouvelles méthodes de détection, Ph.D. Thesis, University of Nantes, 2002.

[4] M. Syrimis, Characterization of knocking combustion and heat transfert in a spark-ignition engine, Ph.D. Thesis, University of Illinois, 1996.

[5] J. H. Lu., D. Ezekoye, A. Liyama, R. Greif, R. F. Sawyer, Effect of Knock on Time Resolved Engine Heat Transfer, SAE Paper No 890158, 1989.

[6] Y. Enomoto, N. Kitahara, M. Takai, Heat losses during knocking in a four-stroke gasoline engine, JSME International Journal, Series B, 37 (1994).

[7] J. Bellettre, M. Tazerout, Numerical Study of unsteady heat transfer around a cylinder. Apllication to knock detection in gas SI engine, in: Proceedings of the Eurotherm 74 "Heat Transfer in Unsteady and Transitional flows", Eindhoven (The Netherlands), 2003, pp. 99-104.

[8] E. Ollivier, B. Duma, J. Bellettre, M. Tazerout, Knock Detection in Gas Engine by Analysis of Transient Heat Transfer, in: Proceedings of International Symposium on Transient Convective Heat and Mass Transfer in Single and Two-Phase Flows, Cesme (Turkey), 2003.

[9] K. Loubar, J. Bellettre, M. Tazerout, Amplification des variations de température par l'emploi de promoteurs de turbulence au voisinage d'un cylindre moteur. Application à la détection du cliquetis, in: Proceedings of Congrès Société Française de Thermique, Giens (France), 2004.

[10] J. B. Heywood, Internal Combustion Engines Fundamentals, McGraw Hill, Singapore, 1988.

[11] V.R. Voller, C. Prakash, A fixed grid numerical modelling methodology for convection-diffusion mushy region phase change problem, International Journal of Heat and Mass Transfer 30 (8) (1987) 1709-1719.

Strojniški vestnik - Journal of Mechanical Engineering 51(2005)7-8, 470-475
UDK - UDC 536.2
Izvirni znanstveni članek - Original scientific paper (1.01)

Numerical computation of turbulent conjugate heat transfer in air heater

Hriberšek, M.[a], Širok, B.[b], Žunič, Z.[a], Škerget, L.[a]

[a] *Faculty of mechanical engineering, Smetanova 17, SI-2000 Maribor, Slovenia,*
[b] *Turboinstitut, Rovšnikova 7, SI-1000 Ljubljana, Slovenia*

Abstract

The contribution deals with numerical simulation of conjugate heat transfer in air heater of the laundry dryer. The heat transfer consists of internal heat generation in the electrical heating coils, forced convection from the coils to the air and heat conduction through the metal walls of the heater. In order to simplify the computational mesh the porous media concept was used for discretization of electrical coils. A special attention was given to the selection of a turbulence model, capable of accurate solution of conjugate heat transfer. After extensive testings the SST model, used in the numerical code CFX5, was selected. The computational results were compared with results of velocity and temperature measurements on the device in the laundry dryer, and good agreement was observed.

Introduction

One of the most important units in a laundry dryer is the air heating system, consisting of a fan and an electrical air heater. The air heater consists of four heating coils, an inner and an outer housing, schematically presented in Fig. 1. Its main task is to heat the recirculated drying air and to uniformly distribute the air to the drying drum. Due to short distances and complex geometry of the heating section the latter task is hard to accomplish. The use of CFD technique can serve as a tool of determination of critical areas in the heater, where nonuniformity of heating and air flow is occuring, and to perform a parametric analysis in order to achieve a desired heat and flow conditions. Nonuniformity of temperature field can have a negative impact of drying material, especially on shrinkage.

The paper gives a deeper insight into numerical modeling of the heat and flow conditions in the air heater of the laundry dryer. In the first part, the main transport phenomena, participating in the heater, are discussed and described by stating the proper physical model. This is followed by description of the geometrical model and boundary conditions, largely determined by the experimental work. A special attention is given to the selection of a turbulence model, capable of accurate solution of conjugate heat transfer. The paper ends with discussion of computational results.

Transport phenomena in air heater

The conjugate heat transfer problem in the air heater can be divided into three main areas:

- non-isothermal flow of air through channels of the heater,

$$\frac{\partial v_j}{\partial x_j} = 0 \quad , \tag{1}$$

$$\frac{Dv_i}{Dt} = \nu_f \frac{\partial^2 v_i}{\partial x_j \partial x_j} - \frac{1}{\rho}\frac{\partial P}{\partial x_i} - \Phi \frac{\nu_f}{K} v_i - \Phi \frac{C_F}{\sqrt{K}} \mid v_i \mid \; v_i, \tag{2}$$

$$\frac{DT}{Dt} = \kappa_f \frac{\partial^2 T}{\partial x_j \partial x_j} + \frac{q_{I,f}}{\rho c} \quad , \tag{3}$$

- transient heat conduction through the plates,

$$\frac{\partial T}{\partial t} = \kappa_s \frac{\partial^2 T}{\partial x_j \partial x_j} \quad . \tag{4}$$

In case of flow through porous region, the parameter $\Phi = 1$, otherwise $\Phi = 0$. The momentum equation for porous part of domain ($\Phi = 1$) contains the Darcy term, the Brinkman term and the Forchheimer term. The equations set (1) - (4) has to be solved numerically by the use of an approximation method.

Nomenclature

C_F	dimensionless form-drag constant	t	time
c_p	specific isobaric heat	T	temperature
$D/D(\ldots)$	the substantial derivative	v_i	the i-th velocity component
f	subscript for air	x_i	i-th coordinate
k	turbulent kinetic energy	ϵ	dissipation rate of k
K	permeability of the porous medium	λ	heat conductivity
P	modified pressure $(p - \rho g_j r_j)$	κ	thermal diffusivity
Pr_t	turbulent Pr number	κ_t	turbulent thermal diffusivity
q_I	specific heat source	ν	kinematic viscosity
s	subscript for solid wall	ν_t	turbulent viscosity
		ρ	mass density

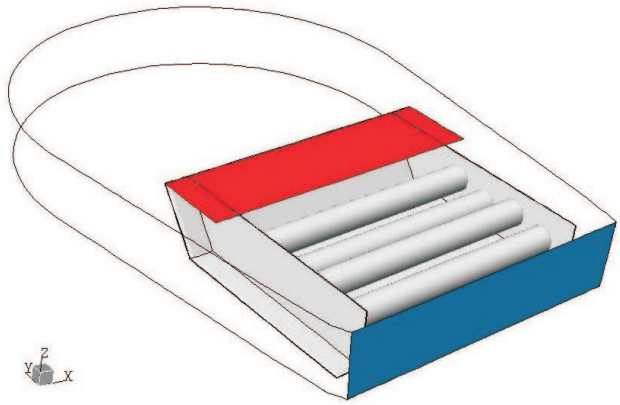

Figure 1: Heater unit with inlet and outlet planes.

Numerical model

Determination of heat and flow conditions in the electrical heater was performed by using CFX-5.6 CFD code. The code is based on the SIMPLEC coupling algorithm with discretisation of the governing equations by the Finite Volume Method (details in [4]).

In order to predict heat and flow conditions in the unit, a conjugate heat transfer model, which includes heat convection between the air and the solid walls and conduction through the walls, had to be implemented. Additionally, the electrical heating coils were modeled as porous medium. This was necessary as the diameter of the wires is two orders of magnitude smaller than dimensions of the heater, what would result in a stretched and dense computational mesh. As the heating coils do not present a significant flow resistance the permeability and porosity of the medium were set reasonably large, and the Forchheimer's resistance coeficient was set as 1, thus representing low resistance to fluid flow in the area of the heating coils.

The air in the unit heats due to heat transfer from hot electrical wires to the fluid. The known electrical power input was used for the computation of the value of volumetric internal heat generation in the porous medium. In order to make the numerical model feasible, the chosen computational domain was limited to the heater, the surrounding cover and a part of the incoming channel from the fan. The resulting computational model consisted of 205,500 finite volumes.

Due to high values of velocities in the domain natural convection effects were not included in the computation. A decoupled computation of flow field and conjugate heat transfer was therefore performed.

The solution procedure with CFX-5.6 was as follows:

1. Prescribe the known velocity profile at the inlet of the domain and the known inlet air temperature.
2. Start with some initial values in the domain: $v_{i,0} = 0$, $T_0 = 0$.
3. Compute flow field inside the fluid domains.
4. Compute conjugate heat transfer with known velocity field from step 3.

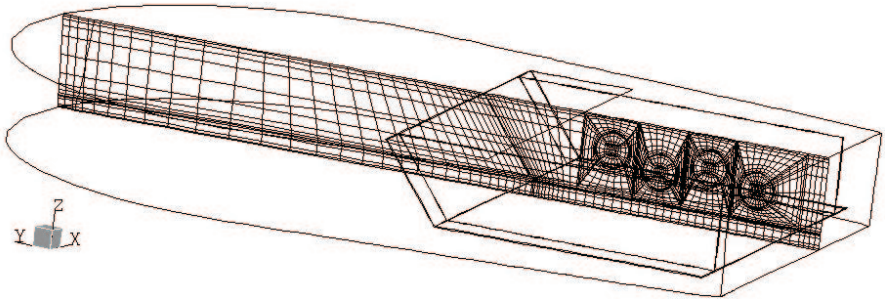

Figure 2: Computational mesh

Turbulence models

Measurements of the inlet velocity field showed that the flow in the heater is in a turbulent regime. This has to be accounted for in the numerical model of the problem. The mostly applied engineering approach is to use the Reynold Averaged Navier-Stokes (RANS) equations for the solution of turbulent flows in complex geometries. In eddy viscosity RANS model, the momentum transfer due to fluctuations in velocities is modeled by the gradient diffusion hypothesis, resulting in a modified values of kinematic viscosities. These are now sums of molecular viscosity and turbulent viscosity,

$$\nu_f = \nu + \nu_t. \tag{5}$$

the latter dependent on flow conditions. A similar approach is used with the energy equation, where the heat diffusivity is a sum of molecular heat diffusivity and turbulent heat diffusivity,

$$\kappa_f = \kappa + \kappa_t \tag{6}$$

In estimating the κ_t the general engineering approach is to set

$$\kappa_t = \frac{\nu_t}{Pr_t} \tag{7}$$

Similarity between the turbulent momentum and turbulent heat transport was assumed and the $Pr_t \approx 0.9$ was set.

In order to solve dynamical equations the turbulent viscosity must be specified. The turbulent viscosity is modeled as the product of a turbulent velocity and turbulent length scale. The standard RANS model is the $k-\epsilon$ model, which solves two additional transport equations, one for turbulent kinetic energy k and one for dissipation rate of turbulent kinetic energy, ϵ. In two-equation models the turbulence velocity scale is computed from the turbulent kinetic energy, and the turbulent length scale is estimated from the turbulent kinetic energy and its dissipation rate.

Different turbulence models are obtained depending on the way in which ν_t is computed. In the $k-\epsilon$ turbulence model the turbulent viscosity is given by relation

$$\nu_t = C_\nu \frac{k^2}{\epsilon}, \tag{8}$$

where ϵ is the rate of turbulent energy dissipation. Both turbulence quantities k and ϵ are determined from the individual transport equations.

While standard two-equation models provide good predictions for many flows of engineering interest, there are applications for which these models fail. Among these some occur also in our case, like flow with boundary layer separation. Additionally, without accounting for the transport of the turbulent shear stress, the standard two equation turbulence models give an overprediction of the eddy-viscosity, which directly affects heat transfer rate in the near wall region. As conjugate heat transfer from the fluid through the inner housing solid wall is influenced by the flow conditions near the solid bounary, accurate prediction of turbulent viscosity and recirculation regions is of main importance in assuring an accurate overall heat transfer.

From equations (3) and (7) it is evident that the most important parameter for an accurate determination of conjugate heat transfer between the fluid and the solid is the value of the turbulent viscosity in the near wall region, i.e. in finite volumes adjacent to the solid wall. From this point of view it is already questionable how a standard wall-function based $k-\epsilon$ model could perform in such a case, resulting in a need for the use of a turbulence model, that accurately resolves transport equations for turbulence quantities up to the wall.

Today, there are already several extensions to general two-equation turbulence models, that occount for this phenomena. One of them is the k-ω based SST model, implemented in CFX 5, which improves flow separation predictions significantly. It accounts for the transport of the turbulent shear stress and gives highly accurate predictions of the onset and the amount of flow separation under adverse pressure gradients. Like any two-equation turbulence model, the $k-\omega$ model solves two additional transport equations, one for the turbulent kinetic energy k, and the other for the turbulent frequency ω.

In the SST model, the proper transport behavior can be obtained by a limiter to the formulation of the eddy-viscosity.. The SST model originates in a combination of the $k-\omega$ model near the wall and the $k-\epsilon$ model away from the wall, i.e. combining the best elements of the $k-\epsilon$ and $k-\omega$ models with the help of special blending functions, [5].

Experimental determination of boundary conditions

The velocity field at the inlet plane was measured by the two-component TSI-LDA system. The measured isolines of velocity components in the z (normal direction regarding the inlet plane) and the x (tangential wide direction regarding the inlet plane) direction clearly indicate that

a) there is a significant outflow region (Fig.3, upper right corner) at the inlet plane, which is a results of a large recirculation region caused by the nonuniform velocity flow from the fan, placed in front of the heater,

b) there is a strong tangential flow (Fig.4, left side) in the x direction.

Both phenomena have a strong influence on development of velocity field inside the heater, namely a build up of two recirculation regions along the side walls of the inner housing walls, as can be seen from the computational results, Fig. 9.

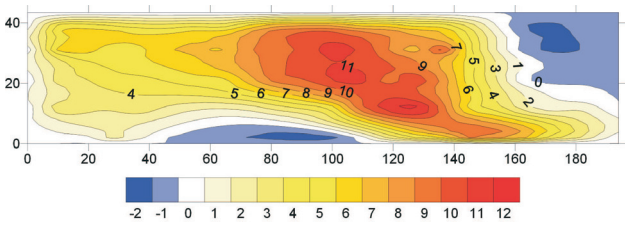

Figure 3: Contours of measured values of v_z velocities at the inlet.

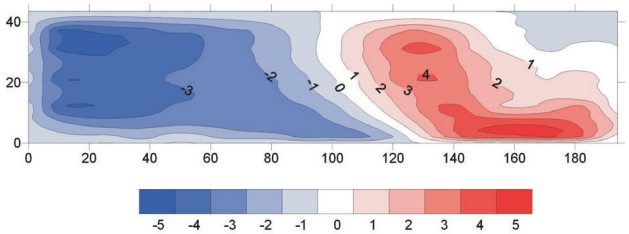

Figure 4: Contours of measured values of v_x velocities at the inlet.

The grid of measured values of velocity components was used for bilinear interpolation of experimental results to the grid points of the computational mesh, and for the consequent prescription of velocity boundary conditions at the inlet plane. At the outlet of the heater, the open boundary conditions ([4]) were prescribed.

At the outer housing of the heater the free convection heat transfer coefficient was prescribed as $4W/m^2K$. The incoming air temperature was $338K$, and the temperature of the ambient air was set as $293K$.

Computational results

To test the computational model on the selected computational mesh both the $k-\epsilon$ and the SST turbulence model were included in the computation. Severe differences occured in the computational results for the computation of conjugate heat transfer. The $k-\epsilon$ model overpredicted values of turbulent viscosity in the near wall region, Fig. 5, resulting in the decrease of heat transfer through the solid walls of the heater. The higher values of effective viscosity in the near wall region slows down the flow and consequently the heat transfer rate, resulting in lower temperatures at the wall and low heat fluxes through the solid walls. The SST turbulence model gave much more realistic predictions of turbulent viscosity, leading to higher temperatures of the walls and higher heat fluxes through the walls, [5]. In the core of the fluid, both models gave similar results, which is due to the nature of the SST model, as it uses the $k-\epsilon$ model for this flow region. These comparisons clearly indicate that the $k-\epsilon$ model in its used form (wall functions) is not appropriate for the conjugate heat transfer computations, and therefore the SST model was used in all further computations.

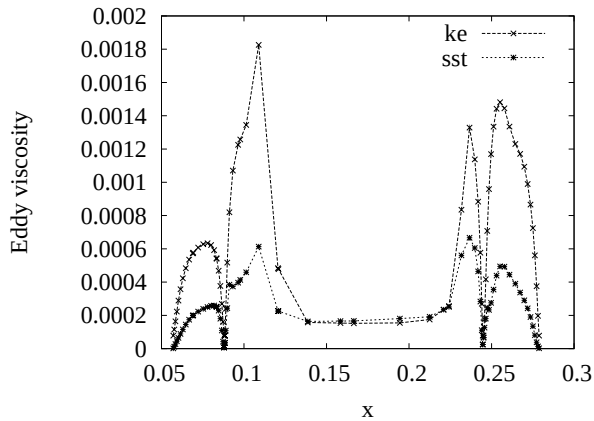

Figure 5: Contours of turbulent viscosities in the cross section through the heater, ke - $k-\epsilon$ model, sst - SST model.

The flow field inside the heater unit is characterized by two large recirculation regions, Fig. 9, one

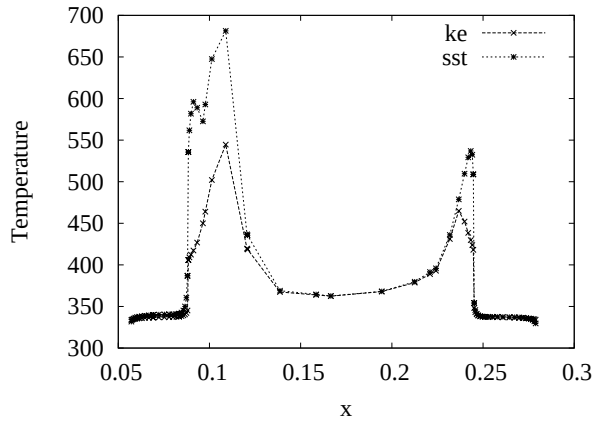

Figure 6: Contours of temperatures in the cross section through the heater, ke - $k-\epsilon$ model, sst - SST model.

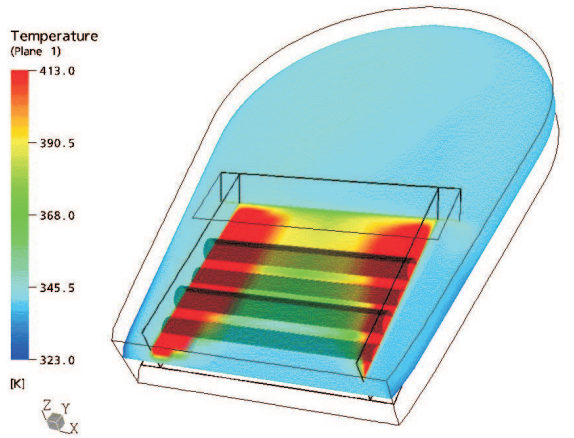

Figure 8: Contours of temperatures for the SST model.

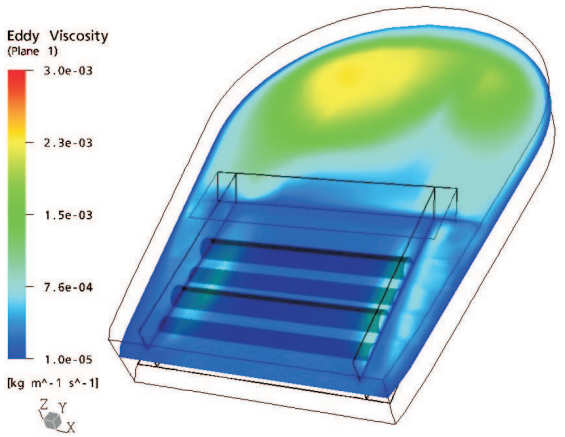

Figure 7: Contours of turbulent viscosity for the SST model.

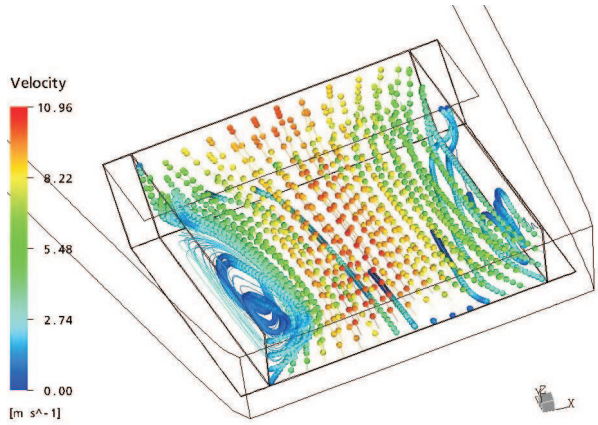

Figure 9: Streaklines in the inner part of the heater.

at the left and one at the right inner solid walls, a result of nonuniform inlet conditions. These regions are responsible for increased temperatures at the outlet of the heater.

In Figure 10 the recorded temperature field at the inlet to the drying drum is presented. As experimental tool the thermovision device AGEMA 570 of FSI Flir Systems was used. When comparing these results with the results of computations the fact that experiment was conducted with no recirculation loop for the heated air should be taken into consideration, i.e. the overall temperature level is lower than computed with numerical model, which considers real conditions inside the operating drying machine. An interesting comparison between the experimental and computational results can be drawn from Figures 11 and 12. The numerical results are in good agreement with experimental temperature field, especially regarding the positions of the high temperature regions, that should be avoided in ideal operating conditions. Also, the quantitative comparison of the temperature levels shows good agreement in the range of $+10K$, considering the temperature difference of $40K$ between the inlet air temperature in experiment and prescribed working temperature in the numerical model.

The existence of recirculation regions at the left and right walls has its impact on temperatures of the coils. In the region, where flow was recirculating, the temperature was much higher than in the region of the main flow, a result of low exchange of heated air from this region to the main flow. This effect can cause undesired increase of temperature of the wires and can cause the connected temperature sensor to disconnect the corresponding coil for a certain period of time. The heat input to the air could be therefore lower than normal, impacting the drying conditions inside the drum.

Conclusions

The contribution presented a development of a feasible numerical model for accurate computation of conjugate heat transfer inside the heater unit of the laun-

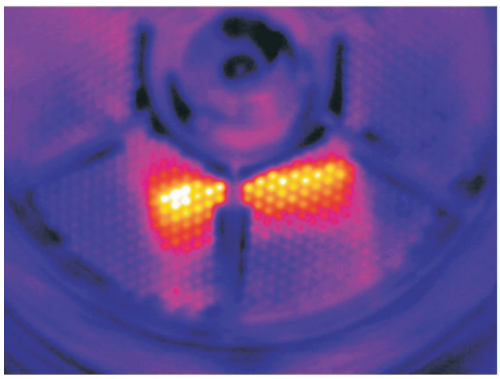

Figure 10: Thermovision recorded temperature field at the outlet.

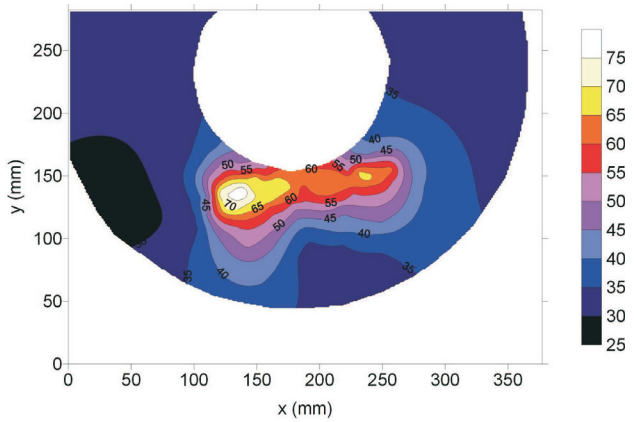

Figure 11: Isotherms of the recorded temperature field at the outlet.

dry dryer. The study of influence of turbulence model on accuracy of computational results for the case of conjugate heat transfer was performed, with comparison of the standar wall function based $k-\epsilon$ model and the SST model. The comparison between the models as well as with the measured temperature field showed that the use of the standard $k-\epsilon$ model results in physically unrealistic heat conditions in the near wall region, whereas the SST model gave accurate computational results. The comparison of results, obtained by using the SST model, with experimental results using Thermovision The developed numerical model can now be used as a main part of parametric study of the air heater performance.

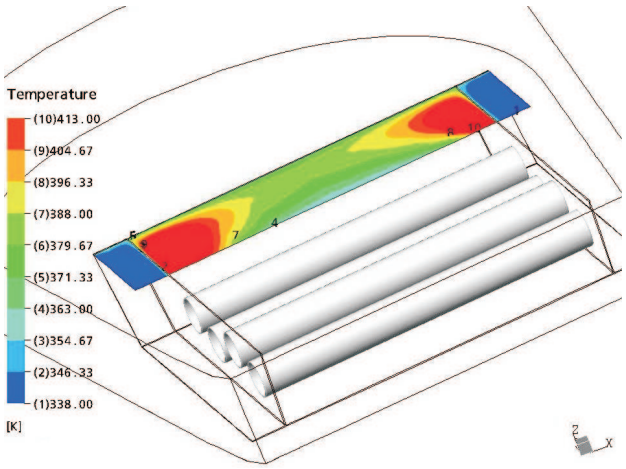

Figure 12: Temperature field at the outlet.

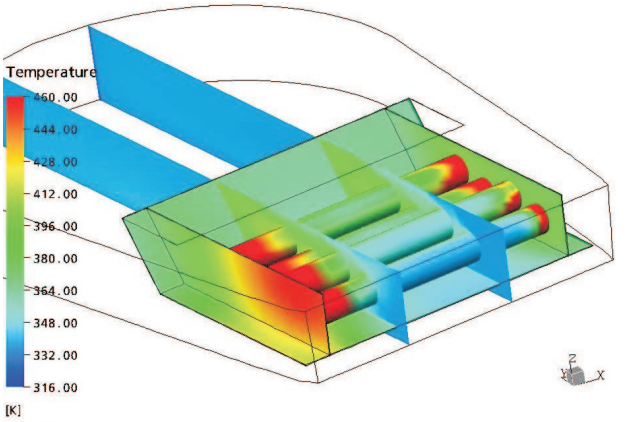

Figure 13: Temperature field in the vicinity of heating coils.

References

[1] Conde, M. R. (1997) Energy conservation with tumbler drying in laundries. *Applied Thermal Engineering*, Vol. 17, No. 12, pp. 1163-1172.

[2] Deans, J. (2001) The modelling of a domestic tumbler dryer. *Applied Thermal Engineering*, Vol. 21, pp. 977-990.

[3] Hriberšek, M., Bašič, S., Škerget, L., Širok, B. (2001) Numerical modeling of heat and fluid flow conditions of a laundry dryer condenser. PIERUCCI, S. (ed.), The Fifth Italian Conference on Chemical and Process Engineering, ICheaP-5, Florence, Italy, May 20-23, 2001. Proceedings. Milano: AIDIC, 2001, vol. 2, pp. 759-764.

[4] CFX5.6 (2003). User's manual, AEA Technology.

[5] Vieser, W., Esch, T., Menter, F.: Heat transfer predictions using advanced two-equation turbulence models. CFX Validation report, CFX-VAL10/1002.

Strojniški vestnik - Journal of Mechanical Engineering 51(2005)7-8, 476-483
UDK - UDC 536.2
Izvirni znanstveni članek - Original scientific paper (1.01)

Application of Meshless Methods for Thermal Analysis

Darrell W. Pepper[1] and Božidar Šarler[2]

[1]*Nevada Center for Advanced Computational Methods, University of Nevada Las Vegas, Las Vegas, NV, 89154-402 7, USA, dwpepper@nscee.edu*
[2]*Laboratory for Multiphase Processes, Nova Gorica Polytechnic, Nova Gorica, Slovenia*

Abstract

Many numerical and analytical schemes exist for solving heat transfer problems. The meshless method is a particularly attractive method that is receiving attention in the engineering and scientific modeling communities. The meshless method is simple, accurate, and requires no polygonalisation. In this study, we focus on the application of meshless methods using radial basis functions (RBFs) – which are simple to implement – for thermal problems. Radial basis functions are the natural generalization of univariate polynomial splines to a multivariate setting that work for arbitrary geometry with high dimensions. RBF functions depend only on the distance from some center point. Using distance functions, RBFs can be easily implemented to model heat transfer in arbitrary dimension or symmetry.

Introduction

For decades, finite difference, finite volume, and finite element methods (FDM/FVM/FEM) have been the dominant numerical schemes employed in most scientific computation. These methods have been used to solve numerous thermal related problems covering a wide range of applications. A common difficulty in these classic numerical methods is the considerable amount of time and effort required to discretize and index domain elements, i.e., creating a mesh. This is often the most time consuming part of the solution process and is far from being fully automated, particularly in 3D. One method for alleviating this difficulty has been to utilize the boundary element method (BEM). The major advantage of the BEM is that only boundary discretization is required rather than domain, thereby reducing the problem by one order. However, the discretization of surfaces in 3-D can still be a complex process even for simple shapes. In addition, these traditional methods are often slowly convergent, frequently requiring the solution of 100's of thousands of equations in order to get acceptable accuracy.

In recent years, a novel numerical technique called "meshless methods" (or "mesh-free methods") has been undergoing strong development and has attracted considerable attention from both science and engineering communities. Currently, meshless methods are now being developed in many research institutions all over the world. Various methods belonging to this family include: Diffuse Element Methods, Smooth Particle Hydrodynamics Methods, Element-Free Galerkin Methods, Partition of Unity Methods, h-p Cloud Methods, Moving Least Squares Methods, Local Petrov-Galerkin Methods, Reproducing Kernel Particle Methods, and Radial Basis Functions.

A common feature of meshless methods is that neither domain nor surface polygonisation is required during the solution process. These methods are designed to handle problems with large deformation, moving boundaries, and complicated geometry. Recently, advances in the development and application of meshless techniques show they can be strong competitors to the more classical FDM/FVM/FEM approaches [1,2], and may likely become a dominant numerical method for solving science and engineering problems in the 21st century. A recent book by Liu [3] discusses meshfree methods, implementation, algorithms, and coding issues for stress-strain problems. Liu [3] also includes Mfree2D, an adaptive stress analysis software package available for free from the web. Atluri and Shen [4] produced a research monograph that describes the meshless method in detail, including much in-depth mathematical basis. They also present comparison results with other schemes.

Nomenclature

c	shape parameter	y	lateral distance
C	transport variable	α	thermal diffusivity ($k/\rho c_p$)
D	diffusion coefficient	ε	emissivity
f	interior functional	σ	Stefan-Boltzmann constant
g	boundary functional	φ	trial function; field variable
h	convective film coefficient	θ	dummy variable
k	thermal conductivity	ψ	approximation function; streamfunction
N	number of nodes	ω	vorticity
q	heat flux	Subscripts	
Q	heat source/sink	i,j	nodal values
r	radial distance	I	internal number of node points
t	time	o	initial value; free parameter
T	temperature	Superscripts	
V	velocity vector	n, n+1	known, unknown values
x	horizontal distance	^	approximate solution

There exists various types of meshless methods and each method has its advantages and disadvantages. Intensive research conducted in many major research institutions all over the world are now working to improve the performance of these approaches. In this study, we focus on the introduction of the basic concept of meshless methods using radial basis functions (RBFs) – which are simple to implement.

Currently, there are two major approaches in this direction: (i) a domain-type meshless method that was developed by Kansa [5] in 1990; (ii) a boundary-type meshless method that has evolved from the BEM [6]. *Radial basis functions* are the natural generalization of univariate polynomial splines to a multivariate setting. The main advantage of this type of approximation is that it works for arbitrary geometry with high dimensions and it does not require any mesh. A RBF is a function whose value depends only on the distance from some center point. Using distance functions, RBFs can be easily implemented to reconstruct a plane or surface using scattered data in 2-D, 3-D or higher dimensional spaces.

Similar to FEM techniques, meshless methods produce banded system matrices that can be handled in similar fashion. Both sets of methods can utilize either direct methods based on Gauss elimination or matrix decomposition methods or iterative methods, e.g., Gauss-Seidel or SOR techniques. When dealing with nonlinear problems, additional iterative loops are needed. Meshless methods generally require more CPU time since the creation of shape functions are more time-consuming and are performed during the computation. However, less time is spent in setting up computational nodes. Results using meshless methods are typically more accurate than conventional numerical methods based on mesh discretizations -thus the ratio of accuracy to CPU is likely to be greater for meshless methods.

Meshless methods hold promising alternative approaches for problems involving fluid flow and heat transfer analyses. The most attractive feature is the lack of a mesh that is required in the more conventional numerical approaches. This becomes particularly interesting in that one can begin to conduct adaptive analyses for CFD problems.

The Meshless Method using RBFs

In 1990, Kansa [5] extended the idea of interpolation scheme using RBFs to solving various types of engineering problems. The method is simple and direct and is becoming very popular in the engineering community. To illustrate the application of the meshless method using Kansa's method, we first consider the elliptic problems. For simplicity, we consider the 2-D Poisson problem with Dirichlet boundary condition

$$\begin{aligned} \nabla^2 T &= f(x,y), \quad (x,y) \in \Omega, \\ T &= g(x,y), \quad (x,y) \in \Gamma. \end{aligned} \tag{1}$$

Notice that the solution of Eq. (1) is in fact nothing but a surface. Techniques in surface interpolation can be applied to solve Eq. (1). To approximate T, Kansa [5] assumed the approximate solution could be obtained using a linear combination of RBFs

$$\hat{T}(x,y) = \sum_{j=1}^{N} T_j \phi(r_j) \tag{2}$$

where $\{T_1, T_2, \ldots, T_N\}$ are the unknown coefficients to be determined, $\varphi(r_j)$ is some form of RBF (trial function), and r is defined as

$$r_j = \sqrt{(x - x_j)^2 + (y - y_j)^2} \tag{3}$$

Since multiquadrics (MQ) are infinitely smooth functions, they are often chosen as the trial function for φ, i.e.,

$$\phi(r_j) = \sqrt{r_j^2 + c^2} = \sqrt{(x - x_j)^2 + (y - y_j)^2 + c^2} \tag{4}$$

where c is a shape parameter provided by the user. The optimal value of c is still a subject of research. Other functions such as polyharmonic splines can also be chosen as the trial function.

By direct differentiation of Eq. (6), the first and second derivatives of φ with respect to x and y can be expressed as

$$\frac{\partial \phi}{\partial x} = \frac{x - x_j}{\sqrt{r_j^2 + c^2}}, \quad \frac{\partial \phi}{\partial y} = \frac{y - y_j}{\sqrt{r_j^2 + c^2}}$$

$$\frac{\partial^2 \phi}{\partial x^2} = \frac{(y - y_j)^2 + c^2}{\sqrt{r_j^2 + c^2}}, \quad \frac{\partial^2 \phi}{\partial y^2} = \frac{(x - x_j)^2 + c^2}{\sqrt{r_j^2 + c^2}} \tag{5}$$

Substituting Eq. (3) into Eq. (1) and using collocation, one obtains

$$\sum_{j=1}^{N} T_j \left(\frac{(x_i - x_j)^2 + (y_i - y_j)^2 + 2c^2}{\left((x_i - x_j)^2 + (y_i - y_j)^2 + c^2\right)^{3/2}} \right) = f(x_i, y_i), \quad i = 1, 2, \ldots, N_I$$

$$\sum_{j=1}^{N} T_j \sqrt{(x_i - x_j)^2 + (y_i - y_j)^2 + c^2} = g(x_i, y_i), \quad i = N_I + 1, N_I + 2, \ldots, N \tag{6}$$

where N_I denotes the total number of interior points and $N_I+1,\ldots, N$ are the boundary points. Figure 1 shows two sets of interpolation points: interior and boundary points. Note that Eq. (6) is a linear system of N X N equations and can be solved by direct Gaussian elimination. Once the unknown coefficients $\{T_1, T_2, \ldots, T_N\}$ are found, the solution of T can be approximated at any point in the domain.

For time dependent problems, we consider the following heat equation as an example:

$$\frac{\partial T}{\partial t} - \alpha \nabla^2 T = f(x, y, T, \nabla T) \tag{7}$$

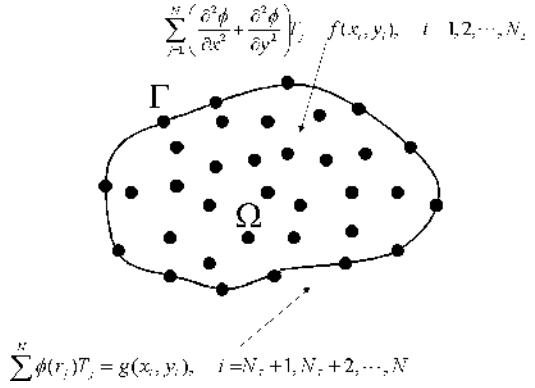

Figure 1. Interior points and boundary points using Kansa's method.

An implicit time marching scheme can be used and Eq. (7) becomes

$$\frac{T^{n+1} - T^n}{\Delta t} - \alpha \nabla^2 T^{n+1} = f(x, y, T^n, \nabla T^n) \tag{8}$$

where Δt denotes the time step, superscript n+1 is the unknown (or next time step) value to be solved, and superscript n is the current known value. The approximate solution can be expressed as

$$\hat{T}(x_i, y_i, t^{n+1}) = \sum_{j=1}^{N} T_j^{n+1} \phi_j(x_i, y_i) \tag{9}$$

Substituting Eq. (9) into Eq. (8), one obtains

$$\sum_{j=1}^{N} T_j^{n+1} \left(\frac{\phi_j}{\Delta t} - \alpha \nabla^2 \phi_j \right)(x_i, y_i) = \frac{1}{\Delta t} T^n(x_i, y_i) + f(x_i, y_i, t^n, T^n(x_i, y_i), \nabla T^n(x_i, y_i)), \quad i = 1, 2, \ldots, N_I$$

$$\sum_{j=1}^{N} T_j^{n+1} \phi(x_i, y_i) = g(x_i, y_i, t^{n+1}), \quad i = N_I + 1, \ldots, N \tag{10}$$

which produces an N X N linear system of equations for the unknown T_j^{n+1}. Note that the right hand side of the first equation in Eq. (10) can be updated before the next time step, i. e.,

$$T^n(x_i,y_i)=\sum_{j=1}^{N}T_j^n\phi_j(x_i,y_i),$$
$$T_x^n(x_i,y_i)=\sum_{j=1}^{N}T_j^n\frac{\partial\phi_j}{\partial x}(x_i,y_i), \quad (11)$$
$$T_y^n(x_i,y_i)=\sum_{j=1}^{N}T_j^n\frac{\partial\phi_j}{\partial y}(x_i,y_i)$$

Heat Transfer Applications

To illustrate the use of meshless methods, let us begin with a simple heat transfer problem. The governing equation for temperature transport can be written as

$$\frac{\partial T}{\partial t}+\mathbf{V}\bullet\nabla T=\alpha\nabla^2T+Q \quad (12)$$

$$q+k\nabla T-h(T-T_\infty)-\varepsilon\sigma(T^4-T_\infty^4)=0 \quad (13)$$

$$T(\mathbf{x},0)=T_o \quad (14)$$

where **V** is the vector velocity, **x** is vector space, T(**x**,t) is temperature, T_∞ is ambient temperature, T_o is initial temperature, D is thermal diffusivity ($\kappa/\rho c_p$), ε is emissivity, σ is the Stefan-Boltzmann constant, h is the convective film coefficient, q is heat flux, and Q is heat source/sink. Velocities are assumed to be known and typically obtained from solution of the equations of motion (a separate program is generally used for fluid flow [7]).

In this first example, a two-dimensional plate is subjected to prescribed temperatures applied along each boundary [8], as shown in Fig. 2. The temperature at the mid-point (1,0.5) is used to compare the numerical solutions with the analytical solution. The analytical solution is given as

$$\theta(x,y)\equiv\frac{T-T_1}{T_2-T_1}=\frac{2}{\pi}\sum_{n=1}^{s}\frac{(-1)^{n+1}+1}{n}\sin\left(\frac{n\pi x}{L}\right)\frac{\sinh(n\pi y/L)}{\sinh(n\pi W/L)}$$

which yields $\theta_{(1,0.5)}$ = 0.445, or T(1,0.5) = 94.5°C. Table 1 lists the final temperatures at the mid-point using a finite element method, a boundary element method, and a meshless method, compared with the exact solution.

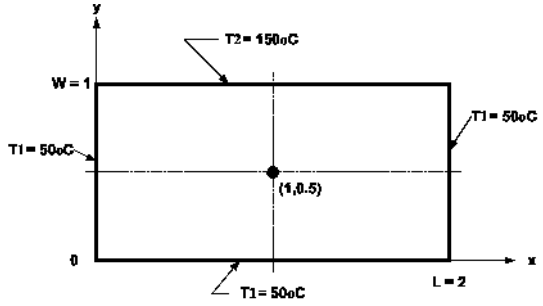

Figure 7: Steady-state conduction in a two-dimensional plate (from [8]).

Table 1. Comparison of results for example 1

Method	mid-pt (°C)	Elements	Nodes
Exact	94.512	0	0
FEM	94.605	256	289
BEM	94.471	64	65
Meshless	94.514	0	325

As a second example, a two-dimensional domain is prescribed with Dirichlet and Neumann boundary conditions applied along the boundaries, as shown in Fig. 3(a,b,c). This problem, described in Huang and Usmani [2], was used to assess an h-adaptive FEM technique for accuracy. A fixed temperature of 100°C is set along side AB; a surface convection of 0°C acts along edge BC and DC with h = 750 W/m°C and k = 52 W/m°C. The temperature at point E is used for comparative purposes. The severe discontinuity in boundary conditions at point B creates a steep temperature gradient between points B and E. Figures 3(b,c) show the initial and final FEM meshes after two adaptations using bilinear triangles. The analytical solution for the temperature at point B is T = 18.2535°C. Table 2 lists the results for the three methods compared with the exact solution. The initial 3-noded triangular mesh began with 25 elements and 19 nodes.

Table 2. Comparison of results for example 2

Method	Pt E (°C)	Elements	Nodes
Exact	18.2535	0	0
FEM	18.1141	256	155
BEM	18.2335	32	32
Meshless	18.253 1	0	83

A simple irregular domain is used for the third example and results compared with the three methods. Results from a fine mesh FEM technique (without adaptation) are used as a reference benchmark [7]. The discretized domain and accompanying boundary conditions set along each

surface are shown in Fig. 4. The FEM results are displayed as contour intervals.

Figure 5(a,b) shows meshless results (using FEM fine mesh nodes for contouring) versus FEM solutions using adapted quadrilateral elements. Heat conduction occurs as a result of constant temperatures set on the top and bottom surfaces, adiabatic faces in the upper right cutout and lower cutout portions, and convective heating along the right and left vertical walls. Adaptive meshing occurs in the corners as a result of steep temperature gradients; this is not evident when using meshless methods.

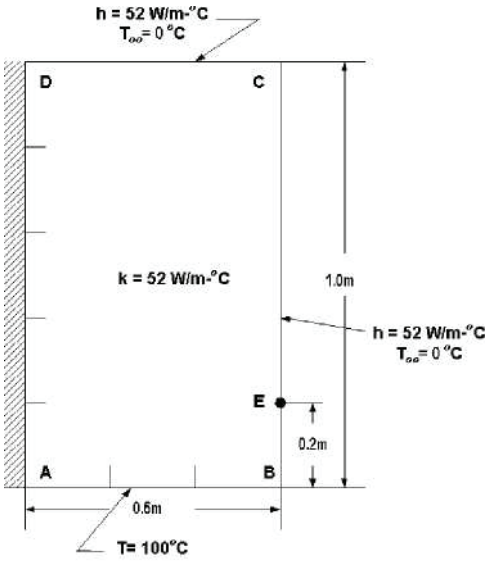

(a)

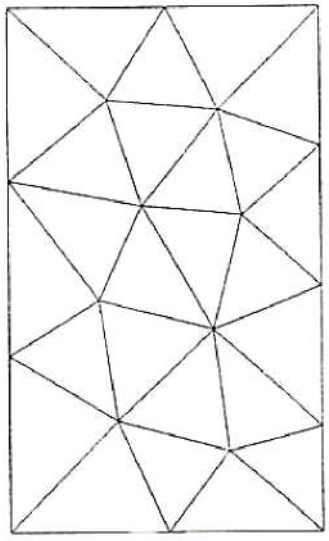

(b)

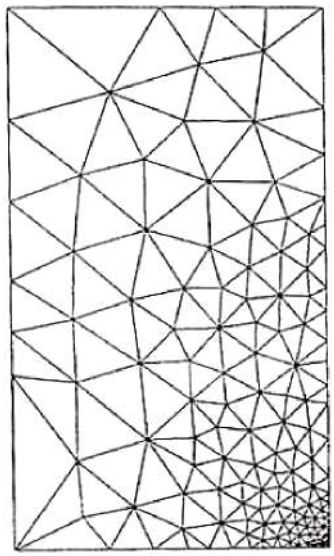

(c)

Figure 3. Problem (a) geometry - boundary conditions, (b) initial FEM mesh, and (c) final FEM adapted mesh (from [2])

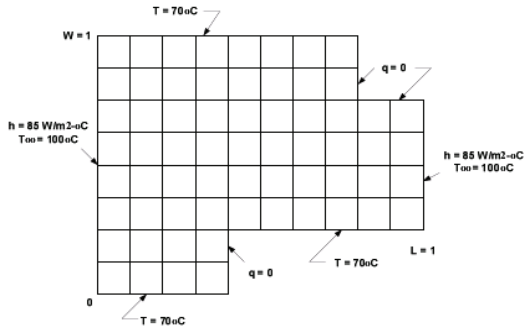

Figure 4: Problem specification for heat transfer in a user-defined domain.

The FEM, BEM, and meshless mid-point values at (0.5,0.5) are listed in Table 3.

Table 3. Comparison of results for example 3

Method	mid-pt (^{o}C)	Elements	Nodes
FEM	75.899	138	178
BEM	75.885	36	37
Meshless	75.893	0	96

All three techniques provide accurate results for the three example cases. The meshless method was clearly the fastest, simplest, and least storage demanding method to employ. Advances being made in meshless methods will eventually enable the scheme to compete with the FEM and BEM on a much broader range of problems [3,4]. Dr. Y. C. Hon[1] is a leading expert in the application of Kansa's method. Much work in engineering

modeling using Kansa's method has been done by his research group.

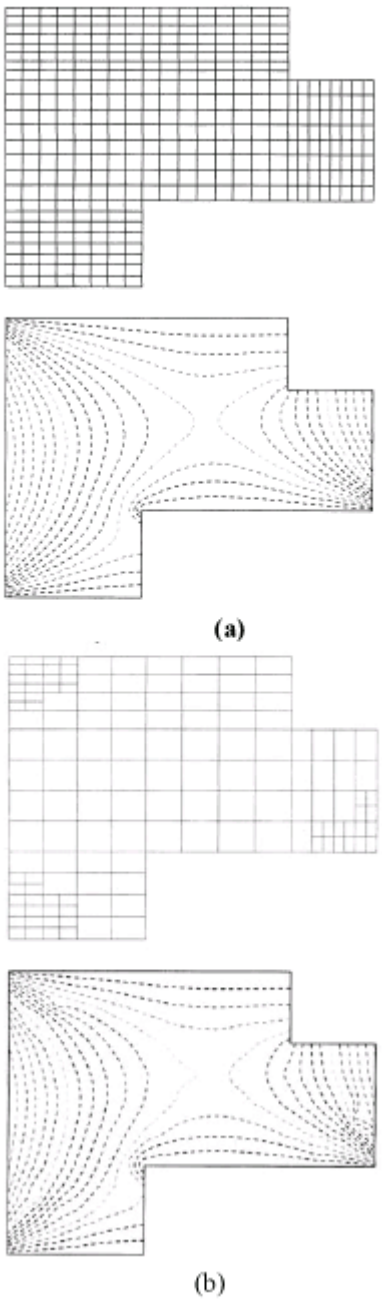

Figure 5: FEM solutions (a) meshless (on FEM fine mesh) and (b) adapted mesh.

[1] Department of Mechanical Engineering, Hong Kong University, Hong Kong, China

Natural Convection Test Case

Natural convection within a 2-D rectangular enclosure is a well-known problem commonly used to test the ability of a numerical algorithm to solve for both fluid flow and heat transfer. The equations are strongly coupled through the buoyancy term in the momentum equations and the temperature. There are various ways to nondimensionalize the equations, and numerous references can be found in the literature and on the web regarding these various forms. The solution to the problem generally splits between solving either the primitive equations for velocity or the vorticity equation, coupled with the transport equation for temperature. The issue in this early development of the meshless approach is not to dwell on various schemes to deal with pressure (e.g., projection methods or the SIMPLE scheme both of which are well known). Hence, most researchers that have developed meshless approaches use the streamfunction-vorticity and temperature equations [3]. These equations are the well-known set generally formulated as follows:

$$\frac{\partial \omega}{\partial t} + \mathbf{V} \bullet \nabla \omega = \mathrm{Pr} \nabla^2 \omega - \mathrm{Pr} \bullet \mathrm{Ra} \bullet \nabla \mathrm{T} \tag{20}$$

$$\frac{\partial \mathrm{T}}{\partial t} + \mathbf{V} \bullet \nabla \mathrm{T} = \nabla^2 \mathrm{T} \tag{21}$$

$$\nabla^2 \psi = -\omega \tag{22}$$

where ω is vorticity and ψ is streamfunction, with the conventional definitions for velocity in terms of the streamfunction gradients. Pr is the Prandtl number (ν/α) and Ra is the Rayleigh number. Figure 6 shows the physical and computational domain with accompanying boundary conditions. Two types of nodal configurations are shown in Fig. 7 (a,b) utilizing 256 nodes. Results are in excellent agreement with well-known results in the literature for $10^3 \leq$ Ra $\leq 10^5$ [3]. Figure 8 (a,b) shows streamlines and isotherms for the differentially heated enclosure for Ra = 10^5. Convergence rates showing the difference in rates between a conventional FDM and applications of two meshless techniques is discussed in Liu [3]. The two meshless methods converged more rapidly than the finite difference scheme.

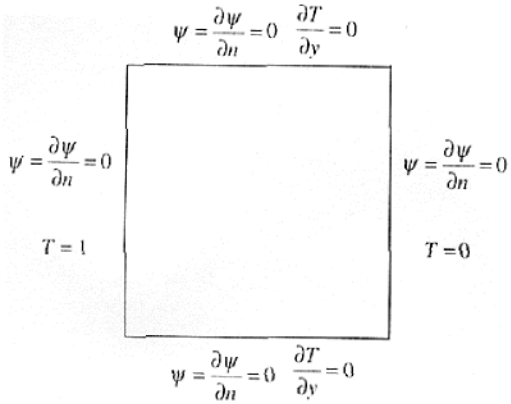

Figure 6. Boundary conditions for natural convection within a rectangular enclosure (from [3]).

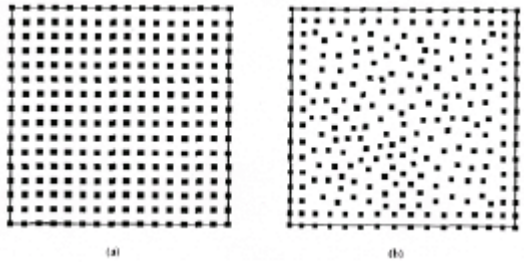

Figure 7. Nodal configurations for a) uniform distribution and b) arbitrary distribution for 256 nodes (after [3]).

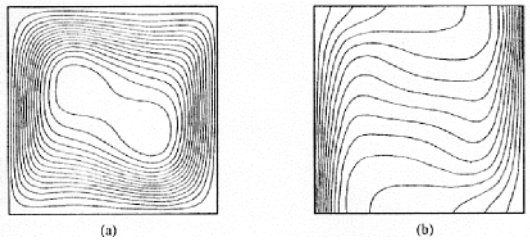

Figure 8. Natural convection results showing a) streamlines and b) isotherms for Ra = 10_5 using the MLPG method (after [3]).

Sarler et al [9] simulated natural convection within a rectangular enclosure using the RBF approach of Kansa [5]. Solving a nonlinear Poisson re-formulation of the general transport equation representing mass, energy, and momentum, the problem was solved by dividing the physical domain into two parts consisting of an internal array of nodes and a set of boundary nodes for the Dirichlet and Neumann conditions. The governing equation for the transport variable is of the form (with C(φ))

$$\frac{\partial}{\partial t}(\rho C) + \nabla \bullet (\rho \mathbf{V} C) = \nabla \bullet (\mathbf{D} \nabla C) + S \tag{23}$$

where ρ, φ, **V**, t, **D**, and S denote density, transport variable, velocity, time, diffusion matrix, and source. The transport variable C consisted of enthalpy C(h(φ = T)), velocity C(φ = u,v), and pressure C(φ = p), with a pressure correction Poisson equation used to resolve the pressure. The nonlinear equations solved with the meshless technique were of the form

$$\nabla^2 \phi = \theta + \nabla \bullet \mathbf{\Theta} \tag{24}$$

$$\theta = \left[\frac{\partial}{\partial t}(\rho' C - S) \right] / \mathbf{D} \tag{25}$$

$$\mathbf{\Theta} = \left[\rho' \mathbf{V} C - D' \nabla \phi \right] / \mathbf{D} \tag{26}$$

where ρ′ denotes density, C(φ) the transport variable, t is time, **V** is velocity, and **D** is the diffusion matrix with D' being the nonlinear anisotropic part. The variable C(φ) denotes the relation between the transported and the diffused variable. The solution requires the use of an iterative technique. The final form of the transformed Poisson equation is

$$\nabla^2 \phi = \theta + \theta_\phi (\phi - \bar{\phi}) + \nabla \bullet \mathbf{\Theta} + \nabla \bullet \mathbf{\Theta}_\phi (\phi - \bar{\phi}) \tag{27}$$

where the bar denotes values from the previous iteration. Time discretization utilizes the relation

$$\theta \approx \left[\frac{\rho C(\phi) - \rho C(\phi_o)}{\Delta t} - S \right] / \mathbf{D} \tag{28}$$

with the unknown field φ approximated by the N global approximation functions $\psi_n(p)$ and their coefficients ς_n, i.e.,

$$\phi(p) \approx \psi_n(p) \varsigma_n, \quad n = 1, 2, \ldots, N_\Gamma \tag{29}$$

The global radial basis function approximation was based on multiquadrics with the free parameter r_o:

$$\psi_n = \left(r_n^2 + r_o^2 \right)^{1/2} \tag{30}$$

The coefficients were calculated from the N collocation equations of which N_Γ were equally distributed over boundary Γ and N_Ω over the domain Ω. Separate relations were established for the boundary condition indicators.

The computational domain was discretized into 80 boundary nodes and 361 domain nodes. The multiquadrics constant r_o was set to 0.2. Steady state results were achieved after 34 iterations for Ra = 10^3, 187 iterations for Ra = 10^4, and 293 iterations for Ra = 10^5. The calculated values for temperature and velocity were in excellent agreement with results obtained using a fine grid FDM [10].

Conclusions

Meshless methods are a unique and novel numerical technique now making inroads into various fields. Their advantages in solving problems associated with crack propagation and stress/strain including deformation over more conventional numerical schemes have been demonstrated repeatedly in the literature. The application of meshless methods for heat transfer is equally advantageous; such methods have become very competitive with both finite volume and finite element methods for problems involving irregular geometries. The requirements for creating grids as well as the detailed input necessary for establishing volume or element properties is greatly reduced or eliminated. However, much has yet to be done before meshless methods can handle a wide range of fluid flow problems and produce results with confidence and surety. Only a small portion of incompressible flow problems has been addressed; advances are just now being made in the area of porous media flows. Application to compressible flows has yet to be addressed.

While meshless methods may be more accurate than FDM/FVM/FEM techniques, they can be much slower with regards to computational time to achieve convergence. This is due in part to some of the effort needed for numerical integration and subsequent use of a direct matrix solver. However, meshless methods do not need any prior knowledge of their nodal arrangement, as in conventional numerical schemes. This makes the method particularly attractive for developing adaptive capabilities. Since much of a modeler's efforts are generally spent on developing a good mesh that will lead to a converged solution, the overall time for obtaining problem solutions using meshless methods can be significantly less.

Additional information regarding FDM, FVM, and FEM algorithms and some of the meshless techniques can be obtained from the web site http://www.unlv.edu/NCACM.

Acknowledgements

We wish to thank Professor C. S. Chen and Professor Jichun Li from the Department of Mathematics at UNLV for their helpful insight and assistance.

References

1. R. W. Lewis, K. Morgan, H. R. Thomas, and K. N. Seetharamu, The Finite Element Method in Heat Transfer Analysis, J. Wiley & Sons: Chichester, UK (1996).
2. H-C. Huang and A. S. Usmani, Finite Element Analysis for Heat Transfer, Springer-Verlag: London, UK (1994).
3. G. R. Liu, Mesh Free Methods: Moving Beyond the Finite Element Method, CRC Press, Boca Raton, FL (2002).
4. S. N. Atluri and S. Shen, The Meshless Local Petrov Galerkin (MLPG) Method, Tech Science Press, Encino, CA (2002).
5. E. J. Kansa, Multiquatric – A Scattered Data Approximation Scheme with Applications to Computational Fluid Dynamics II, Computers Math. Appl., 19, 8/9, (1990), 147-161.
6. S. N. Atluri, H. K. Kim, and J. Y. Cho, J.Y., A Critical Assessment of the Truly Meshless Local Petrov-Galerkin (MLPG), and Local Boundary Integral Equation (LBIE) Methods, Computational Mechanics, 24, (1999), 348-372.
7. D. W. Pepper, D. B. Carrington, and L. Gewali, A Web-based, Adaptive Finite Element Scheme for Heat Transfer and Fluid Flow. ISHMT/ASME 4th Conf. on Heat and Mass Transfer, Jan. 12-14, Pune, India (2000).
8. F. P. Incropera and D. P. DeWitt, Fundamentals of Heat and Mass Transfer, 5th Ed., J. Wiley & Sons: New York (2002).
9. B. Sarler, J. Perko, C. S. Chen, and G.Kuhn, A Meshless Approach to Natural Convection, S. N. Atluri and D. W. Pepper (Eds.), Proceedings of the 22nd ICES Conference, July 31-Aug. 2, 2002, Reno, NV (2002).
10. D. W. Pepper and C. S. Chen, A Meshless Method for Modeling Heat Transfer, S. N. Atluri and D. W. Pepper (Eds.), Proceedings of the 22nd ICES Conference, July 31-Aug. 2, 2002, Reno, NV (2002).

Strojniški vestnik - Journal of Mechanical Engineering 51(2005)7-8, 484-490
UDK - UDC 536.2
Izvirni znanstveni članek - Original scientific paper (1.01)

Numerical Investigation on the Effects of Nozzle Geometry on the Performance of a Pulse Detonation Engine

M. Ruhul Amin[1]*, Hasan Z. Rouf[2], Jean-Luc Cambier[3]

[1]*Department of Mechanical & Industrial Engineering, Montana State University, 220 Roberts Hall, Bozeman, Montana 59717, USA, * e-mail: ramin@me.montana.edu*
[2]*Department of Mechanical and Nuclear Engineering, The Pennsylvania State University, 127 Reber Building, State College, Pennsylvania 16801, USA*
[3]*Propulsion Directorate - Aerophysics Branch, Edwards Air Force Base,10 E. Saturn Blvd., California 93524, USA*

Abstract

A numerical study is presented on the effects of various nozzle geometries and operating conditions on the performance of a Pulse Detonation Engine (PDE). An unsteady numerical simulation model, which is second order accurate in space and first order accurate in time, using an automated Java based computational fluid dynamics (CFD) software is presented. One- and two-dimensional transient CFD models were employed in a systematic manner to study the propulsive performance characteristics of the PDE under different operating conditions. Preliminary studies of the effects of nozzle geometry on the performance characteristics of a generic PDE are presented. The results indicate that an expanding nozzle, capable of adapting with the cycle time and the ambient pressure, is very suitable for optimizing the PDE performance. Addition of a straight, diverging or converging nozzle improves the performance. However, it is observed that there is an optimum value of the exit area of a divergent nozzle for performance improvement. At low ambient pressure addition of a nozzle increases the specific impulse of the PDE tube. It is also seen that a diverging nozzle is more effective than a converging-diverging nozzle at low ambient pressure. The study indicates that increased volume of the reacting fuel mixture has a negative effect on the PDE performance. The results show that a 25% reduction of the reacting fuel mixture leads to approximately 18% increase in the value of the specific impulse.

1. Introduction

The Pulse Detonation Engine (PDE) has recently received considerable interest in the aero-propulsion community due to its potential advantages in performance and inherent simplicity over current propulsion concepts. It is a very promising propulsion concept for aerospace transportation. The operation of the PDE is based on the detonation mode of combustion, which involves the burning of a reactive gas mixture at high pressure and high temperature behind a propagating shock wave. The high-pressure combustion products, acting on the thrust plate at the front end of the engine, produce the forward thrust. The PDE is an unsteady propulsion device, which operates in an intermittent manner governed by a cycle frequency. Fig. 1 shows a schematic of a typical air-breathing pulse detonation engine, which consists of a simple straight cylindrical tube. The details of the operating principle can be seen elsewhere [1, 2]. The design and optimization of a PDE propulsion system are complex due to the unsteady nature of the propulsion cycle and the strong coupling of the propulsive flow with the vehicle configuration and the ambient environment.

A nozzle may significantly affect the performance of a PDE and hence nozzle design is one of the key issues to be resolved. Due to the complexity of the diffraction of detonation wave through a nozzle, the effects of a nozzle on PDE performance are not yet fully understood. The presence of a nozzle may affect the time required to drop the pressure inside the PDE combustor to a certain level at which time the next cycle can be started. Therefore, the effects of the nozzle geometry on the cycle time and PDE performance need to be investigated.

Cambier and Adelman [3] reported a numerical study of a pulse detonation wave engine (PDWE) using quasi one-dimensional computations. The computations were carried out with a shock-capturing total variation diminishing (TVD) algorithm (second order accurate in

Nomenclature

A_{exit}	Nozzle exit area, m^2	m_s	Molar mass of specie *s,* kmol
A_{tube}	Tube exit area, m^2	P	Pressure, Pa
E	Total energy, J/m^3	t	Time, sec
Isp	Specific impulse, sec	T	Absolute temperature, K
Isp_final	Specific impulse final, sec	u	Mean flow velocity, m/sec
Isp_max	Specific impulse maximum, sec	ρ	density, kg/m^3
L_{nozzle}	Nozzle length, m	ρ_s	mass density of specie s, kg/m^3
L_{pde}	PDE tube length, m	$\dot{\omega}_s$	rate of production of specie *s*
$l_{propellant}$	Length of the propellant mixture, m		per unit volume, kg/m^3 sec kmol

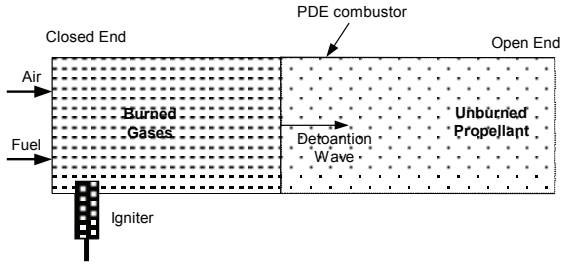

Fig. 1. Schematic of a typical air-breathing pulse detonation engine

space) for multiple species and multi-step finite-rate kinetics. Eidelman et al. [4] performed a two-dimensional simulation of a detonation tube using a second-order Godnunov solver on unstructured grids. A detailed description of the basic operations of a PDE was provided by Bussing and Pappas [1]. The authors concluded that a detonation combustion process is thermally more efficient than a traditional constant pressure combustion process. In a subsequent study performed by Bussing et al. [5], a comparison between open- and closed-end initiations was provided. In recent years Cambier and Tenger [6] reported a computational study of nozzle effects on PDE performance. In the following year Eidelman and Yang [2] reported the effects of adding a nozzle on PDE efficiency. Their results indicate a drastic increase of engine efficiency in the presence of a nozzle. Based on experimental investigations, Cooper et al. [7] reported that the addition of a divergent nozzle has negligible effect on PDE performance; while, the addition of a straight nozzle is very much effective to improve PDE performance. Recently, Mohanraj and Merkle [8] reported multi-cycle performance analysis of a PDE using a quasi one-dimensional model. In this research, results of a systematic study on various nozzle geometries, effects of ambient pressure and the tube fill fraction are presented.

2. Mathematical Formulation and Numerical Methodology

2.1 Governing Equations

The following assumptions were made in the formulation of the transient combustion process in a pulse detonation engine: (i) no species diffusion, (ii) no heat conduction, (iii) heat flow due to density gradient is neglected, (iv) bulk viscosity is neglected, (v) diffusion due to pressure gradient is ignored, (vi) heat capacities are a function of temperature (real gas), (vii) thermal equilibrium (single temperature), (viii) viscous dissipation and viscous work are neglected, and (ix) no body forces.

The time-dependent conservation equations governing the dynamics of the inviscid, non-heat conducting, reacting gas flow, are being solved. The fundamental set of governing equations for the system is:

- Conservation of Mass:

$$\frac{\partial \rho}{\partial t} + \frac{\partial (\rho u)}{\partial x} = 0 \tag{1}$$

- Conservation of momentum:

$$\frac{\partial (\rho u)}{\partial t} + \frac{\partial (\rho u^2 + P)}{\partial x} = 0 \tag{2}$$

- Conservation of Energy:

$$\frac{\partial E}{\partial t} + \frac{\partial (uE + uP)}{\partial x} = 0 \tag{3}$$

Here ρ, u, P, and E are the density, velocity, pressure and total energy respectively. The physical and chemical effects of combustion are modeled by solving the chemical kinetics equations. The general form of the conservation equations for the mass densities of chemical species (index s) is given by the following reaction kinetics equation:

$$\frac{\partial \rho_s}{\partial t} + \vec{\nabla} \cdot (\vec{u}\rho_s) = m_s \dot{\omega}_s \quad (4)$$

where $\vec{u}$ is of course the mean flow velocity, m_s is the molar mass and $\dot{\omega}_s$ is the rate of production of species *s* per unit volume respectively.

2.2 The CFD Model

The combustion in a PDE is unsteady in nature. One-dimensional and two-dimensional unsteady CFD computations are used to get realistic approximations of the unsteady processes associated with a PDE operation. The CFD code *Café-Vienna*, developed by Dr. J.-L. Cambier was used to perform the unsteady computations. *Café-Vienna* is a Java version of the *Mozart* CFD code [9], that computes inviscid flow field using the Euler equations. An inviscid, two-dimensional numerical scheme coupled to the detailed reaction kinetics of the combustion is employed. The PDE environment is characterized by multiple shocks in the flow field. The scheme used here is that of Harten [10], generalized to multiple species; it is second-order accurate in space, total variation diminishing (TVD), and first order accurate in time. The chemical kinetics and the inviscid transport process are coupled via an operator-splitting method.

2.3 Code Validation and Grid Independency Test

The code validation was performed by comparing the computed results with the experimental results of Schauer et al. [11]. In order to demonstrate the numerical accuracy of the present numerical scheme, comparisons were also made with the analytical results of Wintenberger et al. [12] who developed a simple analytical model to approximate the PDE performance. In order to minimize the computation time with a desired level of accuracy, the grid independence test is essential. The grid resolution should ensure that the main detonation features such as detonation speed, temperature, and pressure distribution behind the detonation shock are grid independent, as well as ensure that the computational cost is minimum. In this test, the system configuration is a straight cylindrical tube with constant cross-section, 20 cm in length and 2 cm in radius. The PDE tube is uniformly filled with a stoichiometric hydrogen-air mixture. Both the ambient pressure and the initial fill pressure are chosen to be 1 atm and the initial temperature of the PDE chamber is set at 300 K. Using four different uniform grid sizes one-dimensional simulations were carried out to establish the grid independence. The different grid sizes are: 1, 0.8, 0.4, and 0.2 mm. The initial conditions were kept the same for all the cases. It was observed that for the different grid spacing, all the simulations show very similar detonation behavior. In general, the results with the coarsest grid (grid size 1 mm) fall within 7% of the results obtained using the finest grid (grid size 0.2 mm), except near the region of peak pressure. Therefore, the grid with 1 mm element size was chosen for the current study. Details of the code validation and grid independency test are reported in Cambier et al. [13] and Rouf [14].

3. Results and Discussions

A reference PDE tube, 30 cm in length and 2 cm in radius, is uniformly filled with a stoichiometric hydrogen-air mixture. Both the ambient pressure and the initial fill pressure are chosen to be 1 atm. Initial temperature of the PDE chamber is 300 K. Detonation initiation is assured by having a large amount of energy deposition near the closed-end (thrust wall) of the tube. This is achieved by creating a high pressure and high temperature region near the closed-end. Computations were performed for a single pulse in a two-dimensional-axisymmetric configuration. Three basic nozzle configurations were investigated: diverging nozzle, straight nozzle, and converging nozzle. It was observed that addition of a nozzle increases the performance of the PDE. In this paper the effects of different length of the straight nozzle, exit area of the divergent nozzle, ambient pressure and tube fill fraction are presented.

3.1 Length of Straight Nozzle

Several cases were run to study the effects of the length of a straight nozzle connected with the PDE tube. The nozzle length was systematically varied, whereas the tube length was held constant. The length of the straight nozzle was varied from 5 to 50 cm, giving a range of the length ratio L_{nozzle}/L_{pde} = 0.17 to 1.67.

Fig. 2 shows the maximum specific impulse during a single pulse (*Isp-max*) and the final specific impulse at the end of a single pulse (*Isp-final*) as functions of the nozzle length. It can be observed that both *Isp-final* and *Isp-max* increase nearly linearly with the increase of the nozzle length. Alternately, the observations suggest a higher specific impulse for a longer straight nozzle. To explain this behavior the "no-nozzle" case needs to be considered first. As reported by Li et al. [15] and Li & Kailasanath [16], in the no-nozzle case, when the detonation wave leaves the combustion chamber, it expands very quickly as a spherical wave. In contrast, in the straight nozzle case, when the detonation wave leaves the PDE tube it enters the nozzle section, and therefore, the wave is still confined by the nozzle wall. This is the reason why the shock does not decay as quickly as in the no-nozzle case. This results in an increase in pressure relaxation time and prolongs the thrust generation.

Fig. 3 represents the thrust generation during a single pulse as a function of time for different nozzle lengths. It can be observed that with the increase of the straight nozzle length the thrust generation time is prolonged. A close observation of the thrust profile reveals that in the case of 10 cm long nozzle the thrust becomes negative at around 1.2 ms; meanwhile for the 20 cm long nozzle the thrust takes on a negative value at around 1.5 ms; this means that the thrust generation time is approximately

25% longer for the 20 cm long nozzle. Due to the prolonged thrust generation, a higher impulse is obtained for a longer straight nozzle.

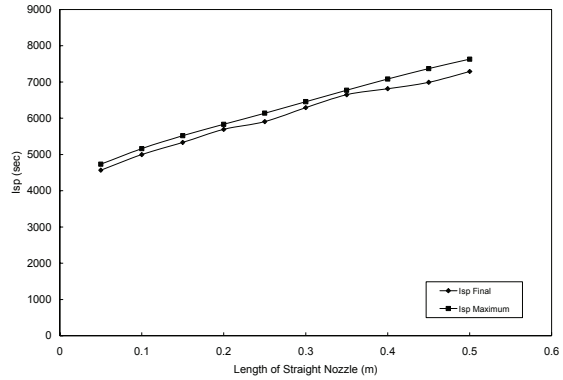

Fig. 2. Specific impulse versus length of straight nozzle

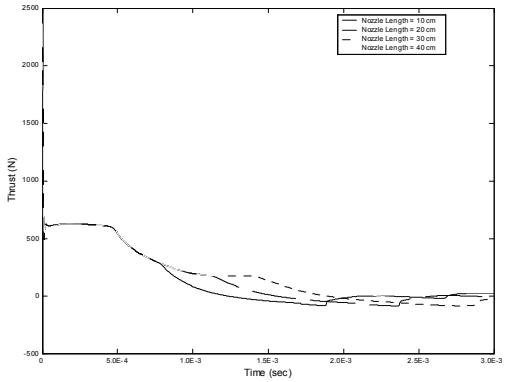

Fig. 3. Instantaneous thrust profiles for different lengths of straight nozzle

As mentioned earlier, reducing the cycle time can optimize the PDE performance. Fig. 4 shows the blow-down time (time when pressure inside PDE chamber reaches 1 atm) as a function of the nozzle length. The results indicate that the increase in length of a straight nozzle leads to an increase in the blow-down time. In other words, the cycling would be faster if the nozzle is shorter.

Fig. 5 shows the average temperature inside the PDE tube as a function of time for different straight nozzle geometries. The results show that when the straight nozzle is longer, the temperature inside the PDE tube drops at a slower rate. This can be explained by the fact that increased nozzle length causes a delay in the arrival of the expansion waves. This delay in turn causes the temperature inside the PDE to drop at a slower rate.

3.2 Exit Area of Diverging Nozzle

To study the effects of the exit area of a divergent nozzle, a cylindrical PDE tube, 30 cm in length with an internal radius of 2 cm, was attached with various geometries of the divergent nozzles. The divergent nozzle was also 30 cm in length and connected at the open-end of the PDE tube. The throat area of the nozzle is equal to the PDE tube area, which means there is no constriction between the tube exit plane and the nozzle exit plane. The exit area of the nozzle was systematically varied, whereas the PDE tube area was held constant. The nozzle exit radius was varied from 2.5 to 7 cm, giving a range of the nozzle expansion ratio (A_{exit}/A_{tube}) of 1.56 to 12.25. The initial amplitude of the oscillatory impulse profile was observed to increase with the increase of the nozzle expansion ratio (i.e. nozzle exit area). Rapid impulse generation was also observed with the increase in nozzle expansion ratio.

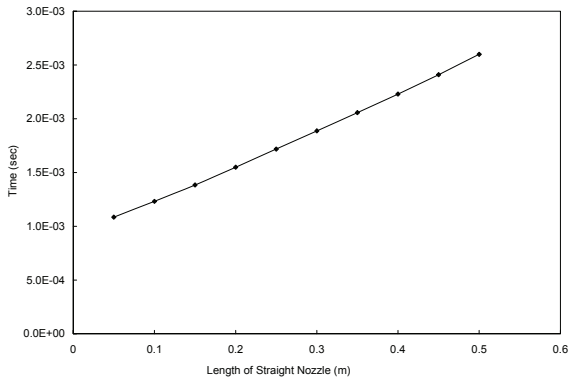

Fig. 4. Blow-down time versus length of straight nozzle

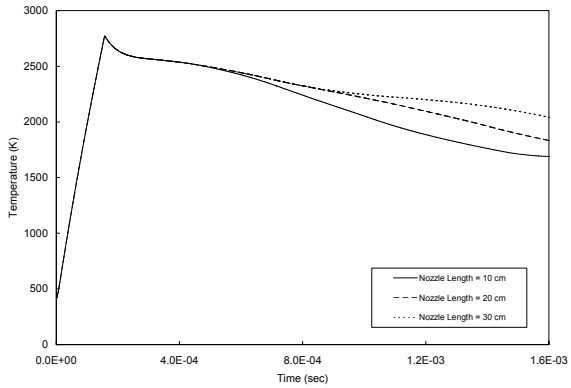

Fig. 5. Effect of straight nozzle length on PDE temperature

In Fig. 6 *Isp-final* (computed from the final impulse at the end of a single pulse) and *Isp-max* (computed from the maximum impulse during a single pulse) are plotted as functions of the expansion ratio. The results indicate that initially both *Isp-final* and *Isp-max* increase with the nozzle expansion ratio. The *Isp-final* reaches a maximum value at an optimal value of the expansion ratio and then it gradually decreases. Whereas the *Isp-max* shows a monotonic behavior, that is, it keeps increasing with the nozzle expansion ratio.

It can be recalled that the PDE performance should be optimized in terms of cycle time also. Fig. 7 shows the blow-down time as a function of the nozzle expansion ratio. It can be observed that the blow-down time

decreases with the nozzle expansion ratio. This means that the cycling would be faster if the nozzle expansion ratio is larger. Therefore, the impact of adding a variable area divergent nozzle with the PDE tube appears potentially attractive. Comparing Figs. 4 and 7, it can be concluded that shorter nozzles with a higher expansion ratio may be an attractive option due to lower values of blow-down time.

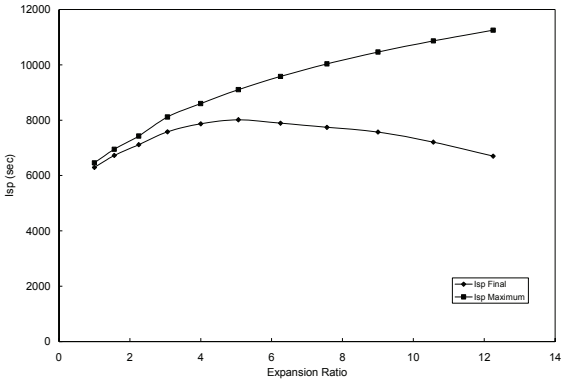

Fig. 6. Specific impulse as function of expansion ratio of a divergent nozzle

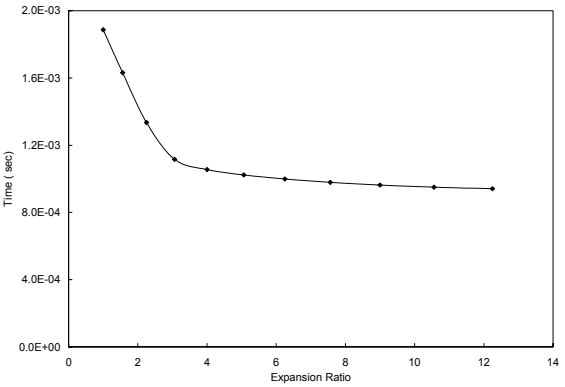

Fig. 7. Blow-down time versus expansion ratio

3.3 Effects of Ambient Pressure

In this section, the effects of the ambient pressure on the performance of a PDE are investigated. This investigation will help to observe the PDE performance at different altitudes. Four different geometries are considered: (i) a straight PDE tube, 10 cm in length and 2 cm in radius; (ii) a straight PDE tube, 30 cm in length and 2 cm in radius (iii) a diverging nozzle, 10 cm in length and 4 cm in exit radius, attached at the open end of the PDE tube (10 cm in length and 2 cm in radius), and (iv) a 10 cm long converging-diverging nozzle, having a throat radius of 1.4 cm and an exit radius of 4 cm, connected with the PDE tube (10 cm in length and 2 cm in radius). Computations were performed for values of ambient pressures as 0.25, 0.50, 0.75, and 1 atm. Like the previous investigations, here the PDE tube is uniformly filled with a stoichiometric hydrogen-air mixture. Here the ambient pressure was varied, while the initial fill pressure was kept constant (1 atm).

Fig. 8 shows the variation of the specific impulse with the ambient pressure for all the four different configurations. From this figure it is evident that with the decrease in the ambient pressure, the specific impulse increases. The performance gain is due to the fact that a reduction in the back-pressure results in a higher pressure difference between the chamber and the ambient. This leads to an increase in the momentum flow rate of the exhaust products directed towards the ambient. Therefore, decreasing the ambient pressure increases the net thrust, which increases the impulse, and hence the specific impulse is increased.

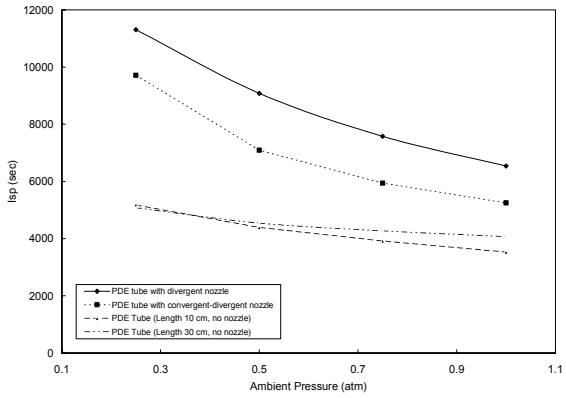

Fig. 8. Specific impulse versus ambient pressure for different configurations

A closer look at Fig. 8 reveals that when a divergent nozzle or a convergent-divergent nozzle is present with the PDE tube, more performance gain can be obtained at lower ambient pressures than the configurations without any nozzle. For the first configuration, where the PDE tube 10 cm long and no nozzle is attached to the tube, a 50% reduction of the ambient pressure increases the specific impulse by 24.4%. For the diverging and the converging-diverging nozzle cases, the same reduction of the ambient pressure leads to an increase of the specific impulse by about 38% and 35% respectively. The observations suggest that at lower back-pressures the presence of a nozzle is very much beneficial. Fig. 8 also implies that a diverging nozzle is more effective than a converging-diverging nozzle at low ambient pressures.

3.4 Effects of Tube Fill Fraction

Several cases were run to study the effects of the size of the propellant mixture in the PDE tube. Fig. 9 shows a schematic of the computed configuration where the PDE tube (of length L_{pde}) is not completely filled with the propellant mixture. The propellant mixture occupies the length $l_{\text{propellant}}$ of the PDE tube and the remaining portion is filled with air. The tube fill fraction (TFF = $l_{\text{propellant}}/L_{pde}$) is the ratio of the volume of the propellant mixture to the volume of the PDE tube. Numerical

results were obtained for a range of values of tube fill fraction from 0.2 to 1.0.

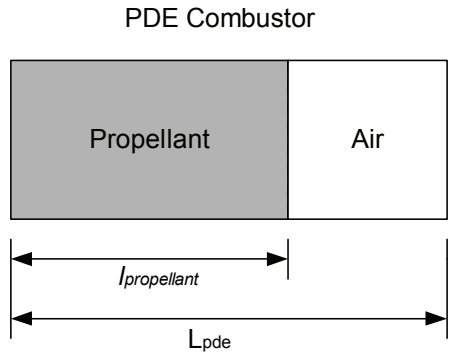

Fig. 9. Schematic of the straight tube PDE with partial tube filling

The variation of the specific impulse (*Isp*) with the tube fill fraction (TFF) is shown in Fig. 10. As shown in this figure, increasing the tube fill fraction (or, the volume of the reactive gas mixture) plays a negative role on the specific impulse. For the values of tube fill fraction 1, 0.75, and 0.50, the *Isp* values are approximately 5325 sec, 6000 sec, and 7250 sec respectively. The results indicate that a 25% reduction of the propellant mixture size leads to an *Isp* increase by approximately 18%; a 50% reduction leads to an *Isp* increase by approximately 36%. This trend has been confirmed by the experimental observations of Schauer et al. [11]. One possible reason for this increase in the specific impulse is that when a tube is partially filled with propellant mixture, the remaining portion will act as a straight nozzle for the exhaust of the detonation products. As already discussed in the previous sections, the presence of a straight nozzle with a PDE tube can significantly increase the PDE performance and the performance increases with the length of the straight nozzle.

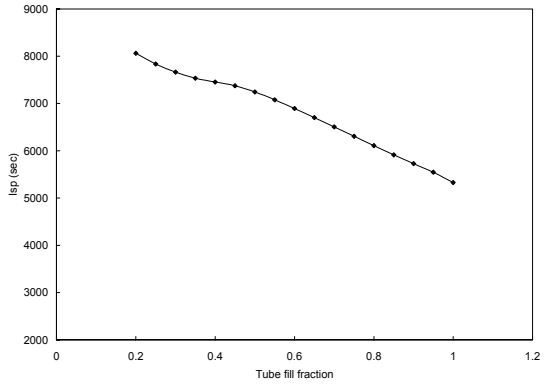

Fig. 10. Specific impulse versus tube fill fraction

Also observed was the pressure profile behind the moving detonation wave while the detonation wave remained inside the PDE tube's non-combustible air section. Fig. 11 shows the pressure profile inside a 10 cm long PDE tube, with a tube fill fraction of 0.6 at times 0.026 ms and 0.064 ms. It can be observed that at 0.026 ms the detonation wave stays approximately 5 cm away from the thrust wall. Since the filling length is 6 cm, the shock front is still inside the propellant mixture. From the pressure profile it can be seen that the peak pressure behind the shock is 13 atm. When the detonation wave enters the non-reactive air section the detonation is quenched, and the shock loses its strength as it no longer receives energy support from the chemical reactions. Fig. 10 shows the pressure profile behind the quenched shock when the shock reaches near the tube-exit at approximately 0.064 ms. It can be seen that the peak pressure behind this quenched shock is only about 8 atm, which is considerably lower than the pressure behind the original shock front.

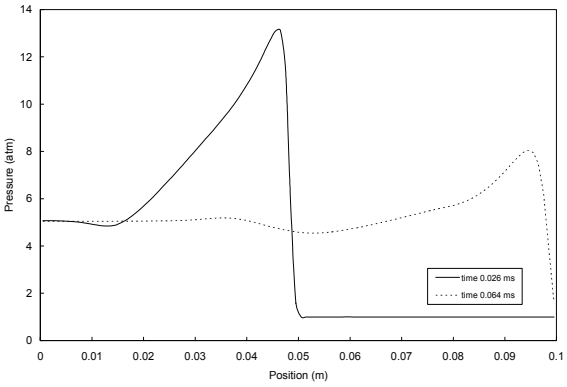

Fig. 11. Pressure profile at two different times for tube fill fraction 0.6

4. Conclusion

The results of a systematic numerical investigation of the effects of nozzle geometry and various operating conditions namely ambient pressure and tube fill fraction on PDE performance characteristics are presented. An automated Java-based CFD software designed with modern object-oriented programming techniques was employed to investigate the propulsive performance characteristics of the PDE. Accuracy of the code was tested by comparing the results with other published results and grid independency test was performed. It can be concluded from the current numerical study that addition of a nozzle to the PDE combustor increases the performance which includes: (i) increased impulse, (ii) prolonged duration of thrust, and (iii) reduced cycle time. Adding a straight nozzle delays the arrival of the expansion wave at the thrust wall from the PDE tube exit, hence, the duration of thrust generation is prolonged. A divergent nozzle also delays the arrival of the expansion wave at the thrust wall. It also increases the effective thrust-wall area. A convergent nozzle causes multiple shock reflections in the nozzle section and increases the impulse generation considerably.

An expanding nozzle can provide a better performance in stagnant ambient air. For an expanding nozzle, there is an optimal expansion ratio at which the maximum

performance can be achieved. For very high altitude operation, i.e., at very low ambient pressure, addition of a nozzle considerably increases the specific impulse of the PDE. The performance gain is due to the increased momentum flow rate of the exhaust products at a lower back-pressure. It is also observed in this study that increased volume of the reactive gas mixture decreases the specific impulse of the PDE tube. This observation is consistent with other published experimental data.

Acknowledgements

This work was supported by US Department of Defense, Contract No. 00014-00-1-0474.

References

[1] T. Bussing and G. Pappas, An introduction to pulse detonation engines, AIAA 94-0263, January 1994.

[2] S. Eidelman and X. Yang, Analysis of the pulse detonation engine efficiency, AIAA 98-3877, July 1998.

[3] J.-L. Cambier and H.G. Adelman, Preliminary numerical simulations of a pulsed detonation wave engine, AIAA 88-2960, July 1988.

[4] S. Eidelman, W. Grossmann and I. Lottati, Computational analysis of pulse detonation engines and applications, AIAA 90-0460, January 1990.

[5] T. Bussing, J.B. Hinkey and L. Kaye, Pulse detonation engine preliminary design considerations, AIAA 94-3220, June 1994.

[6] J.-L. Cambier and J.K. Tegner, Strategies for PDE performance optimization, AIAA 97-2743, July 1997.

[7] M. Cooper, S. Jackson, J. Austin, E. Wintenberger and J.E. Shepherd, Direct experimental impulse measurements for detonations and deflagrations, AIAA 01-3812, July 2001.

[8] R. Mohanraj and C.L. Merkle, A numerical study of pulse detonation engine performance, AIAA 2000-0315, January 2000.

[9] S. Tokarcik-Polsky and J.-L. Cambier, Numerical study of transient flow phenomena in shock tunnels, AIAA Journal, Vol. 32, No. 5, 1994, pp. 971-978.

[10] A. Harten, High resolution schemes for hyperbolic conservation laws, Journal of Computational Physics, Vol. 49, 1983, pp. 357-393.

[11] F. Schauer, J. Stutrud and R. Bradley, Detonation initiation studies and performance results for pulsed detonation engine applications, AIAA 2001-1129, January 2001.

[12] E. Wintenberger and J.M. Austin, M. Cooper, S. Jackson and J.E. Shepherd, An analytical model for the impulse of a single-cycle pulse detonation engine, AIAA 2001-3811, July 2001.

[13] J.-L Cambier, M.R. Amin and H.Z. Rouf, Parametric investigations of a pulse detonation engine operation with an automated performance optimization software, AIAA 2003-0890, January 2003.

[14] H. Z. Rouf, Parametric study for performance optimization of pulse detonation engines, M.S. Thesis, Montana State University, Bozeman, MT, 2003.

[15] C. Li, K. Kailasanath and G. Patnaik, A numerical study of flow field evolution in a pulse detonation engine, AIAA 2000-0314, January 2000.

[16] C. Li, and K. Kailasanath, A numerical study of reactive flows in pulse detonation engines, AIAA 2001-3933, July 2001.

Strojniški vestnik - Journal of Mechanical Engineering 51(2005)7-8, 491-494
UDK - UDC 536.2
Izvirni znanstveni članek - Original scientific paper (1.01)

Numerical Simulation on Mixed Convection in a Porous Medium Heated by a Vertical Cylinder

Ling LI [1,2], Shigeo KIMURA [1,*]

[1] *Institute of Nature and Environmental Technology, Kanazawa University,2-40-20,Kodatsuno, Kanazawa 920-8667, Japan, * e-mail: skimura@t.kanazawa-u.ac.jp*

[2] *Department of Hydraulic Engineering, Tsinghua University, Beijing, China*

Abstract

Numerical simulation has been performed for mixed convection of heated vertical cylinder with a constant temperature in a saturated porous medium subjected to lateral flow. Four different geometric aspect ratios 5,10,25 and 50 were considered, which give ratios of axial length to diameter. Based on dimensional analysis and nonlinear regression, correlations for the Nusselt number against the Rayleigh and the Peclet numbers have been obtained. It is shown that the average Nusselt number (Nu) is a function of the Rayleigh number (Ra_d) and the Peclet number (Pe): $Nu = 3.1\sqrt{Pe}$ for $Ra_d / Pe < 1$, and $\frac{Nu}{Pe^{1/2}} = 3.1 + 0.4\left(\frac{Ra_d}{Pe} - 1\right)^{1/2}$ for $Ra_d / Pe \geq 1$. As compared with $Nu = 3.1\sqrt{Pe}$ for the case of horizontal forced flow around a vertical cylinder, the results of this investigation indicates that heat transfer can be remarkable enhanced by natural convection when forced convection is weak.

INTRODUCTION

Convective heat transfer and fluid flow around vertical cylinder in porous media has recently received considerable attention in geophysical and engineering applications. Such applications include geothermal systems, chemical catalytic reactor, packed sphere beds, grain storage and thermal insulation engineering. However, most existing fundamental studies have focused on natural convection, or forced convection, while a very few have been reported for mixed convection despite its equal importance in many situations. Mixed convection about a vertical cylinder subjected to horizontal flow has not been investigated extensively [1].

Cheng [2] provided an extensive review of the literature on natural convection heat transfer in fluid saturated porous media He also investigated mixed convection from a horizontal circular cylinder in a saturated porous medium with boundary layer approximation[3]. In connecting with the forced convection by lateral flow, the analysis was made by Kimura [4] to cylinders of elliptic cross sections with integral methods. In his paper, Kimura provided the average Nusselt number for the steady state by integral solution with the formulation of $Nu = 3.1\sqrt{Pe}$, where the characteristic length in Nu is taken as the circumferential length πd . In addition, Romero [5] presented solutions for the temperature field due to Darcy flow past a slender body with a prescribed flux distribution embedded in a saturated porous medium. For the natural convection Sano et al. [6] studied the convective flows around a sphere embedded in a porous medium at small Rayleigh number and obtained asymptotic solutions for the transient and steady-state temperature distribution and flow pattern around the sphere. Campos et al. [7] studied the natural convection in the annulus of cylinder filled with porous medium, which has the heated inner wall and the cooled outer wall. However, pure natural or force convection rarely occurs in reality. In low Reynolds number flow conditions, heat transfer mechanisms of both forced convection and natural convection play a vital role and both mechanisms have to be properly accounted for.

Nomenclature

Roman symbols

c_p	specific heat	[J/(kg K)]
d	diameter of cylinder	[m]
d_p	diameter of the solid particle	[m]
g	gravitational acceleration	[m/s^2]
K	permeability	[m^2]
k	thermal conductivity	[W/(m K)]
L	length of cylinder	[m]
Nu	Average Nusselt number	
p	pressure	[Pa]
Pe	Peclet number	
$\overline{q}''$	average heat flux	[W/m^2]
Ra_d	Rayleigh number	
T	temperature	[K]
V	velocity vector	[m/s]
u,v,w	velocity components in the x,y,z system of coordinates	[m/s]
x,y,z	Cartesian coordinates	[m]

Greek symbols

▪ ż	Thermal diffusivity of porous medium ($=k_m/(\rho c_p)_f$)	[m^2/s]
▪ Ŕ	coefficient of thermal expansion	[K^{-1}]
ϕ	porosity of porous medium	
▪ Ď	density	[kg/m^3]
▪ Ę	dynamic viscosity	[Pa s]
▪ Ë	kinematic viscosity	[m^2/s]

Subscripts and superscripts

f	fluid
m	effective
s	solid
w	wall
0	inlet

Recently, numerical results for mixed convection around vertical cylinder by using two-dimensional numerical model have been reported [8,9]. In these research works, fluid flows along the axis of the cylinder are considered so that the problem is axisymmetric. As far as we know, there are very few papers on the problems of mixed convection of a vertical heated cylinder subjected to lateral flow in a saturated porous medium. The work by Ingham and Pop [10] is the only one that dealt with the similar problem. However, they assumed a partially heated infinite vertical cylinder in order to make the mathematical formulations easier. They also relied on the boundary layer approximations, which naturally limit the validity of their results in certain parametric ranges.

In the present work, three-dimensional numerical calculation was performed to simulate the mixed convection in a porous medium heated by vertical cylinder. From a parametric study, average Nusselt numbers were obtained and effects of ratio of length to diameter of cylinder, temperature differences, permeability of porous medium and lateral flow velocity on them were investigated. Results obtained from the simulation for two extreme cases, namely pure natural and forced convection, were compared with those in the literatures in order to test our code.

Governing equations and numerical methods

The analysis is based on solving Darcy's equations for three-dimensional flow around a vertical cylinder placed in porous medium. The vertical cylinder has a constant surface temperature (T_W). Fluid flows around the cylinder axis with a uniform velocity profile (V_0) and a constant fluid temperature (T_0). It is assumed that the flow is steady, laminar, three-dimensional and incompressible. The radiation and thermal dissipation effect are neglected. In addition, permeability and thermal conductivity of porous medium are homogeneous and isotropic, and it is in local thermal equilibrium with the fluid. It is assumed that the thermophysical properties of the fluid are independent of temperature except for the density in the buoyancy term, that is, the Boussinesq approximation is invoked.

The conservation equations for mass, momentum, energy in the fluid region are:

$$\nabla \cdot V = 0 \tag{1}$$

$$V = -\frac{K}{\mu}\nabla(p + \rho g) \tag{2}$$

$$(V \cdot \nabla)T = \alpha \nabla^2 T \tag{3}$$

where α is defined by $\alpha = k_m/(\rho c_p)_f$,and ρ and c_p denote the density and specific heat of the fluid, respectively. The effective thermal conductivity of the porous medium k_m is given by

$$k_m = k_s(1-\phi) + k_f\phi \tag{4}$$

With k_s and k_f representing the thermal conductivity of solid and liquid phase, respectively, and ϕ representing the porosity of the porous medium. At the same time, the permeability K is given by

$$K = \frac{d_p^2\phi^3}{180\cdot(1-\phi)^2} \tag{5}$$

With d_p representing the sphere's diameter of porous medium.

In addition, some nondimensional numbers are defined as follows, Peclect number $Pe = V_0 d / \alpha$; Average Nusselt number $Nu = \bar{q}'' \pi d / [(T_w - T_0) k_m]$; Rayleigh number $Ra_d = g\beta K d (T_w - T_0) / (\alpha \upsilon)$. Note that the Nusselt number is defined by πd . The boundary conditions are summarized in Table .1.

Table 1 The boundary conditions of numerical mode

Boundary type	Inflow	Top (Bottom)	Front (Back)	Outflow	Cylinder Wall
Velocity	$u = U_0$ $v = 0$ $w = 0$	$\partial u / \partial z = 0$ $\partial v / \partial z = 0$ $w = 0$	$\partial u / \partial y = 0$ $v = 0$ $\partial w / \partial y = 0$	Zero gradient	slip
Tempe-rature	$T = T_0$	$\partial T / \partial z = 0$	$\partial T / \partial y = 0$	Zero gradient	$T = T_w$

All the above calculations were performed using the FLUENT code. The governing Eqs. (1)-(3) were discretized using a finite volume method and the SIMPLE algorithm was used to solve the equations. A numerical scheme with non-uniform unstructured grids generated by GAMBIT software was applied to the present physical system. In order to obtain grid independent results, different finest grid spaces adjacent to the wall of size 0.005m, 0.002m and 0.001m are tested. It is proved that the difference between the results predicted based on 0.002m and 0.001m, the finest grid adjacent to the wall, are insignificant (<1%). Thus the finest grid, of size 0.002m and located adjacent to the wall, is chosen to get more detailed situation of the flow field.

Results and discussions

Numerical results compared with analytical solutions.

In order to confirm the validity of the numerical model, the numerical results were compared with analytical solution for forced convection and natural convection in a porous medium heated by a vertical cylinder, respectively. The average Nusselt numbers are in fairly good agreement with the data from References [4,11], as shown in Fig.1 and Fig.2.

Effect of Rayleigh number

Average Nusselt numbers for *L/d*=10 and eight different Rayleigh numbers are shown in Fig.3. Also shown on this graph is Nusselt number for the forced. It has shown that *Nu* is the function of *Ra* and *Pe*. Nu will increase with rising of Ra. When *Pe* is more than 8, *Nu* variations show a forced convection characteristic. However, just after the onset of the buoyancy drive secondary flow. This is a result of the buoyancy forces that become strong enough to destabilize the lateral flow. Moreover, an increase in the Nusselt number with the Rayleigh number is observed.

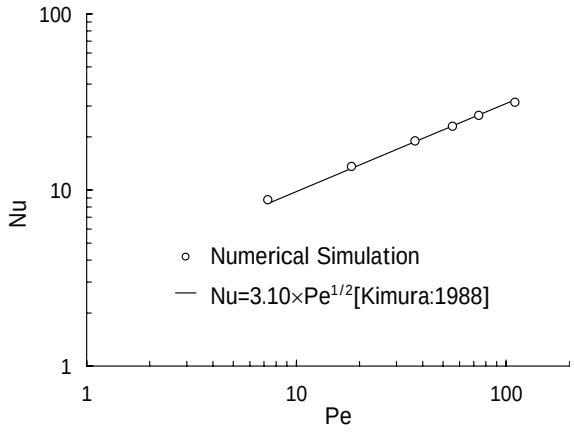

Fig.1. Calculation compared with analytical solution for Forced convection.

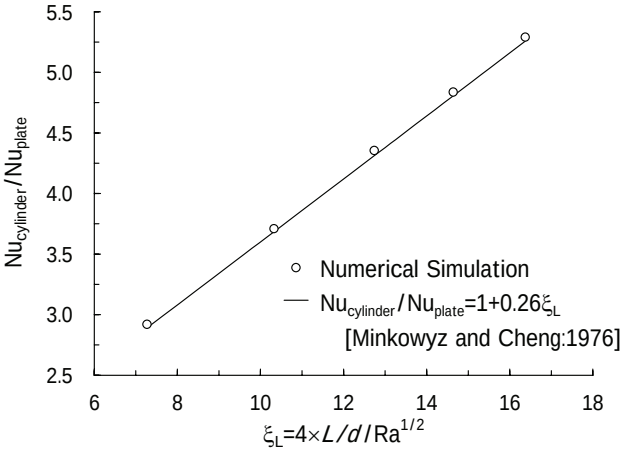

Fig.2. Calculation compared with analytical solution for natural convection(*Ra* is defined by the height).

The region with the secondary flow is described as the mixed convection region. As can be seen from Fig.3, with increase in Ra the point where *Nu* merges with forced convection occurs is shifted towards large *Pe*. Therefore, for large Rayleigh number the Nusselt numbers depart from the forced convection values even at large *Pe*. Even at the smallest Rayleigh number of 0.0119 the secondary flow effects are sufficiently large so that the variation of the Nusselt number is far away from that for forced convection predicted with the formulation of $Nu = 3.1\sqrt{Pe}$. For the largest Rayleigh number the secondary flow effects are largest. Consequently, the larger the Rayleigh number, the larger the mixed convection dominated region, and the larger heat transfer enhancement results.

Correlation formulas for mixed convection

Heat transfer results for mixed convection can be best presented in terms of two governing parameters, $Nu / Pe^{1/2}$ and Ra / Pe (Fig.4). As observed in all cases studied, the good collapse of the data points suggests that

the transition of heat transfer processes occurring around vertical cylinder are fairly gradual.

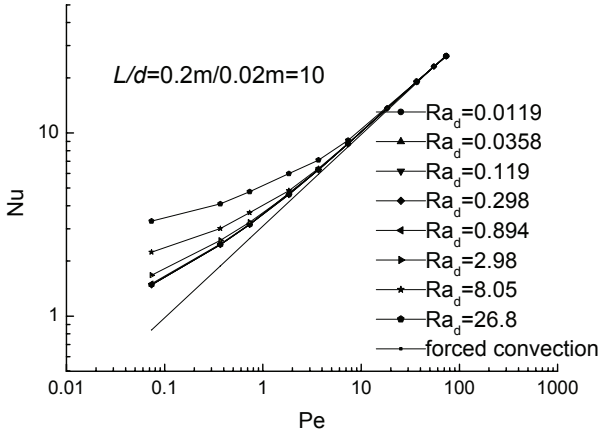

Fig.3. Average Nusselt number with Pe. (L/d=10)

The ratio Ra_d / Pe can be used to indicate the relative strengths of the two modes of convection in a mixed convection environment. It has shown the buoyancy effects become noticeable when Ra_d / Pe approaches unity. For Ra_d / Pe <<1, the forced convection component controls the heat transfer processes, while Ra_d / Pe>>1, buoyancy effects predominate. For forced convection, the correlation of heat transfer results based on numerical data is given by $Nu = 3.1\sqrt{Pe}$, which is in very good agreement with the results of Ref. [4]. For mixed convection, a least-squares fit of the data provided the following correlation:

$$\frac{Nu}{Pe^{1/2}} = 3.1 + 0.4\left(\frac{Ra_d}{Pe} - 1\right)^{1/2} \qquad (6)$$

That is also indicated as a solid line in Fig.4. When the Rayleigh number is increased to large values, one would expect that the effect of forced convection would become negligible in comparison with the effect of natural convection, and consequently the Nusselt number should become nearly independent of the Peclet number. Accordingly, the power of correlation has been used as 1/2, which is consistent with the natural convection results. Eq.(6) reflects correctly the above nature of mixed convection heat transfer.

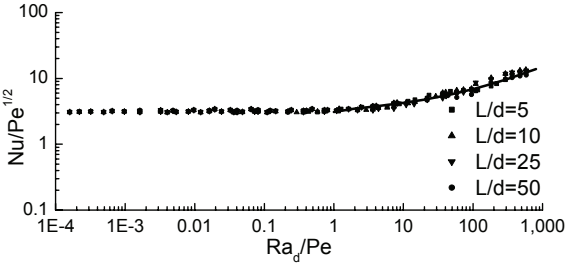

Fig.4. Heat transfer rate in the mixed convection

Conclusions

Mixed convection from a heated vertical cylinder in a saturated porous medium subjected to lateral flow has been examined numerically. It has been shown that the average heat transfer rate from a vertical cylinder is described by the following equations:

$$Nu = 3.1\sqrt{Pe} \quad \text{for } Ra_d / Pe < 1$$

and

$$\frac{Nu}{Pe^{1/2}} = 3.1 + 0.4\left(\frac{Ra_d}{Pe} - 1\right)^{1/2} \quad \text{for } Ra_d / Pe \geq 1.$$

References

[1] D.A. Nield and A. Bejan, Convection in porous media, 2nd edition, Springer, 1999.

[2] P. Cheng, Heat transfer in geothermal systems, Advances in Heat Transfer, Vol.14, Academic Press, New York, 1978, pp.1-105.

[3] P. Cheng, Mixed convection about a horizontal cylinder and a sphere in a fluid-saturated porous medium, Int. J. Heat Mass Transfer 25 (1982) 1245-1246.

[4] S. Kimura, Forced convection heat transfer about an elliptic cylinder in a saturated porous medium, Int. J. Heat Mass Transfer 31 (1988) 197-199.

[5] L. A. Romero, Forced convection past a slender body in a saturated porous medium, SIAM Journal of Applied Mathematics 55 (4) (1995) 975-985.

[6] T. Sano and R. Okihara, Natural convection around a sphere immersed in a porous medium at small Rayleigh numbers, Fluid Dynamics Research 13, (1994) 39-44.

[7] H. Campos, J.C. Morales and V. Lacia, Thermal aspect of a vertical annular enclosure divided into fluid region and a porous region, Int. Commun. Heat Mass transfer 17 (1990) 343-353.

[8] T.K.Aldoss, M.A.Jarrah and B.J.Al-shaer, Mixed convection from a vertical cylinder embedded in porous medium: non-Darcy model, Int.J.Heat Mass Transfer 39 (6) (1996) 1141-1148.

[9] K.A.Yih, Coupled heat and mass transfer in mixed convection about a vertical cylinder in a porous medium: The entire regime, Mechanics Research Communications 25 (6) (1998) 623-630.

[10] D.B. Ingham and I. Pop, A horizontal flow past a partially heated infinite vertical cylinder embedded in porous medium, Int. J. Engng. Sci. 24 (8) (1986) 1351-1363.

[11] W.J.Minkowycz and P.Cheng, Free convection about a vertical cylinder embedded in a porous medium, Int. J. Heat Transfer 19 (1976) 805-813.

Strojniški vestnik - Journal of Mechanical Engineering 51(2005)7-8, 495-500
UDK - UDC 536.2
Izvirni znanstveni članek - Original scientific paper (1.01)

Some Features of Flow and Particle Transport in Porous Structures

M.Aydin[1,2*], G. Balik[2], A. F. Miguel[1] and A. H. Reis[1]

[1]*Geophysics Centre of Evora, University of Evora, Rua Romao Ramalho, 59, 7000-671 Evora, Portugal.*
** e-mail:maydin@uevora.pt*
[2]*Dept. Mech. Eng., Istanbul Technical University, 34439 Gumussuyu, Istanbul, Turkey*

Abstract

There has been a growing interest in the study of porous and complex flow structures due to its impact in technology. This concerns not only environmental but also diagnostic and therapeutic exposure in medical research. Physics of flow within porous structures is especially important to model transport and deposition of viruses, pollutants and drugs deep in these structures. In this work we analyze numerically low and medium Reynolds number flows in axisymmetric cylindrical duct surrounded by a torus. We also consider three different particle sizes (0.02, 0.1 and 20μm) for possible physiological and environmental applications.

Introduction

The study of porous flow structures is of considerable importance in many fields of science and technology [1]. Examples include fields such as energy, biotechnology, environmental sciences etc. The study of these flow structures will help to understand more about fuel cells, particle filters and respiratory tree.

A fuel cell is an electrochemical device that basically consists of two porous electrodes sandwiched around an electrolyte. Oxygen passes over one porous electrode keeping it electronegative while fuel (usually hydrogen) flows over the other (anode). The result of the electrochemical oxidation of fuel is electricity, water and heat. Porous electrodes are crucial to fuel cell performance since they provide high surface area for electrochemical reaction to occur. Microscopic assessment of porous electrodes allows the study in detail these processes in order to improve fuel cell design [2-3].

Porous filters have been used for removing particles with success for many years [4]. Their wide application in air pollution control and in different technologies is due to their reliability in the separation of particles and relatively low operating cost. One of the most important issues in filtration is to know how media's physical properties varied during operating conditions. Filter's collectors (microscopic scale) are properly designed if, during a reasonably long filtering operation, filter's collection efficiency is high and media's flow resistance is below assumed value [5-6]. Description of flow field and particle motion near the filter's collector, as well as, the knowledge of particle cake dynamics provide an important information for a properly design of filter structure.

Inhalation of various particulate pollutants has often been reported to cause short and long term health effects [7-8]. Special attention should be given on the alveolar region where gas-exchange occurs [9]. In order to define strategies for attacking this problem, of particular interest is the study of the patterns of deposition in the alveolar region.

The cases presented motivated this research. There has been many work regarding fluid flow and heat transfer in porous structures in the literature. Most of these studies are viewed as macro structure composed pores. In this work, we take another direction and focus on a pore and its surrounding itself. In this paper we analyze both the velocity and temperature fields, at various Reynolds numbers within and close to a pore considered as an axisymmetric torus. We analyze also particle transportation and deposition on the walls influenced by Reynolds number and particle dimension.

The analysis of the velocity and the temperature fields under imposed heat flux at the surface may help to understand practical cases when a chemical reaction occurs on a catalytic surface (e.g. fuel cells, chemical reactors). On the other hand, the study of particle transport and deposition may illuminate particle deposition in biological flow trees (e.g. bronchial tree).

Nomenclature

f – friction coefficient
F – force (N)
L – distance (m)
R – radius (m)
Re – Reynolds Number, $Re = 2\rho u R_D/\mu$
t – time (s)
T – temperature (K)
u – velocity (m s^{-1})
γ – half angle of porous opening
μ – dynamic viscosity (kg m^{-1} s^{-1})
ρ – density (kg m^{-3})

Subscripts
A – torus
b – Brownian
D – channel
f – fluid
max – maximum value
s – lift
t – thermophoretic

The model

The geometric model is shown in Fig.1. The geometry used in the flow simulations of [10-11] was adapted here. It consists of a cylindrical duct with radius R_D surrounded by a torus. The ratio of duct radius to porous radius R_D/R_A =1.25, the ratio of distance from the central point to inlet to one from exit is $L_1/L_2 = 1$ and half angle of the porous opening $\gamma = 60°$. The model is assumed to be three dimensional and axisymmetric.

The Solution

The steady state flow field is defined by the full Navier-Stokes equations and solved numerically with the finite volume method. The commercial code FLUENT [12] is employed in this study. The non-slip boundary conditions are set along the duct and torus walls. The developed velocity profile is prescribed at the inlet while outflow boundary conditions are set at the exit.

The cell size of the grid where high gradients of velocities are expected has been varied to ensure a grid independent solution.

The grid with 8184 quadrilateral cells and 8575 nodes are found to be appropriate for present study. Its part around the torus is shown in Fig.2. Reynolds number Re is calculated according to $Re = 2\rho u R_D/\mu$ where ρ is density of air, u is averaged velocity at the inlet, R_D is the radius of the channel, and μ is dynamic viscosity of air.

Solution for low Reynolds number converges rapidly and monotonically. It takes around 400 iterations for Re=0.5. We especially choose Re=0.5 due to availability of a numerical solution in the literature [10]. Variations of residuals for continuity and two components of velocity with iterations are shown in Fig.3

Streamlines in the pore region are shown in Fig.4. A separation streamline and a slowly re-circulating region within the pore are clearly seen. The flow structures exactly reflects the corresponding flow streamline topology found in the literature (see Fig.5)

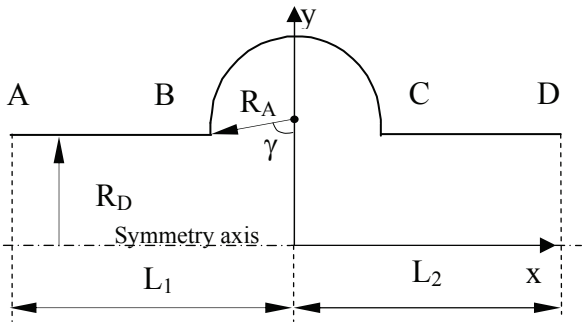

Fig.1 Geometry of the porous structure

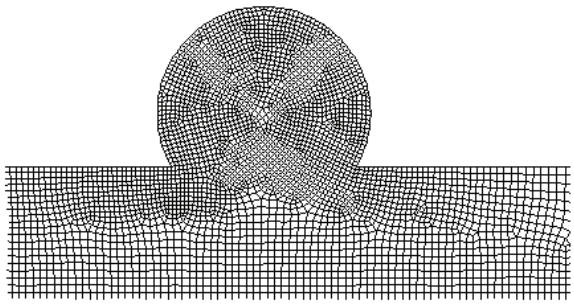

Fig.2 Grid around the pore

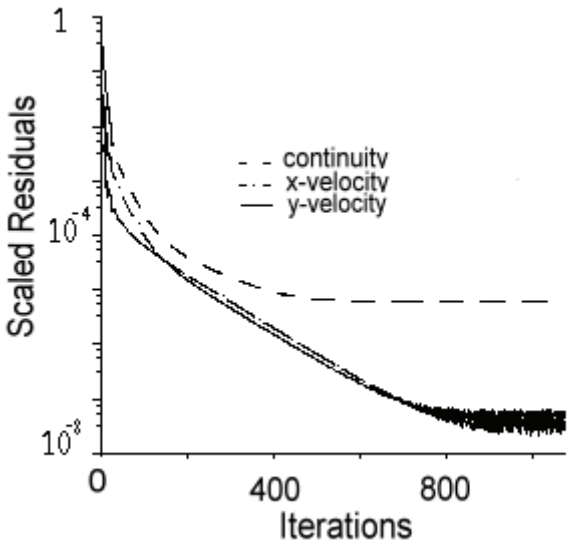

Fig.3 Residuals via iterations

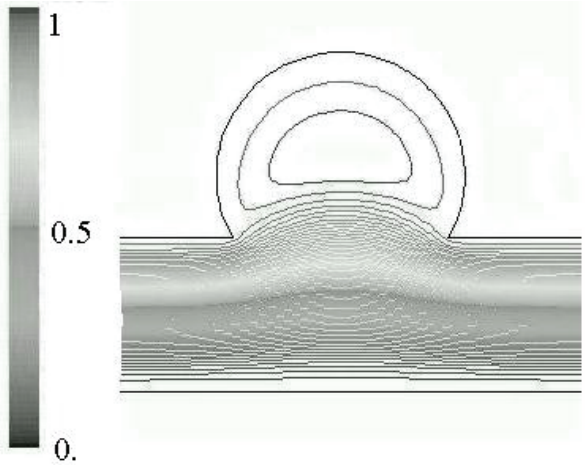

Fig.4 Contours of normalized stream function in the pore at Re=0.5.

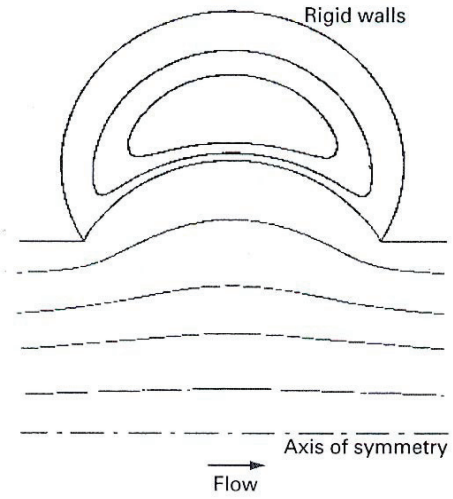

Fig.5 Flow field in the pore by Tippe and Tsuda [10].

We also consider flows at different Re numbers. Velocity vectors at different cross sections of the channel are shown around the pore in Fig 6. Right after the pore, the flow almost fully develops in the case of Re=5. As can be seen from Fig 7, the flow loses its symmetry in the pore region when Re number increases. The center of vortex moves to right close to the wall. It is also noted that fluid streamlines become more rectilinear with increase in Re number.

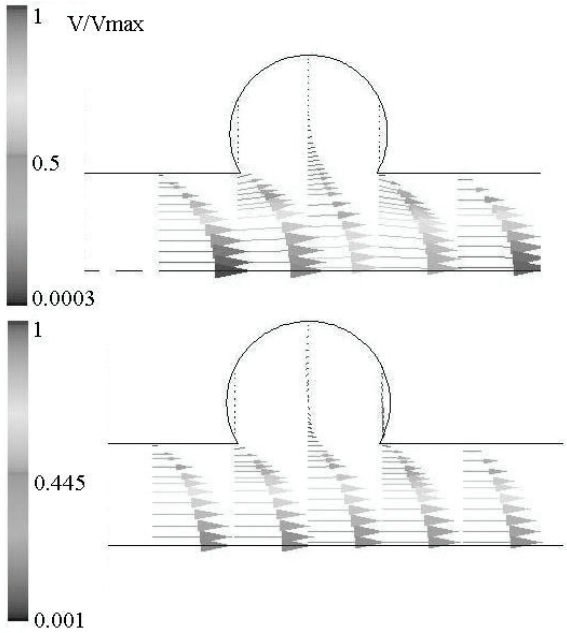

Fig.6 Normalized velocity vectors at different cross sections of the channel: At Re=5 (top) and Re=500 (bottom)

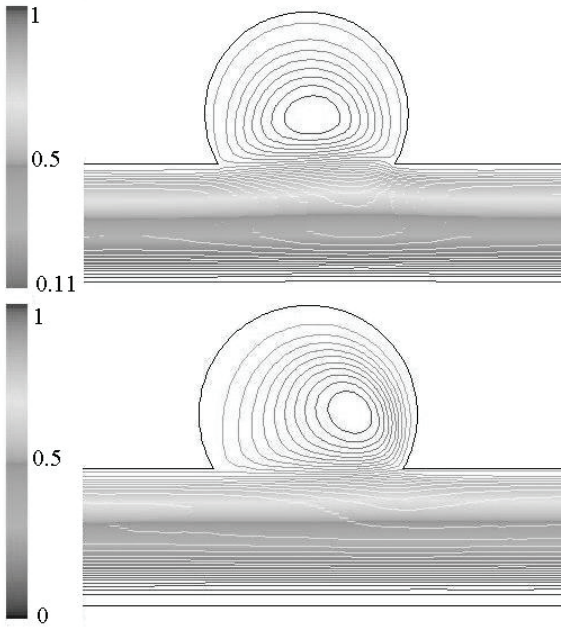

Fig.7 Contours of normalized stream function in the pore: At Re=50 (top) and Re=500 (bottom).

Energy Equation is also included later to treat forced convection problems. For this purpose, we consider a constant heat flux (0.1 W/m^2) over the surface of the pore while fluid enters the duct at 293 K. Along the surface of the duct constant temperature boundary conditions (293 K) are set. Numerical results in non-dimensionalised form are shown for Re=0.5, 5 and 500 in Fig. 8.

Increase in Re number shows that isotherms are progressively affected by the flow field. At Re=0.5 they are almost symmetrical with respect to the plane that cuts perpendicularly through the middle of the torus. At Re=5 isotherm asymmetry becomes already noticeable while at Re=500 we see that a significant temperature difference develops between the left and right parts of the torus. We note that this effect happens under constant heat flux over the surface.

We analyze now the case when an exothermic reaction occurs at the surface and we consider both the flow and temperature fields (see Figs. 7 and 8). We see that in the right part of the torus, convection becomes more effective in delivering the reactant to the surface therefore enhancing the heat generation and the heat flux over the surface. It is expected that the temperature field is affected accordingly, i.e. lowering the temperature difference between the left and right parts shall be perceptible.

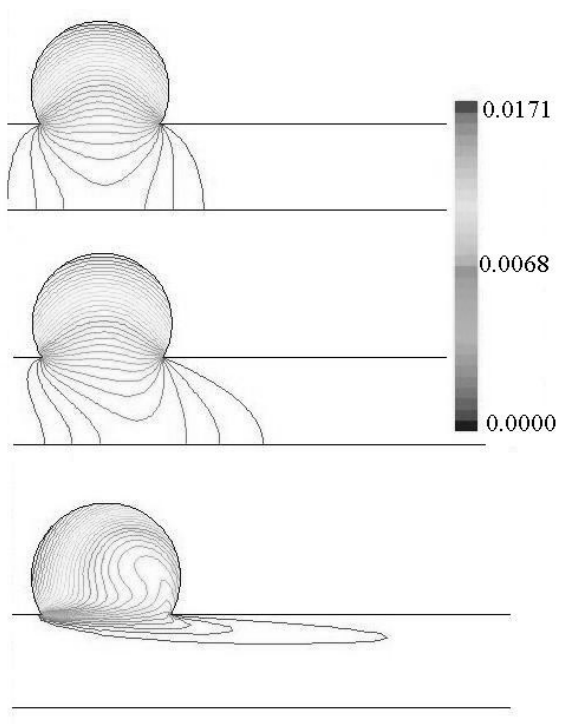

Fig. 8 Non-dimensionalized temperature $(T - T_f)/T_f$ contours around the pore: At Re=0.5 (top), Re=5 (middle) and Re=500 (bottom)

Particle Dynamics

The motion of a spherical particle of diameter d and mass is described by the equation

$$m(d\vec{u}/dt) = -f(\vec{u} - \vec{u}_f) + \vec{F}_s + \vec{F}_b(t) + \vec{F}_t \qquad (1)$$

This equation represents a force balance on the particle, where mass times acceleration (left-hand side) is the resultant of forces acting on a particle (right-hand side). The first term on the right-hand side represents the viscous drag force due to the motion of the particle relative to the motion of the surrounding fluid. The friction coefficient $f = 3\pi\mu d / C_s$ is assumed to be governed by Stoke´s law corrected by the Cunningham factor. The second term is a lift force due to shear. The third term denotes a random force $F(t)$ arising from Brownian collisions. Finally, the fourth term represents thermophoretic force due to temperature gradient [10, 12].

At the mouth of the pore along a vertical surface, particles are injected through the flow. Three different particle sizes (0.02, 0.1 and 20μm) are considered at Re=0.5.

It is observed that fluid velocity near the pore is 10 times lower than one at the centre. Residence time of the particles which follow upper-streams is high and therefore, they are also more likely to get deposited on the walls. Trajectories of the particles are greatly dependent upon initial position.

The number of particles deposited and escaped is documented in Table 1. It is seen that when size of the particles gets bigger, probability to escape is higher for both Re numbers. Smaller particles have a better chance to get deposited in the pore region due to Brownian motion. High Reynolds number flows reduce the probability of deposition for all particles.

At Re=0.5 trajectories of particles of size 20 μm are shown in Fig. 9. As the only force that pushes particles towards the axis of the channel is the lift force F_s (Eq. 1) we conclude that combination of drag and thermophoretic forces is dominant at low Re since the Brownian force only induces small perturbation in particles trajectories (see Fig. 10). The situation changes drastically at higher Re as can be observed in Fig. 11. Here we see that trajectories are curved towards the axis of the channel, therefore proving the dominance of the lift force over other forces.

Table. 1 The number of particle deposited and escaped (%)

Size (μm)	Re=0.5				Re=500			
	AB	BC	CD	Esc	AB	BC	CD	Esc
0.02	4	8	21	67	0	0	4	96
0.1	0	4	8	88	0	0	4	96
20	8	0	0	92	0	0	0	100

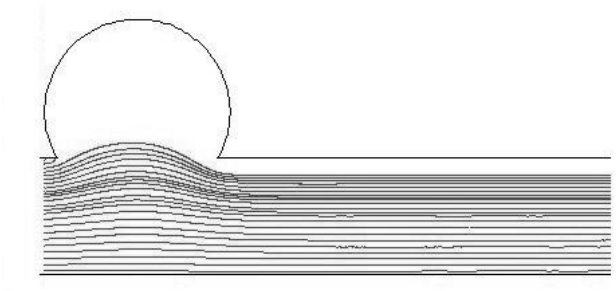

Fig.9 Particle trajectories of particles of size 20 μm at Re=0.5

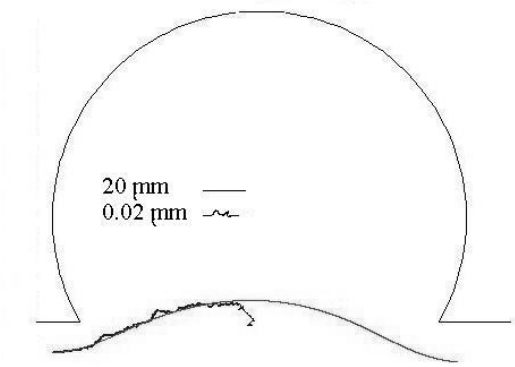

Fig.10 Typical trajectories of 2 particles of size 20 μm and 0.02μm at Re=0.5

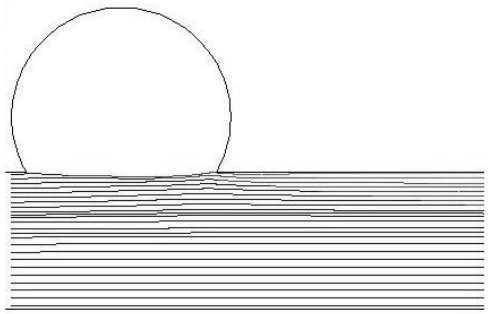

Fig.11 Particle trajectories of particles of size 20 μm at Re=500

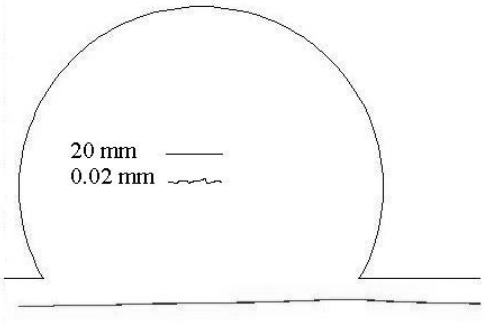

Fig.12 Typical trajectories of 2 particles of size 20 μm and 0.02μm at Re=500

By comparing Figs. (10) and (12) we conclude that the Brownian force becomes negligible at high Re as compared to others. However, as low Re flows are of characteristic of respiration we see how important the Brownian force can be in particle deposition in the bronchial tree.

Conclusions

The analysis carried out in this paper has shown how both the velocity and temperature fields in a channel with an axisymmetric pore change with Reynolds number (Re) under prescribed heat flux over the pore surface. At low Re both fields are almost symmetrical with respect to the plane that cuts perpendicularly through the middle of the torus. As Re increases asymmetry develops in both velocity and temperature fields with decrease in temperature in the flow direction and vortex enhancing in the right part of the torus.

When particles are allowed into the flow at low Re (Re=0.5) we found that particle trajectories are pushed into the pore therefore indicating dominance of drag and thermophorectic forces over lift forces arising from the shear. On the other hand, at Re=500 the lift forces clearly dominate over the other forces this effect being noticeable through the inversion of the curvatures of the trajectories that, in this case, are pushed towards the axis of the channel.

Brownian forces were found to be noticeable only at low Re flows as is the case of respiration and they may play a significant role in particle deposition in the lungs.

Most of the results presented here may also help in the analysis of flows where a reactant in a porous material is delivered to a catalytic surface where a chemical reaction occurs. This is the case of fuel cells and some chemical reactors.

Acknowledgement
The authors would like to acknowledge Foundation for the Science and Technology (FCT) for supporting this work (project POCTI/33012/EME/2000).

References

1. A. Bejan, I. Dincer, S. Lorente, A. F. Miguel and A.H. Reis, Porous and complex flow structures in modern technologies, (2004), Springer-Verlag, New York
2. A. H. Reis, Thermodynamics of fluids in mesoporous media, *in*: *Emerging Technologies and Techniques in Porous Media,* D. B. Ingham et al. (eds), 465-431 (2004) Kluwer Academic Publishers
3. A. H. Reis, A. F. Miguel and M. Aydin, Optimized design of a porous structure for gas transport from opening to surface using constructal theory, Proceedings of International Conference on Applications of Porous Media, (2004) ICAPM, Evora Portugal (in press)

4. A. F. Miguel, Porous Media and Filtration, *in*: *Emerging Technologies and Techniques in Porous Media,* D. B. Ingham et al. (eds) 419-431 (2004), Kluwer Academic Publishers.
5. A. F. Miguel, Effect of Air Humidity on the Evolution of Permeability and Performance of a Fibrous Filter during Loading with Hygroscopic and Non-hygroscopic Particles, *Journal of Aerosol Science* **34**, (2003) 783-799.
6. A. F. Miguel, A. H. Reis and M. Aydin, Dynamic loading of porous filters with fine particles, Proceedings of International Conference on Applications of Porous Media, (2004) ICAPM, Evora, Portugal (in press)
7. J. Schwartz and D. W. Dockery, Increased mortality in Philadelphia associated with daily air pollution concentration, *Am. Rev. Respir. Dis*. **145**, 600 (1992).
8. A. F. Miguel, A. H. Reis M. Aydin, A. M. Silva, Particle deposition in airway bifurcations in different breathing conditions, *Proceedings of European Aerosol Conference* 2004, (in press)
9. A. H. Reis, A. F. Miguel and M. Aydin Constructal theory of flow architecture of the lungs, *Medical Physics* **31**, 1135-1140 (2004)
10. A. Tippe and A. Tsuda, Recirculating flow in an expanding alveolar model: experimental evidence of flow-induced mixing of aerosols in the pulmonary acinus, Journal of Aerosol Science **31**, 8 (1999) 979-986.
11. A. Tsuda, W. J. Federspiel, P. A. Grant Jr, J. F. Fredberg, Axial dispersion of inert species in alveolated channels, Chemical Engineering Science **46**, (5-6) (1991) 1419-1426.
12. FLUENT 6 User´s Guide, Fluent Inc. (2003)

Strojniški vestnik - Journal of Mechanical Engineering 51(2005)7-8, 501-508
UDK - UDC 536.2
Izvirni znanstveni članek - Original scientific paper (1.01)

Effect of asymmetry on the steady thermal convection in a vertical torus filled with a porous medium

Postelnicu Adrian[1], Scurtu Nicoleta[2]

[1]*Department of Thermal Engineering and Fluid Mechanics, Transilvania University, Bdul Eroilor, No 29, Brasov, Romania* e-mail: adip@unitbv.ro*
[2]*Numerical Mathematics and Scientific Computing, Weierstrass-Institute for Applied Analysis and Stochastic (WIAS), Mohrenstrasse 39, 10117 Berlin, Germany*

Abstract

The paper deals with a study on the thermal convection in a fluid saturated porous medium confined in a vertical oriented toroidal loop heated from below and cooled from above, subjected to a vertically uniform temperature gradient. In fact, Sano, O., Journal of the Physical Society of Japan (1987 and 1988) studied such a configuration for clear fluids. We take the steady heat conduction state under a constant vertical temperature gradient (-*k*) as a fundamental solution. A cylindrical system of co-ordinates (r, ϕ, s) is considered for the loop of $2\pi R$ length and cross sectional diameter $2a$, where the ratio a/R is assumed to be very small. We expand all quantities in terms of double Fourier series in ϕ and θ, where $\theta = s/R$. First-order perturbed fields from steady heat conduction state are examined and various plots are given: isotherms in ring and meridian plane, stream lines and velocities. Finally, an attempt is made in order to identify other fundamental solutions: S-type (cellular thermal convection) and A-types (coaxial flow, bidirectional flow and antisymmetric cellular flow).

Introduction

Thermal convection in a vertically oriented torus has various applications in engineering and nature, like cooling systems in nuclear engineering, solar heaters geothermal engineering, etc. Several papers considered this configuration, in Newtonian fluids, see for instance [1] and [2].

On the other hand, natural convection in porous media is of interest in many applications and recent books by Nield and Bejan [3] and Ingham and Pop [4-5] present a comprehensive account of the available information in the field. For example, natural convection in a horizontal porous annulus is well documented in the literature, a whole chapter in the reference [5] being dedicated to this theme. However, studies on thermal convection in toroidal configurations filled with fluid-saturated porous media seem to be scarce in the open literature. One example is the work [6] where it is investigated the natural convection and its stability in a toroidal thermosyphon filled with a porous medium. The onset of the thermal convection in that configuration was studied using a one-dimensional model.

We remark at this point that the stability of flows in porous media differs considerably from that of Newtonian fluids, due to the very specific changes in the hydraulic and thermal properties.

The objective of the present paper is to study the steady thermal convection in a vertical torus filled with a fluid-saturated porous medium. The fluid in the porous medium is considered incompressible and obeying the Boussinesq law. The loop is heated from below and cooled from above and it is subjected to a vertically uniform temperature gradient

Mathematical formulation

We consider a thermal convection in a vertical torus heated from below and cooled from above. We denote the cross sectional diameter of the torus by $2a$ and its loop length by $2\pi R$, where the ratio a/R is assumed to be very small. The x and z axis are taken in the plane of the generator of the torus, with the z axis in the opposite direction of the gravity, see Fig. 1. The reference system (r, ϕ, s) is also introduced, where s is the distance measured counterclockwise from the bottom, along the generator, while r and ϕ are polar co-ordinates of the cross section. The direction $\phi = 0$ is chosen so that it always coincides with the direction from the generator to the outer edge of the torus in the ring xz plane.

Nomenclature

a	half cross-sectional diameter of the torus	β	thermal expansion coefficient
k	vertical temperature gradient	ϕ	polar co-ordinate
K	permeability of the porous medium	μ	dynamic viscosity of the fluid
g	acceleration of gravity	ν	kinematic viscosity of the fluid
p	pressure	ρ	density of the fluid
r	polar co-ordinate	θ	$= s/R$
Ra	Rayleigh number		
(u, v, w)	components of the velocity		**Subscripts**
s	distance measured counterclockwise from the bottom	0	reference conditions
T	temperature		
z	vertical Cartesian co-ordinate		**Superscripts**
		B	base solution for symmetric modes
	Greek symbols	‘	perturbed quantities
α	thermal diffusivity	*	non-dimensional quantities

We analyse the fluid motion through the porous medium on the basis of the following assumptions:

- the flow is steady, laminar and incompressible;
- the liquid and solid matrix are in thermal equilibrium;
- properties of the fluid and of porous matrix are constant except for the density of the fluid which depends on the temperature according to the Boussinesq approximation.

The governing equations for the velocity $\mathbf{v}$, temperature T and pressure p are

$$\nabla \cdot \mathbf{v} = 0 \tag{1}$$

$$\mathbf{v} = -\frac{K}{\mu}\left(\nabla p + \rho_0 \beta g T \mathbf{e}_z\right) \tag{2}$$

$$\mathbf{v} \cdot \nabla T = \alpha \nabla^2 T \tag{3}$$

where ρ_0 is the density of the fluid at the reference temperature T_0, g is the gravitational acceleration, $\mathbf{e}_z$ is an upward unit vector, μ, β, α and K are the dynamic viscosity of the fluid, thermal expansion coefficient, thermal diffusivity and permeability of the porous medium, respectively. We take the steady state as heat conduction under a constant vertical temperature gradient ($-k$), which is in fact a fundamental solution

$$T = T_0 - kz \tag{4}$$

$$p = p_0 - \rho_0 g z - \frac{1}{2}\rho_0 \beta k g z^2 \tag{5}$$

The perturbed fields $\mathbf{v}'$, T' and p' satisfy the following equations, which are correct to the first order

$$\nabla \cdot \mathbf{v}' = 0 \tag{6}$$

$$\mathbf{v}' = -\frac{K}{\mu}\left(\nabla p' + \rho_0 \beta g T' \mathbf{e}_z\right) \tag{7}$$

$$v_z' k = \alpha \nabla^2 T' \tag{8}$$

The boundary conditions are

$$\mathbf{v}' = T' = 0 \text{ , at } r = a \tag{9}$$

Introducing the non-dimensional quantities

$$\mathbf{x}^* = \frac{1}{a}\mathbf{x}, \quad \mathbf{v}^* = \frac{a}{\alpha}\mathbf{v}', \quad p^* = \frac{p' K}{\alpha \mu}, \quad T^* = \frac{T'}{ka} \tag{10}$$

equations (1-3) become

$$\nabla^* \cdot \mathbf{v}^* = 0 \tag{11}$$

$$\mathbf{v}^* = -\nabla^* p^* + Ra T^* \mathbf{e}_z \tag{12}$$

$$v_z^* = -\Delta^* T^* \tag{13}$$

where (3-4) have been used. Further, $Ra = k\beta g K a^2 / (\nu\alpha)$ is the Rayleigh number. The boundary conditions, in dimensionless form, read

$$\mathbf{v}^* = T^* = 0 \text{ , at } r^* = 1 \tag{14}$$

Expressed in terms of the (r, ϕ, s) coordinate system, where the velocity components are u^*, v^* and w^* and dropping the asterisks for convenience, the governing equations are

$$\frac{\partial u}{\partial r} + \frac{u}{r} + \frac{1}{r}\frac{\partial w}{\partial \phi} + \frac{1}{R}\frac{\partial w}{\partial \theta} = 0 \tag{15}$$

$$u = -\frac{\partial p}{\partial r} - RaT\cos\theta\cos\phi \tag{16}$$

$$v = -\frac{1}{r}\frac{\partial p}{\partial \phi} + RaT\cos\theta\sin\phi \tag{17}$$

$$w = RaT\sin\theta \tag{18}$$

$$\left(u\cos\phi - v\sin\phi\right)\cos\theta - w\left(1+\frac{r}{R}\cos\phi\right)\sin\theta = \Delta T \tag{19}$$

where $\Delta = -\frac{\partial^2}{\partial r^2} + \frac{1}{r}\frac{\partial}{\partial r} + \frac{1}{r^2}\frac{\partial^2}{\partial \phi^2} + \frac{1}{R^2}\frac{\partial^2}{\partial \theta^2}$ is the Laplacean and $\theta = s/r$. Collecting the zeroth order of a/R (<<1), equations (15)-(19) become

$$\frac{\partial u}{\partial r} + \frac{u}{r} + \frac{1}{r}\frac{\partial w}{\partial \phi} + \frac{1}{R}\frac{\partial w}{\partial \theta} = 0 \tag{20}$$

$$u = -\frac{\partial p}{\partial r} - RaT\cos\theta\cos\phi \tag{21}$$

$$v = -\frac{1}{r}\frac{\partial p}{\partial \phi} + RaT\cos\theta\sin\varphi \tag{22}$$

$$w = RaT\sin\theta \tag{23}$$

$$\left(u\cos\phi - v\sin\phi\right)\cos\theta - w\sin\theta = \Delta T \tag{24}$$

where $\Delta = -\frac{\partial^2}{\partial r^2} + \frac{1}{r}\frac{\partial}{\partial r} + \frac{1}{r^2}\frac{\partial^2}{\partial \phi^2} + O\left(R^{-2}\right)$, so that these expressions are the same as those given in terms of a straight circular cylindrical coordinate systems, except that directions of v_z and e_z change at different positions along the generator. We confine our attention to the steady thermal convection, which corresponds to neutrally stable states at some particular critical Rayleigh numbers.

Some fundamental solutions for symmetric modes

In this paper we are mainly interested in the analysis of symmetric modes which are caused by experimentally uncontrollable small disturbances under symmetric boundary conditions. The procedure is similar with that used by Sano in [1-2], by expanding all relevant quantities in terms of double Fourier series in ϕ and θ

$$\left(T, p, u\right) = \sum_{m,n=0}^{\infty}\left\{T_{m,n}(r), p_{m,n}(r), u_{m,n}(r)\right\} \cdot \cos m\phi\cos n\theta, \tag{25}$$

$$v = \sum_{m=0,n=1}^{\infty} v_{m,n}(r)\sin m\phi\cos n\theta,$$

$$w = \sum_{m=0,n=1}^{\infty} w_{m,n}(r)\cos m\phi\sin n\theta$$

Results for symmetric modes

Due to the fact that temperature distributions with $m = 0$ and $n = 0$ do not lead to physically realizable symmetric convection in a vertically oriented torus, we focus on the simplest situation, represented by $T_{1,1}$, $w_{1,2}$, $p_{1,2}$, $u_{1,2}$ and $v_{1,2}$ series. By truncating these series at the lowest order, we have

$$\left(u_{1,2}\right)' + \frac{1}{r}\left(u_{1,2} + v_{1,2}\right) + \frac{2}{R}w_{1,2} = 0 \tag{26}$$

$$u_{1,2} + \left(p_{1,2}\right)' = 0 \tag{27}$$

$$v_{1,2} = \frac{1}{r}p_{1,2} \tag{28}$$

$$-w_{1,2} = 2\left[\left(T_{1,1}\right)'' + \frac{1}{r}\left(T_{1,1}\right)' - \frac{1}{r^2}T_{1,1}\right] \tag{29}$$

$$w_{1,2} = \frac{Ra}{2}T_{1,1} \tag{30}$$

$$T_{1,1} = u_{1,2} = v_{1,2} = w_{1,2} = p_{1,2} = 0, \text{ at } r = 1 \tag{31}$$

The solution of the set of equations (26-30) is obtained, after some algebra, in the form

$$T_{1,1} = AJ_1\left(k_n r\right) + BN_1\left(k_n r\right) \tag{32a}$$

$$u_{1,2} = -c_1 + \frac{c_2}{r^2} + A\left\{\left[J_0\left(k_n r\right) - J_2\left(k_n r\right)\right] + B\left[N_0\left(k_n r\right) - N_2\left(k_n r\right)\right]\right\}k_n \tag{32b}$$

$$v_{1,2} = c_1 + \frac{c_2}{r^2} - \frac{4}{rR}\left[AJ_1\left(k_n r\right) + BN_1\left(k_n r\right)\right] \tag{32c}$$

$$w_{1,2} = 2k_n^2\left[AJ_1\left(k_n r\right) + BN_1\left(k_n r\right)\right] \tag{32d}$$

$$p_{1,2} = c_1 r + \frac{c_2}{r^2} - \frac{4}{R}\left[AJ_1\left(k_n r\right) + BN_1\left(k_n r\right)\right] \tag{32b}$$

where J_n are Bessel functions of the first kind of nth order, N_n are Bessel functions of the second kind and nth order, c_1, c_2, A and B are constants and $k_n = Ra^{1/2}/4$.

Imposing the boundary conditions (31), the solutions (32) can be expressed in the form

$$u = u^B \cos\phi \cos 2\theta\,,\ v = v^B \sin\phi \cos 2\theta\,, \quad (33)$$
$$w = w^B \cos\phi \sin 2\theta\,,\ p = p^B \cos\phi \cos 2\theta\,,$$
$$T = T^B \cos\phi \cos\theta$$

where

$$T^B = T_{1,1} = AJ_1(k_{1l}r) \quad (34a)$$

$$u^B = u_{1,2} = \frac{A}{R}\left[-2\left(1+\frac{1}{r^2}\right)J_0(k_{1l}r) + 2k_{1l}\left(J_0(k_{1l}r) - J_2(k_{1l}r)\right)\right] \quad (34b)$$

$$v^B = v_{1,2} = \frac{A}{R}\left[2\left(1-\frac{1}{r^2}\right)J_0(k_{1l}r) - \frac{4}{r}J_1(k_{1l}r)\right] \quad (34c)$$

$$w^B = w_{1,2} = 2k_{1l}{}^2 AJ_1(k_{1l}r) \quad (34d)$$

$$p^B = p_{1,2} = \frac{A}{R}\left[2\left(r-\frac{1}{r}\right)J_0(k_{1l}r) - 4J_1(k_{1l}r)\right] \quad (34e)$$

The solution is valid for $Ra = 4k_{1l}^2$, where k_{1l} (l = 1, 2, 3, …) are the zeroes of J_1, whilst A is a undetermined constant. The first zero of J_1 is k_{1l} = 3.831706, so that the critical Rayleigh number is Ra_1 = 58.72788.

Fig. 2 shows the isotherms in the ring plane (xz-plane), $T = T^B(r)\cos\theta$ = const. Next, in Fig. 3 there are plotted the temperature distributions in the meridian plane ($\theta = 0$, or $\theta = \pi$). The streamlines in the ring plane (xz-plane) are represented in Fig. 4. We notice that in the xz-plane $\mathbf{v} = (u, 0, w)$, so the flow is assumed as two-dimensional. Such a plot for clear fluids, based on the same assumption, can be found in Sano [1]. We can use here the same argument as there: such as a stream function gives good qualitative patterns for the flow in the loop with small a/R, when the w component exceeds the others in the most part of the porous medium. Finally, Fig. 5 shows the (u, v) velocity fields, in vector representation, in the meridian plane ($\theta = 0$ or $\theta = \pi$).

All the previous results belong to the so-called S-type modes, specifically denoted by S_1^2. Type S has also cellular thermal convection at $Ra = 2k_{1l}^2$, denoted by S_1^1 and is defined by

$$u = 0.5u^B \cos\phi \cos\theta\,, \quad (35)$$
$$v = 0.5v^B \sin\phi \cos\theta\,,\ w = w^B \cos\phi \sin\theta\,,$$
$$p = 0.5p^B \cos\phi \cos\theta\,,\ T = T^B \cos\phi$$

Some fundamental solutions for antisymmetric modes

There are several types of antisymmetric modes, as for clear fluids, see [2]. Let us begin with the A-type modes, characterized by

$$(T, p, u) = \sum_{m,n=0}^{\infty}\{T_{m,n}(r), p_{m,n}(r), u_{m,n}(r)\} \cdot \cos m\phi \sin n\theta\,, \quad (36)$$
$$v = \sum_{m=0,n=1}^{\infty} v_{m,n}(r)\sin m\phi \sin n\theta\,,$$
$$w = \sum_{m=0,n=1}^{\infty} w_{m,n}(r)\cos m\phi \cos n\theta$$

This type include a family of coaxial flow along the loop at $Ra = 2k_{0l}^2$, which is denoted as in [2] by A_0^0. The distribution of the relevant quantities in this case is

$$u = v = 0\,,\ w = Ak_{0l}^2 J_0(k_{0l}r)\,, \quad (37)$$
$$T = AJ_0(k_{0l}r)\sin\theta$$

where l = 1, 2, …

Another A-type of solution corresponds to a bidirectional flow at $Ra = 2k_{1l}^2$, denoted by A_1^0. In this case,

$$u = v = 0\,,\ w = w^B \cos\phi\,, \quad (38)$$
$$T = T^B \cos\phi \sin\theta$$

At $Ra = 4k_{1l}^2$, where l = 1, 2, …, we obtain an antisymmetric cellular flow, called A_1^2. Now the distributions are

$$u = u^B \cos\phi \sin 2\theta\,, \quad (39)$$
$$v = v^B \sin\phi \sin 2\theta\,,\ w = -w^B \cos\phi \cos 2\theta\,,$$
$$p = p^B \cos\phi \sin 2\theta\,,\ T = T^B \cos\phi \sin\theta$$

Other fundamental solutions

By inverting the sine and cosine terms in ϕ for S- and A-mode types, we can obtain other fundamental solutions, see also Sano [2], for clear fluids.

The $\widetilde{S}$ -type is obtained from (25) as follows

$$(T, p, u) = \sum_{m,n=0}^{\infty}\{T_{m,n}(r), p_{m,n}(r), u_{m,n}(r)\} \cdot \sin m\phi \cos n\theta\,, \quad (40)$$
$$v = \sum_{m=0,n=1}^{\infty} v_{m,n}(r)\cos m\phi \cos n\theta\,,$$

$$w = \sum_{m=0,n=1}^{\infty} w_{m,n}(r) \sin m\phi \sin n\theta$$

The $\widetilde{A}$ -type is obtained from (25) in the form

$$(T, p, u) = \sum_{m,n=0}^{\infty} \{T_{m,n}(r), p_{m,n}(r), u_{m,n}(r)\} \cdot \sin m\phi \sin n\theta , \quad (41)$$

$$v = \sum_{m=0,n=1}^{\infty} v_{m,n}(r) \cos m\phi \sin n\theta ,$$

$$w = \sum_{m=0,n=1}^{\infty} w_{m,n}(r) \sin m\phi \cos n\theta$$

The fundamental solutions are readily obtained from their counterparts in S- and A-modes, according to the basic rule stated above (inverting the sine and cosine terms in ϕ). For example, the fundamental solution for $\widetilde{A}_1^2$ -type flow is obtained from (39) as

$$u = u^B \sin\phi \sin 2\theta , \quad (42)$$
$$v = v^B \cos\phi \sin 2\theta , \; w = -w^B \sin\phi \cos 2\theta ,$$
$$p = p^B \sin\phi \sin 2\theta , \; T = T^B \sin\phi \sin\theta .$$

Conclusion

An analysis of steady thermal convection in a vertical torus filled with fluid-saturated porous medium was presented in this paper. Many similarities were found between this physical case and that of vertical torus filled with Newtonian fluid [1-2].

Taking the steady state as heat conduction under a constant vertical temperature gradient, all the perturbed quantities have been expanded in double Fourier series but only the lowest order terms have been retained in the analysis. The main reason in doing so was to keep close the procedure to that one used in clear fluids [1-2], in order to facilitate (qualitative) comparisons, and this line of study gave fruitful results.

It is worth to check the influence of higher modes, given by increasing of the truncated terms in the Fourier expansions. A further step is the superposition of the antisymmetric modes, which can be performed similarly as in [2]. The results of these tasks will be presented elsewhere.

References

[1] O. Sano, Steady thermal convection in a vertical torus, Journal of the Physical Society of Japan, 56 (11) (1987) 3893-3898.

[2] O. Sano, Effect of asymmetry thermal convection in a vertical torus, Journal of the Physical Society of Japan, 57 (5) (1988) 1662-1668.

[3] D.A. Nield, A. Bejan, Convection in Porous Media (2nd edition), Springer, New York, 1999.

[4] D. Ingham, I. Pop (eds), Transport Phenomena in Porous Media I, Pergamon, Oxford, 1998.

[5] D. Ingham, I. Pop (eds), Transport Phenomena in Porous Media II, Pergamon, Oxford, 2002.

[6] Y.Y. Jiang, M. Shoji, Thermal convection in a porous toroidal thermosyphon, International Journal of Heat and Mass Transfer, 45 (2002) 3459-3470.

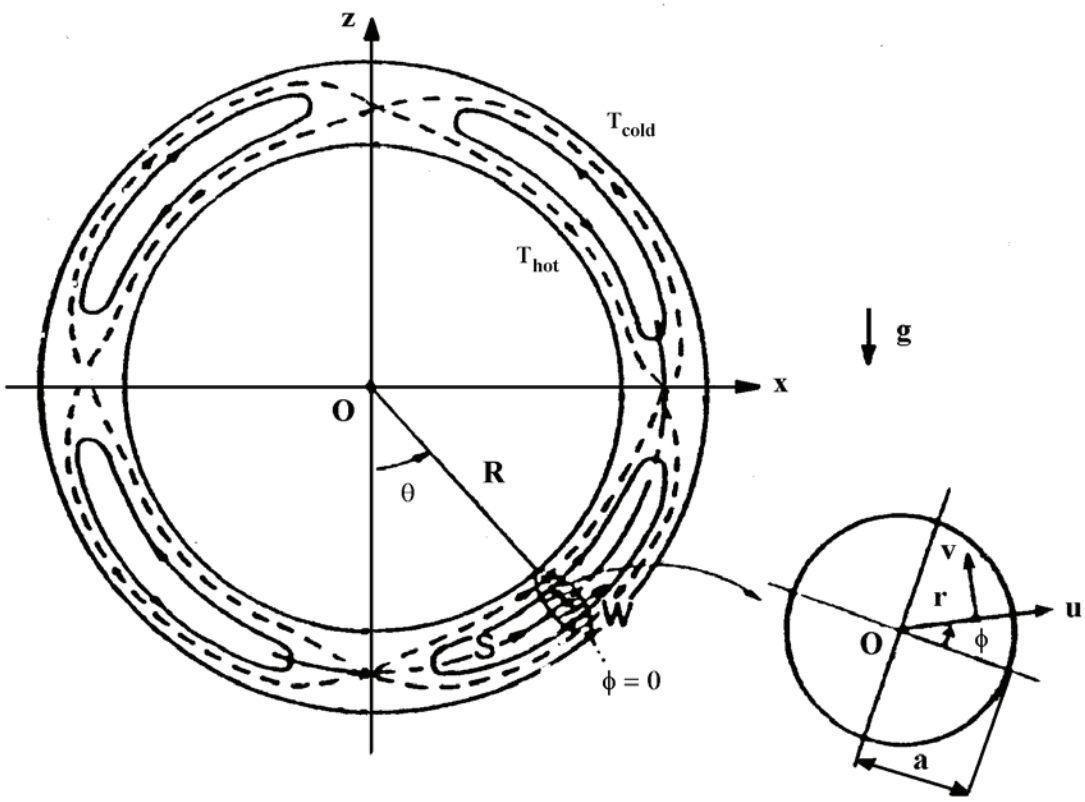

Fig. 1. Sketch of the physical problem.

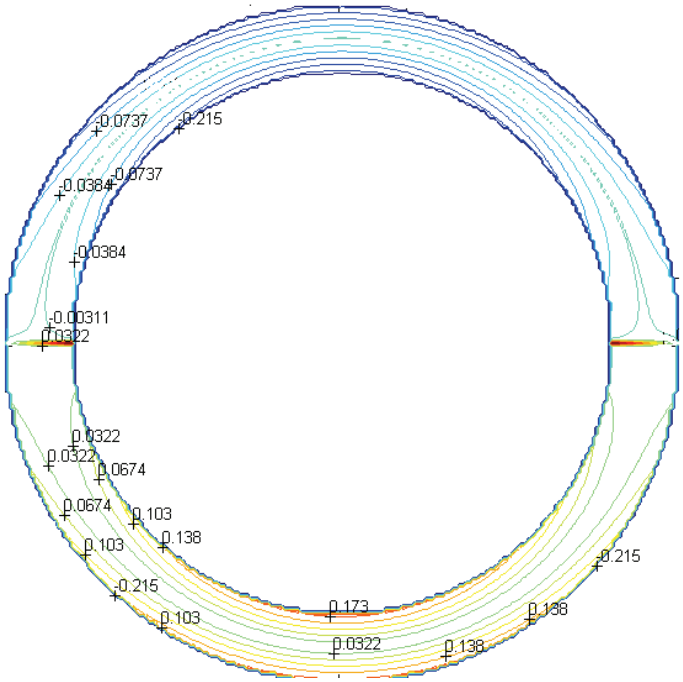

Fig. 2 Isotherms in the ring plane (*xz*-plane).

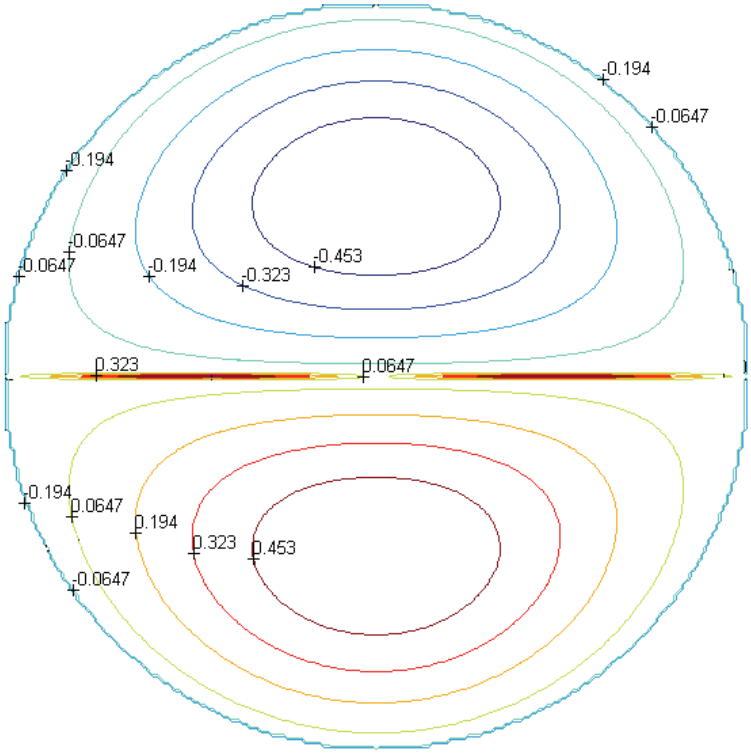

Fig. 3 Isotherms in the meridian plane ($\theta = 0$ or $\theta = \pi$).

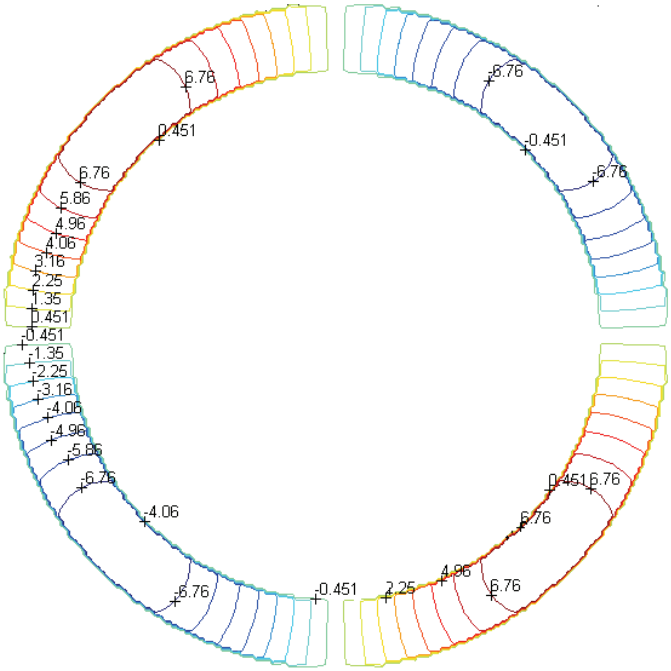

Fig. 4 Streamlines in the ring plane (*xz*-plane).

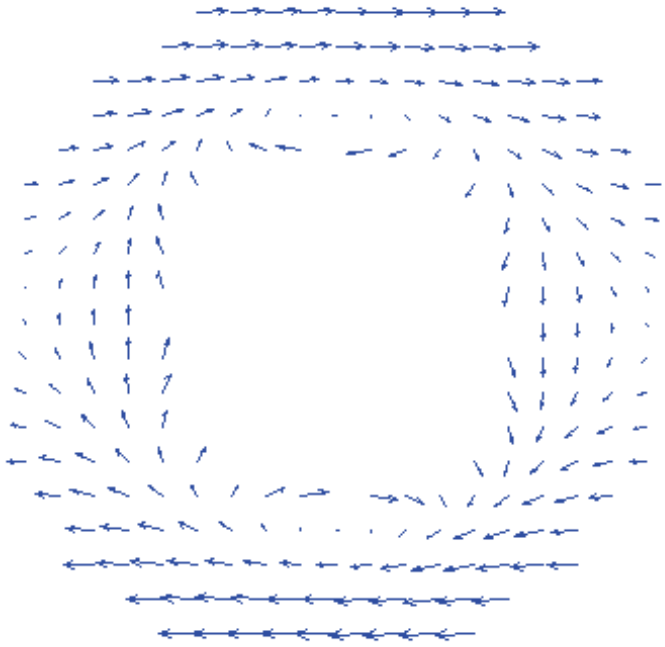

Fig. 5. (u, v) velocity fields in the meridian plane ($\theta = 0$ or $\theta = \pi$).

Strojniški vestnik - Journal of Mechanical Engineering 51(2005)7-8, 509-518
UDK - UDC 536.2
Izvirni znanstveni članek - Original scientific paper (1.01)

Comparison of Flow Characteristics of Centrifugal Compressors by Numerical Modelling of Flow

Zvonimir Guzović*, Mario Baburić, Dubravko Matijašević

Faculty of Mechanical Engineering and Naval Architecture, University of Zagreb, Ivana Lučića 5, Zagreb, Croatia,
**zvonimir.guzovic@fsb.hr*

Abstract

The centrifugal impellers are used in a wide variety of turbo-machineries, ranging from low pressure fans for cooling of electric motor to high pressure ratio gas turbine compressors, from tiny cryo-cooler compressors to large industrial petrochemical compressor stations. The relative flow in centrifugal impeller is very complex due to different fluid dynamics phenomenon and their interactions. It is subjected to the complex secondary flows and significant separation of the boundary layers, which result in non-uniformity of outlet flow both in tangential direction (e.g. "jet-wake" flow) and axial direction. By the development of experimental and computational techniques the considerable progress in understanding of complex flow effects in impeller is made.

The wide-spread use of reactive impellers with backswept blades in all state-of-the-art designs of compressors has resulted in significant improvements of aero and thermodynamics characteristics of impeller (e.g. distribution of outlet flow velocities).

The increasingly present appearance in the several recent years of calculations by means of verified and validated users software based on the engineering numerical methods enables an increasingly wide replacement of time-consuming experimental investigations (i.e. of physical modelling), which give a limited number of data of integral character, by mathematical modelling which gives a large number of data over a short time, enabling not only integral but also structural analysis. This results in rapid and significant improvements of aero and thermodynamics characteristics and in the end in energy conversion efficiency.

The aim of the paper is to apply expert knowledge in carrying out numerical modelling of the flow in centrifugal compressor by means of users software. The algorithm is presented on the comparison of aero and thermodynamics characteristics of centrifugal compressors with reactive impellers with backswept normal and "S" shape blades. The comparison shows that the compressor with impeller with "S" shape blades has better aero and thermodynamics characteristics and thus also the energy conversion efficiency. Since there are experimental measurements of aero and thermodynamics characteristics of the numerically investigated compressors in literature, the verification and validation of the users software have been performed simultaneously. Also the alternating modelling of the flow and change of impeller blades geometry with the aim of improving the aero and thermodynamics characteristics up to attaining of maximum possible efficiency of energy conversion presents the algorithm of geometry optimisation of the impeller design with backswept blades.

Introduction

The centrifugal compressors are widely used in a variety of applications because of their ability to achieve high pressure ratios in a relatively short axial distance and due to their rugged construction.

In designs of stationary compressors, with medium values of circumferential velocity (up to u= 300 m/s), the centrifugal impellers with radial inlet of flow on the blades are applied. Usually, with such impellers the exit angle of blades is β_2'<90 deg and they are conditionally named reactive. In design of compressors e.g. dedicated to the charge of internal combustion engines and in smaller power gas-turbine plants, which feature significant circumferential velocities (about u= 500 m/s), due to the strength conditions the impellers are performed with axial inlet of flow on blades (i.e. axial–radial impellers). In many cases such impellers are designed

Nomenclature

c_p - specific heat at constant pressure, J/kgK;
D - diameter, m;
f – rotational frequency, s^{-1};
k – thermal conductivity, W/mK;
$\dot{m}$ - mass flow rate, kg/s;
p - pressure, Pa;
R – radius, m;
r – commpresion (pressure) ratio, -;
T – temperature, K;
u – circumferential velocity, m/s;
z – number of impeller blades, -;

Greek Letters
β' - impeller blade angle, deg;
η - isentropic efficiency, -;
μ - dynamic viscosity, kg/m s;
ρ - mass density, kg/m^3;

Subscripts
in – inlet;
out – outlet;
nom – nominal value;
ref – reference value;
hub – at hub of impeller;
tip – at tip of blade;
conv – convex surface of impeller blade;
conc – concave surface of impeller blade;
0 – total pressure;
1 – impeller inlet;
2 – impeller outlet;
3 – vaneless diffuser outlet;
4 – spiral casing outlet;

with exit angle of blades β_2'<90 deg. On the other hand, the axial–radial impellers are usually performed due to manufacturing simplicity as impellers with β_2'= 90 deg, with inducer which represents the axial cascade in which the blade incline angle is increased from β_1' (on inlet) to β_1'= 90 deg (on exit). In this part of impeller the directrixes of the blade surface are directed along the radius. In the radial part of the impeller, due to the realization of the exit angle β_2'<90 deg, the blade is curved round the circular arc in the plane of rotation, while its surface is also linear with direction of blades directrixes parallel to the axis, Fig. 1, impeller *2a*. The blade incline angle in this part of impeller is changed from β'= 90 deg to the value of the exit angle β_2'. In the region between the axial and the radial part of the impeller, i.e. in the area of transition from axial to radial direction, the blade incline angle equals 90 deg.

In such design of blades of the reactive impeller (called impeller with normal blades or «the first type impeller») their shape and consequently the shape of channels is less favourable than in impellers with radial blades (β_2'= 90 deg) and more than in case of reactive impeller with radial inlet of flow on blades. With such shape of blade the angle of its incline in the change from β_1' to β_2' assumes also the value β'= 90 deg, resulting in the change of sign of the blade lateral surface curvature. In these conditions the advantages of reactive impeller are annulled due to the increase in losses, caused by this shape of the blade. Due to the decrease in losses in the centrifugal reactive impeller with axial inlet of flow on blades it is necessary to insure monotonous change of blade incline angle from β_1' to β_2', i.e. without assuming the value β'= 90 deg. The blade shape also changes monotonously along the entire length, without the change of sign of the curvature of its lateral surface.

The centrifugal impellers of this type are applied in pumps, where the direction of inlet of flow on the blades is close to axial. The blade surface of impeller of this pump has curvilinear directrixes, which significantly complicates their manufacturing. Due to the simplicity of manufacturing of the reactive axial-radial impeller with monotonous change of angle β', it is desirable to preserve the blade surface straight, i.e. that the blade surface has straight directrixes, which are at a certain angle to the impeller axis and intersect it. In this case the blade surface has the shape of a screw surface or simply the "S" shape, with directrixes directed along the normal to the middle line of the impeller meridional section, Fig. 1, impeller *2b* (called impeller with "S" shape blades or "the second type impeller").

One of the methods of determining the optimal surface shape of "S" blade, i.e. of change of the blade incline angle from β_1' to β_2' is by means of experimental investigation. Unfortunately the experimental investigations are time-consuming and the limited number of obtained data is most frequently of integral character. Therefore, the design optimization of the impeller blades with the aim of improving the aero and thermodynamics characteristics, i.e. efficiency of energy conversion is adequately slow. Fortunately, the recent increasingly present appearance of calculations by means of user software based on the verified and validated engineering numerical methods enables an increasingly wide replacement of experimental investigations (i.e. of physical modelling) by mathematical modelling. These methods enable not only structural but also integral analysis of the flow and energy conversion processes in the impeller. A large number of data obtained over a short time results in rapid and significant improvements of aero and thermodynamics characteristics, and eventually in the energy conversion efficiency.

The paper presents the algorithm of numerical modelling of flow in the centrifugal compressor, based on the application of expert knowledge and the usage of user software. The algorithm is presented on the comparison of aero and thermodynamics characteristics of centrifugal compressors with reactive impellers with backswept normal and "S" shape blades whose geometries and results of experimental investigations are presented in literature [1]. Thus it was possible to simultaneously perform the verification and validation of the users software.

In principle the algorithm serves for optimization of the impeller design, i.e. improvement of its aero and thermodynamics characteristics and thus also the processes of energy conversion with the aim of attaining maximum possible isentropic efficiency. The first step in the optimization process of impeller design is obtaining the initial three-dimensional geometry on the basis of results of aero and thermodynamics calculations and other empirical data by means of the graph-analytic method fully automated on the computer [2], [3]. The obtained impeller geometry can be considered as «well-designed». The final (optimal) geometry is obtained after a definite number of iterations between numerical calculations (modelling) of flow and changes of geometry of impeller blades. The optimal geometry assumes these aero and thermodynamics characteristics of flow in impeller which result in maximum possible isentropic efficiency.

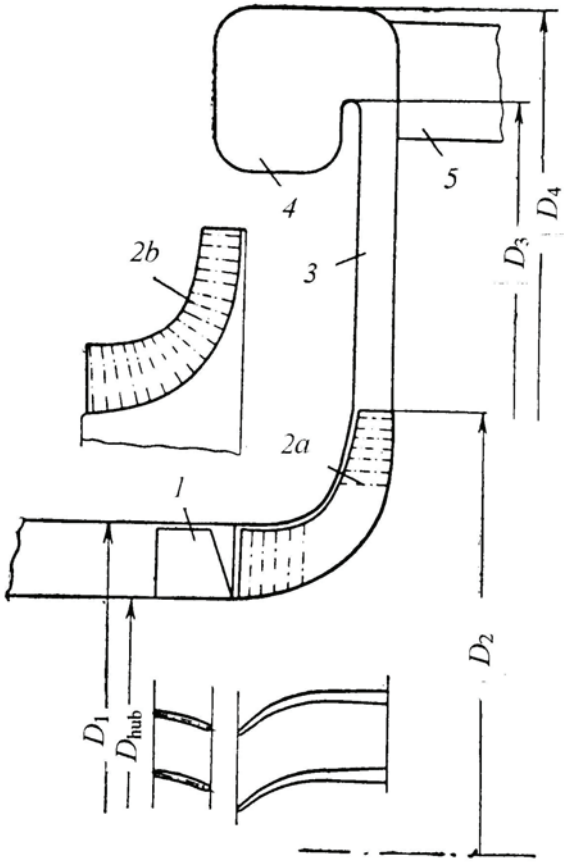

Fig. 1. The scheme of investigated compressor: *1*-inlet guide vanes; *2a, 2b*-impeller with "normal" i.e. "S" shape blades; *3*-vaneless diffuser; *4*-spiral casing; *5*-connection

Flow behaviour in impeller

The impellers of centrifugal compressors are characterized by long three-dimensional blade channels with high curvature. The blades make 90 deg turn in the meridional plane and have opposite angle turns in inlet axial part (the inducer) and exit radial part (the exducer). In the inducer the blade angle with respect to the tangent direction increases, thus allowing the pressure rise through internal flow diffusion. In the exducer where blade loading is dominated by Coriolis forces, the blade angle is reduced in order to prevent excessive loading.

The real flow that develops in centrifugal impeller, under the combined effects of deceleration, Coriolis force and meridional curvature, and which simultaneously acts on the boundary layers on channels walls, is very complex [4], [5], [6]. The Coriolis force component perpendicular to the rotating blade surface influences the boundary layer stability: on the blade suction side the turbulence production is inhibited and the boundary layer becomes prone to separation. Due to the complex transition of the flow and rotational forces, strong secondary flows are produced. These secondary flows, along with separated flow regions, lead to strong crossflow velocity components, which transport the fluid with low momentum and high total-pressure loss into the mainstream. Also in unshrouded impellers the interaction of the low-momentum fluid in the boundary layer with the tip leakage flows is significant.

First of all, the complex secondary flows and significant boundary layer separation, as well as the interaction of the low-momentum fluid in the boundary layer with the tip leakage flows result in the impeller outlet flow non-uniformity in which the low-velocity wake region is close to the suction surface and jet region near the pressure surface of the blade. This flow pattern is called the "jet-wake" flow [5], [6]. The mixing of this "jet-wake" flow is the source of significant loss generation. The outlet flow velocity field is non-uniform both in circumferential (pitchwise) and in axial (spanwise) direction. While the circumferential variations in the outlet flow level up very rapidly, at the same time the axial variations in the flow seem to persist well into the diffuser. This axial flow variation has an adverse effect on the pressure recovery of the diffuser (vaned or vaneless) and it is one of the main causes of stage instability in compressors. Therefore, the minimization or possible suppression of the formation of the outlet flow non-uniformity should not only lead to substantial improvement in stage performance but also result in increases in the stable operating range of the turbomachine.

In order to design impellers with a more uniform outlet flow field, it is important to understand the basic mechanisms behind the generation of the outlet flow non-uniformity and then produce appropriate design guidelines to minimize their effects by changes to the impeller geometry [3].

The dominant influence of secondary flows on the generation of the "jet-wake" flow has been known for as

many as about forty years [4], [5], [6]. The use of blade lean or spanwise stacking (i.e. of "S" shape blade) can minimize the secondary flows in the impeller and obtain a more uniform outlet flow field. The use of excessive amounts of blade lean, however, can result in structural problems or manufacturing difficulties.

Presentation of experimental investigations results

Fig. 1 presents the scheme of experimental stage from [1] at which the experimental investigations of both impellers have been carried out. The stage consists of inlet guide vanes which give to the flow on in the impeller inlet a certain pre-whirl, of reactive impeller with backswept normal ("the first type impeller") or "S" shape ("the second type impeller") blades, of vaneless diffuser of relatively large length in radial direction and of spiral casing with two connections, which turn the flow in axial direction. The stage with "the first type impeller" features the following design values and geometrical characteristics: u_{2nom}= 341 m/s; f_{nom}= 586.67 s^{-1}; p_{in0}= 103,300 Pa; T_{in}= 288 K; D_2= 185 mm; D_1/D_2= 0.729; D_{hub}/D_1= 0.785; D_3/D_2= 1.7; D_4/D_2= 1.915.

Fig. 2 denotes with *a* "the first type impeller", and Table 1 gives the blade geometry by means of coordinates of its concave and convex surfaces. The number of impeller blades is z= 27. The inducer inlet angles on diameters D_1 and D_{hub}: $\beta_{1,tip}'$= 44 deg and $\beta_{1,hub}'$= 51 deg. Along the inducer, on all sections the angles increase up to β'= 90 deg. On the radial part in rotational surface the blade is curved along the circle arc with the radius of R= 26.7 mm. The exit blade angle β_2'= 61.01 deg.

Fig. 2 denotes with *b* "the second type impeller", and Table 2 gives the blade geometry by means of coordinates of its concave and convex surfaces. It has in the meridional section the same shape as «the first type impeller», also the same number of blades z and exit blade angle β_2'. The values of inducer inlet angles are somewhat lower ($\beta_{1,tip}'$ = 38 deg and $\beta_{1,hub}'$ = 45 deg).

The experimental investigations of the stage with both types of impeller are carried out with total pressure on inlet p_{in0}= 1 bar and p_{in0}> 1 bar. At the inlet into the stage for measuring the air flow, the measuring collector with 100 mm diameter is built in. Between the collector and the investigated stage the diffuser with divergence angle of 8 deg is installed. The total pressure of air on the stage inlet is measured at five points by the measuring devices for total pressure and the temperature by resistance thermometer, installed in pipe before the measuring collector. The measurement results of total pressure on inlet are arithmetically averaged.

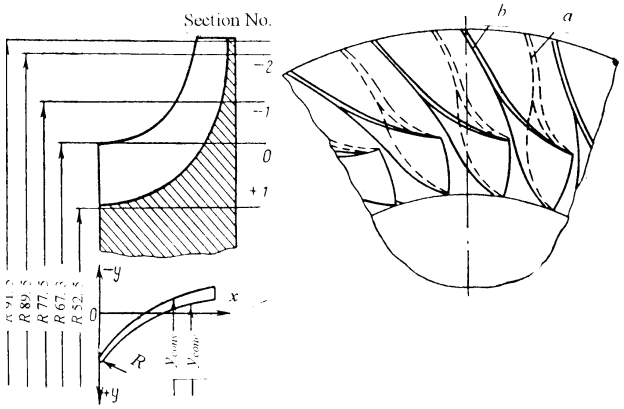

Fig. 2. The reactive impellers with backswept normal (*a*) and "S" shape (*b*) blades

Table 1. The blade geometry of "the first type impeller" (coordinates of concave and convex surfaces)

Section No.	X	0	3.5	7	9.5	12	14.5	16	17	19	21	23	25	27	29	31	R
1	y_{conv}	6.34	3.56	1.48	0.36	-0.47	-1.00	-1.19	-1.2								0.43
	y_{conc}	7.35	5.09	3.26	2.30	1.66	1.30	1.24	1.2								
0	y_{conv}	8.45	5.00	2.39	1.00	0	-0.64	-0.89	-0.9	-0.97	-1.05	-1.13	-1.20	-1.28	-1.35	-1.43	0.25
	y_{conc}	9.12	6.12	3.71	2.43	1.52	1.02	0.91	0.9	0.97	1.05	1.13	1.20	1.28	1.35	1.43	
-1	y_{conv}								-0.7	-0.78	-0.85	-0.93	-1.00	-1.08	-1.15	-1.23	
	y_{conc}								0.7	0.78	0.85	0.93	1.00	1.08	1.15	1.23	
-3	y_{conv}									-4.30	-4.39	-4.47	-4.56	-4.64	-4.73	-4.81	
	y_{conc}									-3.68	-3.59	-3.51	-3.42	-3.34	-3.25	-3.17	

Table 2. The blade geometry of "the second type impeller" (coordinates of concave and convex surfaces)

Section No.	x	0	2.5	5	7.5	10	12.5	15	19	21	23	25	27	31	R
1	y_{conv}	9.23	6.35	4.75	3.60	2.70									0.43
	y_{conc}	10.12	8.32	7.15	6.04	5.18									
0	y_{conv}	11.10	7.34	4.20	1.90	0.15	-1.33	-2.56	-4.20	-4.87	-5.47	-6.00	-6.50		0.25
	y_{conc}	11.87	8.60	5.95	4.05	2.36	0.90	-0.48	-2.00	-2.63	-3.12	-3.50	-4.00		
-1	y_{conv}								-11.03	-11.46	-11.8	-12.13	-12.41	-12.81	
	y_{conc}								-8.97	-9.31	-9.57	-9.78	-9.96	-10.24	
-2	y_{conv}										-21.06	-21.16	-21.27	-21.63	
	y_{conc}										-20.31	-20.20	-20.10	-20.01	

The measurements results of the total pressure and temperature after the stage are carried out in exit collector at sixteen points. The measurements of total pressure and total temperature on exit are also arithmetically averaged.

The compressor stage is driven by direct current electric motor. In the course of investigations the power delivered to shaft of compressor stage is determined. This is enabled the calculation of compressor isentropic efficiency both by the delivered power and by the temperatures.

The compression ratio r= 1.85 and the isentropic efficiency η= 0.7 are determined by the mass flow $\dot{m}$= 0.7 kg/s and rotational frequency f= 586.67 s^{-1} at stage with "the first type impeller" on the basis of the measurement results. Simultaneously, the same quantities for stage with "the second type impeller" have been obtained about 11% higher. On the basis of this, the authors [1] have concluded that the obtained improvement of characteristics of stage with "the second type impeller" is based on the increase of impeller efficiency. They explain the latter by more favourable blades shape and consequently the impeller channels, which decreases the losses in impeller. The losses are decreased due to the reduction of blade turning angle, reduction of relative velocities gradient in inlet part of impeller and due to monotonous change of blade lean along the length and keeping of curvature sign of the blade surface unchanged.

The complete interpretation of previous results will be given by the numerical modelling of the flow in compressors with the described "first and second type impeller", which are presented in the next chapter.

Investigation of compressors by numerical modelling of flow

On compressors with both type of impellers, whose geometry and results of experimental investigations of aero and thermodynamics characteristics are presented in previous chapters from [1], now the same investigations are performed by numerical modelling of flow.

Discretisation of geometrical domain by the grid of finite volumes

Before the very numerical simulation in CFD (Computational Fluid Dynamics) user software, the discretisation of geometrical investigated domain has been made; in this case by grid of the finite volumes. The grid of the finite volumes coincides with the geometrical domain. The domain in this case represents the configuration of inlet guide vanes, reactive impeller with normal ("the first type impeller") or "S" shape ("the second type impeller") backswept blades and vaneless diffuser. Due to the periodic rotational symmetry of configuration of inlet guide vanes, the impeller and vaneless diffuser it is sufficient to model the flow in one segment of impeller, and downstream in one segment of inlet guide vanes and upstream in one segment of vaneless diffuser by the application of adequate boundary conditions on boundaries of rotational symmetry. The segment of impeller is extended between symmetrals of two neighbouring channels with the blade in the middle. It is similar to the downstream located segment of inlet guide vanes which is also extended between the symmetrals of two neighbouring channels with stator blade in the middle, while the segment of vaneless diffuser with width which is equal to the exit width of the impeller channel is located upstream. With this, the necessity for processor and memory power of computer in the course of CFD simulation is significantly reduced, enabling the usage of grid of finite volumes of higher density than in the case of the entire physical domain modelling. For the creation of the grid of finite volumes the user software GAMBIT was used.

Since in the domain, one part rotates (impeller), and the other two parts rest (inlet guide vanes and vaneless diffuser), the separated grids of finite volumes are made for these particular parts of domain. The first is the made part of the domain of inlet guide vanes segment which is equal in both modelled cases, and then the other two parts of domain, the segments of impeller and of the vaneless diffuser, for both types of impellers. Before numerical calculation the different parts of domain are combined in the user software FLUENT in a single complete domain with clearly defined interface.

The finite volume grid for the compressor with "the first type impeller" is presented in Fig. 3, and for the compressor with "the second type impeller" in Fig. 4.

In the first case the domain is discretised with 277,740 finite volumes, and in the second case with 221,376 finite volumes. In both cases the grids are completely made of finite volumes shaped as hexahedron.

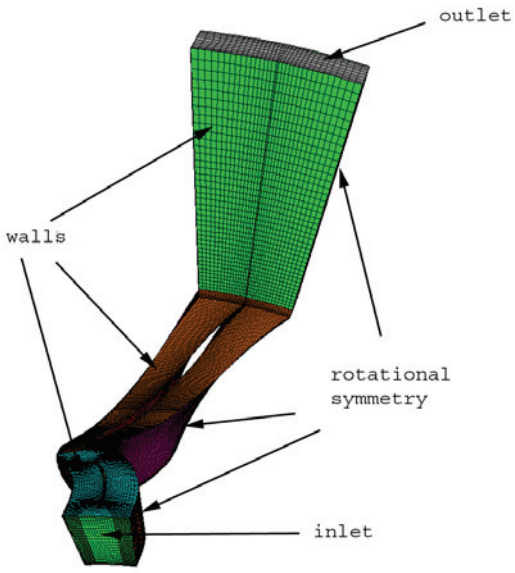

Fig. 3. The finite volume grid for the compressor with "the first type impeller"

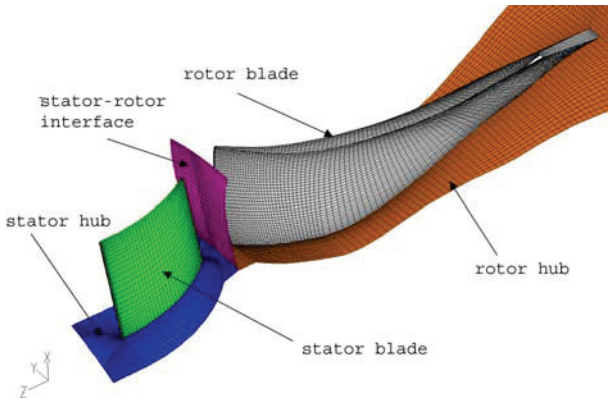

Fig. 4. The finite volume grid for the compressor with "the second type impeller" (part)

Numerical calculation

For complete defining of the mathematical model used in numerical calculations it is necessary to set the boundary conditions on the boundary surfaces of the domain, which describe the physical conditions on domain boundaries. In this numerical calculation there are unambiguously defined boundary surfaces of the domain: inlet and outlet surface, surfaces of stator and rotor blades, walls of disc, impeller hub and inducer hub, surfaces of rotational symmetry and interfaces. Figs. 3 and 4 present a domain with the defined boundary surfaces.

On the inlet surface the mass flow of air $\dot{m}$= 0.026 kg/s, inlet temperature T_{in}= 288 K and inlet pressure p_{in}= 100,000 Pa have been set. On the outlet surface the outlet pressure p_{out}= 185,000 Pa (i.e. "pressure outlet") has been set. In all the walls the adiabatic boundary condition is used, and with stationary walls (inlet guide vanes, shroud, vaneless diffuser) the rotational frequency is set f= 0 and at the impeller wall the rotational frequency round the axial axis f= 586.67 s^{-1}. On the surface of rotational symmetry the boundary condition of rotational symmetry is used.

The working fluid is air whose density is calculated by equation for ideal gas. Also, the following physical properties are used in calculations: specific heat at constant pressure c_p= 1006.43 J/kgK; thermal conductivity k= 0.0242 W/mK; viscosity μ= 1.7894*10^{-5} kg/sm. The reference pressure is taken p_{ref}= 100,000 Pa.

The numerical calculation is performed in CFD user software FLUENT. Since in the domain one part rotates (impeller) and the other two rest (inlet guide vanes and vaneless diffuser), it is not possible to perform the stationary simulation provided the consistence of the mathematical model with real physical state is maintained. Therefore, the numerical calculation is performed by means of non-stationary mathematical model, which takes into consideration the relative movement between inlet guide vanes and the impeller, as well as between the impeller and the vaneless diffuser (i.e. sliding mesh).

Other characteristics of the numerical calculations are:

- the non-stationary, three-dimensional solver, with non-conjugate solution of main equations and absolute formulation of velocity has been used;
- along with standard k-ε turbulence model, also the standard wall functions for modelling of viscose layer near the wall are used;
- in energy calculation the enthalpy equation, assumption of adiabatic walls and fluid heating close to wall due to viscose friction (option of viscose heating) are included;
- from the numerical theses the following are used: the Simple algorithm of velocity and pressure conjugation, the second order upwind scheme as discretisation method and sub-relaxation factors;
- the equations of flow, turbulence and energy (enthalpy) are solved;
- the time interval is chosen so that in calculation 50 time intervals for one period are needed, i.e. that the relative position of impeller towards the inlet guide vanes and vaneless diffuser is equal to the initial one;
- the calculation is completed when the calculation results start to be repeated periodically.

The results of numerical modelling of flow

Figs. 5 – 18 present the results of numerical modelling of flow in centrifugal compressors with «the first and second types of impellers.

In both cases the sufficiently uniform distributions of absolute pressure along impeller channels are observed, Figs. 5 - 6. Obviously, the distributions of density are visually similar to distributions of absolute pressure, Figs. 7 - 8, because these two quantities are directly related by the state equation of ideal gas and they are proportional. The temperature distributions for both cases are presented in Figs. 9 - 10. Similarly as with the previous two quantities, the temperature distributions are uniform, and clearly visible areas of increased temperature are close to the walls, which results in the viscose friction close to the walls. The distributions of relative velocities for both types of impellers are presented in Figs. 11 - 12. In Fig. 11 in case of "the first type of impeller" an area near the shroud is observed, which starts from the location of transition from axial to radial direction, of accumulation of low momentum fluid and with high losses. This is explained by the intensive secondary flow which displaces the low momentum fluid toward shroud (i.e. toward casing), and which is, as other investigators have indicated, characteristic for impellers with axial inducer [5], [6]. As shown in Fig. 12, with "the second type of impeller", the existence of the secondary flows is not observed at all. Therefore it may be concluded that the replacement of normal blades by "S" shape blades effectively eliminates the occurrence of the secondary flows.

The distributions of Mach numbers for both types of impellers are presented in Figs. 13 - 14. From the distributions it is possible to conclude that in the region of the inducer, near the inlet edge toward the periphery of

blades the values of Mach number are increased, but still below the critical ones, which positively influences the stability of boundary layers.

The distributions of relative velocities on the radius R= 0.075 m (Figs. 15 - 16) and in outlet section (Figs. 17-18) for both types of impellers are especially illustrative. At first sight it may be observed that in both sections the distributions of relative velocities with "the second type of impeller" are more uniform (Figs. 15 and 17) than with "the first type of impeller" (Figs. 16 and 18). However, it should be noted that in neither type of impeller in the outlet sections the "jet-wake" is not present, only with "the first type of impeller" it is possible to speak about its almost negligible presence. The distributions of velocities both in axial and in circumferential direction are satisfactorily uniform, especially with "the second type of impeller". This contributes to effective diffuser operation, which is confirmed by Figs. 5-6, where significant pressure increase is observed with uniform distribution. All this tells about the positive influence of the usage of reactive impellers with the aim of preventing the flow non-uniformity at the outlet from impeller, i.e. of "jet-wake" flow, especially of "the second type of impeller".

On the basis of calculation results of temperatures and pressures during one period the isentropic efficiency has been calculated. The values of isentropic efficiency during one period for compressor with "the first type of impeller» are presented in Fig. 19, while the same for compressor with "the second type of impeller" are presented in Fig. 20. The average value of isentropic efficiency during one period for compressor with "the first type of impeller" is η= 0.784, while for compressor with "the second type impeller" is η= 0.85. Generally, the numerical modelling has yielded higher values than by experimental measurements, but the mutual difference is 10% as well as with experimental measurements. The obtained higher value of isentropic efficiency in compressors with impeller with "S" shape blades than with compressors with impeller with normal blades can be explained by the fact that with the impeller with "S" shape blades the secondary flow is almost eliminated. This is also indicated with the attained average values of pressure ratios: r= 1.855 versus r= 1.812. The first value is equal to the value obtained during experimental measurements, and the second value is 2% lower.

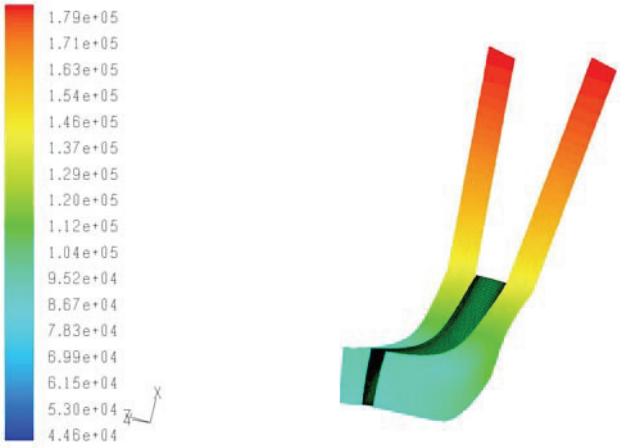

Fig. 5. Distribution of absolute pressure along compressor with "the first type of impeller"

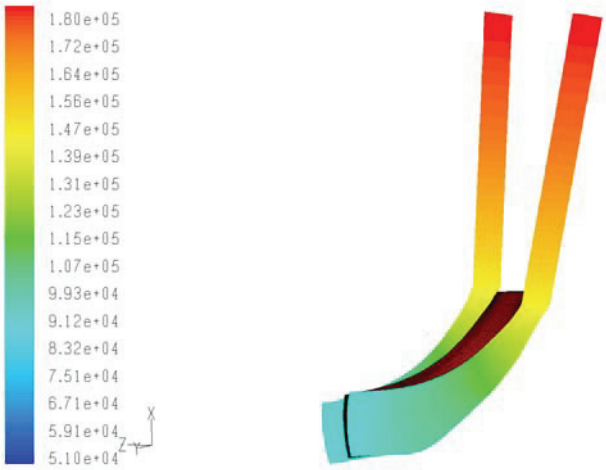

Fig. 6. Distribution of absolute pressure along compressor with "the second type of impeller"

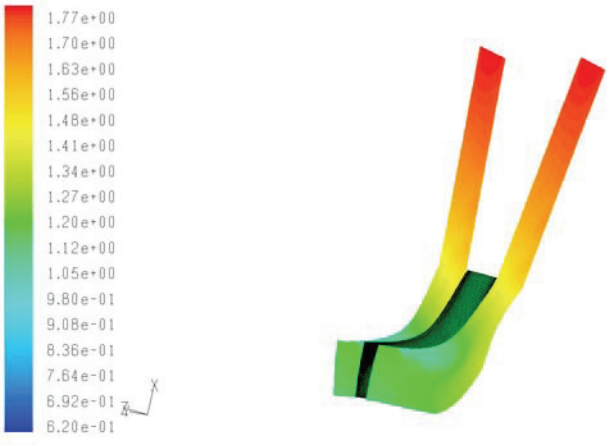

Fig. 7. Distribution of density along compressor with "the first type of impeller"

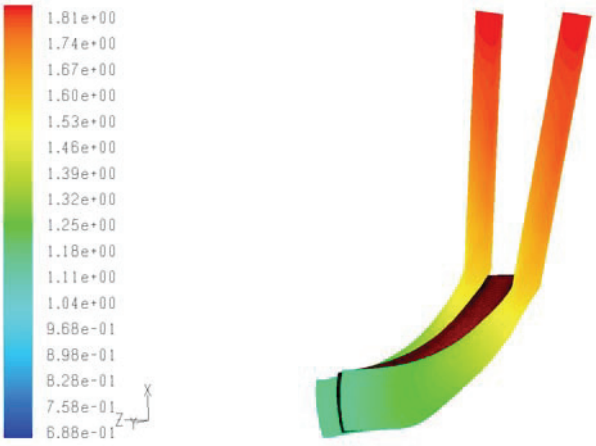

Fig. 8. Distribution of density along compressor with "the second type of impeller"

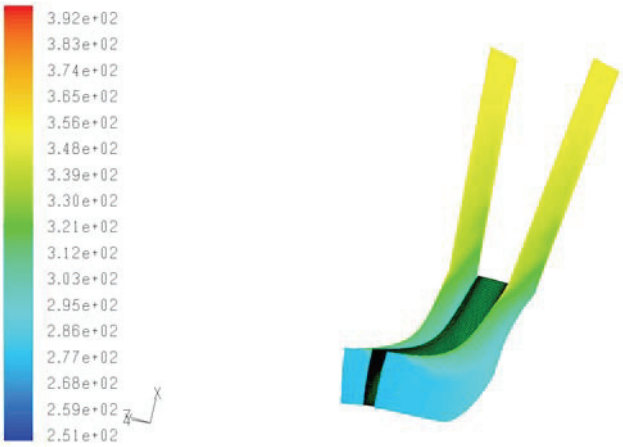

Fig. 9. Distribution of temperature along compressor with "the first type of impeller"

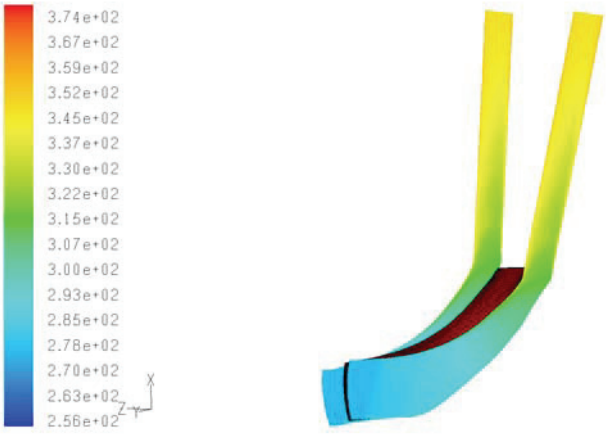

Fig. 10. Distribution of temperature along compressor with "the second type of impeller"

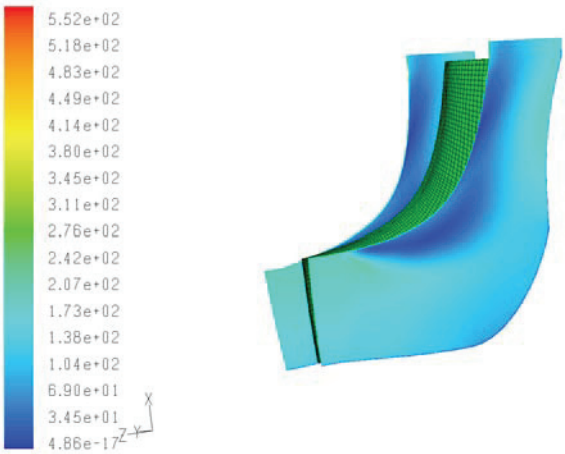

Fig. 11. Distribution of relative velocity along "the first type of impeller"

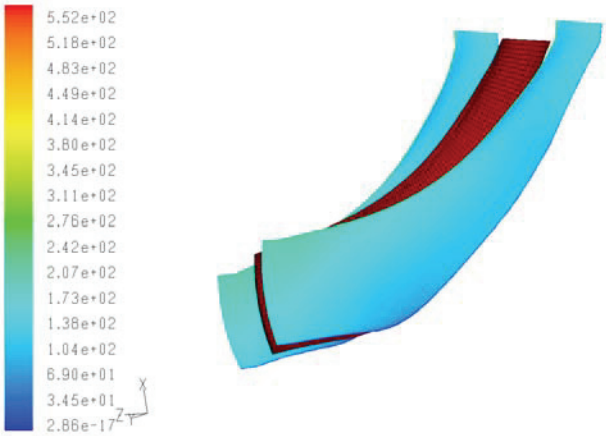

Fig. 12. Distribution of relative velocity along "the second type of impeller"

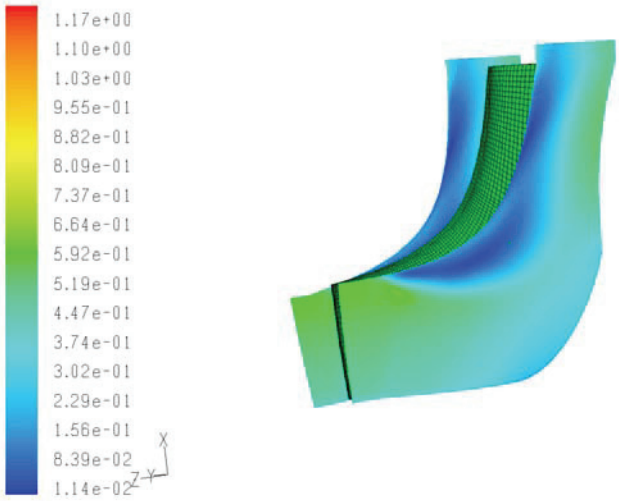

Fig. 13. Distribution of relative Mach number along "the first type of impeller"

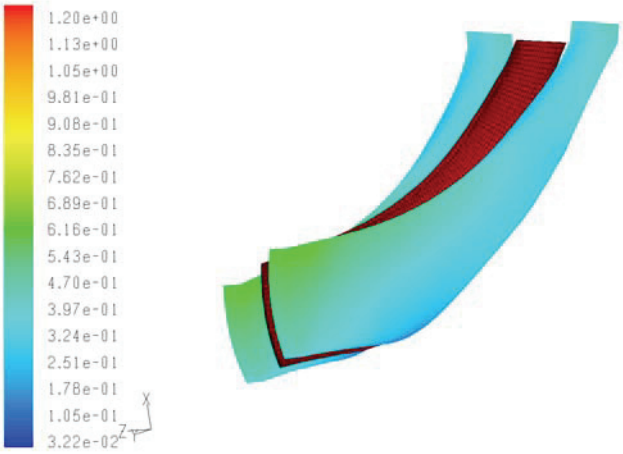

Fig. 14. Distribution of relative Mach number along "the second type of impeller"

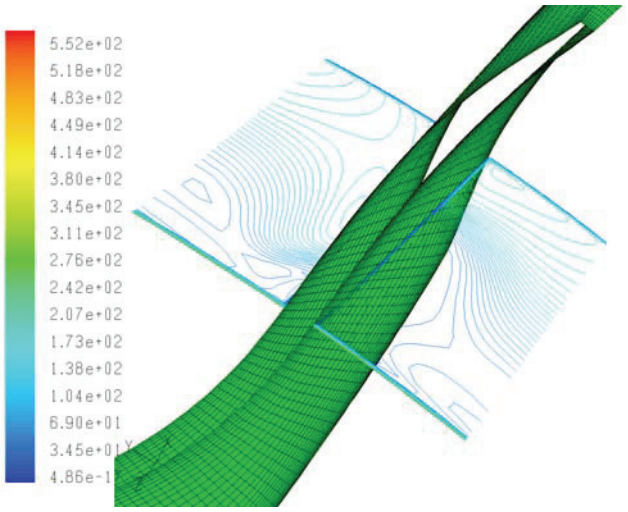

Fig. 15. Distribution of relative velocity at "the first type of impeller" on R= 0.075m

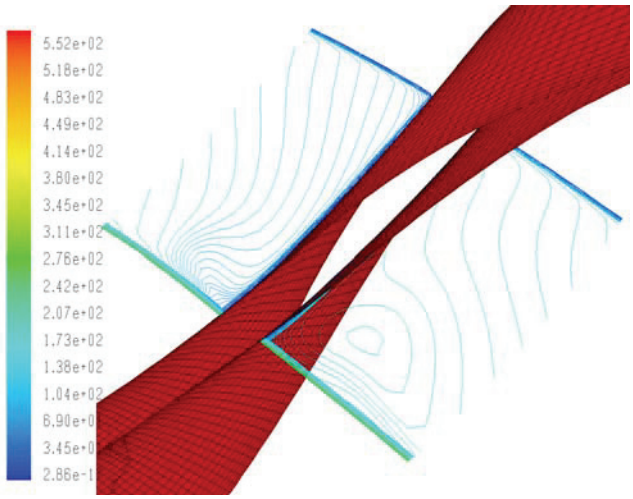

Fig. 16. Distribution of relative velocity at "the second type of impeller" on R= 0.075m

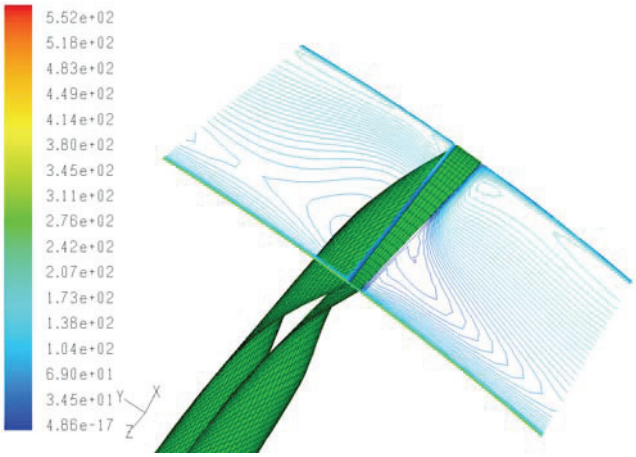

Fig. 17. Distribution of relative velocity at "the first type of impeller" in outlet section

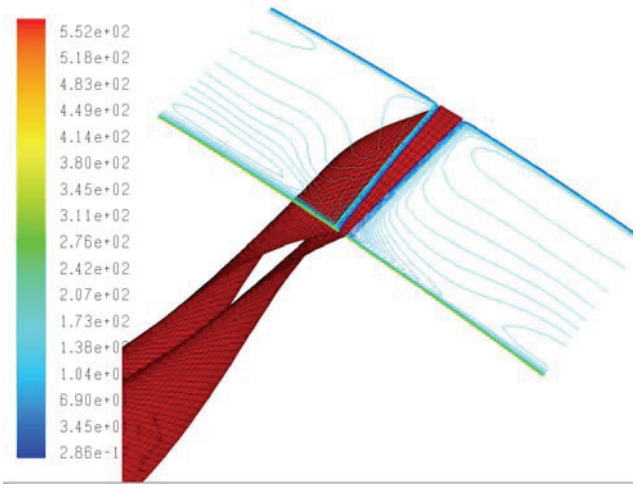

Fig. 18. Distribution of relative velocity at "the second type of impeller" in outlet section

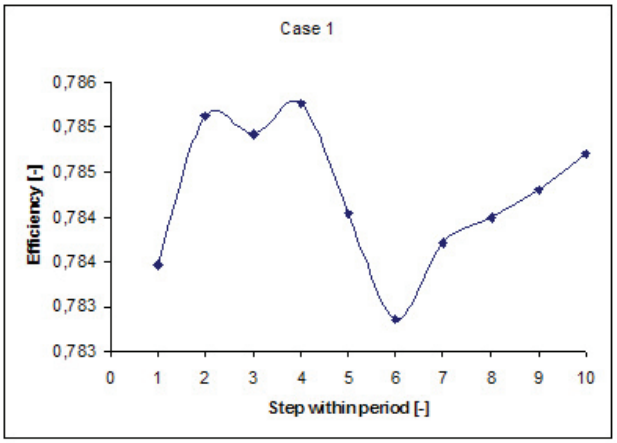

Fig. 19. The values of isentropic efficiency during one period for compressor with "the first type of impeller"

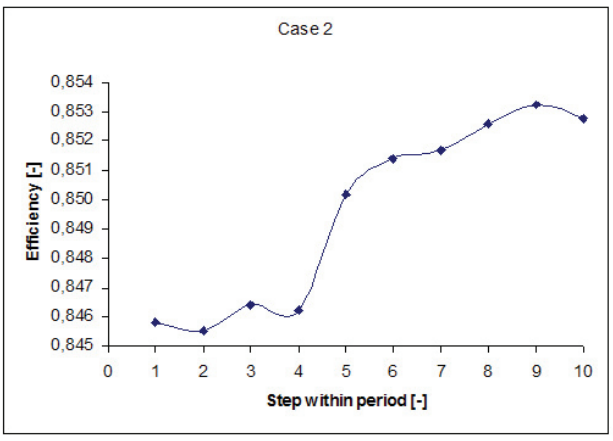

Fig. 20. The values of isentropic efficiency during one period for compressor with "the second type of impeller"

Conclusion

The paper presents the possibility of investigating the flow phenomenon in centrifugal compressor by means of verified and validated user software and of required expert knowledge. The algorithm of numerical modelling of flow is presented in comparison of flow characteristics and efficiencies of compressors with two types of reactive impellers with backswept blades, with normal blades and "S" shape blades. The better is the compressor with impeller with "S" shape blades: as the numerical modelling of flow shows, it almost completely eliminates secondary flows and the calculation of efficiency gives efficiency higher by about 10%. It can be concluded that both types of reactive impellers effectively prevent the flow non-uniformities on the outlet from impellers, i.e. the "jet-wake" flow is almost inexistent on impellers outlets. Since the experimental measurements exist for the modelled compressors, it was possible to carry out the verification and validation of user software. The agreement between the results obtained by numerical modelling and by experiments is satisfactory, which enables complete replacement of the time-consuming experimental investigations by much rapid numerical simulations.

The represented numerical modelling of flow in centrifugal compressor makes it possible to carry out the optimisation of basic part of compressor (e.g. impeller) with the aim of improving the efficiency of machinery. Based on the results of numerical calculations, the correction of design is made with the aim of improving the flow characteristics, i.e. of energy conversion process, until achievement of maximum possible efficiency.

References

[1] I.A. Gurvich, L.L. Levaschov, M.H. Etingof, Results of experimental investigation of centrifugal compressor stage, (in Russian), Teploenergetika (2) (1980) 34-38.

[2] Z. Guzovic, B. Matijasevic, I. Novko, CAD Modelling of the Optimal Axial-Radial Impeller of the Centrifugal Compressor for CAM, Proceedings of the 10th International DAAAM Symposium, Ed. B. Katalinic, Vienna, (1999) 175-176.

[3] B. Matijasevic, K. Horvat, Z. Guzovic, Design Optimization of Centrifugal Compressor Impeller by Numerical Modelling, Proceedings of the 6th International Research/Expert Conference TMT 2002, Eds. S. Brdarevic, S. Ekinovic, R. Compamys, J. Vivancos, Neum, Bosnia and Herzegovina, (2002) 413-416.

[4] M.D. Hathaway, R.M. Chriss, J.R. Wood, A.J. Strazisar, Experimental and Computational Investigation of the NASA Low-Speed Centrifugal Compressor Flow Field, Journal of Turbomachinery, 120 (1993) 527-542.

[5] M. Zangeneh , Inviscid-Viscous Interaction Method for Three-DimensionalInverse Design of Centrifugal Impellers, Journal of Turbomachinery, 120 (1994) 280-290.

[6] M. Zangeneh, A. Goto, H. Harad, On the Design Criteria for Suppression of Secondary Flows in Centrifugal and Mixed Flow Impellers, Journal of Turbomachinery, 120 (1998) 723-735.

Strojniški vestnik - Journal of Mechanical Engineering 51(2005)7-8, 519-526
UDK - UDC 536.2
Izvirni znanstveni članek - Original scientific paper (1.01)

Heat transfer distribution for a free/porous system with forced convection and heat generation - a numerical study

Antonio C.M. Sousa[1,2*]

[1]*Departamento de Engenharia Mecânica; Universidade de Aveiro;*
Campus Universitário de Santiago; 3810-193 Aveiro-Portugal.
[2]*Department of Mechanical Engineering; University of New Brunswick;*
*Fredericton, NB, Canada E3B 5A3,*asousa@unb.ca*

Abstract

This paper reports on a numerical study for steady flow and heat transfer distribution for a configuration relevant to Liquid Composite Molding, where a gap between a porous substrate and the solid boundary of a mold cavity yields an edge flow. The flow within the porous domain is modeled by the Brinkman-Forchheimer formulation, and the edge flow itself is described by the Navier-Stokes equations. The cure of the fluid (resin) is simulated as a volumetric heat generation. The predictions are obtained using a well-tested control-volume finite element method, however, a novel methodology had to be devised to define the interface between the free and porous system. The most relevant finding is the critical role of the gap upon the quality of the part. The presence of the gap can reduce substantially the average flow through the porous substrate, therefore yielding high temperature levels in this region. These temperatures may be sufficiently high to cause serious defects to the part being molded.

Introduction

Numerical and analytical investigations of flow and heat transfer distribution in composite systems containing simultaneously a porous and an open fluid domain are receiving renewed interest from the scientific and engineering community due to the demand for the development of models that can enhance mold design in the area of Liquid Composite Molding (LCM)[1,2]. LCM processes, such as Resin Transfer Molding (RTM) are preferred manufacturing processes for large structural components of complicated shape made out of polymer composites. These processes, in general, are characterized by their high cost-effectiveness, relatively simple tooling requirements, low cycle times, and net-shape production. They require the impregnation of a polymeric resin through a porous preform, which is placed in the mold cavity, and it can be composed of glass, carbon, or Kevlar fibres. The main difficulty with these processes is usually associated with the eventual presence of small clearances between the preform and the mold edges, which result from rough cutting, ill fitting, or deformation of the preform. The clearance yields a preferential flow path, which can disrupt the filling of the mold and the impregnation of the preform, resulting in poor quality of the part due to voids, residual stresses, and poor bonding between the fibres and the resin. This preferential flow, which involves the interface between a porous and non-porous medium, poses a major phenomenological challenge, and it has been the focus of intense research over the years. In the past, most models for edge flows used the Darcy's Law, and they were formulated either on the basis of an analytical formulation for the interface [3], e.g. [1,2], or on the basis of an equivalent permeability for the edge [1,2,4]. Both approaches, however, do not take into account the transverse flow, which can be important, and based on analyses using a transverse flow factor, as discussed in [2], often, it cannot be neglected. Moreover, although the Darcy's Law with appropriate modifications [5] can successfully replicate the flow features for random fibre mats as well as woven fibre mats, significant deviations from the Darcy's Law predictions were documented [6].

To overcome these shortcomings a state-of-the-art model for the flow [7] was developed, and it is based on the Navier-Stokes equations combined with the Brinkman-Forchheimer equations. In the present work, the above-mentioned model [7] is further enhanced by taking into consideration thermal effects. For this purpose a heat transfer submodel is built in. The cure process [8], which yields an exothermic reaction, is modeled, although in a somewhat simplified form, as a steady, uniform volumetric heat generation in the fluid. Control of this exothermic reaction is critical in what concerns the component's final structural integrity and quality. The heat dissipation is investigated in terms of a non-

Nomenclature

Da	Darcy number, ND	*y*	cartesian co-ordinate, m
F	Forchheimer coefficient, ND	*Greek symbols*	
H	channel height (reference dimension), m	α	thermal diffusivity, m^2s^{-1}
k	thermal conductivity, Wm^{-1}	α_1	viscosity ratio, ND
L	channel length, m	δ_{ij}	Kronecker delta, ND
m	mass flow rate, $kg.s^{-1}$	ΔT	temperature difference, K
n	unit normal vector, ND	ε	porosity, ND
p	pressure, $N.m^{-2}$	*K*	permeability, m^2
Pr	Prandtl number, ND	μ	dynamic viscosity, $kg.s^{-1}.m^{-1}$
q''	heat flux, Wm^{-2}	ν	kinematic viscosity, $m^2.s^{-1}$
$\dot{q}'''_g$	heat generation, Wm^{-3}	μ_B	Brinkman modified effective viscosity, $kg.s^{-}.m^{-1}$
R_c	ratio of thermal conductivities, ND	ρ	density, $kg.m^{-3}$
Re	Reynolds number, ND	σ	total stress, $N.m^{-2}$
t	unit tangent vector, ND	*Subscripts*	
T	temperature, K	*B*	Brinkman value
U	cartesian velocity component in the x-direction, $m.s^{-1}$	*ch*	channel
		f	"free" fluid domain
u	reference velocity, $m.s^{-1}$	*i*	interface
	y-direction, $m.s^{-1}$	*i,j*	cartesian subscripts ; tensorial notation
v	cartesian velocity component in the y-direction, $m.s^{-}$	*in*	inlet
		fd	free domain
V	volume, m^3	*pd*	porous domain
V	velocity vector, $m.s^{-1}$	*ref*	reference value
	* normalized variable	s	solid
x	cartesian co-ordinate, m	*	normalized variable

dimensional heat generation, Reynolds number, Darcy number, and the fluid and porous medium properties. The influence of the gap, and in particular its dimensions, upon the heat dissipation from the core region of the porous medium is also investigated.

The present model, in what concerns the flow modeling, as already mentioned, follows closely [7], and it can be succinctly described as follows: 1. The flow within the porous medium is governed by the Brinkman-Forchheimer model; 2. The Navier-Stokes equations are used in the modeling of the edge flow, i.e. the "free" medium. This approach, by combining the Navier-Stokes equations with the Brinkman-Forchheimer equations, avoids the well-known difficulties associated with linking the Navier-Stokes and the Darcy equations [9,10]; 3. At the "free"/porous medium interface, the only approximation required is to assume that the fluid fully supports the tangential and normal stresses; and 4. The cure is modeled by assuming a steady, uniform volumetric heat generation within the fluid. For the sake of completeness, an overview of the model's development is presented.

Physical and numerical modelling

Physical domain and geometry

The two-dimensional configuration under analysis is presented in Fig. 1. The fluid enters the mold cavity from the left, with a constant velocity, flows through the porous medium, (the shadowed region of Fig. 1) or through the top and right-hand side channels (edge flow), leaving the mold cavity through its right-hand side. In the exit region the outflow conditions are placed further downstream to reduce their influence upon the upstream flow. The flow and energy transfer are assumed to be steady and laminar. The fluid physical properties are taken as constant.

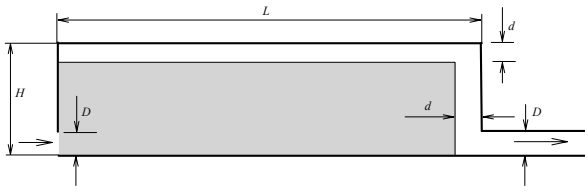

Figure 1. Domain and geometry (Dimensions: *H*=25mm; *L*/*H*=5; *D*/*H*=0.1).

Free fluid region

The flow in the open region is governed by the continuity and Navier-Stokes equations. Defining the dimensionless variables: $x_{*i} = x_i / H$, $u_{*i} = u_i / U$, $p_* = p / \left(\rho U^2 \right)$, and $Re = \rho UH / \mu$, the dimensionless version of the governing equations, using the indicial notation $\left(i, j = 1, 2 \right)$, becomes:

$$\frac{\partial}{\partial x_{*i}}\left(u_{*i}\right)=0 \tag{1}$$

$$\frac{\partial}{\partial x_{*i}}\left(u_{*i}u_{*j}\right)=-\frac{\partial p_*}{\partial x_{*j}}+\frac{\partial}{\partial x_{*i}}\left(\frac{1}{Re}\frac{\partial u_{*j}}{\partial x_{*i}}\right) \tag{2}$$

Taking the reference temperature difference as $\Delta T_{ref}=RePrU^2/c_P$, the Prandtl number, $Pr=\nu/\alpha$ and the dimensionless heat generation $\dot{q}'''_{g*}=\dot{q}'''_g H^2/\left(\rho\alpha U^2\right)$, the energy conservation equation in the open domain becomes:

$$\frac{\partial}{\partial x_{*i}}\left(u_{*i}T_*\right)=\frac{\partial}{\partial x_{*i}}\left(\frac{1}{RePr}\frac{\partial T_*}{\partial x_{*i}}\right)+\frac{\dot{q}'''_{*g}}{\left(RePr\right)^2} \tag{3}$$

Since the 'artificial' exit region was considered of small length it is assumed to be a region with no volumetric heat generation.

Fluid-saturated porous region

The dimensionless mass conservation equation in the porous medium is exactly the same as for the open fluid domain, (Eq. (1)). The fluid flow in the porous domain is governed by the Brinkman-Forchheimer equations, [11,12], that give, in dimensionless form:

$$\frac{\partial}{\partial x_{*i}}\left(\frac{1}{\varepsilon}u_{*i}u_{*j}\right)=-\frac{\partial p_*}{\partial x_{*j}}+\frac{\partial}{\partial x_{*i}}\left(\frac{\alpha_1}{Re\varepsilon}\frac{\partial u_{*j}}{\partial x_{*i}}\right)-\left(\frac{F\varepsilon}{\sqrt{Da}}\left|\mathbf{V}_*\right|+\frac{1}{ReDa}\right)u_{*j} \tag{4}$$

where ε is the permeability of the porous medium, $\alpha_1=\mu_B/\mu$ is the ratio between the Brinkman viscosity and the fluid viscosity, $F=1.75/\sqrt{150\varepsilon^5}$ is the Forchheimer coefficient, $Da=K/H^2$ is the Darcy number, and $|\mathbf{V}_*|$ is the modulus of the dimensionless velocity vector.

The thermal conductivity of the porous medium is given by the combination of the porous solid matrix and saturating fluid thermal conductivities. In this work it is used a geometric mean approach [12], given by $k=k_f^{\varepsilon}k_s^{(1-\varepsilon)}=k_f Rc^{(1-\varepsilon)}$, where Rc is the ratio of thermal conductivities, $Rc=k_s/k_f$. The dimensionless energy conservation equation in the porous domain is therefore given by:

$$\frac{\partial}{\partial x_{*i}}\left(u_{*i}T_*\right)=\frac{\partial}{\partial x_{*i}}\left(\frac{Rc^{(1-\varepsilon)}}{RePr}\frac{\partial T_*}{\partial x_{*i}}\right)+\frac{\dot{q}'''_{g*}\varepsilon}{\left(RePr\right)^2} \tag{5}$$

In the porous domain, only the volume fraction ε is filled with liquid, where heat is being generated.

Interface

At the interface of the fluid-saturated porous and open domains, mass, momentum, and energy balances must be satisfied as discussed in [10]. It is assumed here that there are no phase change phenomena or chemical reactions, and local thermodynamic equilibrium prevails. Mass conservation at each point of the interface implies that, in dimensionless form,

$$\left(\mathbf{V}_*.\mathbf{n}_*\right)_{fd}=\left(\mathbf{V}_*.\mathbf{n}_*\right)_{pd} \tag{6}$$

where the subscripts *fd* and *pd* indicate free domain and porous domain values, respectively, and $\mathbf{n}_*$ is a unit vector normal to the interface.

Taking the dimensionless stress

$$\sigma_{*ij}=\left(1/Re\right)\left(\partial u_{*i}/\partial x_{*j}+\partial u_{*j}/\partial x_{*i}\right)-p_*\delta_{ij},$$

the continuity of the normal and shear stresses is

$$\begin{aligned}\left(\mathbf{n}_*.\mathbf{n}_*.\boldsymbol{\sigma}_*\right)_{fd}&=\left(\mathbf{n}_*.\mathbf{n}_*.\boldsymbol{\sigma}_*\right)_{pd}\\ \left(\mathbf{t}_*.\mathbf{n}_*.\boldsymbol{\sigma}_*\right)_{fd}&=\left(\mathbf{t}_*.\mathbf{n}_*.\boldsymbol{\sigma}_*\right)_{pd}\end{aligned} \tag{7}$$

$\mathbf{t}_*$ being the dimensionless unit vector tangent to the interface. In addition, it is assumed that the pressure is continuous across the interface, that is,

$$\left(p_*\right)_{fd}=\left(p_*\right)_{pd} \tag{8}$$

The mass conservation equation, Eq. (6), requires equal normal velocities on both open- and porous-domain sides. The *essential* velocity continuity condition at the interface [13], however, implies:

$$\left(\mathbf{V}_*\right)_{fd}=\left(\mathbf{V}_*\right)_{pd} \tag{9}$$

Equation (7) requires that, at the interface, the viscous part of the total normal stress and the shear stress are supported only by the fluid contained in the porous medium. An approach, which has been used in previous work dealing with the Brinkman-Forchheimer model, [13,14].

In what concerns heat transfer, thermodynamic equilibrium at the interface imposes that

$$\left(T_*\right)_{fd}=\left(T_*\right)_{pd} \tag{10}$$

and the energy balance at the interface gives

$$\left(\mathbf{n}_*.\dot{\mathbf{q}}_*{}''\right)_{fd}=\left(\mathbf{n}_*.\dot{\mathbf{q}}_*{}''\right)_{pd} \tag{11}$$

where the total energy flux is defined as

$$\begin{aligned}\left(q''_{*i}\right)_{fd}&=u_{*i}T_*-\frac{1}{RePr}\frac{\partial T_*}{\partial x_{*i}}\\ \left(q''_{*i}\right)_{pd}&=u_{*i}T_*-\frac{Rc^{(1-\varepsilon)}}{RePr}\frac{\partial T_*}{\partial x_{*i}}\end{aligned} \tag{12}$$

Numerical modelling

The physical model is solved using a two-dimensional laminar version of the control-volume finite element method (CVFEM) described in [15]. Similar procedure is followed for the discretization of the Brinkman-Forchheimer equations, with the source terms described by the terms multiplying u_{*j} in Eq. (4).

The calculation domain, as fully reported in [10], is first discretized into three-node triangular elements. The nodes of this finite element mesh are the vertices of the triangular elements. The grid is designed so that there is a line of nodes along the entire interface between the

open and the fluid-saturated porous domains. The discretization of the calculation domain yields polygonal control volumes surrounding the nodes in the finite element mesh. Part of the resulting finite element mesh, and a polygonal control volume surrounding a node on the interface (*P*) are illustrated in Fig. 1.

The thermophysical properties are stored at the centroid of each element and assumed to prevail over the respective element. In this work, these properties include mass density, dynamic viscosity, specific heat, and thermal conductivity of the fluid in the open domain, and Brinkman (or effective) dynamic viscosity, effective thermal conductivity, porosity, and permeability in the fluid-saturated porous medium. All dependent variables are stored at the same nodes in the finite element mesh, leading to a co-located formulation [15,16].

The momentum equations in the free and porous domains are integrated over each of the polygonal control volumes. Then, each of these integro-differential equations is approximated by a discretized equation that connects the dependent variables at each node in the finite element mesh to those at its immediate neighboring nodes. In the derivation of algebraic approximations to the various terms in the integro-differential equations, the dependent variables are interpolated over each element by similar interpolation functions, giving rise to an equal-order CVFEM. In the approximation of advection transport terms, the advected dependent variables are interpolated by flow-oriented exponential upwind functions in each element, and linear interpolations of the dependent variables are used to approximate the viscous or diffusion transport terms. The pressure is interpolated linearly in each element. The velocity components that are involved in the mass flux terms are interpolated using the so-called momentum interpolation scheme [17]. Full details of the formulation steps are available in [10]. The temperature field is calculated based on the discretized form of Eqs. 3 and 5, and using the converged velocity field.

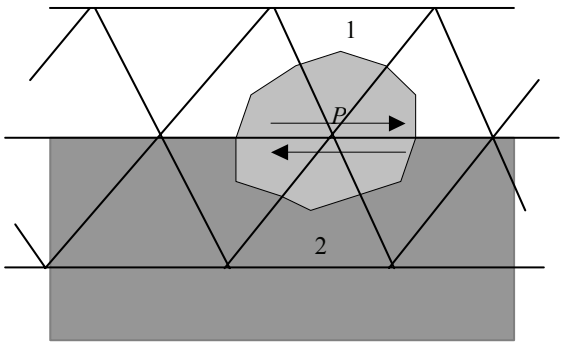

Figure 2. Control volume associated with a node *P* located on the interface between adjacent free (1) and fluid-saturated porous (2) regions of the calculation domain.

The overall iterative solution procedure can be summarized, at each iteration level, as follows: (*i*) based on guessed or latest available values of the velocity components, density, and viscosity, the discretized equations for the velocity components are constructed, except for contributions of the pressure-gradient terms, and the appropriate boundary conditions are introduced by manipulation of the coefficients and constants of these equations; (*ii*) pseudo-velocities and pressure coefficients are evaluated at each node; (*iii*) discretized equations for the pressure are obtained, and pressure or mass flow boundary conditions are introduced in the coefficients of such equations; (*iv*) a new pressure field is calculated; (*v*) the terms corresponding to the pressure gradient are introduced into the discretized momentum equations, based on the newly calculated pressure field, and the new velocity field is evaluated. This sequential procedure is repeated until suitable convergence criteria are satisfied. Then, the energy equations, Eqs. 3 and 5, in discretized form, and combined with the converged velocity field are solved iteratively. In this work, only structured grids with a line-by-line arrangement of the nodes were used. The discretized equations were solved using a simple line-Gauss Seidel iterative procedure, with a block correction algorithm, as a convergence accelerator. Detailed description of the overall iterative solution procedure can be found in [10,15]. This solution procedure was considered to have converged when the maximum normalized residues in the discretized momentum and pressure equations, and discretized energy equations were all less than 10^{-6}.

Model justification and testing

In this section is reported a very small sample of the extensive testing to which the model was subjected, and which is reported in some detail in [7,10].

Transverse flow

As already mentioned, models for edge flows based on the Darcy Law, which are formulated using an analytical formulation for the interface [1,2,3], or an equivalent permeability for the edge [1,2,4] do not take into account transverse flow. Close observation of the flow along the gap of width "d" (Fig. 1), reveals the strong influence of the transverse flow, which is depicted in Fig. 3, where the velocity vectors for the flow within the gap are shown.

Figure 3 is nearly self-explanatory; Fig. 3(a) clearly denotes a flow that resembles plane Poiseuille flow, however, Figs. 3(b) and (c) present flow complexities, which are well beyond the capability of the Darcy Law – based models already discussed [1,2,3,4].

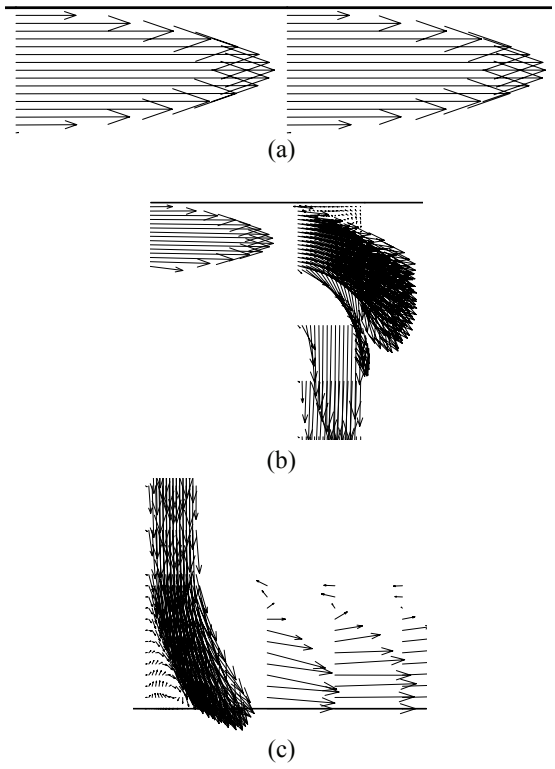

Figure 3. Vectorial form of the velocity within the gap for the two-channel configuration (ε = 0.7, Re = 10^{-1}, Da = 10^{-6}) in three different regions, namely: a) Halfway the top channel; b) Bend between the top and RHS channel, and c) Outlet.

Isothermal testing

Flow through a plane channel with a porous plug is selected as an illustrative example. This problem involves flow through a parallel-plate channel with a porous plug, as shown schematically in Fig. 4, under an imposed overall pressure drop. For distances sufficiently far from the porous plug, the flow is fully developed. In the vicinity of the porous plug, the flow is not fully developed. Nevertheless, in this case, the fluid flows in a direction that is essentially normal to the interfaces between the open and fluid-saturated porous domains. As in the problem presented in the preceding subsection, the governing dimensionless parameters are the Reynolds number based on the mean velocity, $Re = \rho \bar{u} H / \mu$, the Darcy number for the porous domain, $Da = K / H^2$, the porosity of the porous domain, ε, and the viscosity ratio, $\alpha_1 = \mu_B / \mu$.

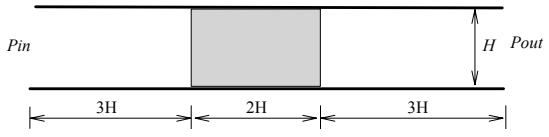

Figure 4. Geometry and computational domain for the plane channel with a porous plug.

It is assumed that at distances of 3H upstream and downstream of the porous plug, the y-direction component of velocity, v, is zero and a cyclic boundary condition [10] can be applied to u, the streamwise component of the velocity. At the center of the porous plug, an essentially plug flow is expected if the permeability is low. The domain dimensions, a fixed value of the streamwise overall pressure drop ($\Delta p = 1.0$ N/m^2), the Darcy number, a fixed value of porosity ($\varepsilon = 0.7$), and the viscosity ratio were imposed, and the properties ρ and μ were adjusted in order to obtain the desired Reynolds number, which is $Re = 1$ for all the results presented for this problem.

Preliminary numerical tests of the asymptotic type have shown that a $(21+21+21)\times 21$ mesh, with a geometrically increasing node density towards the interfaces between the free and porous domains interfaces, in the streamwise direction, with a factor of 1.2, and a uniform node distribution in the y direction, gives essentially grid independent results.

Results for $Da = 10^{-2}$ and $\alpha_1 = 1$ are presented in Fig. 5a where, on the left-hand side, is presented the centerline u velocity dependence on the streamwise dimensionless coordinate x/H, and on the right-hand side is presented the centerline pressure dependence on x/H. It is observed in Fig. 5a that the velocity field changes markedly due to the presence of the porous plug, this change being examined in this work via the variation of the u velocity along the centerline. On the left-hand and right-hand boundaries of the open domains, the u velocity variation in the y direction is essentially parabolic, and in the central region of the porous plug, this profile adjusts to be more flat (nearly a plug flow profile), with a lower centerline u velocity within the porous domain. The flow field is almost one-dimensional over most of the open and porous domains, but it is two-dimensional in the vicinity of the interfaces between the open and porous domains, where adjustments of the velocity field occur. In this case, as already mentioned, this adjustment occurs in a thin region, the extent of which scales as $\delta/H \sim \sqrt{Da} = 10^{-1}$. From the right-hand side of Fig. 5a it is observed that the centerline pressure presents distinct behaviors in the free and porous regions, with an essentially linearly decreasing profile in each, but with greater slope in the porous region, as expected. These results are in good qualitative agreement with the corresponding results in the literature.

For Da = 10^{-3} and $\alpha_1 = 1$, the results are presented in Fig. 5b. In this case, it is observed that marked changes in the centerline u velocity occur in a narrower region than that for Da = 10^{-2} and $\alpha_1 = 1$, as now, $\delta/H \sim \sqrt{Da} = 10^{-3/2}$. Also, in this problem, a lower Darcy number corresponds to lower permeability, thus the global pressure drop occurs almost fully in the porous domain, as illustrated by the right-hand side of Fig. 5b.

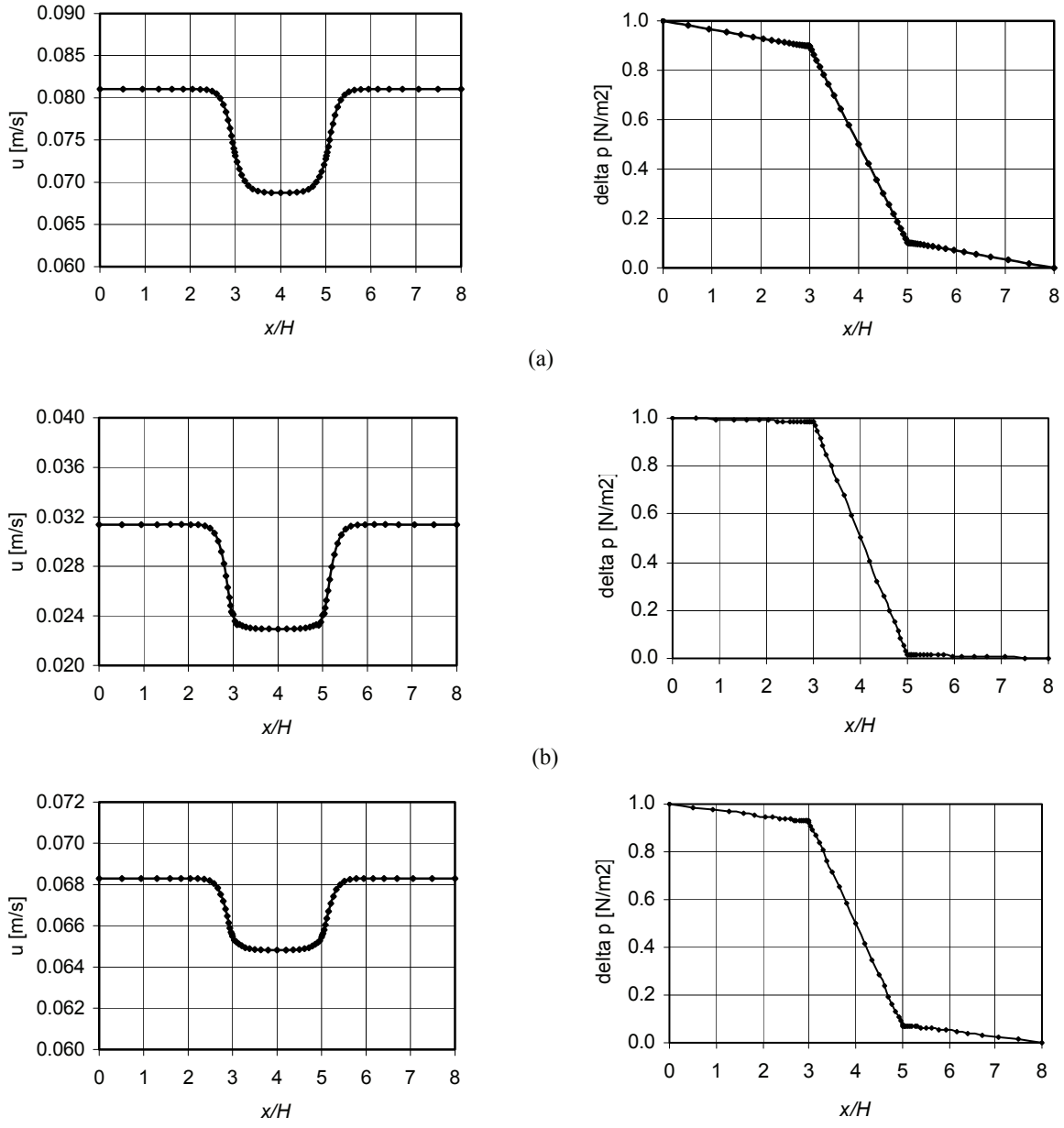

Figure 5. Centerline u velocity (left) and pressure (right) for Δp=1.0 N/m^2, ε=0.7 and Re=1 for (a) Da=10^{-2} and α=1; (b) Da=10^{-3} and α=1; and (c) Da=10^{-2} and α=5.

Results for the same conditions as those considered previously (Fig. 5a), but with $\alpha_1 = 5$, are presented in Fig. 5c. As the effective viscosity is now higher within the porous domain, the centerline u velocity presents a flatter profile than in Fig. 5a, and an increase in the pressure drop over the porous domain is observed.

Results and discussion

Numerical simulations were conducted using a non-uniform structured grid with 81 columns of nodes in the x direction and 55 rows of nodes in the y direction, with 17 rows of nodes in the channel region (of width d), and 13 rows of nodes in the inlet and outlet zones (of width D). The selection of this grid is determined on the basis of extensive grid convergence testing [18].

The results were obtained for the geometry presented in Fig. 1, considering $L/H = 5$, $D/H = 0.1$, $\varepsilon = 0.54$, $\alpha = 1$, $Rc = 100$, and $\dot{q}'''_{g*} = 10^9$. The remaining governing dimensionless parameters were subjected to change in order to observe their influence on the resulting flow and temperature distributions.

The first analysis that should be undertaken is related with the gap width. From Figs. 6 and 7, it can clearly be

observed that a change from $d/H = 0.04$ to $d/H = 0.02$, (i.e. a decrease of 0.02 in the dimensionless mold cavity clearance), results in substantial alterations in what concerns the flow through the porous medium. Figure 6 clearly shows a preferential flow through the top and right hand side channels in detriment of the flow through the porous medium, whereas in Fig. 7 it can be observed that a decrease in the clearance width minimizes the edge flow, yielding an increase of the flow through the porous medium. A pressure fall can be observed near the inlet region for $d/H = 0.04$ whereas, for $d/H = 0.02$, the pressure is more uniformly distributed along the bed. In what concerns the global dimensionless pressure difference, it can be observed that this parameter is considerably higher for the smaller gap (i.e. for $d/H = 0.02$ and $(\Delta p_* = 3.1\times10^5)$ for $d/H = 0.04$. In terms of temperature fields, the larger gap leads to a larger region subjected to high temperatures in the vicinity of the mold exit. Furthermore, the maximum global dimensionless temperature difference is considerably higher for the larger gap (i.e. $\Delta T_* = 3.5\times10^4$ for $d/H = 0.04$, and $\Delta T_* = 1.9\times10^4$ for $d/H = 0.02$).

The influence of Darcy number is also relevant, as expected. When comparing the results shown in Figs. 6 and 8 for $Da = 10^{-6}$ and $Da = 10^{-8}$, respectively, representing the permeability variation of the porous medium, it can be noted the emphasis on the preferential flow through the gap towards the exit (i.e. greater contribution to the edge flow effect). In this case, the main pressure decrease occurs closer to the inlet region, with the global dimensionless pressure difference assuming a value of $\Delta p_* = 2.4\times10^7$. As the interior of the porous medium remains essentially without flow, the hot region increases both in area and temperature level, where the global dimensionless temperature difference becomes $\Delta T_* = 4.8\times10^4$.

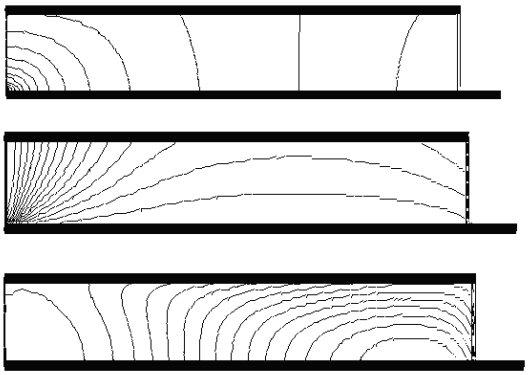

Figure 6. Dimensionless streamlines, isobars and isotherms for $d/H = 0.04$, $Da = 10^{-6}$, $Re = 1$ and $Pr = 1000$.

The influence of the Reynolds number was studied for *Re*=1 and *Re*=0.1 with *d/H*=0.04, $Da=10^{-6}$, and *Pr*=1000. Both figures present similar behavior in what concerns the flow field (isobars and streamlines), however the global dimensionless pressure difference is considerably higher for *Re*=0.1 than for *Re*=1, and is equal to $\Delta p_* = 3.1\times10^6$.

The isotherms do not exhibit a hot spot and the temperature rise is quite uniform along the bed. However, a lower Reynolds number leads to higher temperatures, with the maximum global dimensionless temperature difference reaching a value of $\Delta T_* = 2.2\times10^6$.

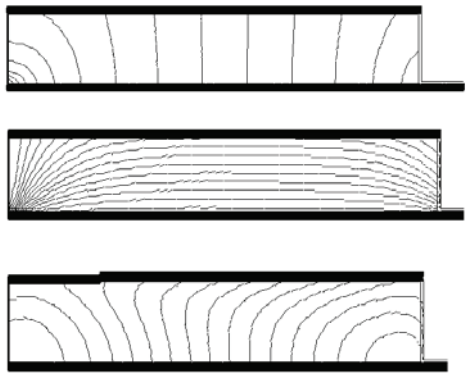

Figure 7. Dimensionless streamlines, isobars and isotherms for $d/H = 0.02$, $Da = 10^{-6}$, $Re = 1$ and $Pr = 1000$.

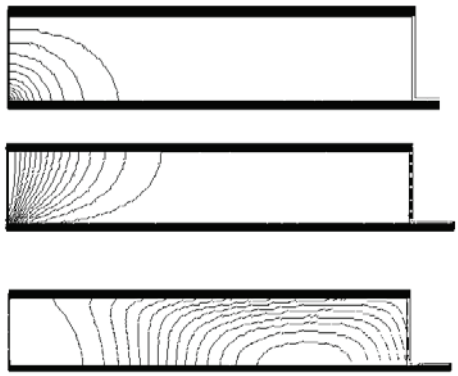

Figure 8. Dimensionless streamlines, isobars and isotherms for *d/H*=0.04, $Da = 10^{-8}$, $Re = 1$ and $Pr = 1000$.

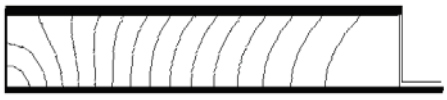

Figure 9. Dimensionless isotherms for $d/H = 0.04$, $Da = 10^{-6}$, $Re = 0.1$ and $Pr = 1000$.

In what concerns Prandtl number, it should be noted from Fig. 10, that a rise of this parameter to 10000 from 1000 (Fig. 6) infers a significant fall on the temperature level along the interface i.e $\Delta T_* = 565$ vs. $\Delta T_* = 3.5\times10^4$. The combination of higher Prandtl number with lower Reynolds number (Fig. 11), where the fluid assumes, as compared to the situation depicted in Fig. 6, a greater heat removal capability and lower mass flow rate, respectively, becomes evident from the isotherms, where $\Delta T_* = 3.5\times10^4$.

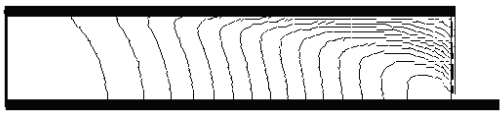

Figure 10. Dimensionless isotherms for $d/H = 0.04$, $Da = 10^{-6}$, $Re = 1$ and $Pr = 10000$.

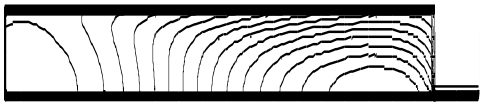

Figure 11. Dimensionless isotherms for $d/H = 0.04$, $Da = 10^{-6}$, $Re = 0.1$ and $Pr = 10000$.

Conclusion

The present work reviews a detailed physical model for situations involving fluid flow and heat transfer in fluid domains partially filled with a porous medium. Special attention was given to the boundary conditions at the interface between the open and porous domains, and to the situations of steady volumetric heat generation. In addition, the physical justification for the model is reported along with an illustrative testing example. The results were obtained for a set of governing dimensionless parameters relevant to the LCM processes. The analysis of the results highlights the influence of the gap width over the flow and thermal fields. In what concerns the thermal field, the temperature distribution is highly affected by the range of the governing parameters. It was found that large regions in the mold are susceptible to become subjected to deficient wetting and poor heat removal capability due to building up of high temperature levels within the component. The predictions identify conditions that may lead to the production of components of inferior quality, which, in extreme cases, have to be rejected.

Acknowledgement

The author acknowledges the finanical support received for this work from FCT (Portugal) – Project POCTI/EME/36263/2000, and NSERC (Canada) – Discovery Grant 12875 (ACMS). The valuable and numerous contributions to this research project made by Profs. V.A.F. Costa and M.S.A. Oliveira (U. Aveiro), Prof. L.A. Oliveira (U. Coimbra), and Prof. B.R. Baliga (McGill U.) are also acknowledged

References

[1] S. Bickerton, S.G. Advani, Characterization and modeling of race-tracking in liquid composite molding processes, Composites Science and Technology 59 (1999) 2215-2229.

[2] A. Hammami, R. Gauvin, F. Trochu, Modeling the edge effect in liquid composites molding, Composites: Part A, 29A (1998) 603-609.

[3] G.S. Beavers, D.D. Joseph, Boundary conditions at a naturally permeable wall, J. Fluid Mech., 30 (1967) 197-207.

[4] W.-B. Young, C.-L. Lai, Analysis of the edge effect in resin transfer molding, Composites, 28A (1997) 817-822.

[5] K.M. Pillai, Governing equations for unsaturated flow through woven fiber mats. Part 1. Isothermal flows, Composites, 33A (2002) 1007-1019.

[6] S. Bickerton, E.M. Sozer, P. Simácek, S.G. Advani, Fabric structure and mold curvature effects on preform permeability and mold filling in the RTM process. Part II. Predictions and comparisons with experiments, Composites: 31A (2000) 439-458.

[7] V.A.F. Costa, M.S.A. Oliveira, A.C.M. Sousa, Numerical simulation of non-Darcian flows through spaces partially filled with a porous medium, in: A.A. Mohamad (Ed.), Proc., The 3rd Intal. Conference on Computational Heat and Mass Transfer, U. of Calgary Press, Calgary, Canada, 2003, pp. 135-143.

[8] V.A.F. Costa, A.C.M. Sousa, Modeling of Flow and Thermo-Kinetics During the Cure of Thick Laminated Composites, International Journal of Thermal Sciences, 42 (1) (2003) 15-22.

[9] M.K. Alkam, M.A. Al-Nimr, Transient Non-Darcian Forced Convection Flow in a Pipe Partially Filled with a Porous Material, Int. J. Heat Mass Transfer, 41 (1998) 347-356.

[10] V.A.F. Costa, L.A. Oliveira, B.R. Baliga, A.C.M. Sousa, Numerical simulation of coupled viscous flows in adjacent porous and open domains using a control volume finite element method (accepted for publication in Numerical Heat Transfer, Nov., 2003).

[11] M. Kaviany, Principles of Heat Transfer in Porous Media, Springer Verlag, New York, 1991.

[12] D. A. Nield, A. Bejan, Convection in Porous Media, 2nd. Ed., Springer Verlag, New York, 1999.

[13] D. K. Gartling, C. E. Hickox, R. C. Givler, Simulation of coupled viscous and porous flow problems, Comp. Fluid Dynamics, **7**, (1996) 23-48.

[14] A. G. Salinger, R. Aris, J. J. Derby, Finite element formulations for large-scale, coupled flows in adjacent porous and open fluid domains, Int. J. for Num. Methods in Fluids, 18, (1994) 1185-1209.

[15] V.A.F. Costa, L.A. Oliveira, A.R. Figueiredo, A Control Volume Based Finite Element Method for Three-Dimensional Incompressible Turbulent Fluid Flow, Heat Transfer, and Related Phenomena, International Journal for Numerical Methods in Fluids, 21 (1995) 591-615.

[16] B.R. Baliga, Control-volume finite element methods for fluid flow and heat transfer, in: W.J. Minkowycz, E.M. Sparrow (Eds.), Advances in Numerical Heat Transfer, vol. 1, Chapter 3, 1997, pp. 97-135.

[17] C. Prakash, S.V. Patankar, A control-volume-based finite-element method for solving the Navier-Stokes equations using equal-order velocity-pressure interpolation, Num. Heat Transfer, 8 (1985) 259-280.

[18] V.A.F. Costa, M.S.A. Oliveira, A.C.M. Sousa, Numerical evaluation of heat dissipation by non-Darcian forced convection in porous/fluid systems, Heat Transfer VIII, Adv. Computational Methods, B. Sundén et al. (Eds.), Southampton, U.K., 2004, 99-108. (Invited Contribution)

Strojniški vestnik - Journal of Mechanical Engineering 51(2005)7-8, 527-533
UDK - UDC 536.2
Izvirni znanstveni članek - Original scientific paper (1.01)

THE GALERKIN METHOD SOLUTION OF THE CONJUGATE HEAT TRANSFER PROBLEMS FOR THE CROSS-FLOW CONDITIONS

Andrej Horvat
ANSYS CFX
Harwell International Business Centre
Fermi Avenue
Didcot, Oxfordshire, OX11 0QR
United Kingdom

Borut Mavko
Reactor Engineering Division
"Jožef Stefan" Institute
Jamova 39
Ljubljana, SI-1001
Slovenia

Ivan Catton
Mechanical and Aerospace Engineering Department
The Henry Samueli School of Engineering and Applied Science
University of California, Los Angeles
Los Angeles, California, 90095-1597
United States of America

ABSTRACT

A conjugate heat transfer model of fluid flow across a solid heat conducting structure has been built. Two examples are presented: a.) air-stream cooling of the solid structure and b.) flow across rods with volumetric heat generation. To construct the model, a Volume Average Technique (VAT) has been applied to the momentum and the energy transport equations for a fluid and a solid phase to develop a specific form of porous media flow equations. The model equations have been solved with the semi-analytical Galerkin method.

The detailed velocity and temperature fields in the fluid flow and the solid structure have been obtained. Using the solution fields, the whole-section drag coefficient C_d and the whole-section Nusselt number Nu have been also calculated. To validate the developed solution procedure, the results have been compared to the results of the finite volume method and to the experimental data. The comparison demonstrates an excellent agreement.

INTRODUCTION

Heat transfer conditions in a heat exchanger are a well known and extensively studied subject. Also, today available computational power gives us an opportunity to build increasingly detailed physical models of heat transfer processes. Nevertheless, direct computations of whole heat exchanger installations are at present still far from an everyday engineering practice. In order to resolve most of the flow features and at the same time keep the model simple enough to serve as an engineering tool, averaging of fluid and heat flow variables has to be performed.

A Volume Averaging Technique (VAT) has been developing from the 1960s and it has been applied to a number of different fluid dynamics and heat transfer problems. Recently, it has been applied to model processes in heat exchangers and heat sinks (Hu, 2001, Horvat & Catton, 2001 & 2003). Using VAT, the transport processes in a heat exchanger are modeled as porous media flow (Travkin & Catton, 1999). This generalization allows us to unify the heat transfer calculation techniques for different kinds of heat exchangers and their structures. The case-specific geometrical arrangements, material properties and fluid flow conditions enter the computational algorithm only as a series of precalculated coefficients. The clear separation between the model and the case-specific coefficients simplifies the model and speeds up calculations.

In most cases, the developed set of VAT equations has been solved with the finite difference or the finite volume method. Lately, efforts have been made to obtain the solution also by the Galerkin method (Horvat & Catton, 2003).

The Galerkin method is a semi-analytical method, where a solution field is anticipated to be a series of orthogonal functions. As the solution depends only on a number of orthogonal functions and not on a number of grid nodes, highly accurate solutions can be obtained. In the present paper, two applications of the Galerkin method are given. In the first case, we present a closed-form solution for the conjugate heat transfer problem of air-stream cooling of a solid structure. In the second case, a solution for water flow across rods with volumetric heat generation is given. Although the Galerkin method has limited applicability in complex geometries, its highly accurate solutions are an important benchmark on which other numerical results can be tested. Further, the VAT formulation lends itself to the Galerkin method because most of the geometric complexity is absorbed into the closure relationships.

GEOMETRY LAYOUT

For both cases (i.e. the air-stream cooling of the solid structure and the flow across rods with volumetric heat generation), a similar geometry has been used (Fig. 1).

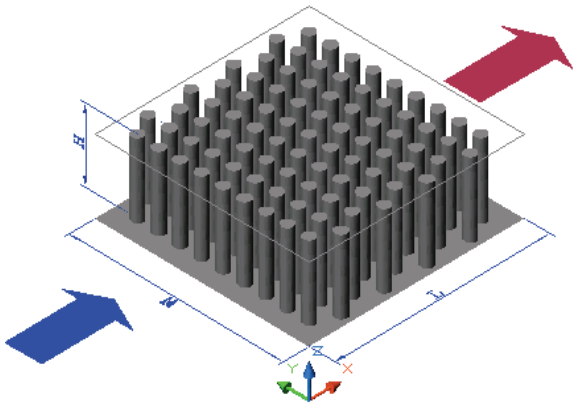

Figure 1: General geometrical layout

A cold stream of fluid enters from the left and is heated by the solid structure as it passes the test section. The flow is bounded at the bottom by an isothermal wall, where no-slip boundary conditions are prescribed. At the top, the flow is considered open. The details on boundary conditions for each specific case will be given later.

In the first case, the length L as well as the width W of the aluminum solid structure are 11.43 cm, whereas the height H is 3.81 cm. The simulation domain consists of 31 rows of pin-fins in the streamwise direction and 31 rows of pin-fins in the transverse direction. The diameter of the pin-fins d is 0.3175 cm. A pitch-to-diameter ratio in the streamwise direction p_x/d is set to 1.06 and in the transverse direction p_y/d is 2.12.

In the second case, the aluminum rods with internal heat generation rate I have a diameter d of 0.9525 cm. Their height is 20 cm. They are arranged in 64 rows in the streamwise direction and in 16 rows in the transverse direction. In the streamwise direction, a pitch-to-diameter ratio p_x/d is 1.0 and in the transverse direction p_y/d is 2.0. At the bottom, the rods are attached to an isothermal plate that is 60.96 cm long and 30.48 cm width.

In both cases, the entering flow profile is assumed to be fully developed.

MATHEMATICAL MODEL

Flow across a solid structure can be described with basic mass, momentum and heat transport equations (Horvat, 2002). In order to develop a unified approach for different geometries and material properties, the transport equations are averaged over a representative elementary volume (Fig. 2).

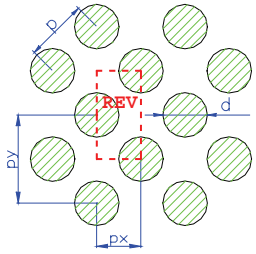

Figure 2: Representative elementary volume

This volume averaging leads to a closure problem where interface exchange of momentum and heat between a fluid and a solid has to be described with additional empirical relations e.g. a local drag coefficient f and a local heat transfer coefficient h. Reliable data for the local drag coefficient f and the heat transfer coefficient h have been found in Launder & Massey (1978), Žukauskas & Ulinskas (1985), and Kays & London (1998).

In both cases, the simulated system has been further simplified by assuming flow with a dominating streamwise velocity component and a constant pressure drop across the structure. As a consequence, the velocity changes only vertically in the z-direction. This means that the streamwise pressure gradient across the entire simulation domain is balanced with the hydrodynamic resistance of the structure and with the shear stress. Thus, the momentum equation can be written in the differential form as

$$-\alpha_f \hat{\mu}_f \frac{\partial^2 \hat{u}}{\partial \hat{z}^2} + \frac{1}{2} f \hat{\rho}_f \hat{u}^2 \hat{S} = \frac{\Delta \hat{p}}{\hat{L}} \quad . \tag{1}$$

The energy transport equation for the fluid flow has also been developed using the unidirectional velocity assumption. The temperature field in the fluid results from the balance between thermal convection in the streamwise direction, thermal diffusion and the heat transferred from the solid structure to the fluid flow:

$$\alpha_f \hat{\rho}_f \hat{c}_f \hat{u} \frac{\partial \hat{T}_f}{\partial \hat{x}} = \alpha_f \hat{\lambda}_f \frac{\partial^2 \hat{T}_f}{\partial \hat{z}^2} - \hat{h}\left(\hat{T}_f - \hat{T}_s\right)\hat{S} \quad . \tag{2}$$

The rod bundle structure in each REV is not connected in the horizontal directions (see Fig. 1). As a consequence, only the internal heat generation I and the thermal diffusion in the vertical direction are in balance with the heat leaving the structure through the fluid-solid interface. The thermal diffusion in the horizontal directions can be neglected. This simplifies the energy equation for the solid structure to:

$$0 = \alpha_s \hat{\lambda}_s \frac{\partial^2 \hat{T}_s}{\partial \hat{z}^2} + \hat{h}\left(\hat{T}_f - \hat{T}_s\right)\hat{S} + \alpha_s \hat{I} \, . \tag{3}$$

In the case of the air-stream cooling of the solid structure, the last term is zero as there is no volumetric heat generation in the solid structure.

Boundary conditions for the set of equations (1-3) are given below

$$\begin{aligned} &\hat{x} = 0: \quad \hat{T}_f = \hat{T}_{in} \, , \\ &\hat{z} = 0: \quad \hat{u} = 0 \, , \quad \hat{T}_f = \hat{T}_g \, , \quad \hat{T}_s = \hat{T}_g \, , \\ &\hat{z} = \hat{H}: \quad \hat{u} = 0 \, , \quad \frac{\partial \hat{T}_f}{\partial \hat{z}} = 0 \, , \quad \frac{\partial \hat{T}_s}{\partial \hat{z}} = 0 \, , \end{aligned} \tag{4}$$

and are valid for both cases.

SOLUTION METHOD

To construct the solution method, the transport equations (1-3) have been scaled and converted into a dimensionless form:

$$-M_2 \frac{\partial^2 u}{\partial z^2} + M_3 u^2 = M_4 \, , \tag{5}$$

$$F_1 u \frac{\partial T_f}{\partial x} = F_4 \frac{\partial^2 T_f}{\partial z^2} - F_5 \left(T_f - T_s\right) \, , \tag{6}$$

$$0 = S_1 \frac{\partial^2 T_s}{\partial z^2} + S_2 \left(T_f - T_s\right) - S_3 \, , \tag{7}$$

where M_2, M_3, M_4, F_1, F_4, F_5, S_1, S_2 and S_3 are constants. In the same way, the boundary conditions (4) have been transformed to

$$\begin{aligned} &x = 0: \quad T_f = 1 \, , \\ &z = 0: \quad u = 0 \, , \quad T_f = 0 \, , \quad T_s = 0 \, , \\ &z = 1: \quad u = 0 \, , \quad \frac{\partial T_f}{\partial z} = 0 \, , \quad \frac{\partial T_s}{\partial z} = 0 \, . \end{aligned} \tag{8}$$

The momentum equation (5) has the same form and the same boundary conditions in both cases. To obtain its solution, the momentum equation has been linearized to:

$$-M_2\frac{\partial^2 u}{\partial z^2}+Ku=M_4\,, \tag{9}$$

where $K= M_3|u|$. Taking into account the boundary conditions (8), the solution of Eq. (9) is:

$$u=G_1 exp(\varepsilon z)+G_2 exp(-\varepsilon z)+G_3\,. \tag{10}$$

The solution has the same form in both cases with different values of the constants ε, G_1, G_2 and G_3.

Although the principles of the Galerkin method are the same for both cases, the differences in the solution procedure for the energy equations (6 & 7) require a separate treatment for each case.

Air-Stream Cooling of the Solid Structure

To find a solution to the conjugate problem, both equations (6 & 7) are combined into a single expression for the solid phase temperature T_s :

$$D_1 u\frac{\partial T_s}{\partial x}+D_2\frac{\partial^4 T_s}{\partial z^4}-D_3\frac{\partial^2 T_s}{\partial z^2}-D_4 u\frac{\partial^3 T_s}{\partial x\partial z^2}=0\,, \tag{11}$$

where D_1, D_2, D_3 and D_4 are constants. Further, separation of variables is used:

$$T_s=X(x)Z(z)\,. \tag{12}$$

where the solution in the *z*-direction is anticipated in the form of a series:

$$Z=A_k Z_k\,,\ Z_k=\sin(\gamma_k z)\,,\ \gamma_k=\frac{2k-1}{2}\pi\,,\ k=1,n\,, \tag{13}$$

to satisfy the boundary conditions (8). Introducing (13) into (11) and regrouping the expression, we can write

$$X' A_k u\left\{D_1+\gamma_k^2 D_4\right\}Z_k+XA_k\left\{\gamma_k^4 D_2+\gamma_k^2 D_3\right\}Z_k=error\,. \tag{14}$$

As the series is finite, there is a certain discrepancy associated with the series expansion (14). This error is orthogonal to the set of functions used for the expansion and can be reduced by multiplying the equation (14) with Z_j (j = 1,n) and integrating it from 0 to 1:

$$X' A_k\int_0^1 u\left\{D_1+\gamma_k^2 D_4\right\}Z_k Z_j\,dz+XA_k\int_0^1\left\{\gamma_k^4 D_2+\gamma_k^2 D_3\right\}Z_k Z_j\,dz=0\,. \tag{15}$$

In a matrix form, Eq. (15) is written as

$$X' A_k J_{kj}^{(1)}+X\,A_k J_{kj}^{(2)}=0\,, \tag{16}$$

where $J_{kj}^{(1)}$ and $J_{kj}^{(1)}$ are integrals that are calculated analytically. As the *x* and *z* dependent parts of Eq. (16) can be separated:

$$\beta=-\frac{X'}{X}=\frac{A_k J_{kj}^{(2)}}{A_k J_{kj}^{(1)}}\,, \tag{17}$$

separate equations are written for the *x*-direction:

$$X'+\beta X=0\,, \tag{18}$$

and for the *z*-direction:

$$\left(J_{kj}^{(2)}-\beta J_{kj}^{(1)}\right)A_k=0\,. \tag{19}$$

The solution of Eq. (18) is obtained by integration:

$$X=C\exp(-\beta x)\,, \tag{20}$$

where C and β are arbitrary constants.

Equation (19) is an extended eigenvalue problem that has non-trivial solutions if

$$Det\left(J_{kj}^{(2)}-\beta J_{kj}^{(1)}\right)=0\,. \tag{21}$$

From the condition (21), a set of n eigenvalues β are determined. Furthermore, each eigenvalue β_j (j=1,n) corresponds to a specific j eigenvector A_k that is also calculated.

Using the solutions of Eq. (18) and of the matrix system (21), one can construct the temperature field for the solid phase :

$$T_s=C_j X_j A_{jk} Z_k\,, \tag{22}$$

and for the fluid phase:

$$T_f=C_j A_{jk}\left(1+\frac{S_1}{S_2}\gamma_k^2\right)Z_k\,, \tag{23}$$

where C_j is a vector of coefficients that is found from the boundary condition $T_f(0, z)$ = 1. Applying it to Eq. (23), one can write:

$$C_j A_{jk}\left(1+\frac{S_1}{S_2}\gamma_k^2\right)Z_k=1\,. \tag{24}$$

Again, multiplying Eq. (24) by Z_i (i=1,n) and integrating it from 0 to 1:

$$C_j A_{jk}\left(1+\frac{S_1}{S_2}\gamma_k^2\right)\int_0^1 Z_k Z_i dz=\int_0^1 Z_i dz\,, \tag{25}$$

the orthogonality condition reduces Eq. (25) to

$$C_j A_{ji}\left(1+\frac{S_1}{S_2}\gamma_i^2\right)J_i^{(1)}=J_i^{(2)}\,, \tag{26}$$

where $J_i^{(1)}$ and $J_i^{(2)}$ are analytically calculated integrals. Writing Eq. (26) in a matrix form:

$$C_j A_{ji}=\frac{J_i^{(2)}}{\left(1+\frac{S_1}{S_2}\gamma_i^2\right)J_i^{(1)}}\,, \tag{27}$$

the unknown coefficients C_j are calculated by inversion of the matrix system (27).

Flow Across Rods with Volumetric Heat Generation

In the case of internal heat generation in the solid structure, Eq. (11) has an additional term:

$$D_1 u\frac{\partial T_s}{\partial x}+D_2\frac{\partial^4 T_s}{\partial z^4}-D_3\frac{\partial^2 T_s}{\partial z^2}-D_4 u\frac{\partial^3 T_s}{\partial x\partial z^2}+D_5=0\,, \tag{28}$$

which significantly complicates the solution procedure. The solid-phase temperature field T_s needs to be separated as

$$T_s(x,z)=T_b(z)+t_s(x,z)\,, \tag{29}$$

where T_b is a temperature field in absence of forced convection across the rod bundle (u = 0) and t_s is a solid-phase temperature residue. Inserting the decomposition (29) into Eq. (28), a separate equation is written for the temperature T_b :

$$D_2\frac{\partial^4 T_b}{\partial z^4}-D_3\frac{\partial^2 T_b}{\partial z^2}+D_5=0\,, \tag{30}$$

and for the temperature t_s :

$$D_1 u\frac{\partial t_s}{\partial x}+D_2\frac{\partial^4 t_s}{\partial z^4}-D_3\frac{\partial^2 t_s}{\partial z^2}-D_4 u\frac{\partial^3 t_s}{\partial x\partial z^2}=0\,. \tag{31}$$

The boundary conditions (4) are transformed to

$$\begin{aligned} &x=0: \quad t_s=1\,, \\ &z=0: \quad t_s=0\,, \quad T_b=0\quad, \\ &z=1: \quad \frac{\partial t_s}{\partial z}=0\,, \quad \frac{\partial T_b}{\partial z}=0\ . \end{aligned} \tag{32}$$

A solution of Eq. (30) is found in the following form :

$$T_b=B_1 exp(\xi z)+B_2 exp(-\xi z)+B_3+B_4 z+B_5 z^2\,, \tag{33}$$

where ξ, B_1, B_2, B_3, B_4, and B_5 are constants to be determined from the boundary conditions (32).

Equation (31) has the same form as Eq. (28) in the previous case. Therefore, separation of variables is used:

$$t_s=X(x)Z(z)\ . \tag{34}$$

Again, the solution for the z-direction of Eq. (31) is expressed as a finite set of n orthogonal functions:

$$Z=A_k Z_k\,,\ Z_k=\sin(\gamma_k z)\,,\ \gamma_k=\frac{2k-1}{2}\pi\,,\ k=1,n\,, \tag{35}$$

and the procedure to find $X(x)$ and $Z(z)$ is the same as in the previous case (Eqs. 14-21). Finally, the solution for temperature t_s can be expressed as:

$$t_s=C_j X_j A_{jk} Z_k\,, \tag{36}$$

where C_j is a vector of coefficients that has to be determined. Adding the temperature fields T_b (Eq. 33) to t_s (Eq. 36), the expression for the dimensionless solid-phase temperature T_s is written as

$$T_s=\left(B_1 exp(\xi z)+B_2 exp(-\xi z)+B_3+B_4 z+B_5 z^2\right)+C_j X_j A_{jk} Z_k\,. \tag{37}$$

Recalling Eq. (7) and inserting the expression for the solid-structure temperature T_s (Eq. 37), the dimensionless fluid temperature is given by

$$\begin{aligned} T_f=&C_j A_{jk}\left(1+\frac{S_1}{S_2}\gamma_k^2\right)Z_k \\ &+B_1\left(1-\frac{S_1}{S_2}\xi^2\right)exp(\xi z)+B_2\left(1-\frac{S_1}{S_2}\xi^2\right)exp(-\xi z)\ . \\ &+\left(B_3-2B_5\frac{S_1}{S_2}+\frac{S_3}{S_2}\right)+B_4 z+B_5 z^2 \end{aligned} \tag{38}$$

The coefficients C_j are found with help of the boundary condition $T_f(0, z) = 1$. Imposing it onto Eq. (38), the following form is obtained:

$$\begin{aligned} &C_j A_{jk}\left(1+\frac{S_1}{S_2}\gamma_k^2\right)Z_k=B_1\left(\frac{S_1}{S_2}\xi^2-1\right)exp(\xi z) \\ &+B_2\left(\frac{S_1}{S_2}\xi^2-1\right)exp(-\xi z)+\left(1-B_3+2B_5\frac{S_1}{S_2}-\frac{S_3}{S_2}\right)-B_4 z-B_5 z^2\ , \end{aligned} \tag{39}$$

Next, Eq. (39) is multiplied by orthogonal functions Z_i (i=1,n) and integrated from 0 to 1:

$$\begin{aligned} &C_j A_{jk}\left(1+\frac{S_1}{S_2}\gamma_k^2\right)\int_0^1 Z_k Z_i dz=B_1\left(\frac{S_1}{S_2}\xi^2-1\right)\int_0^1 exp(\xi z)Z_i dz \\ &+B_2\left(\frac{S_1}{S_2}\xi^2-1\right)\int_0^1 exp(-\xi z)Z_i dz \\ &+\left(1-B_3+2B_5\frac{S_1}{S_2}-\frac{S_3}{S_2}\right)\int_0^1 Z_i dz-B_4\int_0^1 z Z_i dz-B_5\int_0^1 z^2 Z_i dz \end{aligned} \tag{40}$$

Due to orthogonality of basis functions Z_i, the expression (40) is simplified to :

$$\begin{aligned} &C_j A_{ji}\left(1+\frac{S_1}{S_2}\gamma_i^2\right)J_i^{(1)}=B_1\left(\frac{S_1}{S_2}\xi^2-1\right)J_i^{(2)}+B_2\left(\frac{S_1}{S_2}\xi^2-1\right)J_i^{(3)} \\ &+\left(1-B_3+2B_5\frac{S_1}{S_2}-\frac{S_3}{S_2}\right)J_i^{(4)}-B_4 J_i^{(5)}-B_5 J_i^{(6)} \end{aligned} \tag{41}$$

where $J_i^{(1)}$, $J_i^{(2)}$, $J_i^{(3)}$, $J_i^{(4)}$, $J_i^{(5)}$ and $J_i^{(6)}$ are analytically calculated integrals. Writing Eq. (41) in the matrix form:

$$C_j A_{ji}=\frac{RHS}{\left(1+\frac{S_1}{S_2}\gamma_i^2\right)J_i^{(1)}} \tag{42}$$

the unknown coefficients C_j are calculated by inversion of the matrix system (42).

RESULTS AND DISCUSSION

The calculations have been performed for different pressure drops and thermal inputs (Table 1 & 2). The imposed pressure drop causes flow across the heated solid structure. As the structure is cooled, a steady temperature field is formed in the fluid as well as in the structure.

The results obtained with the Galerkin method have been compared with the results of the VAT model solved with the finite volume method, and in the first case also with the experimental data of Rizzi et al. (2001). Comparisons have been

made for the velocity field u, the temperature field in the fluid flow T_f and in the solid structure T_s. Further, the whole-section values of the drag coefficient C_d and the Nusselt number Nu have been compared with results from the finite volume method and with the experimental data.

Air-Stream Cooling of the Solid Structure

Calculations have been performed at heating power Q =50W, 125W and 220W to match the experimental data obtained by Rizzi et al. (2001). In this section we present only calculated values of the whole-section drag coefficient C_d and Nusselt number Nu for the heating power Q = 125W. It should be noted that although different heating power Q is used, there exists a similarity in force convection heat removal from the heat sink structure.

Simulations of the heat sink thermal behavior have been done for a range of pressure drops Δp and boundary temperatures T_{in} and T_g, that are summarized in Table 1.

Table 1: Boundary conditions - preset values.

No.	Δp[Pa]	T_{in} [°C]	T_g [°C]
1	5.0	23.0	103.8
2	10.0	23.0	74.6
3	20.0	23.0	58.8
4	40.0	23.0	48.2
5	74.7	23.2	41.8
6	179.3	23.2	35.7
7	274.0	23.0	33.6
8	361.1	22.8	32.3

For calculations performed with the Galerkin method, 34 mesh points in x- and 140 mesh points z-direction have been used to simulate heat transfer processes in the fluid- and the solid-phase. As the accuracy of the semi-analytical Galerkin method is essentially connected with the number of the orthogonal functions used for expansion, Eq. (22), 45 basis functions have been used in this case.

Based on the calculated velocity and temperature fields, the whole-section drag coefficient

$$C_d = 2\frac{\Delta\hat{p}\hat{A}_\perp}{\hat{\rho}_f [\hat{u}]^2 \hat{A}_o} \tag{43}$$

and the whole-section Nusselt number

$$Nu = \frac{[\hat{Q}]\hat{d}_h}{([\hat{T}_s]-[\hat{T}_f])\hat{A}_o \hat{\lambda}_f} \tag{44}$$

are estimated as functions of Reynolds number.

Figure 3 shows the whole-section drag coefficient C_d (Eq. 43) as a function of Reynolds number. The results calculated with the Galerkin method are close to the results obtained with the finite volume method as well as to the experimental data. Slight discrepancy from the experimental data at higher Reynolds number is due to transition to turbulence, which is evident on the experimental results, but is not captured by the model.

Figure 4 shows the whole-section Nusselt number Nu (Eq. 44), as a function of Reynolds number. The differences between the Galerkin method results, the finite volume method results and the experimental data are negligible as the Reynolds number increases from Re = 762 to Re = 1893.

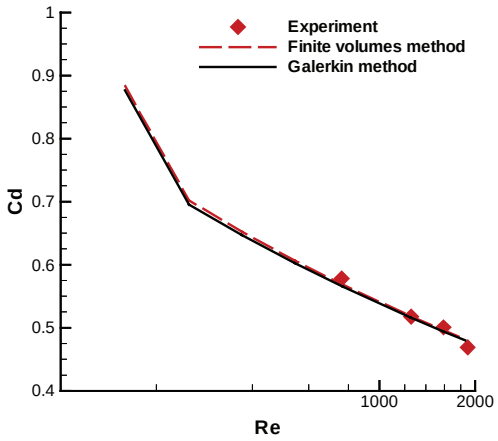

Figure 3: Whole-section drag coefficient C_d , 125W

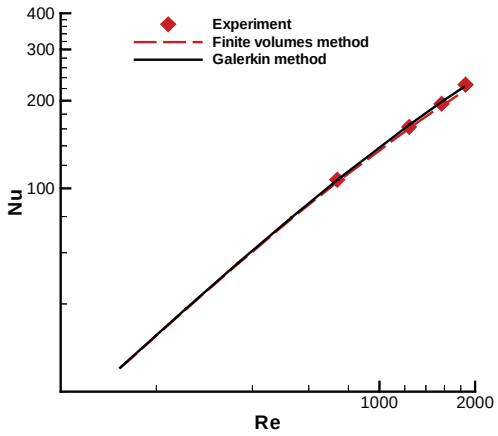

Figure 4: Whole-section Nusselt number Nu, 125W

Flow Across Rods with Volumetric Heat Generation

Three sets of calculations of the water flow across the heat generating rod bundle have been performed for the volumetric heat generation rate of 0.0 W/cm^3, 0.5 W/cm^3 and 2.0 W/cm^3. Due to space limitations, only the results for the last case are presented. The boundary values of pressure drops Δp and temperatures T_{in} and T_g used in this case are summarized in Table 2.

Table 2: Boundary conditions - preset values.

No.	Δp[Pa]	T_{in} [°C]	T_g [°C]
1	40.0	35.0	39.0
2	80.0	35.0	39.0
3	120.0	35.0	39.0
4	160.0	35.0	39.0
5	200.0	35.0	39.0
6	240.0	35.0	39.0
7	280.0	35.0	39.0
8	320.0	35.0	39.0
9	360.0	35.0	39.0

All calculations with the Galerkin approach have been done with 80 eigenfunctions. For the finite volume method simulations, 64 grid points have been used in the *x*-direction, and 80 grid points in *z*-direction.

Although, the whole section drag coefficient C_d and the Nusselt number *Nu* have also been determined, we have chosen to present the comparison of the velocity and the temperature fields calculated with the Galerkin method and the finite volume method.

Figure 5 shows the velocity distributions obtained with the Galerkin method (marked as GM) and the finite volume method (marked as FVM). Note that the core of the simulation domain has a flat velocity profile due to the drag associated with the submerged rods. The results comparison reveals an excellent agreement between both methods, although the VAT momentum equation in the present Galerkin solver (Eq. 9) is simply linearized.

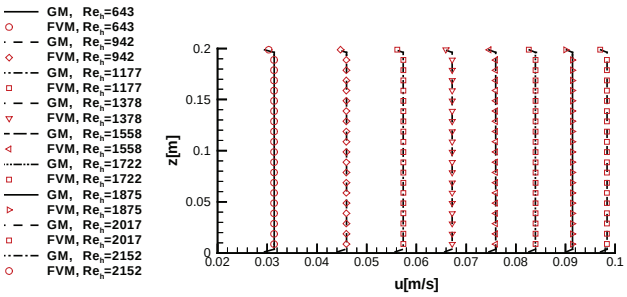

Figure 5: Velocity distribution for different Reynolds numbers

Figure 6 gives a temperature field cross-section in the water flow for the Reynolds number *Re* = 2152. The internal heat generation in the rods is set to I = 2.0 W/cm^3. The temperature fields are presented in the Celsius scale. Bold isotherms denote the results obtained with the Galerkin method and halftone (red) isotherms denotes temperatures obtained with the finite-volume method. Isotherms show that the fluid temperature increases in the horizontal direction, from the inflow to the outflow due to heat generating rods. Heating from the isothermal bottom is of minor importance.

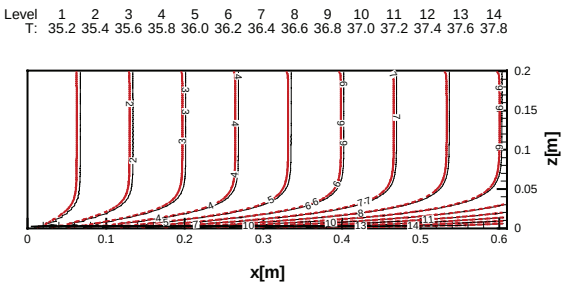

Figure 6: Temperature field in the water flow; I = 2.0 W/cm^3, *Re* = 2152; (—) Galerkin method, (– –) Finite volume method

Figure 7 shows the temperature in the aluminum structure. As the temperature of the fluid flow is higher at the exit than at the entrance, lack of cooling increases the temperatures in the solid structure. Due to higher thermal conductivity of the aluminum rods, the temperature field in the solid structure reveals higher vertical gradients close to the isothermal bottom surface than in the water flow.

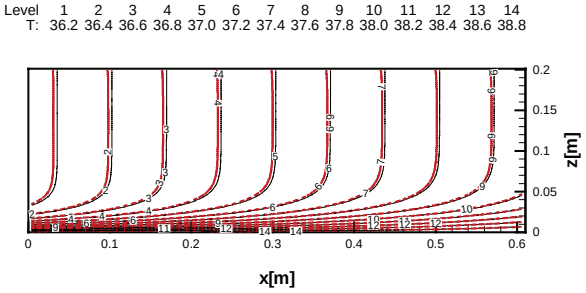

Figure 7: Temperature field in the solid rods; I = 2.0 W/cm^3, *Re* = 2152; (—) Galerkin method, (– –) Finite volume method

CONCLUSIONS

The paper presents an effort to utilize the Galerkin method for solving conjugate heat transfer problems in cross-flow condition.

In the scope of this work, the Volume Averaging Technique (VAT) was used to develop a specific form of the porous media flow models. The advantage of using VAT is that the computational algorithm is fast running, but still able to present a detailed picture of temperature fields in the fluid flow as well as in the solid structure.

The semi-analytical Galerkin procedure was developed to solve the system of equations. To show applicability of the Galerkin method, two examples were presented. In the first example, the velocity and the temperature fields were calculated for the air cooling of the aluminum heat sink. The second example showed the solution procedure for the flow across rods with volumetric heat generation.

The present paper gives only a part of results. Namely, for both cases, the whole-section drag coefficient C_d and the Nusselt number *Nu* were calculated and compared with the results of the finite volume method and in the first case also with the experimental data (Rizzi et al., 2001). The comparisons showed excellent agreement. The detailed velocity and temperature fields in the coolant flow as well as in the heat conducting structure were also calculated and compared with the results of the finite volume method. The comparisons show negligible differences between the results of both methods.

The present results demonstrate that the selected Galerkin approach is capable of solving thermal problems where the thermal conductivity and volumetric heat generation in the solid structure significantly influence the heat transfer and therefore have to be taken into account.

REFERENCES

Horvat, A. & Catton, I., 2001, Development of an Integral Computer Code for Simulation of Heat Exchangers, *Proc. Nuclear Energy in Central Europe 2001*, Portorož, Slovenia, Paper 213.

Horvat, A., 2002, Calculation of Conjugate Heat Transfer in a Heat Sink Using Volume Averaging Technique (VAT), M.Sc. Thesis, University of California, Los Angeles, USA.

Horvat, A. & Catton, I., 2003, Numerical Technique for Modeling Conjugate Heat Transfer in an Electronic Device Heat Sink, *Int. J. Heat Mass Transfer*, vol. 46, pp. 2155-2168.

Horvat, A. & Catton, I., 2003, Application of Galerkin Method to Conjugate Heat Transfer Calculation, *Numerical Heat Transfer B: Fundamentals*, vol. 44, No. 6, pp. 509-531.

Hu, K., 2001, Flow and Heat Transfer over Rough Surfaces in Porous Media, Ph.D. Thesis, University of California, Los Angeles, USA.

Kays, W.S. & London, A.L., 1998, *Compact Heat Exchangers*, 3rd Ed., Krieger Publishing Company, Malabar, Florida, pp. 152-155.

Launder, B.E. & Massey, T.H., 1978, The Numerical Prediction of Viscous Flow and Heat Transfer in Tube Banks, *J. Heat Transfer*, vol. 100, pp. 565-571.

Rizzi, M., Canino, M., Hu, K., Jones, S., Travkin, V., Catton, I., 2001, Experimental Investigation of Pin Fin Heat Sink Effectiveness, *Proc. 35th National Heat Transfer Conference*, Anaheim, California.

Travkin, V.S. & Catton, I., 1999, Transport Phenomena in Heterogeneous Media Based on Volume Averaging Theory, *Advans. Heat Transfer*, vol. 34, pp. 1-143.

Žukauskas, A. & Ulinskas, A., 1985, Efficiency Parameters for Heat Transfer in Tube Banks, *J. Heat Transfer Engineering*, vol. 5, No.1, pp. 19-25.

ACKNOWLEDGEMENTS

A. Horvat gratefully acknowledges the financial support received from the Kerze-Cheyovich scholarship and the Ministry of Higher Education, Science and Technology of RS under the project "Determination of morphological parameters for optimization of heat exchanger surfaces ".

NOMENCLATURE

A_o	interface area [m^2]
A_{ji}	eigenvectors [dimensionless]
$A_\perp$	$=W \cdot H$, channel flow area [m^2]
B_1	$= (S_3/S_1 - 2B_5)/(1+\xi^2 exp(2\xi))$ [dimensionless]
B_2	$= B_1 exp(2\xi)$ [dimensionless]
B_3	$= - B_1 - B_2$ [dimensionless]
B_4	$= -2\ B_5 - B_1\xi\ exp(\xi) + B_2\xi\ exp(-\xi)$ [dimensionless]
B_5	$= D_5/(2D_3)$ [dimensionless]
c_f	fluid specific heat [J/kgK]
C_d	drag coefficient [dimensionless]
d	diameter [m]
d_h	hydraulic diameter ($=4\Omega_f/A_o$) [m]
D_1	$= F_1$ [dimensionless]
D_2	$= F_4 S_1 / S_2$ [dimensionless]
D_3	$= F_5 S_1 / S_2 + F_4$ [dimensionless]
D_4	$= F_1 S_1 / S_2$ [dimensionless]
D_5	$= F_1 S_3 / S_1$ [dimensionless]
f	local drag coefficient [dimensionless]
F_1	$= \alpha_f c_f \rho_f U d_h / (\lambda_f L)$ [dimensionless]
F_4	$= \alpha_f d_h^2 / H^2$ [dimensionless]
F_5	$= h\ d_h^2 S / \lambda_f$ [dimensionless]
G_1	$= - M_4 / (K(1-\exp(\varepsilon)))$
G_2	$= -G_1 - M_4 / K$
G_3	$= M_4 / K$
h	heat transfer coefficient [W/m^2 K]
I	volumetric heat generation rate [W/m^3]
J_{kj}	analytically calculated integrals [dimensionless]
K	$= M_3 \lvert u \rvert$ [dimensionless]
L	length of the simulation domain [m]
M_2	$= \alpha_f \mu_f d_h / (\rho_f U H^2)$ [dimensionless]
M_3	$= f d_h S / 2$ [dimensionless]
M_4	$= d_h / L$ [dimensionless]
Nu	Nusselt number [dimensionless]
p	pitch [m]
Δp	pressure drop across simulation domain [Pa]
Q	thermal power [W]
Re	Reynolds number ($=\rho_f u d_h / \mu_f$) [dimensionless]
RHS	right-hand-side of the equation
S	specific interface surface [1/m]
S_1	$= \alpha_s d_h^2 / H^2$ [dimensionless]
S_2	$= h d_h^2 S / \lambda_s$ [dimensionless]
S_3	$= \alpha_s d_h^2 I / (\lambda_s (T_g - T_{in}))$ [dimensionless]
t_s	solid phase temperature residue [dimensionless]
T_b	solid phase temp. in absence of convection, [dimensionless]
T_f	fluid temperature [K], [dimensionless]
T_g	bottom temperature [K], [dimensionless]
T_{in}	inflow temperature [K], [dimensionless]
T_s	solid temperature [K] , [dimensionless]
U	velocity scale ($=\sqrt{\Delta p / \rho_f}$) [m/s]

Greek letters

α_f	fluid fraction [dimensionless]
α_s	solid fraction ($1-\alpha_f$) [dimensionless]
β	eigenvalues [dimensionless]
γ	$= \pi\ (2n-1)/2$ [dimensionless]
ε	$= \sqrt{K / M_2}$ [dimensionless]
Z	z - dependent part of T [dimensionless]
λ_f	fluid thermal conductivity [W/mK]
λ_s	solid thermal conductivity [W/mK]
ξ	$= \sqrt{D_3 / D_2}$ [dimensionless]
X	x - dependent part of T [dimensionless]
Ω_f	fluid volume [m^3]

Strojniški vestnik - Journal of Mechanical Engineering 51(2005)7-8, 534-537
UDK - UDC 536.2
Izvirni znanstveni članek - Original scientific paper (1.01)

Experimentation and Simulation of Thermal Energy Storage System with Non-Phase Change Materials

Thanakom Soontornchainacksaeng

Department of Mechanical Engineering,Faculty of Engineering
King Mongkut's lnstitute of Technology North Bangkok, Bangkok 10800, Thailand
e-mail : tss@kmitnb.ac.th

Abstract

This research a simulation study and experiment on the thermal energy storage system with non-phase change materials in the range of 50° - 150°C, this system is consisted of the storage tank size of 0.58 m in diameter, and 0.88 m in height, containing each set of the charging coil, and the discharging coil, embedded in the combination of 90% by volume of the used – engine oil, and 10% by volume of the river – water rocks. An electric heater is used as the heat source. The simulation of thermal-energy storage system with the mathematic modeling for the theoretical analysis of the system, and by using the Newton – Raphson method in the simulation process during the energy charging and discharging processes, The limitation of the charging oil temperature is maintained at 140°C with the flow rate in the range of 10 to18 l/min, whereas the inlet temperature of the discharge oil is maintained at 30°C with the flow rate of 6 to 14 l/min.

The computer simulation results with the charging time of 2 hours, and the oil flow rate of 14 l/min, The temperature of our storage media is increased by 60°C with the amount of heat gain by 23 MJ. And by our further simulation on discharging for 1 hour period, with the oil flow rate of 10 l/min, the storage temperature is decreased by 58°C, with the amount of heat removal of 23 MJ. It is found that results from the experiment are differed from the simulation by 3–5 %

Introduction

The Thermal energy may be stored as sensible heat. Sensible heat storage systems utilize the heat capacity and the change in temperature of the material during the process of charging or discharging - temperature of the storage material rises when energy is absorbed and drops when energy is withdrawn. One of the most attractive features of sensible heat storage systems is that charging and discharging operations can be expected to be completely reversible for an unlimited number of cycles. In the utilization of solar energy or waste heat from industrial, the storage of the energy received is of particular interest and importance because of the intermittent nature of solar energy. The energy storage system in this case must be able to retain the energy absorbed for at least a few days in order to be able to supply energy} as needed, on cloudy days when the energy input is small. For a small solar energy storage system time period of the variation is one day. Therefore, the storage system must be designed with both the energy input and the demand as important considerations.

S. Somasundaram, M.K. Drost, D.R. Brown, and Z.I. Antoniak.(1993), to study the "Intergrate thermal energy storage in power plant". There are committed to used the oil-rock storage or molten nitrate salt storage which to be better than anothers storage

T. Soontornchainacksaeng et al (1995) to study the water thermal energy storage system play an important role for continuous utilization of non-permanent existing energy source such as solar heating system. Storage tank can be separated into 3 parts which are ; 209 l – thermal storage tank containing 184 l of water, 30 cm-diameter charging coil made of 0.5 in. copper tube, and 30 cm-diameter discharging coil made of 0.5 in copper tube. The efficiency of thermal storage system while charging at all flow rate are nearly the same at 89% and the efficiency of the system while discharging at all flow rate are also the same of about 63%.

This paper considers the study and simulation of thermal-energy storage system with non-phase materials in the ranges of 50 to 150^{O}C. By using the Newton-raphson method in the simulation process during the energy charging and discharging processes.

Energy storage system principle

The study and simulation of thermal-energy storage system to be established and testing from the principle of the systems in fig. 1 shown the principle of energy storage system consist of ; storage tank is 0.58 m of diameters, 0.88 m of height and heating coils during charge and discharge. The heating coils are used copper tube, 0.016 m of outside diameter, includes the river-water rocks and used-engine oil test bed.

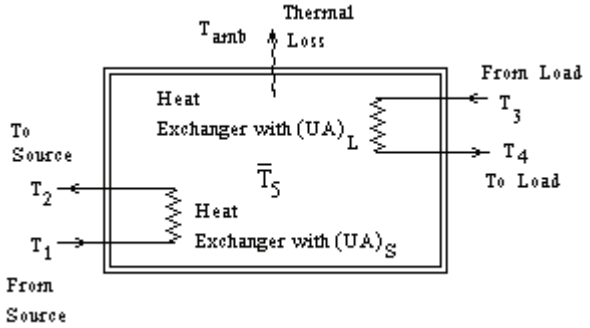

Fig. 1 principle of energy storage system

Assumptions of the system simulation are followings ; both of charge and discharge processes,

(1) The both of charge and discharge temperature are steady state conditions
(2) Non-stratified storage in the tank
(3) No mass transfer
(4) Constant temperature surroundings

Mathematical models of System

The energy storage system in fig. 1 can be to solved and show that in two cases, are consists in the case of charge and discharge temperatures following ;

(1) Charge the temperature into the systems

Heat losses during charge the energy into storage system have the relation as following ;

$$\Sigma Q_{loss} = \frac{1}{R_T}(\overline{T}_5 - T_{amb}) \qquad (1)$$

Heat storage in the system to be calculated from equation(2)

$$\Sigma Q_{st} = m.c_m(\overline{T}_{5,fi} - \overline{T}_{5,ini}) \qquad (2)$$

The outlet temperature of charge coils can be calculated form the equation(3) as following;

$$T_2 = \exp(\frac{-(U.A)_S}{\dot{m}_s.C_{f,s}})(T_1 - \overline{T}_5) + \overline{T}_5 \qquad (3)$$

The average temperature are into the storage tank is given the relation as following ;

$$\overline{T}_5(t) = C_1 + C_2.\exp(x_1.t) \qquad (4)$$

(2) Discharge the temperature from the systems

The discharge heat process are losses from the storage tank during these processes, may be calculated with the equation(5),

$$\Sigma Q_{loss} = \frac{1}{R_T}(\overline{T}_5 - T_{amb}) \qquad (5)$$

The discharge temperature are calculated with equation (6) , So

$$\Sigma Q_{out} = m.c_m(\overline{T}_{5,fi} - \overline{T}_{5,ini}) \qquad (6)$$

the outlet temperature are calculated with equation (7) , so

$$T_4 = \overline{T}_5 - \exp(\frac{-(U.A)_L}{\dot{m}_L.C_{f,L}})(\overline{T}_5 - T_3) \qquad (7)$$

The average temperature are into the storage tank during these processes with the relation as following ;

$$\overline{T}_5(t) = C_3 + C_4.\exp(x_2.t) \qquad (8)$$

These simulation are used the Newton – Raphson method and can be able to show that the relation of the variables of two cases that are charge and discharge processes.

Results of the system simulation

The parameters of the simulation systems are consisted of the flow rate of the oils in coils heat exchangers, ratio of rocks and oil by volume and the time used to charge and discharge in the storage system. The results of the simulations system are shown with the relations in Fig. 2 the average storage temperatures and heat storage,

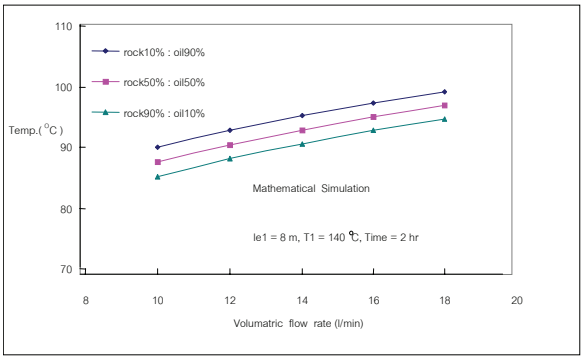

Fig. 2 The average temperatures in storage tank and volumetric flow rate (to charging 2 h)

In the Fig. 3, we found that when we choose the medium substance to collected heat with high heat capacity and high density as rock and oil respectively. It can be increased the heat storage to 4% approximately

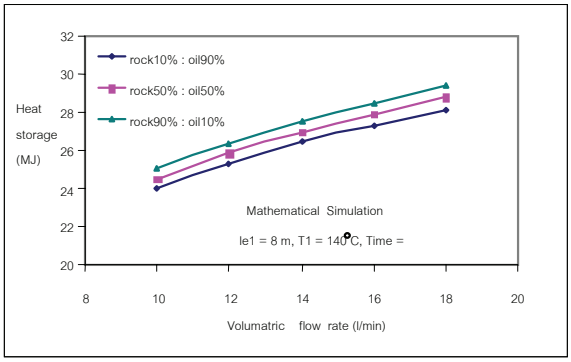

Fig. 3 Heat storage and volumetric flow rate (to charging 2 h)

In the Fig. 4 and 5 , when the thermal storage have high the heat capacity, It can be to discharged the heat from the storage system increase to 10% approximately

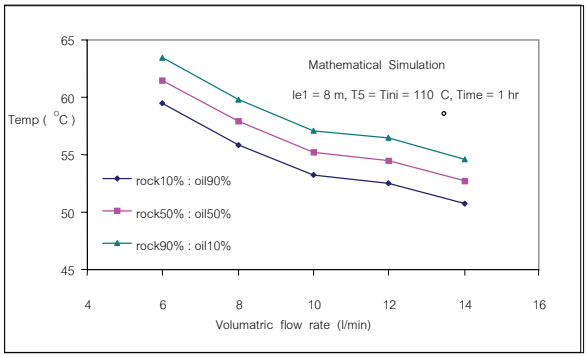

Fig. 4 The average temperatures in storage tank and volumetric flow rate (to discharging 1 h)

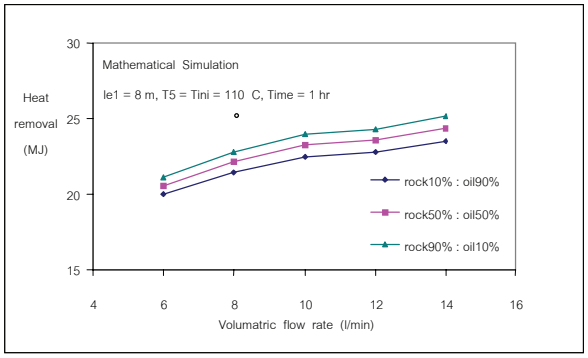

Fig. 5 Heat removal and volumetric flow rate (to discharging 1 h)

Experimental set-up

The experimental set-up is shown schematically in Figure 6 and 7. Its consisted of one storage and one water tank the two tanks which each of tank was 0.58 m diameters, 0.88 m high and 200 litres volume, gear pumps type GC-25 the inlet-out diameters was 1 inch, 55 l/min volumetric flow rate, electrically heated is 12 kW, water pump is 0.75 hp , flow controller, flow measurement tank, water tank and others accessories. So, the figure 6 is shown the schematic for charging systems and the figure 7 is shown the schematic for discharging systems respectively.

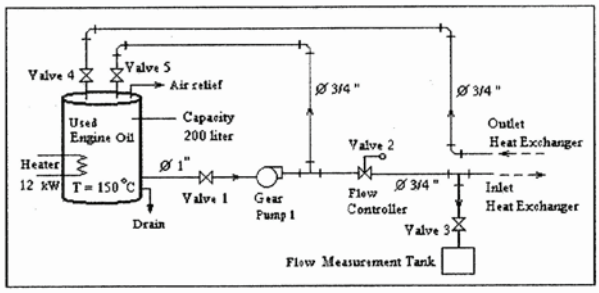

Fig. 6 Schematic representation of the experimental set-up in case of charging process.

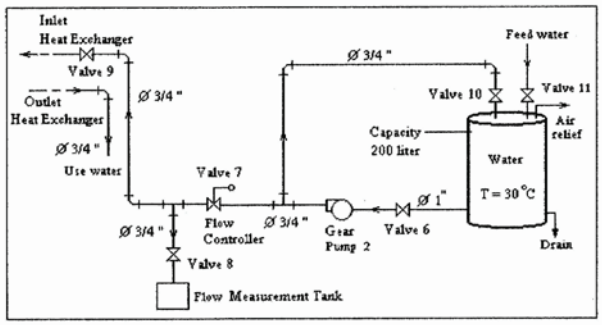

Fig. 7 Schematic representation of the experimental set-up in case of discharging process.

From the principle of this sensible heat storage system use materials that store energy as sensible heat. In this experimental; are used the engine-oil and rocks. The efficiency of thermal storage can be defined as the ratio of heat output to heat input, heat output being lower than the input by the amount of heat as in fig. 3 - 5. However, in the case of sensible heat storage the temperature of storage medium drops due to heat losses.

Experiment and simulation comparison

The Experiment and simulation comparison are shown schematically in Figure 8 and 11, these are consisted of two cases, the first case is the charging process and the another case is the discharging process, are shown in these followings,

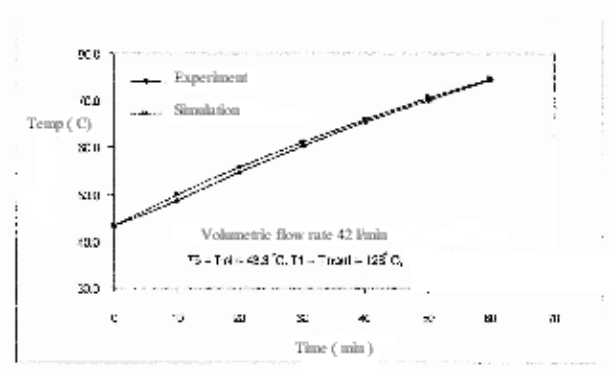

Fig. 8 The variations of the storage temperatures between experiment and simulations in case of charging systems

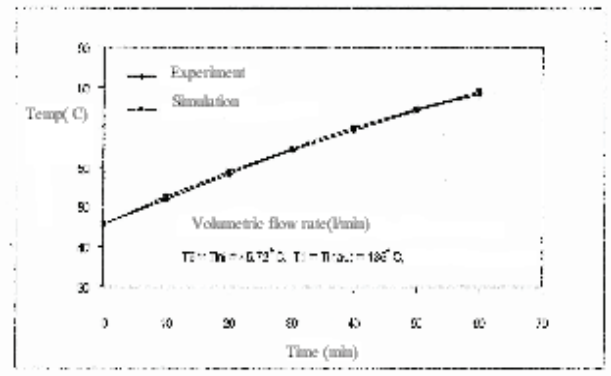

Fig. 9 The variations of the storage temperatures between experiment and simulations in case of

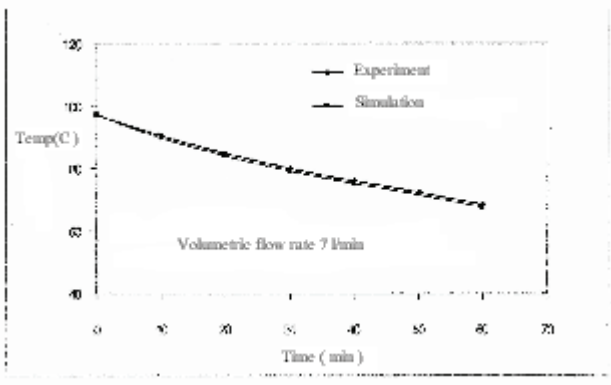

charging systems

Fig. 10 The variations of the storage temperatures between experiment and simulations in case of discharging systems

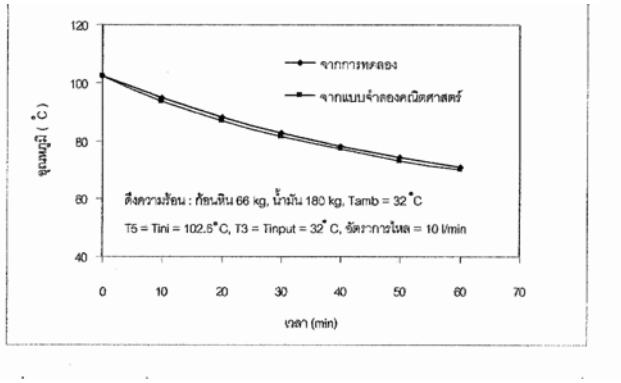

Fig. 11 The variations of the storage temperatures between experiment and simulations in case of discharging systems

Conclusions

Results of an experimentation and simulation on the our thermal energy storage systems which using the rocks and oil to be combined as storage materials in our system. We found that the ratio of rocks and oil have to be effect with the storage capacity. The computer simulation results with the charging time of 2 hours, and the oil flow rate of 14 l/min, The temperature of our storage medium is increased by 60° C with the amount of heat gain by 23 MJ. And by our further simulation on discharging for 1 hour period, with the oil flow rate of 10 l/min, the storage temperature is decreased by 58°C, with the amount of heat removal of 23 MJ. It is found that results from the experiment are differed from the simulation by 3–5 %

Acknowledgements

This work is supported by the Departement of mechanical engineering, Faculty of Engineering, King Mongkut's Institute of Technology North Bangkok and A. Thongchoi is a student and my assistant at the King Mongkut's Institute of Technology North Bangkok

References

T. Soontornchainacksaeng, J. Tontiwongwatana "Simulation of thermal energy storage with water " Department of Mechanical Engineering. Faculty of Engineering. King Mongkut's Institute of Technology north Bangkok., 1996

T. Soontornchainacksaeng "Heat Transfer" Top Publishing co.ltd., Bangkok, 2003.

T. Soontornchainacksaeng "Energy management" Departement of Mechanical Engineering, Faculty of Engineering, King Moungkut's of Technology North Bangkok, 1998.

S. Somasundaram, M.K. Drost, D.R. Brown, and Z.I. Antoniak. "Intergrate thermal energy storage in power plant" International Journal of Mechanical Engineering September 1993:84-90

Ramachadra K. Patil "Design a helical – coil heat exchanger" International Journal of Chemical Engineering December 13, 1982 : p. 85-88

Strojniški vestnik - Journal of Mechanical Engineering 51(2005)7-8, 539-540
Navodila avtorjem - Instructions for Authors

Navodila avtorjem - Instructions for Authors

Članki morajo vsebovati:
- naslov, povzetek, besedilo članka in podnaslove slik v slovenskem in angleškem jeziku,
- dvojezične preglednice in slike (diagrami, risbe ali fotografije),
- seznam literature in
- podatke o avtorjih.

Strojniški vestnik izhaja od leta 1992 v dveh jezikih, tj. v slovenščini in angleščini, zato je obvezen prevod v angleščino. Obe besedili morata biti strokovno in jezikovno med seboj usklajeni. Članki naj bodo kratki in naj obsegajo približno 8 strani. Izjemoma so strokovni članki, na željo avtorja, lahko tudi samo v slovenščini, vsebovati pa morajo angleški povzetek.

Za članke iz tujine (v primeru, da so vsi avtorji tujci) morajo prevod v slovenščino priskrbeti avtorji. Prevajanje lahko proti plačilu organizira uredništvo. Če je članek ocenjen kot znanstveni, je lahko objavljen tudi samo v angleščini s slovenskim povzetkom, ki ga pripravi uredništvo.

VSEBINA ČLANKA

Članek naj bo napisan v naslednji obliki:
- Naslov, ki primerno opisuje vsebino članka.
- Povzetek, ki naj bo skrajšana oblika članka in naj ne presega 250 besed. Povzetek mora vsebovati osnove, jedro in cilje raziskave, uporabljeno metodologijo dela,povzetek rezulatov in osnovne sklepe.
- Uvod, v katerem naj bo pregled novejšega stanja in zadostne informacije za razumevanje ter pregled rezultatov dela, predstavljenih v članku.
- Teorija.
- Eksperimentalni del, ki naj vsebuje podatke o postavitvi preskusa in metode, uporabljene pri pridobitvi rezultatov.
- Rezultati, ki naj bodo jasno prikazani, po potrebi v obliki slik in preglednic.
- Razprava, v kateri naj bodo prikazane povezave in posplošitve, uporabljene za pridobitev rezultatov. Prikazana naj bo tudi pomembnost rezultatov in primerjava s poprej objavljenimi deli. (Zaradi narave posameznih raziskav so lahko rezultati in razprava, za jasnost in preprostejše bralčevo razumevanje, združeni v eno poglavje.)
- Sklepi, v katerih naj bo prikazan en ali več sklepov, ki izhajajo iz rezultatov in razprave.
- Literatura, ki mora biti v besedilu oštevilčena zaporedno in označena z oglatimi oklepaji [1] ter na koncu članka zbrana v seznamu literature. Vse opombe naj bodo označene z uporabo dvignjene številke[1].

OBLIKA ČLANKA

Besedilo članka naj bo pripravljeno v urejevalnilku Microsoft Word. Članek nam dostavite v elektronski obliki.

Ne uporabljajte urejevalnika LaTeX, saj program, s katerim pripravljamo Strojniški vestnik, ne uporablja njegovega formata.

Enačbe naj bodo v besedilu postavljene v ločene vrstice in na desnem robu označene s tekočo številko v okroglih oklepajih

Papers submitted for publication should comprise:
- Title, Abstract, Main Body of Text and Figure Captions in Slovene and English,
- Bilingual Tables and Figures (graphs, drawings or photographs),
- List of references and
- Information about the authors.

Since 1992, the Journal of Mechanical Engineering has been published bilingually, in Slovenian and English. The two texts must be compatible both in terms of technical content and language. Papers should be as short as possible and should on average comprise 8 pages. In exceptional cases, at the request of the authors, speciality papers may be written only in Slovene, but must include an English abstract.

For papers from abroad (in case that none of authors is Slovene) authors should provide Slovenian translation. Translation could be organised by editorial, but the authors have to pay for it. If the paper is reviewed as scientific, it can be published only in English language with Slovenian abstract, that is prepared by the editorial board.

THE FORMAT OF THE PAPER

The paper should be written in the following format:
- A Title, which adequately describes the content of the paper.
- An Abstract, which should be viewed as a mini version of the paper and should not exceed 250 words. The Abstract should state the principal objectives and the scope of the investigation, the methodology employed, summarize the results and state the principal conclusions.
- An Introduction, which should provide a review of recent literature and sufficient background information to allow the results of the paper to be understood and evaluated.
- A Theory
- An Experimental section, which should provide details of the experimental set-up and the methods used for obtaining the results.
- A Results section, which should clearly and concisely present the data using figures and tables where appropriate.
- A Discussion section, which should describe the relationships and generalisations shown by the results and discuss the significance of the results making comparisons with previously published work. (Because of the nature of some studies it may be appropriate to combine the Results and Discussion sections into a single section to improve the clarity and make it easier for the reader.)
- Conclusions, which should present one or more conclusions that have been drawn from the results and subsequent discussion.
- References, which must be numbered consecutively in the text using square brackets [1] and collected together in a reference list at the end of the paper. Any footnotes should be indicated by the use of a superscript[1].

THE LAYOUT OF THE TEXT

Texts should be written in Microsoft Word format. Paper must be submitted in electronic version.

Do not use a LaTeX text editor, since this is not compatible with the publishing procedure of the Journal of Mechanical Engineering.

Equations should be on a separate line in the main body of the text and marked on the right-hand side of the page with numbers in round brackets.

Enote in okrajšave

V besedilu, preglednicah in slikah uporabljajte le standardne označbe in okrajšave SI. Simbole fizikalnih veličin v besedilu pišite poševno (kurzivno), (npr. *v, T, n* itn.). Simbole enot, ki sestojijo iz črk, pa pokončno (npr. ms^{-1}, K, min, mm itn.).

Vse okrajšave naj bodo, ko se prvič pojavijo, napisane v celoti v **slovenskem jeziku**, npr. časovno spremenljiva geometrija (ČSG).

Slike

Slike morajo biti zaporedno oštevilčene in označene, v besedilu in podnaslovu, kot sl. 1, sl. 2 itn. Posnete naj bodo v ločljivosti, primerni za tisk, v kateremkoli od razširjenih formatov, npr. BMP, JPG, GIF. Diagrami in risbe morajo biti pripravljeni v vektorskem formatu.

Pri označevanju osi v diagramih, kadar je le mogoče, uporabite označbe veličin (npr. *t, v, m* itn.), da ni potrebno dvojezično označevanje. V diagramih z več krivuljami, mora biti vsaka krivulja označena. Pomen oznake mora biti pojasnjen v podnapisu slike.

Vse označbe na slikah morajo biti dvojezične.

Preglednice

Preglednice morajo biti zaporedno oštevilčene in označene, v besedilu in podnaslovu, kot preglednica 1, preglednica 2 itn. V preglednicah ne uporabljajte izpisanih imen veličin, ampak samo ustrezne simbole, da se izognemo dvojezični podvojitvi imen. K fizikalnim veličinam, npr. *t* (pisano poševno), pripišite enote (pisano pokončno) v novo vrsto brez oklepajev.

Vsi podnaslovi preglednic morajo biti dvojezični.

Seznam literature

Vsa literatura mora biti navedena v seznamu na koncu članka v prikazani obliki po vrsti za revije, zbornike in knjige:

[1] Tarng, Y.S., Y.S. Wang (1994) A new adaptive controller for constant turning force. *Int J Adv Manuf Technol* 9(1994) London, pp. 211-216.

[2] Čuš, F., J. Balič (1996) Rationale Gestaltung der organisatorischen Abläufe im Werkzeugwesen. *Proceedings of International Conference on Computer Integration Manufacturing,* Zakopane, 14.-17. maj 1996.

[3] Oertli, P.C. (1977) Praktische Wirtschaftskybernetik. *Carl Hanser Verlag,* München.

Podatki o avtorjih

Članku priložite tudi podatke o avtorjih: imena, nazive, popolne poštne naslove in naslove elektronske pošte.

SPREJEM ČLANKOV IN AVTORSKE PRAVICE

Uredništvo Strojniškega vestnika si pridržuje pravico do odločanja o sprejemu članka za objavo, strokovno oceno recenzentov in morebitnem predlogu za krajšanje ali izpopolnitev ter terminološke in jezikovne korekture.

Avtor mora predložiti pisno izjavo, da je besedilo njegovo izvirno delo in ni bilo v dani obliki še nikjer objavljeno. Z objavo preidejo avtorske pravice na Strojniški vestnik. Pri morebitnih kasnejših objavah mora biti SV naveden kot vir.

Units and abbreviations

Only standard SI symbols and abbreviations should be used in the text, tables and figures. Symbols for physical quantities in the text should be written in italics (e.g. *v, T, n,* etc.). Symbols for units that consist of letters should be in plain text (e.g. ms^{-1}, K, min, mm, etc.).

All abbreviations should be spelt out in full on first appearance, e.g., variable time geometry (VTG).

Figures

Figures must be cited in consecutive numerical order in the text and referred to in both the text and the caption as Fig. 1, Fig. 2, etc. Pictures may be saved in resolution good enough for printing in any common format, e.g. BMP, GIF, JPG. However, graphs and line drawings sholud be prepared as vector images.

When labelling axes, physical quantities, e.g. *t, v, m,* etc. should be used whenever possible to minimise the need to label the axes in two languages. Multi-curve graphs should have individual curves marked with a symbol, the meaning of the symbol should be explained in the figure caption.

All figure captions must be bilingual.

Tables

Tables must be cited in consecutive numerical order in the text and referred to in both the text and the caption as Table 1, Table 2, etc. The use of names for quantities in tables should be avoided if possible: corresponding symbols are preferred to minimise the need to use both Slovenian and English names. In addition to the physical quantity, e.g. *t* (in italics), units (normal text), should be added in new line without brackets.

All table captions must be bilingual.

The list of references

References should be collected at the end of the paper in the following styles for journals, proceedings and books, respectively:

[1] Tarng, Y.S., Y.S. Wang (1994) A new adaptive controller for constant turning force. *Int J Adv Manuf Technol* 9(1994) London, pp. 211-216.

[2] Čuš, F., J. Balič (1996) Rationale Gestaltung der organisatorischen Abläufe im Werkzeugwesen. *Proceedings of International Conference on Computer Integration Manufacturing,* Zakopane, 14.-17. maj 1996.

[3] Oertli, P.C. (1977) Praktische Wirtschaftskybernetik. *Carl Hanser Verlag,* München.

Author information

The information about the authors should be enclosed with the paper: names, complete postal and e-mail addresses.

ACCEPTANCE OF PAPERS AND COPYRIGHT

The Editorial Committee of the Journal of Mechanical Engineering reserves the right to decide whether a paper is acceptable for publication, obtain professional reviews for submitted papers, and if necessary, require changes to the content, length or language.

Authors must also enclose a written statement that the paper is original unpublished work, and not under consideration for publication elsewhere. On publication, copyright for the paper shall pass to the Journal of Mechanical Engineering. The JME must be stated as a source in all later publications.